# Metal-Ligand Redox Interaction in the Multielectron Chemistry of Porphyrinogen Coordination Compounds

Julien Bachmann

*Chimiste Diplômé*, University of Lausanne (2001)

Submitted to the Department of Chemistry
In Partial Fulfillment of the Requirements
For the Degree of

DOCTOR OF PHILOSOPHY IN INORGANIC CHEMISTRY

at the

MASSACHUSETTS INSTITUTE OF TECHNOLOGY

June 2006

© 2006 Massachusetts Institute of Technology. All rights reserved.

Signature of Author: ________________________________________

Department of Chemistry
May 15, 2006

Certified by: ________________________________________

Daniel G. Nocera
W. M. Keck Professor of Energy and Professor of Chemistry
Thesis Supervisor

Accepted by: ________________________________________

Robert W. Field
Haslam and Dewey Professor of Chemistry
Chairman, Department Committee on Graduate Studies

This doctoral thesis has been examined by a Committee of the Department of Chemistry as follows:

Professor Richard R. Schrock ____________________________________________

Frederick G. Keyes Professor of Chemistry
Chairman

Professor Daniel G. Nocera ____________________________________________

W. M. Keck Professor of Energy and Professor of Chemistry
Thesis Supervisor

Professor Stephen J. Lippard ____________________________________________

Arthur Amos Noyes Professor of Chemistry

“Everything you can imagine is real.”

*Pablo Picasso*

*to Sandrine and Igor*

# METAL-LIGAND REDOX INTERACTION IN THE MULTIELECTRON CHEMISTRY OF PORPHYRINOGEN COORDINATION COMPOUNDS

by Julien Bachmann

Submitted to the Department of Chemistry
on May 15, 2006 in partial fulfillment
of the requirements for the degree of
Doctor of Philosophy in Inorganic Chemistry

## Abstract

Metal complexes of the macrocycle porphyrinogen (calix[4]pyrrole) are studied with an emphasis on the redox activity ("non-innocence") of the ligand (Chapter I).

Porphyrinogen complexes of spherical, redox-inert metal dications exist in three oxidation states, dianionic, neutral, and dicationic, characterized structurally by zero, one, and two direct bonds between adjacent pyrroles, respectively. All three are isolated on the preparative scale, and interconverted electrochemically (Chapter II). Each carbon-carbon bond functions as a reservoir of two redox equivalents. The neutral oxidation state exhibits an optical intervalence charge transfer transition, characteristic of ligand-based two-electron mixed valency (Chapter III). Dianionic zinc porphyrinogen reacts with carbon dioxide, and neutral zirconium(IV) porphyrinogen with dioxygen. Two zirconium porphyrinogen units can carry a water molecule as an oxo bridging the metals and two protons on the ligands (Chapter IV).

Iron porphyrinogen has three available oxidation states, a dianion, a monoanion, and a dication. The interconversion of the latter two is a selective three-electron transformation, preparatively and electrochemically (Chapter V). Crystallographic analysis shows that both anionic oxidation states contain the reduced ligand, whereas the dicationic state is based on the oxidized ligand (with two C—C bonds). Paramagnetic NMR confirms the structures in solution. Spectroscopies (EPR, Mössbauer) allow the assignment of well-defined individual oxidation and spin states states for the metal within each overall oxidation state of the complex (Chapter VI). The iron porphyrinogen dication is an oxidant based on an iron(II) center; it oxidizes iodide to diiodine (Chapter VII). The cobalt(II) porphyrinogen dianion can take up two protons, then photoreact to yield reduction of at least one proton to a metal-bound hydride, as evidenced by infrared spectroscopy (Chapter VIII).

Overall, the results afford a picture of metal-porphyrinogens including structure, electronic structure, and reactivity. The ligand supplements the central metal ion by functioning as a multielectron reservoir. Therefore, the (metal-based) coordination and (ligand-based) redox properties of a given porphyrinogen complex are largely decoupled from each other and can be chosen independently (Chapter IX).

Thesis supervisor: Daniel G. Nocera
W. M. Keck Professor of Energy and Professor of Chemistry

# Abstracts

## Chapter I
## A perspective on multielectron reactions and the agents that perform them

Pure electron transfer (ET) is the simplest type of redox reaction. More complex redox transformations can involve the exchange of several electrons as well as nuclei, as in proton-coupled electron transfers, group transfers and oxidative additions / reductive eliminations. As a general characteristic, such reactions are slow when performed *via* a concerted pathway, this because acid-base and ET reactive coordinates mutually affect each other. Enzymes often accelerate them by decoupling the acid-base coordinate from the ET coordinate and performing the reaction in a series of steps, each involving a pure ET or pure acid-base event. This is particularly true in metalloenzymes implicated in the metabolism of dioxygen. One of the methods evolved by biological systems to partly separate ET and acid-base coordinates is the use of a ligand as an ancillary redox reservoir. In synthetic systems, instances of such ligand-based redox activity have been established, however the phenomenon has remained very limited in terms of applications and extensions to multiple redox equivalents. Porphyrinogen is a ligand with demonstrated extensive redox possibilities (four equivalents) but properties that have remained undefined to date. Its accurate study is proposed.

## Chapter II
## Electron transfer series of porphyrinogen complexes with redox-inert metal dications — synthesis and structures

Porphyrinogen complexes of the redox-inert, spherical dications of magnesium, zinc and calcium can be prepared in three oxidation states — dianionic ($[LM^{II}]^{2-}$), neutral ($[L^{\Delta}M^{II}]$), and dicationic ($[L^{\Delta\Delta}M^{II}]^{2+}$), in the exclusive presence of counter-ions that are redox-inactive, spectroscopically silent, and chemically unreactive. The dianions are defined structurally in solution by NMR to contain the reduced, $D_{2d}$-symmetric ligand $L^{4-}$, and the dications the oxidized, $C_{2v}$-symmetric $L^{\Delta\Delta}$. The solid-state structure of $[L^{\Delta}Zn]$ shows that the intermediary oxidation state $L^{\Delta 2-}$ of the ligand features a dipyrrole oxidized by two electrons and with a direct C—C bond, juxtaposed with a reduced dipyrrole. The presence of a C—C bond creates an equilateral cyclopropane (Δ) between a pair of adjacent pyrroles. The structure of $[L^{\Delta}Mg]$ is qualitatively and quantitatively identical to that of $[L^{\Delta}Zn]$, with the exception of the position of the $M^{2+}$ ion within the macrocycle: relative to $Zn^{2+}$, the smaller $Mg^{2+}$ moves closer to the smaller cleft defined by the oxidized dipyrrole. The electrochemistry of Zn-porphyrinogen is defined by two waves at +0.21 and +0.63 V *vs* NHE, corresponding to the redox couples $[L^{\Delta}M^{II}]$ / $[LM^{II}]^{2-}$and $[L^{\Delta\Delta}M^{II}]^{2+}$ / $[L^{\Delta}M^{II}]$, respectively.

## Chapter III
## Electron transfer series of porphyrinogen complexes with redox-inert metal dications — electronic structures

The $[L^{\Delta}M^{II}]$ complexes are red, orange, and yellow for $M = Mg$, Zn, and Ca, respectively, whereas the reduced and oxidized counterparts are colorless. The energy dependence of the corresponding UV-vis absorption on solvent polarity and metal ion position is consistent with its assignment to an intervalence charge transfer (IVCT) transition. Theoretical methods give a comprehensive picture of the two-electron mixed-valent nature of the $L^{\Delta 2-}$ ligand, the localization of the HOMOs on the reduced dipyrrole and of the LUMOs on the oxidized dipyrrole, and the electrostatic effect of the central metal ion which gives rise to the observed tuning of the IVCT as a function of structure. Ultrafast spectroscopy establishes that no excited state has a lifetime exceeding 20 ps, an observation attributed to the large reorganization necessary between the mixed-valent ground state and the valence-symmetric excited state. However, a structurally fourfold symmetrical triplet excited state exists at very low energy.

### Chapter IV

### Reactivity of porphyrinogen complexes of redox-inactive $d^0$ and $d^{10}$ metal ions

The ligand *meso*-octabenzylporphyrinogen is synthesized from pyrrole and dibenzylketone. The metallation of it and the octamethyl version to the corresponding zirconium(IV) complexes are performed with a homoleptic zirconium amide reagent. Structurally, the high Lewis acidity of the Zr(IV) center is manifested in the presentation of one of the porphyrinogen pyrroles in $\eta^5$ mode. A 2:1 adduct of Zr-porphyrinogen with water is characterized in which water has been split to its constituent ions: the oxide bridges both Zr centers, and the protons are coordinated to a $C^{\alpha}$ atom of two pyrroles. Preliminary experiments show that the neutral Zr(IV)-octabenzylporphyrinogen reacts with dioxygen and xenon difluoride, and Zn-octamethylporphyrinogen with carbon dioxide.

### Chapter V

### Electron transfer series of iron porphyrinogen — synthesis and structures

Iron porphyrinogen can be isolated in three oxidation states (OSs) — dianionic ($[LFe^{II}]^{2-}$), monoanionic ($LFe^{III}]^{-}$), and dicationic ($[L^{\Delta\Delta}Fe^{II}]^{2+}$) — as salts of counter-ions that are exclusively redox-inactive, spectroscopically silent, and chemically inert. The transformation between $[LFe^{III}]^{-}$ and $[L^{\Delta\Delta}Fe^{II}]^{2+}$ is a selective three-electron event. The two redox couples appear electrochemically at –0.57 and +0.77 V *vs* NHE. In the solid state, the anionic species exist as $D_{2d}$-symmetrical entities based on a square coordination of the metal, while the pyrrole nitrogens of the dication define a rectangle, the short sides of which correspond to each cyclopropanated dipyrrole. Relative to this rectangle, the iron center is out-of-plane, completing its coordination with an acetonitrile solvent molecule. Structural analysis of the three paramagnetic species in solution is possible by NMR. $^1H$ and $^2H$ spectra of the *meso*-deuterated compounds reveal their symmetry properties simply and unambiguously

### Chapter VI

### Electron transfer series of iron porphyrinogen — electronic structures

Within each of the three overall OSs available to the Fe-porphyrinogen entity, an integer individual OS of the ligand is assigned unambiguously from the structural information provided in the solid state by diffraction methods, and in solution by NMR, given that each "Δ" C—C bond is worth two units of OS. Individual OSs for the metal are determined spectroscopically and magnetically. EPR, Mössbauer, UV-vis spectroscopies as well as SQUID magnetometry concur to assign a Fe(III, S = 3/2) to $[LFe^{III}]^{-}$, Fe(II, S = 2) to $[LFe^{II}]^{2-}$, and Fe(II, S = 1) to $[L^{\Delta\Delta}Fe^{II}]^{2+}$. Theoretical methods confirm that metal-based and ligand-based orbitals are clearly separated from each other, which results in less than 1% of the spin being located on the organic periphery. Ultrafast techniques are used to probe the dynamics of the system, and establish that the charge-transfer excited state decays extremely quickly because the large structural reorganization that it requires strongly couples it to the ground state through the corresponding vibrational mode(s).

Chapter VII

## Multielectron reactivity of the iron porphyrinogen dication, $[\mathrm{L}^{\Delta\Delta}\mathrm{Fe}^{\mathrm{II}}]^{2+}$

The iron porphyrinogen dication, $[\mathrm{L}^{\Delta\Delta}\mathrm{Fe}^{\mathrm{II}}]^{2+}$, is an unusual oxidant based on a low-valent Fe(II) center. Its low Lewis acidic character manifests itself in its reaction with iodide: instead of forming a thermodynamically stable adduct with the halide, it oxidizes it stoichiometrically to the dihalogen. The chloride adduct is stable, however, and can be obtained either from $[\mathrm{L}^{\Delta\Delta}\mathrm{Fe}^{\mathrm{II}}]^{2+}$ by reaction with a chloride salt or from $[[\mathrm{L}^{\Delta\Delta}\mathrm{Fe}^{\mathrm{II}}]^{2+}$ by oxidation with $\mathrm{AuCl}_3$ or $\mathrm{PhICl}_2$. The trimethylsiloxo adduct yields an oxidant upon cleavage of the Si—O bond with a fluoride, which is then reduced to $[\mathrm{LFe}^{\mathrm{III}}]^-$ upon reaction with a variety of substrates, however without detectable formation of products of O atom transfer. Such behavior is attributed to preferential H atom abstraction from solvent and substrate.

Chapter VIII

## Photochemical reduction of a proton by cobalt porphyrinogen

The cobalt(II) porphyrinogen dianion features a square coordination of Co(II) by the four pyrroles. Its electrochemistry shows two waves at −0.30 and +0.65 V, akin to those observed with the related Fe compound. It can be protonated by two equivalents of pyridinium with retention of the Co ion, both protons being bonded to the ligand as witnessed in NMR by a complete loss of symmetry. The protonated species undergoes a clean photoreaction in the near UV in dichloromethane, and the photoproduct has regained fourfold symmetry. The presence of a $^1$H NMR signal at extreme downfield shifts ($\delta > +140$ ppm) and of infrared bands in the 1900-cm$^{-1}$ region are evidence for the presence of at least one Co—H bond. Thus, cobalt(II) porphyrinogen is able to simultaneously store two protons and two electrons thanks to the active participation of the ligand, and photochemically reduces a proton to a hydride.

Chapter IX

## Conclusions and outlook

The findings of the previous seven Chapters are reviewed and put in perspective. The dissertation establishes synthetic methods to obtain oxidized metal porphyrinogens without special stabilization by complicated transition metal-containing polynuclear counter-ions. Electrochemical benchmarks are defined, and series of species differing only by their OS are compared structurally. A palette of experimental and theoretical techniques contribute to drawing a detailed picture of the electronic structures in ground and, to some extent, excited states. Complexes of oxidized porphyrinogen tend to react in single-electron steps that are challenging to control but are reminiscent of the behavior of redox metalloenzymes. This is likely a hallmark of ligand-based redox activity, and could potentially be exploited towards the design of novel chemical transformations.

# Table of contents

Title page 1
Thesis Committee 2
Dedication 5
Abstracts 7

Table of contents 13
List of Figures 18
List of Schemes 21
List of Tables 23
List of abbreviations 25

**Chapter I. A perspective on multielectron reactions and the agents that perform them 31**

1. Redox reactions 32
    a. Single electron transfer 32
    b. More involved redox reactions 33
    c. Commonalities of all multicomponent redox reactions, and coping strategies 39
2. Redox-active ligands 46
    a. Small molecules, the oxidation state of which changes upon coordination 47
    b. Constructs with redox-active fragments appended onto ligands 48
    c. Genuine redox-active ligands 49
    d. Limitations of well-established classes of redox-active ligands, and appealing features of porphyrinogen 51
3. Metal porphyrinogens 53
    a. Background 53
    b. Goals 57
4. References 58

**Chapter II. Electron transfer series of porphyrinogen complexes with redox-inert metal dications — synthesis and structures . . . 69**

1. Introduction . . . 70
2. Synthesis . . . 71
    a. Metallations . . . 71
    b. Oxidations . . . 72
3. Structures . . . 74
    a. Structural information provided spectroscopically . . . 74
    b. Crystal structures . . . 77
4. Electrochemistry . . . 80
5. Conclusions . . . 81
6. Experimental section . . . 82
    a. Synthesis . . . 82
    b. Spectroscopy . . . 87
    c. Electrochemistry . . . 87
    d. Crystallography . . . 88
7. References . . . 89

**Chapter III. Electron transfer series of porphyrinogen complexes with redox-inert metal dications — electronic structures . . . 91**

1. Mixed valency in a variety of flavors and colors . . . 92
2. Origin of a visible color . . . 93
    a. UV-vis spectra . . . 93
    b. Theoretical description . . . 96
3. Structural tuning of the IVCT . . . 102
4. Excited state dynamics . . . 104
5. Conclusions . . . 105
6. Experimental section . . . 107
    a. Physical measurements . . . 107
    b. Computational methods . . . 108
    c. Transient absorption spectroscopy . . . 109
7. References . . . 110

**Chapter IV. Reactivity of porphyrinogen complexes of redox-inactive $d^0$ and $d^{10}$ metal ions . . . 113**

1. Introduction . . . 114
2. A new porphyrinogen ligand . . . 114
   a. From 4-*tert*butylcyclohexanone . . . 115
   b. From 3,3,5,5-tetramethylcyclohexanone . . . 116
   c. From dibenzylketone . . . 118
3. Zirconium porphyrinogen . . . 119
   a. Coordination chemistry . . . 119
   b. Redox chemistry . . . 127
4. Reaction of zinc porphyrinogen with $CO_2$ . . . 129
5. Conclusions . . . 130
6. Experimental section . . . 131
   a. Synthesis . . . 131
   b. X-ray crystal structure determinations . . . 134
7. References . . . 135

**Chapter V. Electron transfer series of iron porphyrinogen — synthesis and structures . . . 137**

1. Introduction . . . 138
2. Synthesis . . . 139
   a. Metallation . . . 139
   b. Oxidation-reduction . . . 143
3. Electrochemistry . . . 144
4. Structures . . . 147
   a. In the solid state — by crystallography . . . 147
   b. In solution — by NMR . . . 153
5. Conclusions . . . 155
6. Experimental section . . . 157
   a. Synthesis . . . 157
   b. X-ray crystal structure determinations . . . 159
   c. Physical measurements . . . 161
   d. Electrochemistry . . . 161
7. References . . . 162

**Chapter VI. Electron transfer series of iron porphyrinogen — electronic structures** 167

1. Introduction 168
2. Experimental characterization of the ground state 169
    - a. Results from NMR and X-ray crystallography 169
    - b. UV-vis absorption 169
    - c. EPR 170
    - d. Mössbauer 171
    - e. Magnetism 173
    - f. In summary 173
3. Theory 173
    - a. On the assignment of individual oxidation states 173
    - b. On the nature of the $C^{\alpha}$—$C^{\alpha}$ bonding 177
4. Excited-state dynamics 180
5. Conclusions 181
6. Experimental section 182
    - a. Steady-state measurements 182
    - b. Transient absorption spectroscopy 183
    - c. Computational methods 184
7. References 184

**Chapter VII. Multielectron reactivity of the iron porphyrinogen dication, $[L^{\Delta\Delta}Fe^{II}]^{2+}$** 189

1. Introduction 190
2. Results 190
3. Conclusions 199
4. Experimental section 202
    - a. Synthesis and reactivity 202
    - b. X-ray crystal structure determinations 205
    - c. Physical methods 206
5. References 207

**Chapter VIII. Photochemical reduction of a proton by cobalt porphyrinogen 211**
1. Introduction 212
2. Cobalt porphyrinogens, synthesis and structure 213
    a. Metallation and oxidation 213
    b. Structures 215
3. Protonation and photoreaction 219
    a. Protonation 219
    b. Photoreaction 221
4. Conclusions 223
5. Experimental section 225
    a. Synthesis 225
    b. Physical techniques 227
6. References 228

**Chapter IX. Conclusions and outlook 233**
1. Electron transfer series of metal-porphyrinogens 234
    a. Preparation with “simple” counter-ions 234
    b. Electrochemistry 235
2. Electronic structures 238
3. Potential for multielectron reactivity 240
    a. The facts 240
    b. Novel avenues 241
    c. Hydrogen atom abstraction in chemistry and biology 242
    d. A last word 244
4. References 244

Acknowledgements 249
Biographical note 254
*Curriculum vitae* 255
List of publications 256

# List of Figures

## Chapter I

Figure I.1. Single electron transfer
Figure I.2. Two contrasting PCET mechanisms in closely related systems
Figure I.3. Three lines of reactivity originating from the porphyrinogen structure

## Chapter II

Figure II.1. Crystal structure of zinc difluorophosphate
Figure II.2. $^1$H and $^{13}$C NMR spectra of $Li_2(THF)_4[LZn]$
Figure II.3. β-Pyrrole region of the $^1$H NMR spectra of $[LZn]^{2-}$ and $[L^{\Delta\Delta}Zn]^{2+}$
Figure II.4. Crystal structures of $[L^{\Delta}M(NCMe)] \cdot CH_2Cl_2$, M = Zn, Mg
Figure II.5. Electrochemistry of zinc porphyrinogen

## Chapter III

Figure III.1. UV-vis absorption spectra of $Li_2(THF)_x[LZn]$, $[L^{\Delta}Zn(CH_3CN)]$, and $[L^{\Delta\Delta}Zn](BF_4)_2$
Figure III.2. A simplified representation of the IVCT in $[L^{\Delta}Zn]$, and its consequence on the molecular dipole $\mu_D$.
Figure III.3. Computed Kohn-Sham MO diagram of $[L^{\Delta}Zn(NCMe)]$ in the gas phase
Figure III.4. A simplified description of the orbital interactions leading to the MO structure of the oxidized (neutral) dipyrromethane unit
Figure III.5. Comparison of computed singlet and triplet states of neutral zinc porphyrinogen
Figure III.6. UV-visible absorption spectra of $[L^{\Delta}Mg]$, $[L^{\Delta}Zn]$ and $[L^{\Delta}Ca]$
Figure III.7. TA signal of $[L^{\Delta}Mg]$
Figure III.8. Fundamental differences between one- and two-electron mixed valency and their respective IVCT states

### Chapter IV

Figure IV.1. Crystal structure of 2,5-bis(3′,3′,5′,5′-tetramethylcyclohex-1′-enyl)pyrrole

Figure IV.2. Crystal structure of octabenzylporphyrinogen

Figure IV.3. Crystal structures of $\mathrm{LZr^{IV}(NHMe_2)(THF)}$ and $\mathrm{^{Ph}LZr^{IV}(NHMe_2)(THF) \bullet THF}$

Figure IV.4. Crystal structure of $\mathrm{[HLZr^{IV}]_2O}$

Figure IV.5. Fluorescence of an oxidation product of $\mathrm{LZr^{IV}(NHMe_2)(THF)}$ by $\mathrm{Me_3NO}$ in the presence of $\mathrm{Me_3SnCl}$

### Chapter V

Figure V.1. Crystal structure of $\mathrm{[(THF)_3Fe^{II}(\mu\text{-}Cl)_3Fe^{II}(THF)_3]\ [(THF)_4Fe^{II}(\mu\text{-}Cl)_2Fe^{II}(THF)_4]_{1/2}\ [LFe^{III}]_2 \bullet 2\ PhCH_3}$

Figure V.2. Electrochemistry of iron porphyrinogen

Figure V.3. Crystal structure of $\mathrm{[(diglyme)_2Na]\ [LFe^{III}]}$

Figure V.4. Crystal structure of $\mathrm{[(THF)(pyO)Na]_2\ [LFe^{II}]}$

Figure V.5. Crystal structure of $\mathrm{[L^{\Delta\Delta}Fe^{II}(NCCH_3)]\ [(C_2B_9H_{11})_2Co]_2 \bullet 2\ CH_3CN \bullet 2\ \mathit{o}\text{-}C_6H_4Cl_2}$

Figure V.6. Comparison of the iron porphyrinogen framework in its three available oxidation states

Figure V.7. $^2$H (left) and $^1$H (right) NMR spectra of the three paramagnetic iron $d_{24}$-porphyrinogen species

### Chapter VI

Figure VI.1. UV-visible absorption spectra of $\mathrm{Na_2(THF)_2[LFe^{II}]}$, $\mathrm{Na(THF)_2[LFe^{III}]}$, and $\mathrm{[L^{\Delta\Delta}Fe^{II}](BF_4)_2}$

Figure VI.2. Frozen-solution X-band EPR spectra of $\mathrm{(Bu_4N)[LFe^{III}]}$ and $\mathrm{[L\,Fe^{II}](BF_4)_2}$ at 4.5 K

Figure VI.3. Fitted $^{57}$Fe Mössbauer spectra of powdered $\mathrm{Na_2(THF)_2[LFe^{II}]}$, $\mathrm{(Cp^*{}_2Fe)[LFe^{III}]}$, and $\mathrm{[L^{\Delta\Delta}Fe^{II}](BF_4)_2}$ at 4.2 K

Figure VI.4. DFT computed Kohn-Sham MO diagrams for $\mathrm{[LFe^{II}]^{2-}}$ and $\mathrm{[LFe^{III}]^{-}}$ in the gas phase

Figure VI.5. DFT computed Kohn-Sham MO diagram for $\mathrm{[L^{\Delta\Delta}Fe^{II}(NCMe)]^{2+}}$ in the gas phase

Figure VI.6. Comparison of relevant ligand-based π-type Kohn-Sham orbitals of $L^{4-}$ and $L^{\Delta\Delta}$

Figure VI.7. Schematic view of the symmetry lowering caused by oxidation of the porphyrinogen tetraanion, compared with a similar phenomenon encountered for the cyclobutadiene dianion

Figure VI.8. Transient absorption of $Na[LFe^{III}]$

**Chapter VII**

Figure VII.1. Crystal structure of $[L^{\Delta\Delta}Fe^{II}Cl](FeCl_4)$

Figure VII.2. Paramagnetic region in the $^1H$ NMR spectrum of $[L^{\Delta\Delta}Fe^{II}—OSiMe_3](OSiMe_3)$

Figure VII.3. Stoichiometry of $[L^{\Delta\Delta}Fe^{II}]^{2+} + I^-$

Figure VII.4. Crystal structure of $\{ (Ph_4P)[LFe^{III}] \}_2 \cdot MeCN \cdot o\text{-}C_6H_4Cl_2$

**Chapter VIII**

Figure VIII.1. Electrochemistry of cobalt porphyrinogen

Figure VIII.2. Crystal structure of the Co(II) octabenzylporphyrinogen dianion

Figure VIII.3. $^1H$ NMR spectrum of $Na_2(THF)$ $[^{Ph}LCo^{II}]$

Figure VIII.4. $^1H$ NMR spectra of $H_2LCo^{II}$ in $CD_2Cl_2$, $H_2LCo^{II}$ in pyridine / $CD_3CN$, and its photoproduct in $CD_2Cl_2$

Figure VIII.5. Time evolution of the photoreaction of $H_2LCo^{II}$ in $CH_2Cl_2$

Figure VIII.6. Two regions of the infrared spectra of dichloromethane solutions of unirradiated $H_2LCo^{II}$ and of $H_2{}^{Ph}LCo^{II}$ after partial photoreaction

# List of Schemes

**Chapter I**

Scheme I.1. Two examples of PCET

Scheme I.2. Two cases of oxygen atom transfer

Scheme I.3. Suzuki-Miyaura coupling of an aryl halide with an aryl boronate

Scheme I.4. Examples of characterized small-molecule transformations in chemistry and biology

Scheme I.5. Two OAT reactions with disparate mechanisms

Scheme I.6. Three different coping strategies evolved by metalloenzymes to deal with the multielectron nature of the $O_2$ substrate

Scheme I.7. Two examples of ligands with several appended one-electron redox units

Scheme I.8. A common and well-established type of genuine redox-active ligands

Scheme I.9. Structure and three oxidation states of the ligand porphyrinogen

Scheme I.10. Biosynthesis of protoporphyrin 9, showing a prophyrinogen as a prominent intermediate

Scheme I.11. Stepwise transformation of porphyrinogen to porphyrin

**Chapter II**

Scheme II.1. Synthesis of electron transfer series of octamethylporphyrinogen complexes of zinc, magnesium and calcium

**Chapter III**

Scheme III.1. Three flavors of mixed valency

Scheme III.2. Schematic representation of the highest occupied $\pi$ orbitals of the pyrrolyl anion

### Chapter IV

Scheme IV.1. Diastereomers of *meso*-tetrakis(3′-*tert*butylpentan-1′,5′-diyl)porphyrinogen.
Scheme IV.2. Condensation of pyrrole with a bulky ketone

### Chapter V

Scheme V.1. Preparation of the three oxidation states of iron porphyrinogen
Scheme V.2. Two contrasting approaches to multielectron redox chemistry of mononuclear iron complexes

### Chapter VII

Scheme VII.1. Acyloin condensation of diethyl adipate to 1,2-bis(trimethylsilyloxy)cyclohexane
Scheme VII.2. Reactivity of oxidized iron porphyrinogen

### Chapter VIII

Scheme VIII.1. The active site of the Fe-only hydrogenase and a hypothetical cobalt porphyrinogen in equivalent protonation and redox states

### Chapter IX

Scheme IX.1. Four examples of electrochemical processes involving increasing amounts of structural reorganization, or changes in bonding
Scheme IX.2. Preparation of antimony porphyrinogen in two oxidation states

# List of Tables

## Chapter II

Table II.1. Summary of X-ray crystallographic data for $[(THF)_2Zn(O_2PF_2)_2]_\infty$

Table II.2. Selected geometric parameters for $[(THF)_2Zn(O_2PF_2)_2]_\infty$

Table II.3. Summary of X-ray crystallographic data for $[L^{\Delta}M(NCMe)] \bullet CH_2Cl_2$, M = Zn, Mg

Table II.4. Selected geometric parameters for $[L^{\Delta}M(NCMe)] \bullet CH_2Cl_2$, M = Zn, Mg

## Chapter III

Table III.1. Comparison of structural and electronic parameters for computed singlet and triplet states of $[L^{\Delta}Zn(NCMe)]$

## Chapter IV

Table IV.1. Summary of X-ray crystallographic data for 2,5-bis(3′,3′,5′,5′-tetramethylcyclohex-1′-enyl)pyrrole

Table IV.2. Selected bond lengths for 2,5-bis(3′,3′,5′,5′-tetramethylcyclohex-1′-enyl)pyrrole

Table IV.3. Summary of X-ray crystallographic data for octabenzylporphyrinogen, $^{Ph}LH_4 \bullet 4\ PhMe$

Table IV.4. Comparison of selected metric parameters for $LZr^{IV}(NHMe_2)(THF)$ and $^{Ph}LZr^{IV}(NHMe_2)(THF) \bullet THF$

Table IV.5. Summary of X-ray crystallographic data for $LZr^{IV}(NHMe_2)(THF)$ and $^{Ph}LZr^{IV}(NHMe_2)(THF) \bullet THF$

Table IV.6. Summary of X-ray crystallographic data for $[HLZr^{IV}]_2O$

Table IV.7. Selected metric parameters for $[HLZr^{IV}]_2O$

**Chapter V**

Table V.1. Summary of X-ray crystallographic data for $[(THF)_3Fe^{II}(\mu\text{-}Cl)_3Fe^{II}(THF)_3]$ $[(THF)_4Fe^{II}(\mu\text{-}Cl)_2Fe^{II}(THF)_4]_{1/2}$ $[LFe^{III}]_2$ • 2 $PhCH_3$

Table V.2. Selected geometric parameters for $[(THF)_3Fe^{II}(\mu\text{-}Cl)_3Fe^{II}(THF)_3]$ $[(THF)_4Fe^{II}(\mu\text{-}Cl)_2Fe^{II}(THF)_4]_{1/2}$ $[LFe^{III}]_2$ • 2 $PhCH_3$

Table V.3. Summary of crystallographic data for iron porphyrinogens

Table V.4. Comparison of geometric parameters for $[LFe^{II}]^{2-}$, $[LFe^{III}]^{-}$ and $[L^{\Delta\Delta}Fe^{II}]^{2+}$ in their respective crystal structures

**Chapter VII**

Table V.1. Summary of X-ray crystallographic data for $[L^{\Delta\Delta}Fe^{II}Cl](FeCl_4)$

Table V.2. Selected geometric parameters for $[L^{\Delta\Delta}Fe^{II}Cl](FeCl_4)$

Table VII.3. Summary of X-ray crystallographic data for $\{ (Ph_4P)[LFe^{III}] \}_2$ • MeCN • *o*-$C_6H_4Cl_2$

Table VII.4. Selected bond lengths in $\{ (Ph_4P)[LFe^{III}] \}_2$ • MeCN • *o*-$C_6H_4Cl_2$

**Chapter VIII**

Table VIII.1. Summary of X-ray crystallographic data for $\{Na(DME)_3\}_2$ $[^{Ph}LCo^{II}]$

Table VIII.2. Selected bond lengths in $\{Na(DME)_3\}_2$ $[^{Ph}LCo^{II}]$

# List of abbreviations

| | |
|---|---|
| Å | Ångstrøm (1 Å = $10^{-10}$ m) |
| A, mA, $\mu$A, nA | Ampere (1 A = 1 C/s), milliampere, microampere, nanoampere |
| $a$, $b$, $c$ | lengths of the three edges of a crystallographic unit cell |
| $\alpha$, $\beta$, $\gamma$ | values of the three angles between the edges of a unit cell |
| ADF | Amsterdam Density Functional™ |
| amu | atomic mass unit |
| Anal. | Elemental analysis |
| atm | atmosphere (1 atm = 101325 Pa, 1 Pa = 1 N/m$^2$) |
| β | Bohr magneton |
| br | broad |
| Bu | butyl |
| $\chi$ | magnetic susceptibility |
| calcd | calculated |
| CCD | charge-coupled device |
| corr$^{3-}$ | a generic corrole trianion |
| cot | cyclooctatetraene |
| Cp$^-$ | cyclopentadienyl anion |
| Cp$^{*-}$ | pentamethylcyclopentadienyl anion |
| CV | cyclic voltammetry |
| diox | 1,4-dioxane |
| DFT | density functional theory |
| digly | diglyme |
| DME | 1,2-dimethoxyethane |
| DMSO | dimethylsulfoxide (Me$_2$SO) |
| DPV | differential pulse voltammetry |
| *E. Coli* | *Escherichia Coli* |
| EI | electroionization |
| EPR | electron paramagnetic resonance spectroscopy |
| ESI | electrospray ionization |

| | |
|---|---|
| Et | ethyl |
| ET | electron transfer |
| $F$ | intensity of diffracted peak (crystallographic structure factor) |
| $F(000)$ | intensity of diffraction peak at $h = k = \ell = 0$ |
| $F_c$, $F_o$ | calculated $F$, observed $F$ |
| Fc | ferrocene (dicyclopentadienyliron) |
| FWHM | full width at half maximum |
| GC | gas chromatography |
| GGA | generalized gradient approximation |
| GOF | crystallographic goodness of fit, GOF = $(\Sigma\, w(F_o^2 - F_c^2)^2/(n - p))^{1/2}$, where $n$ is the number of data (total number of observed reflections except those systematically absent, no reflections eliminated on the basis of a threshold) and $p$ is the number of parameters refined |
| $h$, $k$, $\ell$ | reflection coordinates (indices) in reciprocal (Fourier) space |
| HAT | hydrogen atom transfer |
| HOMO | highest occupied molecular orbital |
| hr. | hours |
| I | intensity |
| ISC | intersystem crossing |
| IR | infrared |
| IVCT | intervalence charge transfer |
| J, kJ | Joule, kilojoule (1 J = 1 N m) |
| $J$ | coupling |
| $L^{4-}$, $L^{\Delta\,2-}$, $L^{\Delta\Delta}$ | the three available OSs of the octamethylporphyrinogen ligand |
| $\lambda$ | wavelength |
| L, mL | liter, milliliter |
| LUMO | lowest unoccupied molecular orbital |
| $\mu$ | dipole moment |
| m, mm, nm | meter or multiplet, millimeter, nanometer |
| Me | methyl |
| Mes | mesityl (2,4,6-trimethylphenyl) |

| | |
|---|---|
| min. | minutes |
| MO | molecular orbital |
| mol | mole (1 mol = $6.022 \cdot 10^{23}$ units) |
| MS | mass spectrometry |
| NAD | nicotinamide adenine dinucleotide |
| NADH + $H^+$ | one-electron reduced form of NAD |
| NHE | normal hydrogen electrode |
| NIR | near infrared |
| NMR | nuclear magnetic resonance |
| OAT | oxygen atom transfer |
| Occup. | orbital occupancy |
| OEC | oxygen-evolving complex of photosystem II |
| $OEP^{2-}$ | octaethylporphyrin dianion |
| OPA | optical parametric amplifier |
| OS | oxidation state |
| PCET | proton-coupled electron transfer |
| Ph | phenyl |
| $^{Ph}L^{4-}$, $^{Ph}L^{\Delta 2-}$, $^{Ph}L^{\Delta\Delta}$ | the three available OSs of the octabenzylporphyrinogen ligand |
| ppm | part(s) per million (1 ppm = $10^{-6}$) |
| PSII | photosystem II |
| py; pyO | pyridine; pyridine-*N*-oxide |
| $R$ | agreement factor |
| r. t. | room temperature |
| $\sigma$ | standard deviation |
| s, ns, ps, fs | singlet or second, nanosecond, picosecond, femtosecond |
| S | molecular spin quantum number |
| SCF | self-consistent field |
| SOMO | singly occupied molecular orbital |
| SQUID | superconducting quantum interference device |
| $\theta$ | angle between crystal's Bragg plane and X-ray beam |
| t | triplet |
| $T$ | absolute temperature |

| | |
|---|---|
| TA | transient absorption |
| tBu | *tert*-butyl (1,1-dimethylethyl) |
| TD-DFT | time-dependent DFT |
| THF | tetrahydrofuran |
| TIP | temperature-independent paramagnetism |
| $TMP^{2-}$ | tetrakis-*meso*-mesitylporphyrin dianion |
| TOF | time-of-flight |
| $Tp^{-}$ | trispyrazolylborate |
| $TPP^{2-}$ | tetrakis-*meso*-phenylporphyrin dianion |
| TTF | tetrathiafulvalene |
| UV (UV-vis) | ultraviolet (ultraviolet – visible) |
| $V$ | unit cell volume |
| $w$ | weighted |
| XPS | X-ray photoelectron spectroscopy |
| xs | excess |
| $Z$ | number of formula units in the unit cell |
| zfs | zero-field splitting |

# Chapter I

# A perspective on multielectron reactions and the agents that perform them

# I.1. Redox reactions

Inorganic chemists traditionally distinguish between acid-base reactions and oxidations-reductions. The principles governing the former are well established,[1] based on reliable kinetic observations dating from the early 20th century[2] and theoretical foundations laid slightly later.[3,4] In contrast to this, redox chemistry remains an area in which much remains to be tested and discovered, despite a large body of existing experimental and theoretical work.

## I.1.a. Single electron transfer

The first measurements of the rates of electron transfer (ET) were enabled in the 1950's by advances in nuclear chemistry, which allowed tagging of one reactant in self-exchange reactions of the type

$$\left[\,{}^{*}\mathrm{Fe(CN)_6}\,\right]^{4-} + \left[\,\mathrm{Fe(CN)_6}\,\right]^{3-} \rightleftharpoons \left[\,{}^{*}\mathrm{Fe(CN)_6}\,\right]^{3-} + \left[\,\mathrm{Fe(CN)_6}\,\right]^{4-}$$

where *Fe denotes a mixture of iron radioisotopes, in other words, radiolabeled iron.[5-24] The data allowed differentiation between outer-sphere ET, which was found to be fast and to occur between coordinatively inert ions such as $[\mathrm{Fe(CN)_6}]^{a-}$ (a = 3, 4) and $[\mathrm{MnO_4}]^{b-}$ (b = 1, 2), and inner-sphere ET, which gave rise to slower rates because it was gated by a rate-determining acid-base event. However, at the time the experiments did not give any insight into the essence of the (much faster) ET event itself. The process was first described (and its dynamics *predicted*) theoretically when the Franck-Condon principle, describing the probabilities of vibronic transitions,[25,26] was applied to ET events, initially by Libby[27] and Weiss.[28] Marcus[29-32] and Hush[33] developed the idea within a transition state model and formulated a complete theory.

The theoretical predictions could not be tested until new experimental techniques became available. The main hurdles were the necessity to maintain a known and fixed distance between reactants — in essence, to study intramolecular ET — and the very fast nature of such ET events. An initial approach to the problem relied on the broadening of a frequency-domain signal, namely in the electron paramagnetic resonance (EPR) of cyclophanes.[34] The first very successful strategy was pioneered by Taube, with the preparation of a wealth of dinuclear transition metal compounds, asymmetrical at first,[35] and later on symmetrical, mixed-valent ones,[36-40] the near-infrared (NIR) and electrochemical properties of which could be analyzed in a framework developed by Hush to yield ET rate constants.[41] Early examples of direct resolution of ET in the time domain were achieved by stopped-flow[42] and temperature-jump[43] techniques. The second very fruitful strategy, developed by Gray, was the application of short laser pulses to both the photogeneration of redox-active excited states and the probing of the ensuing redox reaction. In its initial implementation, the technique relied on ET between a dissolved transition metal complex and the redox cofactor of a protein;[44-46] later on, the inorganic center was covalently attached to a single site of the peptide's surface, for an accurate control of distance and orientation between both redox entities.[47-51] The Marcus theory was finally validated unambiguously with the experimental observation of the quadratic dependence of the logarithm of ET rate with driving force, especially in the so-called "inverted region", which features a *decrease* in rate when a reaction becomes increasingly favorable thermodynamically.[52-54]

### I.1.b. More involved redox reactions

The transfer of a single electron between two well-defined redox centers is quite well understood.[55] But it only represents a small fraction of all redox reactions. In most cases, electron transfer occurs either in a concerted event that also involves bond rearrangement, or in a multistep process that overall corresponds to the transfer of several electrons and one or more nuclei. Such reactions are indeed the more prevalent ones in organometallic chemistry, in the catalysis of fine organic transformations and in processes of industrial importance, as well as in biology. To date, there exists no general theoretical framework that accounts for them.

*Proton-coupled electron transfer*

The simplest case is proton-coupled electron transfer (PCET), whereby the motion of the electron either is affected by the position of a proton, $H^+$ (along or across the ET

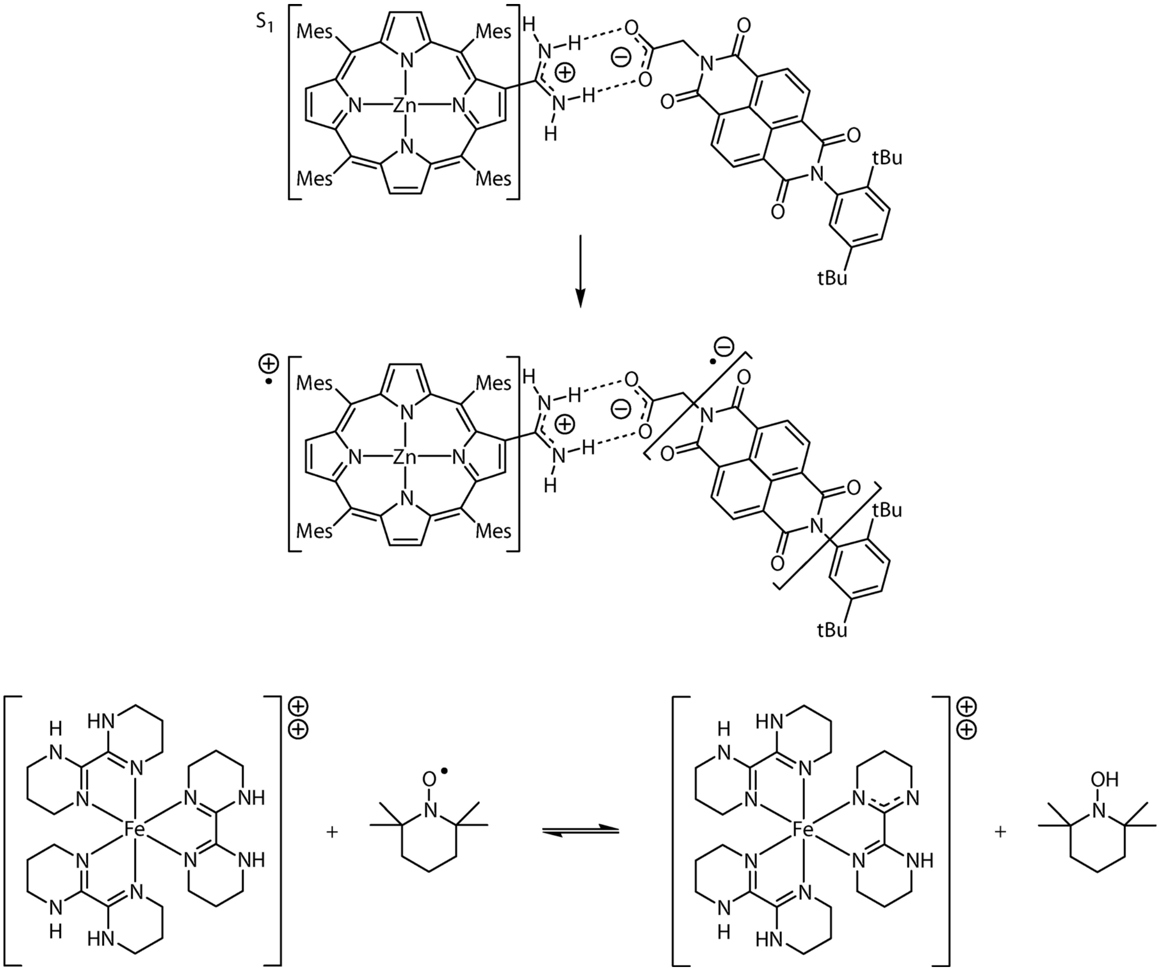

**Scheme I.1.** Two examples of PCET.[57,62] Mes = mesityl = 2,4,6-trimethylphenyl; tBu = *tert*-butyl = 1,1-dimethylethyl.

path), or is accompanied (in a simultaneous or consecutive fashion) by the transfer of the proton.[55-60] Scheme I.1 displays representative examples of those two prototypical limits. In the upper panel, a porphyrin singlet excited state transfers an electron to the naphthalene diimide acceptor through a salt bridge. The presence of the salt bridge and its isotopic constitution affect the observed ET rates, although there is no evidence of complete proton transfer within the salt bridge.[57,61] In the lower panel, a transition metal complex transfers both an electron (mostly from the metal ion) and a proton (from the ligand) to an organic radical.[62] One can arguably consider PCET as a particular case of Marcus-type ET,[58] in which the proton is part of the medium and its vibrational mode dominates the solvent reorganization coordinate. However, two special features, firstly its extreme case hydrogen atom transfer (HAT) and secondly the small mass and quantum nature of $H^+$, make it distinct. Phenomenologically, HAT, that is, the situation in which electron and proton move together in time and (approximately) in space, is more akin to atom transfer (*vide infra*) than to pure ET. From a theoretical viewpoint, the treatment of the medium as an ensemble of classical oscillators does not apply to $H^+$.

Because in thermodynamic terms PCET and HAT amount to an electrostatic stabilization of ET, they are a prevalent method of charge transfer and storage in non-aqueous media such as proteins and lipidic membranes. For example, in the *Escherichia Coli* (*E. Coli*) ribonucleotide reductase (which catalyzes the conversion of nucleotides to deoxynucleotides), a radical is transferred over a 35-Å PCET pathway from tyrosine Y122 adjacent to the diiron initiaton cofactor to cysteine C439 in the active site.[55] The photolyase of *E. Coli* (which repairs photoadducts of nucleobase pairs) similarly shuttles a redox equivalent between the flavin adenine dinucleotide cofactor and the active-site tryptophan W306 13 Å away.[63] Perhaps most prominently, PCET lies at the heart of nature's energy management. Stepwise oxidation of the manganese-(hydr)oxo cluster constituting the oxygen-evolving complex (OEC) of plant photosystem II (PSII) by the neighboring tyrosine $Y_Z$ to yield $O_2$ from $H_2O$ involves shuttling of four electrons and four protons.[64,65] Charge transfer between PSII and neighboring membrane-bound cytochromes occurs *via* the so-called quinone pool: each quinone must accept and deliver both $e^-$ and $H^+$ in order to remain neutral and thereby membrane-soluble.[65] And in respiration, the creation of a transmembrane gradient of proton concentration is effected by coupling proton translocation to electron transfer.[66,67]

### *Group transfer*

As alluded to in the context of HAT, a transformation in which, overall and formally, one or several electrons are transferred together with a mononuclear or polynuclear ion can be called group transfer. The simplest situation is illustrated in the upper panel of Scheme I.2 by the so-called oxygen atom transfer (OAT) between oxochromium porphyrins and phosphines.[68,69] Because the most stable oxidation state of O is the oxide (formally O(–II) as a ligand), the reaction entails the reduction of Cr(IV) to Cr(II) and concomitant oxidation of P(III) to P(V). This case is the simplest from a

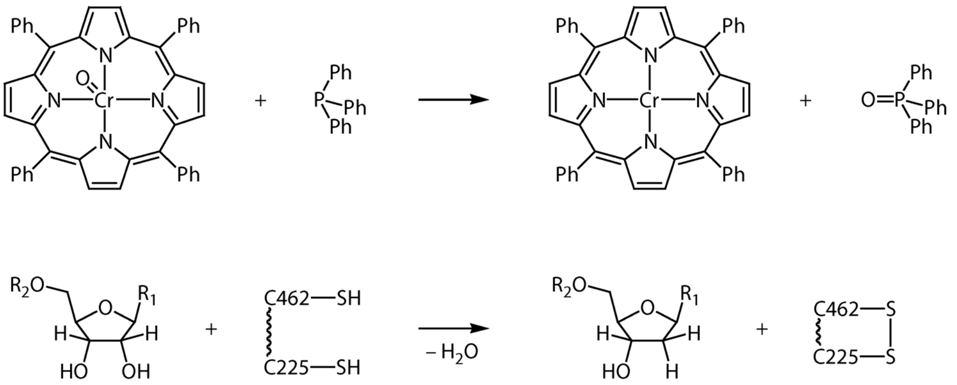

**Scheme I.2.** Two cases of oxygen atom transfer.[68,69,55] The upper reaction occurs in a single mechanistic step and transfers the O atom from one atom (or ion) to another; the lower one is a multistep process involving rearrangement of several covalent bonds. $R_1$ represents a nucleic base and $R_2$ a diphosphate group.

mechanistic viewpoint (single step), and is classified as redox only because of formal oxidation state assignments. In fact, the closest description of the process is the transfer of an O atom, with concerted Cr=O and P=O bond breaking and forming, respectively. The other extreme of OAT is typified by the reaction catalyzed by RNR, namely the extrusion (or insertion) of a formal O atom into (or from) a C—H bond (lower panel of Scheme I.2). This case involves a multistep mechanism made of pure ET events and protonation of the leaving hydroxy group;[70] thus, the formal O(–II) assignment approximates the physical reality reasonably well.

Although a variety of other group transfers are well-documented, O atom transfer holds a preeminent position among them, essentially because epoxidations and dihydroxylations have become, in their enantioselective versions, workhorses in asymmetric organic synthesis.[71-73]

*Organometallic transformations as redox reactions*

Many C—C and C—H bond-forming and bond-breaking reactions of interest to organic chemistry are catalyzed by transition metal complexes, the metal center of which undergoes changes in oxidation state during catalysis. Among a wealth of other examples, the Suzuki-Miyaura coupling[74] of Scheme I.3 illustrates that many oxidative addition / reductive elimination steps of organometallic transformations can in principle be treated as group transfers. For example, the $L_2Pd$ fragment is formally

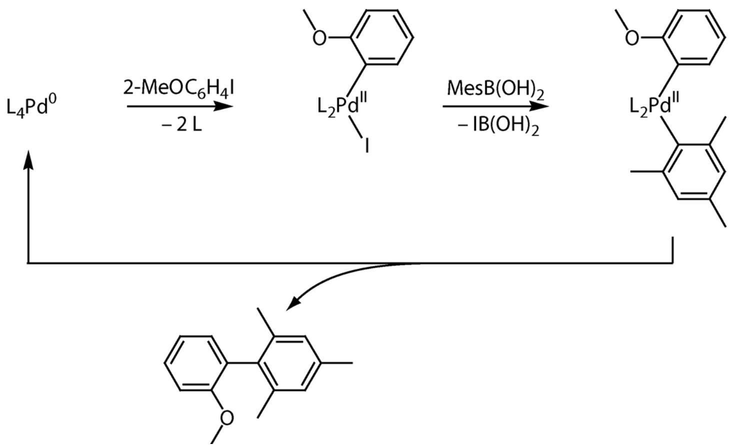

**Scheme I.3.** Suzuki-Miyaura coupling of an aryl halide with an aryl boronate. The oxidative addition can be considered as the transfer of an $L_2Pd$ group into a C—I bond, and the reductive elimination its extrusion from a C—C bond. Mes = mesityl, L = triphenylphosphine, 2-MeOC$_6$H$_4$I = 2-methoxyphenyl iodide.

transferred into the aryl—I bond. More generally, a variety of reactions between or at coordinated ligands result in changes in the formal oxidation state of the metal.

*Multielectron processes in small-molecule management*

The management of simple entities such as $O_2$, $H_2O$, $H_2O_2$, $O_2^{\bullet -}$, $N_2$, $NO_2^-$, $NH_3$ and $CO_2$ in biology and chemistry proceeds through multistep mechanisms, many of which are atom transfers or PCETs. It is, however, worthy of separate consideration because of its importance to life and technology, and because inorganic chemists tend to consider it as a field of study of its own. Among the processes of colossal importance based on such reactions are aerobic and anaerobic respiration, fuel cell operation, fermentation, photosynthesis, destruction of reactive oxygen species in cells, and nitrogen fixation (by bacteria in a metalloenzyme, or industrially by the Haber-Bosch process).

Some particularly well-resolved cases from that list are illustrated by Scheme I.4. The first, featuring the splitting of the inert molecule dinitrogen by two molybdenum centers, can be described as a double N atom transfer to Mo(III).[75] The very closely related system presented immediately below achieves the same transformation by a completely different mechanism, that is, a series of PCETs.[76] Then, catalytic turnover from the nitride is made possible by destabilization of dinuclear

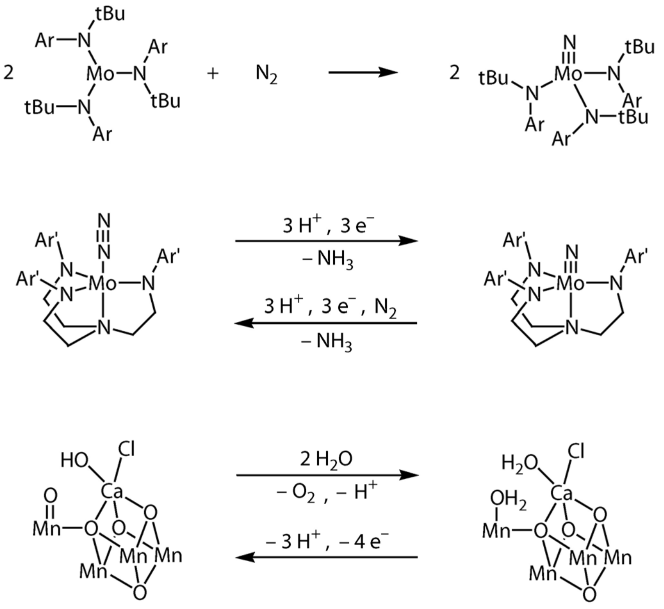

**Scheme I.4.** Examples of characterized small-molecule transformations in chemistry and biology. In the upper panel, dinitrogen is split into two nitrides by two transition metal complexes: the six-electron reduction is achieved in a dinuclear system, by the transformation of two Mo(III) centers to Mo(VI).[75] In the central panel, the same transformation is obtained in a mononuclear compound by three PCET events; moreover, the second N atom is further functionalized, and the inorganic center concomitantly reduced, by three additional PCETs.[76] In the lower panel, dioxygen is formed from coordinated O centers in formal O(–II) oxidation state by the OEC of PSII in what can be considered a group transfer reaction; then, acid-base and ET events regenerate the $O_2$-evolving state.[78] tBu = *tert*butyl; Ar = 3,5-dimethylphenyl; Ar′ = 3,5-bis(2,4,6-triisopropylphenyl)phenyl; the structure of the OEC is putative, and is a fragment (*i. e.*, charges are not balanced and not all ligands are represented).

species (by steric bulk), weakening of the Mo≡N bond (by geometric changes destabilizing the π-bonding Mo $d_{xz}$ and $d_{yz}$ orbitals), and subtle tuning of the external proton and electron donor strengths. The machinery of photosystem II, which photochemically produces $O_2$ from $H_2O$ in order to use the electrons generated for energy storage, uses several photoinduced PCETs[77] to produce a high-valent manganese(V) oxo and high-valent appended manganese-based cluster. Dioxygen evolution occurs by transfer of the O atom to a neighboring hydroxide (or water).[78-80]

## I.1.c. Commonalities of all multicomponent redox reactions, and coping strategies

*A simple description of ET, PCET, and HAT*

Paragraph I.1.b sampled an extraordinarily wide variety of reactions. A majority of useful inorganic reactions are of redox nature, and most of them are more involved than pure single ET. However, some common traits can be found in that perplexing diversity.

In Marcus terms,[29-33] single ET can be described in a three-dimensional space

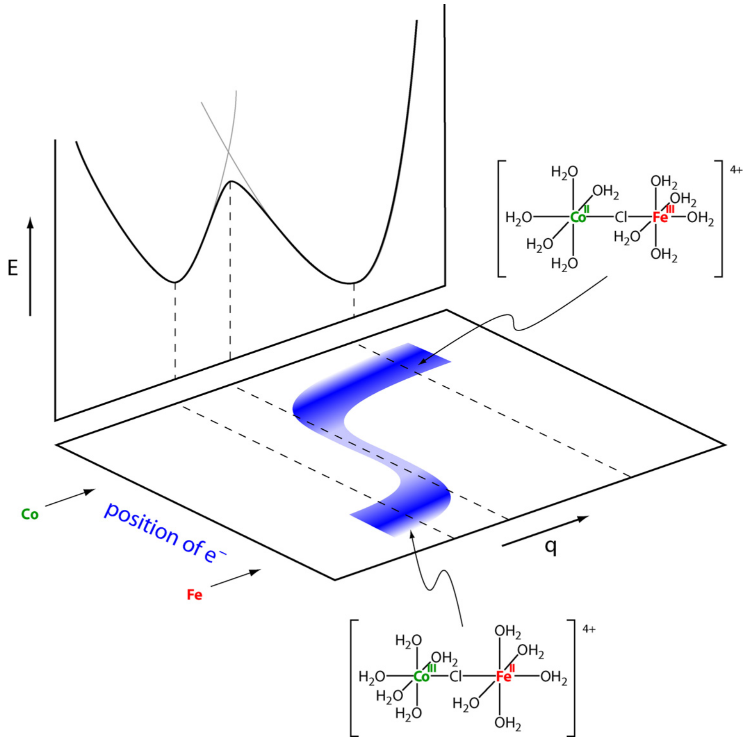

**Figure I.1.** Single electron transfer. Inner-sphere ET between aquated $[Co^{III}Cl]^{2+}$ and $[Fe^{II}]^{2+}$ is taken as an example. The electron moves from its initial localization on Fe to Co when the surroundings have moved along a complex nuclear coordinate q to a midpoint (particularly, when Co-ligand bonds have lengthened and Fe-ligand ones have shortened) where Franck-Condon overlap between the vibrational wavefunctions of starting material and product is optimal, at which point it tunnels over. The vertical panel represents the vibrational wells of isolated starting material and product (gray) and the composite energy curve resulting from their interaction (black). The blue ribbon approximates the evolution of the system during an ET event.

represented in Figure I.1. The position of the electron depends on a complex nuclear coordinate (labeled q), which in energetic terms gives rise to a double well. The course of the reaction in the electron coordinate / nuclear coordinate plane can be loosely described as consisting of three segments. The first is along the vibrational axis, the second corresponds to the electron tunneling through the metal-metal axis, and the last represents the end of the vibrational rearrangement. It is worth emphasizing that a diagonal pathway is not possible — it would correspond to a continuous motion of

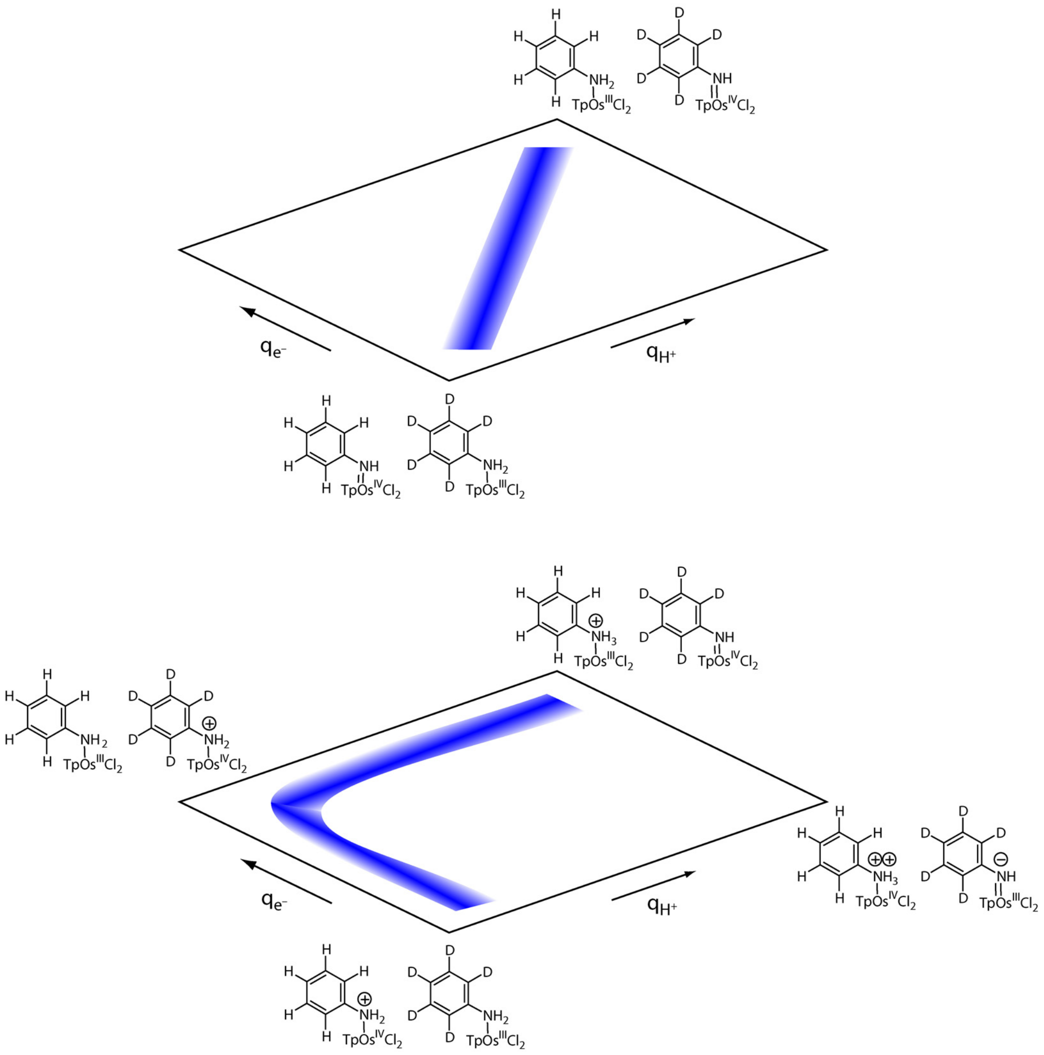

**Figure I.2.** Two contrasting PCET mechanisms in closely related systems.[81] In the upper panel, the pair of corresponding Os(IV) anilide and Os(III) aniline exchange the $e^-$ and the $H^+$ as an H atom in a concerted, "diagonal" fashion. In the lower panel, a protonated pair carries out the exchange in separate proton transfer and ET. $Tp^-$ = trispyrazolylborate.

the electron through space between the metal centers, which does not happen in the physical reality.

Despite its higher complexity, PCET can be qualitatively described in a similar manner. If the $q_{H+}$ coordinate convolutes the motion of the proton with the other nuclear rearrangements (which is an approximation because of the disparate masses), then the plane of $q_{H+}$ and $q_{e-}$ ($q_{e-}$ being the electron coordinate) defines the space of the reaction (energy could be added as a third dimension). In such a representation, the two extreme PCET mechanisms described in I.1.b can be clearly opposed (Figure I.2). PCET in the Os(IV) anilide / Os(III) aniline system studied in detail by Soper and Mayer[81] occurs along a *diagonal* trace as a (slow) concerted HAT, without intermediate (upper panel). Trace acid acts as a catalyst because the protonated Os(IV) anilide / Os(III) aniline pair achieves a stepwise PCET in *two orthogonal segments*, as a (fast) sequence of consecutive proton transfer and electron transfer with a distinct intermediate.

Finally, group transfer is in this formalism very analogous to PCET. The mechanisms of the two disparate examples of OAT of 1.1.b are illustrated in Scheme I.5, again with an emphasis on the two orthogonal constitutive coordinates, acid-base (horizontal, transfers of $H^+$ and O(–II)) and ET (vertical). It is immediately apparent that OAT from oxo chromium porphyrin to phosphine is diagonal,[68] just as concerted HAT is, and that, conversely, extrusion of O from a ribose C—H bond under RNR catalysis occurs in discrete, "orthogonal" acid-base and ET steps,[70] just as consecutive PCET does.

With this, the reaction types of I.1.b have been somewhat unified in terms of their possible mechanisms. They have other aspects in common as well. The entanglement of electron and acid-base coordinates often leads to practical limitations. Mayer's example (Figure I.2) is particularly telling: concerted HAT is particularly slow. In the absence of catalysis, separation of the acid-base and electron coordinates is impossible because both mutually affect each other through metal-ligand bonding and through electrostatic forces. Both possible first steps of a hypothetical stepwise sequence, that is, protonation of the high-oxidation state (high-OS) Os anilide on the one hand, and ET to it on the other hand, are unreasonable, the

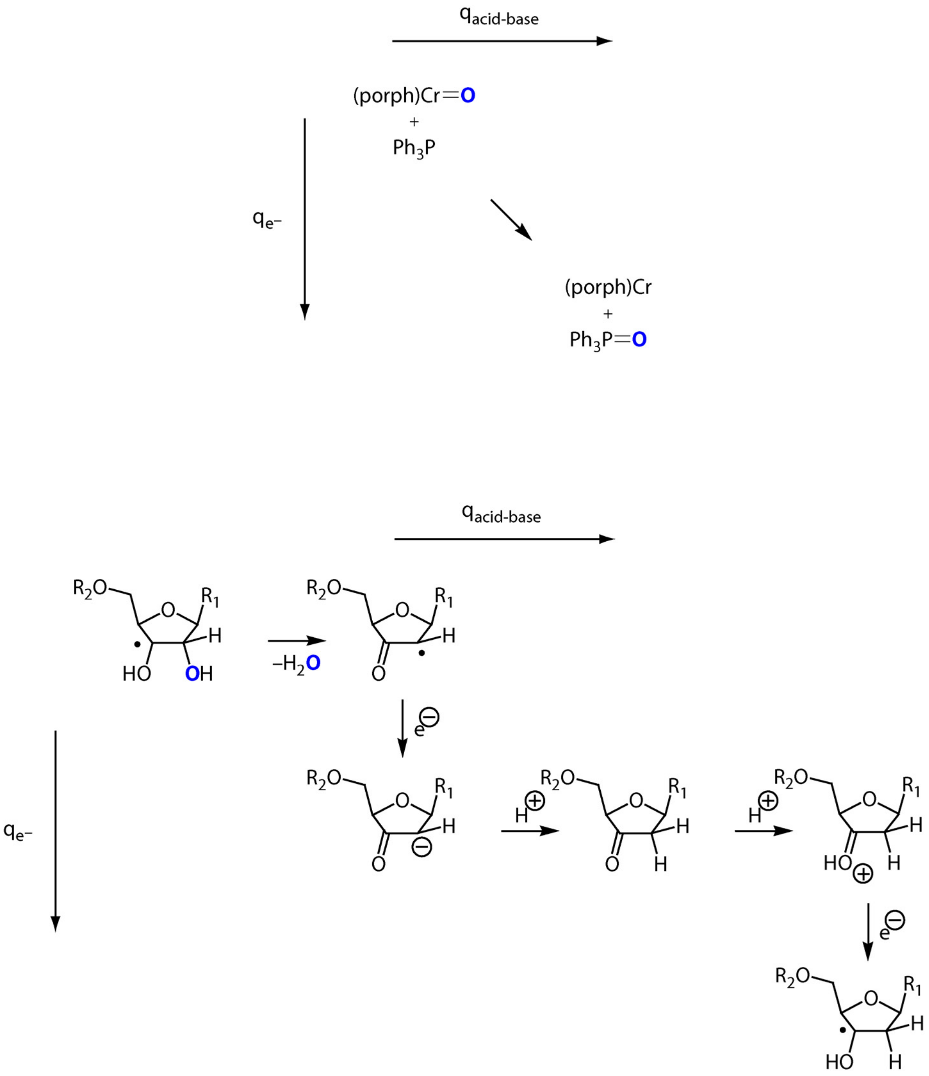
$q_{acid-base}$
(porph)Cr=O
+
$Ph_3P$
$q_{e^-}$
(porph)Cr
+
$Ph_3P$=O
$q_{acid-base}$
$R_2O$
$R_1$
H
HO
OH
$-H_2O$
O
$e^\ominus$
$q_{e^-}$
$H^\oplus$
HO
$e^\ominus$

**Scheme I.5.** Two OAT reactions with disparate mechanisms. In the upper panel, OAT from an oxo chromium porphyrin to a phosphine occurs in a concerted manner, “diagonally” across the ET / acid-base plane. In the lower panel, extrusion of an O atom from a ribose C—H bond under RNR catalysis happens in a series of “orthogonal” steps, each of which is purely ET or purely Brønsted in nature. $R_1$ represents a nucleic base, $R_2$ a diphosphate group, and (porph) a porphyrin dianion.

Os=N multiple bond is too strong. The kinetic bottleneck is only circumvented when an additional proton is part of the system: it disrupts the mutual stabilization of a high metal OS and a deprotonated ligand prone to multiple bonding, and allows the system to take the stepwise path. The double nature of the metal’s d orbitals — as those exchanging electrons *and* carrying the coordination bonding to the ligand —

lies at the heart of the slow rates of coupled acid-base / redox processes occurring at many mononuclear coordination complexes.

This limitation becomes even more stringent when one deals with multielectron processes, such as group transfers. OATs (two-electron processes) from ($O_2$-derived) metal oxos to organic substrates, being of the concerted nature, not the stepwise one, often are affected: the stability of the multiple bond between the reduced oxo and the high-valent metal center tends to restrict reactivity to thermodynamically facile substrates, despite the remarkable oxidizing power of $O_2$. Further, dinitrogen activation and reductive cleavage (a six-electron process) remains highly challenging to chemists, despite isolated successes (cf. Scheme I.4). Most known examples of cleavage are driven thermodynamically by the formation of a very strong M≡N triple bond, which often is then extremely inert to further functionalization of the concerted, or “diagonal”, type. Indeed, the only known example of room-temperature catalytic $N_2$ conversion to ammonia in solution was achieved by subtly tuning the thermodynamics to a unique situation that allows the reaction to be broken down and performed in individual “orthogonal” steps.

The function of many enzymes can be reviewed from this perspective — in numerous cases, multielectron enzymes operate at least in part by separating ET activity from Lewis and Brønsted acid-base events (functionally and spatially). Quite dramatically, the mechanism proposed for the chemistry of ribonucleotide reductase[70] (Scheme I.5) involves cysteine residues which carry out ET steps, and acid-base groups which perform proton transfers. Thus, RNR uses no metal ion in its active site, and separates $H^+$ and $e^-$ coordinates almost perfectly.

*How metalloenzymes cope with the multielectron nature of $O_2$*

Of the redox enzymes the active sites of which do contain at least one transition metal ion, many have evolved strategies to avoid the kinetic bottleneck of an excessively stable high-valent, multiply bonded metal-substrate oxidizing intermediate. Such strategies are particularly prevalent for the proteins involved in $O_2$ management, as shown in Scheme I.6, because of the four-electron couple between $O_2$ and O(–II) (as found in $H_2O$, ROH).

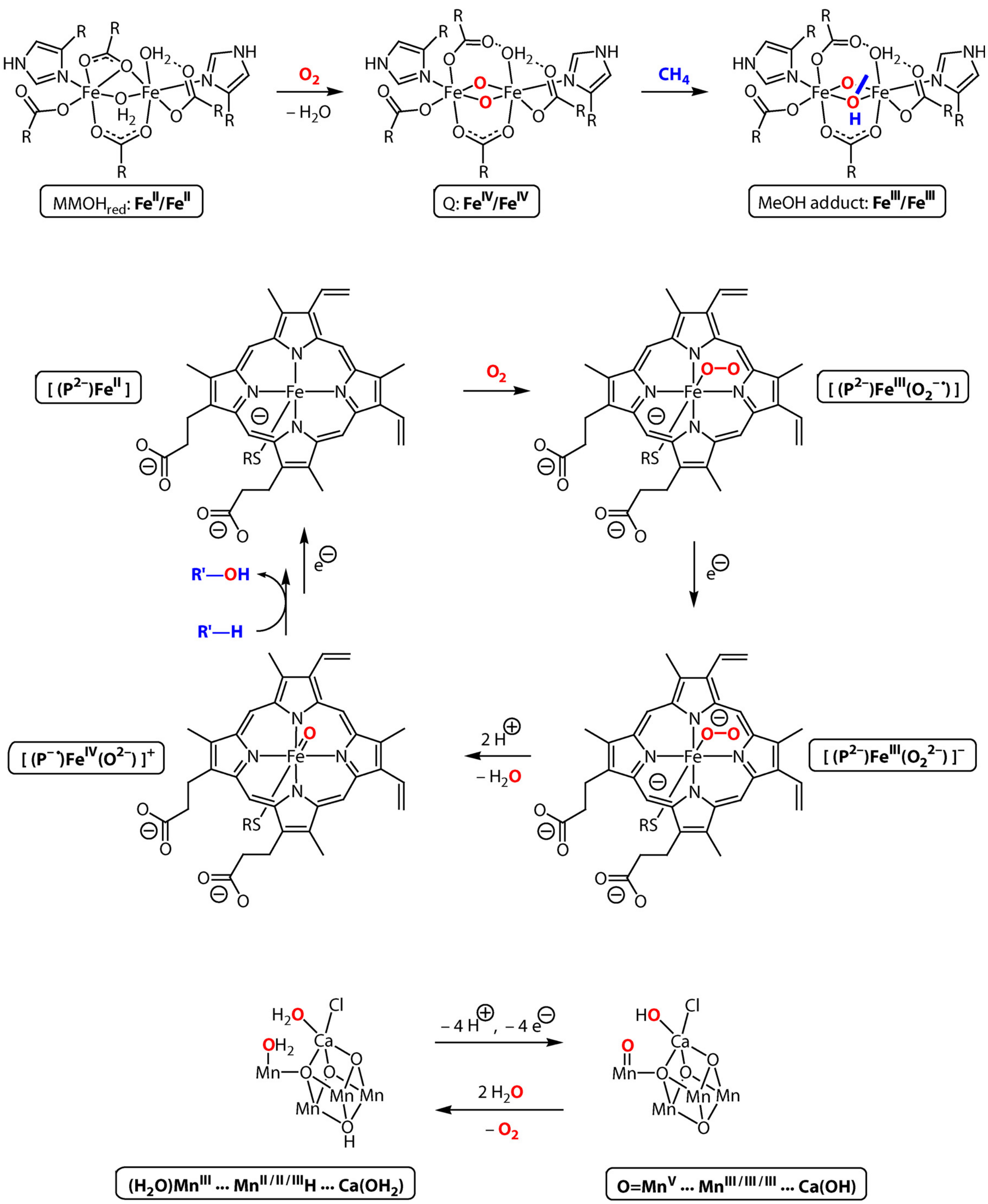
MMOH$_{red}$: Fe$^{II}$/Fe$^{II}$
O$_2$
– H$_2$O
Q: Fe$^{IV}$/Fe$^{IV}$
CH$_4$
MeOH adduct: Fe$^{III}$/Fe$^{III}$
[ (P$^{2-}$)Fe$^{II}$ ]
O$_2$
[ (P$^{2-}$)Fe$^{III}$(O$_2^{-\bullet}$) ]
e$^{-}$
e$^{-}$
R'—OH
R'—H
[ (P$^{-\bullet}$)Fe$^{IV}$(O$^{2-}$) ]$^{+}$
2 H$^{+}$
– H$_2$O
[ (P$^{2-}$)Fe$^{III}$(O$_2^{2-}$) ]$^{-}$
RS
– 4 H$^{+}$, – 4 e$^{-}$
2 H$_2$O
– O$_2$
(H$_2$O)Mn$^{III}$ ... Mn$^{II/II/III}$H ... Ca(OH$_2$)
O=Mn$^{V}$ ... Mn$^{III/III/III}$ ... Ca(OH)

**Scheme I.6.** Three different coping strategies evolved by metalloenzymes to deal with the multielectron nature of the $O_2$ substrate. In the upper panel, the MMO hydroxylase uses a dinuclear center and shuttles between Fe$^{II}$/Fe$^{II}$ and Fe$^{IV}$/Fe$^{IV}$.[82] In the middle panel, cytochrome P450 involves an external reductant between the $O_2$ binding event and the O—O bond breaking, and calls the porphyrin ligand to take a redox-active role.[83-84] And in the lower panel, the OEC of PSII uses a Mn-oxo cluster as an ancillary redox (and acid-base) reservoir.[78-80] R represents the protein's peptidic backbone.

Monooxygenases use $O_2$ as the oxidant to hydroxylate a C—H bond; of the four redox equivalents provided by each $O_2$ molecule, only two are used in productive catalysis, the other two are transferred to a sacrificial reductant such as NADH + $H^+$ (nicotinamide adenine dinucleotide), with $H_2O$ as by-product. The hydroxylase in the soluble methane monooxygenase (MMO) complex of *Methanococcus capsulatus* (Bath), a methanotroph, uses a dinuclear strategy to cope with $O_2$, such that it oscillates between $Fe^{II}/Fe^{II}$ and $Fe^{IV}/Fe^{IV}$ as its extreme oxidation states (upper panel of Scheme I.6).[82] Cytochrome P450, which hydroxylates a variety of less thermodynamically challenging substrates, is mononuclear, but overcomes the difficulty of addressing the four-electron entity $O_2$ with the mostly two-electron metal Fe by using two artifices (central panel of Scheme I.6).[83,84] Firstly, $O_2$ coordination at Fe(II) does not immediately result in its cleavage. Instead, $O_2$ is only reduced by a single electron to a superoxide (bound to Fe(III)), the next step involving external reduction of the entity to the Fe(III) peroxide. Secondly, the elimination of water after double protonation requires *two* additional electrons from the inorganic center, which is nearly impossible from Fe(III),[a,85-87] and one of them is provided by the porphyrin periphery. Thus, an Fe(IV) porphyrin cation radical serves as a masked Fe(V) center.

The function of the OEC in PSII of green plants and photosynthetic bacteria is to extract electrons from the transformation of water into dioxygen and protons for the eventual storage of chemical energy in the synthesis of sugars from $CO_2$. Thereby, its importance to aerobic life, and indirectly to engineering, is primordial. The transitional metal used is this time Mn (lower panel of Scheme I.6).[77-80] A single Mn center holds a substrate water which is oxidized stepwise to a high-valent Mn-oxo, whereas the second substrate water is presumably deprotonated upon coordination to a redox-inert $Ca^{2+}$ cation. Since the Mn ion that holds $H_2O$ can only shuttle by two redox units (from $Mn^{III}$—$OH_2$ to $Mn^{V}$=O), it is supplemented by an ancillary redox-active trinuclear manganese-oxo cluster which provides a nearby two-electron redox reservoir.

---

[a] The oxidation state Fe(V) has been in exceptional cases invoked in intermediates or observed spectroscopically in unstable compounds,[85-87] and remains controversial.

## I.2. Redox-active ligands

The necessity for catalytic inorganic centers to provide two or more redox equivalents in multielectron reactions while avoiding the kinetic bottleneck of too stable high-valent, multiply bonded metal-substrate intermediates — most prevalently in small molecule activation and management — has prompted biological systems to develop three main strategies to alleviate the redox requirements on the substrate-binding metal: share the redox burden between *(i) two* substrate-binding metal ions working in concert, *(ii)* the substrate-binding ion and its *redox-active ligand*, or *(iii)* the substrate-binding ion and a neighboring *redox-active cluster*. Such strategies can be an inspiration for chemists attempting to approach nature's efficiency, selectivity and control in small molecule management. Certainly, the limitations and approaches of synthetic inorganic chemists are different from those of biological organisms: the former confront more stringent restrictions in time, tackle problems in (somewhat) logical terms, and have access to the whole periodic table, whereas the latter have evolved for billions of years, building large structures of redundant complication by trial and error, and from a relatively small set of elements and building blocks. Nevertheless, nature can be a source of inspiration to the chemist. In particular, the vast majority of inorganic chemistry has dealt with mononuclear complexes of metal ions with redox-inert ligands, and there is still ample space for experimentation in the concepts *(i)* to *(iii)* listed above.

This thesis explores idea *(ii)*, that is, the use of a redox-active ligand in concert with a central metal ion. Traditionally, inorganic chemists tend to consider a metal ion as both the Lewis acid-base center (in particular, the site of substrate binding) and the sole redox actor, therefore use one or several chelating or macrocyclic ligands — cyclopentadienyl ($Cp^-$), trispyrazolylborate ($Tp^-$), porphyrins, calixarenes, salens, bis(diphenylphosphino)ethane, and many more — aptly called *ancillary*. For the most part, ancillary ligands prevent undesirable reaction pathways by blocking a number of coordination sites with an inert barrier, and adjust the steric and electronic properties of the metal ion in a purely *static* manner. Breaking free from this restrictive (however successful) thinking, and reserving a more active role for the supporting ligand(s), might open up different horizons in inorganic chemistry.

### I.2.a. Small molecules, the oxidation state of which changes upon coordination

Some ligands have long given rise to discussions concerning the best description of their oxidation state (OS) in coordination complexes, because their most stable OS in the free form often does not approximate their real behavior when coordinated. In other words, they oxidize or reduce the metal (or may do so) upon coordination. Nitrous oxide, the open-shell, neutral molecule $^{\bullet}NO$, is a case in point.[88] In its coordination compounds it is usually considered formally as either the cation $NO^+$ (isoelectronic to CO) or the anion $NO^-$ (isoelectronic to $O_2$). For example, reaction of NO gas with iron(III) octaethyl- or tetraphenylporphyrin (OEP or TPP) yields a linear Fe—N≡O unit, that is, formally Fe(II) ($NO^+$).[89,90]

Reaction of sodium metal with naphthalene in ethers yields the green solvated adduct $(C_{10}H_8)Na(solv)_n$, where solv designates coordinating solvent molecules.[91] Its very color is indicative of its nature: an anion radical delocalized in the aromatic system, coordinating a stable $Na^+$ cation. The naphthalenide anion radical is quite frequent as $\eta^4$ or $\eta^6$ ligand in complexes of low-valent transition metals as well.[92,93] The phenomenon extends to other polyaromatics, a prevalent example being the bent magnesium anthracene, $(C_{14}H_{10})Mg(THF)_3$ (THF = tetrahydrofuran).[94]

Cyclooctatetraene (cot) presents a two-electron example in the same category. As an isolated species it exists as the ruffled neutral molecule. However, most of its (s- and f-block) metal complexes feature it as a flat octagon, therefore the $10\pi$, aromatic dianion $C_8H_8^{2-}$.[95-97] Zero-valent transition metal complexes of cot, however, bind it as a neutral diene.[98]

Those ligands are redox-active in the sense that their OS in the complex can be different from that of the free entity; however, they do not usually display any redox changes once coordinated (but for some adaptation to changes in the metal's OS brought about by external redox agents, manifested by hapticity changes).[99-104] For that reason, they cannot be used as supporting redox agents in coordination compounds.

## I.2.b. Constructs with redox-active fragments appended onto ligands

A very different class of redox-active ligands encompasses molecules built from fragments with an engineering approach. Robust units with well-established, reliable redox properties, in particular ferrocene (Fc) and tetrathiafulvalene (TTF), can be grafted onto ligands, the coordination properties of which usually remain unchanged (Scheme I.7).[105-111]

The number of redox-active units on each ligand, as well as the type of tether, can be varied to obtain different electrochemical behaviors. In many cases, compounds possessing several such tethered redox-active units exhibit a single

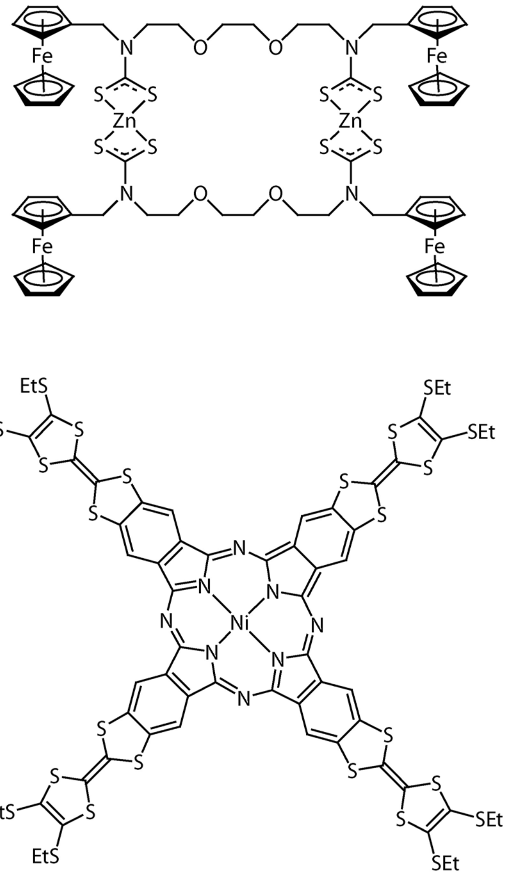

**Scheme I.7.** Two examples of ligands with several appended one-electron redox units. In the upper panel, Fc moieties are loosely connected to a dithiocarbamate – crown ether framework, with potential applications in sensing.[105] In the lower panel, TTFs are fused into the $\pi$ system of a phthalocyanin, with potential applications in magnetic materials.[110]

(broadened) electrochemical signal, indicative of very limited electronic interaction between the redox actors at the periphery and the center of the coordination complex. Consequently, such constructs are, for the time being, mostly interesting in applications based on electrostatic interactions, such as ion sensing. Exploration of the properties of such constructs in (multielectron) reaction chemistry, however, deserves an interest which, to date, is absent from the literature.

### I.2.c. Genuine redox-active ligands

In order to draw clear-cut lines, we will call “genuine redox-active ligand” an organic molecule or ion that inherently is able to coordinate to a metal cation in a certain OS and, once coordinated, change OS upon reaction with external redox agents.

*Ditihiolenes and catecholates*

The first examples of such behavior (dithiolene complexes of group 9 to group 11 ions, Scheme I.8) were investigated in the 1960’s by magnetometry, EPR and electronic absorption spectroscopy, initially by Schrauzer and Mayweg,[112,113] then in great detail by Davison and Holm,[114-123] on the one hand, and by Gray,[124-128] on the other hand. Controversy arose because EPR parameters, that is, the presence of hyperfine coupling to the central metal nucleus (where applicable) and a relatively wide spread of *g* values, indicated the presence of unpaired spin density on the central metal in paramagnetic complexes such as $[(R_2C_2S_2)_2Ni]^-$. After a fierce crusade fought by the Don Quixote from Columbia against “the myth of nickel(III)”,[128] it was quickly recognized that the electronic structure consists of a mostly ligand-based radical with strong stabilization in the covalent binding to the transition metal. “The persisting problem is the establishment of the quantitative degree of metal orbital involvement in these series of complexes which possess, in the phraseology of Schrauzer and Mayweg,[113] ‘delocalized ground states.’ ”[122]

Wieghardt reinvestigated the question more recently, in similar compounds (mostly dithiolenes and catecholates of late transition metals) but with a wider variety of spectroscopic techniques and with modern theoretical methods.[129-139] The conclusions have not changed, and density functional theoretical (DFT) treatment

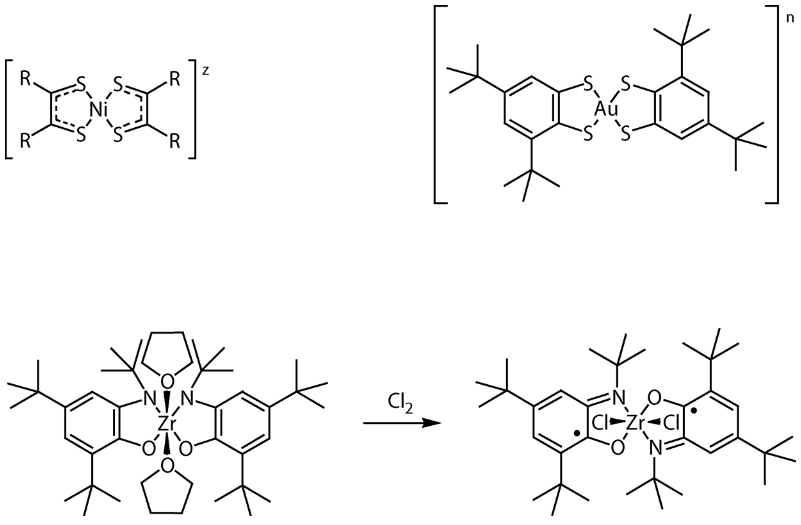

**Scheme I.8.** A common and well-established type of genuine redox-active ligands. Upper left, the main target of the initial studies (z = −2, −1, 0; R = Ph, $CF_3$, CN, $CH_3$, …).[112-128] Upper right, a particularly well-resolved case described by Wieghardt (n = −1, 0).[132] Lower panel, exploitation of ligand-based redox activity to supplement a central metal's abilities.[141]

shows that the redox-active Kohn-Sham orbitals[140] are delocalized between both ligands and the central metal ion, the ligands contributing the larger coefficients (thence their description as being "non-innocent").

Moving beyond a purely descriptive approach to ligand non-innocence, Heyduk recently demonstrated that the redox activity of a ligand set can be used to supplement the central metal's abilities, achieving a formal oxidative addition of $Cl_2$ onto a Zr(IV), $d^0$ complex.[141]

*Porphinoid macrocycles*

That the active oxidant in the catalytic cycle of cytochrome P450 ("compound I") is an oxo Fe(IV) porphyrin $\pi$-cation radical, not an oxo Fe(V), only began to be recognized after Groves was able to oxidize chloro iron(III) TMP with a peroxyacid at low temperature, spectroscopically identify the intermediate generated as porphyrin-based radical, then show that it behaves as a very active oxygenating agent.[142] However, Dolphin and Felton had proposed such an electronic structure for compound I ten years earlier,[143] and had already been able to characterize oxidized states of zinc and magnesium porphyrins in the late 1960's.[144,145]

Other tetrapyrrole macrocycles show comparable redox activity, in particular chlorins[146,147] and corroles. The degree of "non-innocence" of corroles in their iron complexes has been the subject of some debate. It is absolutely clear that oxidation of (corr)$Fe^{IV}$—($C_6H_5$) (where corr represents a generic corrole) is macrocycle-based, yielding the stable and completely characterized ($corr^{+\bullet}$)$Fe^{IV}$—($C_6H_5$).[148] It was then suggested on the basis of its paramagnetic nuclear magnetic resonance (NMR) shifts that even (corr)$Fe^{IV}$—Cl should be reformulated as ($corr^{+\bullet}$)$Fe^{III}$—Cl.[149] However, to date this claim has not been confirmed.[150] Thus, the commonly accepted view is that corrole differs from porphyrin in its ability to stabilize some higher-OS metal ions, but that its redox activity is similar.

### I.2.d. Limitations of well-established classes of redox-active ligands, and appealing features of porphyrinogen

Apart from isolated examples, all known cases of ligands the OS of which can be changed in their coordination complexes upon electrolysis or reaction with chemical redox agents either *(i)* are related to dithiolenes or catecholates (i. e. based on a HE—C=C—EH backbone in the reduced, protonated state, with E = O, S, NR and R = alkyl) or *(ii)* belong to the tetrapyrrole family of macrocycles.

As a study case from the viewpoint of redox-active ancillary ligands, porphinoid macrocycles *(ii)* combine the advantages of (a) displaying redox-active orbitals quite well distinguishable from those of the metal, yet in electronic communication with them, and (b) featuring very favorable spectral properties in the ultraviolet and visible regions (UV-vis). However, they can only store a single oxidizing or reducing equivalent (and a second one under forcing conditions). The chelates in category *(i)* have a broader range of redox storage in that two such ligands can in principle accommodate up to four redox equivalents, but they still react in *single*-electron steps, which presumably will not allow them to function as *selective* multielectron agents in the context of small molecule chemistry. Furthermore, their characterization (more specifically, the deciphering of how an overall charge is shared between metal and ligand(s) and the assignment of well-defined respective OSs) is complicated by the fact that their redox-active orbitals are directly adjacent to the metal-binding atoms and involved in bonding to it.

A model system for the study of ligand-based redox activity and the interaction of a multielectron reservoir ligand with a central metal ion would ideally present the following characteristics: (a) versatile coordination abilities; (b) a wide range of available oxidation states; (c) some mechanism that might potentially yield a selectivity for multielectron events over single-electron ones; (d) redox sites that are distinct from the metal, yet in reasonable electronic interaction with it; (e) spectroscopic handles; (f) structural simplicity, ease of preparation and handling. Phenanthroline dione has some potential in that respect, in particular as a two-electron PCET agent, but the information available about it in the literature is scarce.[151,152] This thesis will focus on a tetrapyrrolic macrocycle with a potential for four-electron reactivity, porphyrinogen (also called calix[4]pyrrole, see Scheme I.9). As detailed in the next section and throughout this thesis, it completely fulfills the requirements delineated above: (a) it has been shown to coordinate main group metals, early and late transition metals, as well as lanthanides and actinides; (b) it can be oxidized from a tetraanion to a neutral state; (c) oxidation results in the formation of C—C bonds (an entity with a two-electron nature) within the ligand framework; (d) structural changes upon oxidation occur at the α position of the pyrroles, not at the coordinating N; (e) redox changes are accompanied by changes in its NMR, IR and sometimes UV-vis spectra; (f) its fourfold symmetric structure results from a one-step preparation from commodity chemicals.

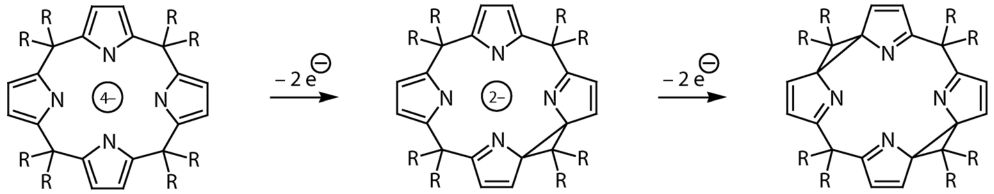

**Scheme I.9.** Structure and three oxidation states of the ligand porphyrinogen. R represents an alkyl group.

# I.3. Metal porphyrinogens

## I.3.a. Background

Von Baeyer marveled in 1886: "*Vor einiger Zeit beobachtete ich die Bildung eines schön kristallisierenden Kondensationsproduktes von Pyrrol mit Aceton, welches vielleicht für den einen oder den anderen Fachgenossen von Interesse ist.*"[153] — "I had observed for a while the formation of a condensation product of pyrrole with acetone that nicely crystallizes, and which might be of interest to some specialist." The compound was of course *meso*-octamethylporphyrinogen, the cyclic tetramer of pyrrole and acetone after quadruple condensation.

Interest, however, remained minimal until chemists and biologists started to investigate the biosynthesis of porphyrin cofactors, an example of which is delineated in Scheme I.10.[154] According to Granick and Mauzerall, 2-(aminomethyl)pyrrole building blocks are assembled and cyclized to yield a porphyrinogen first, which then

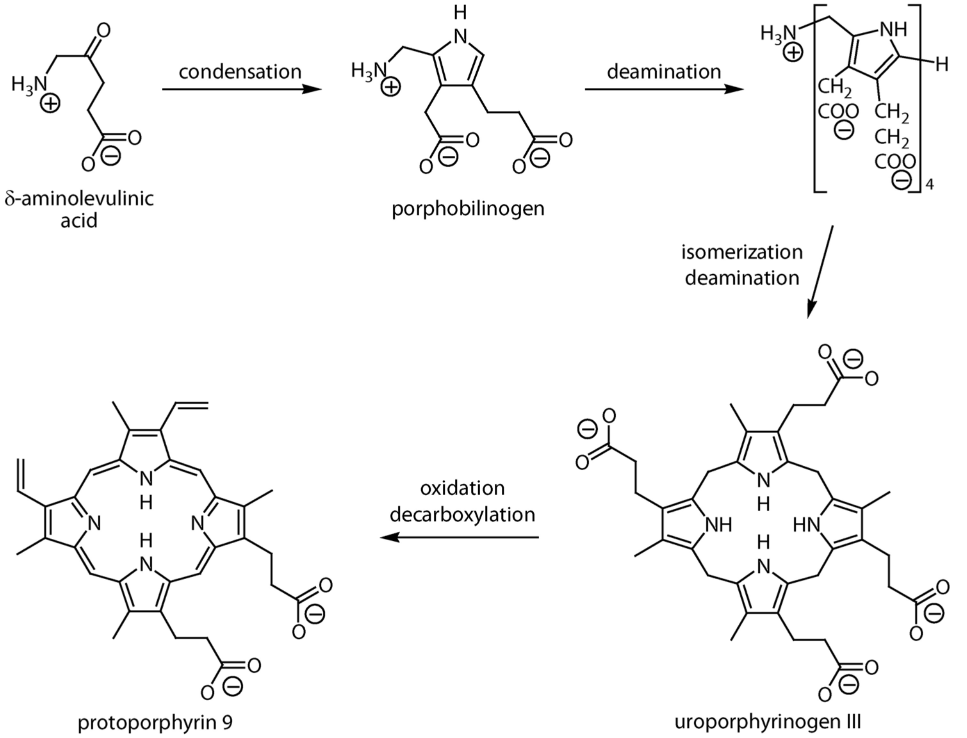
condensation
deamination
isomerization
deamination
oxidation
decarboxylation
δ-aminolevulinic acid
porphobilinogen
protoporphyrin 9
uroporphyrinogen III

**Scheme I.10.** Biosynthesis of protoporphyrin 9, showing a prophyrinogen as a prominent intermediate.[154]

is oxidized to the porphyrin. They also attempted to prove the biological relevance of porphyrinogen by chemical reduction of porphyrin: upon reaction of free base porphyrins with reductants of different thermodynamics, they identified products with various UV-vis spectral signatures, which they assigned to dihydroporphyrin (phlorin), tetrahydroporphyrin (porphomethene) and hexahydroporphyrin (porphyrinogen, no visible absorption).[155] Moreover, those reduction products were shown to be reoxidized when recombined with apo-cytochromes to yield functional enzymes.[156] In fact, the uncontrollable oxidation of *meso*-unsubstituted porphyrinogen to the corresponding porphyrin had long been known and put to use in the simple Rothemund synthesis of the parent porphyrin, porphin.[157]

Despite the difficulty of preparing and handling the inherently unstable *meso*-unsubstituted porphyrinogens by reduction, on the one hand, and the confirmation of the structure of *meso*-octamethylporphyrinogen ("which kept for several months without discoloration"),[158] on the other hand, nobody seems to have manifested an interest in the study of *meso*-octaalkylporphyrinogens as ligands for coordination chemistry until Floriani in 1991.[159]

As summarized graphically in Figure I.3, porphyrinogen displays an extraordinary versatility both in acid-base and in redox terms, and gives rise to a quite wide variety of structures, among which porphyrin is but one extreme, the most oxidized and overall thermodynamic sink. Additionally, protonated porphyrinogen is a quadruple hydrogen bonder, and as such has been used as an anion sensor.[111,160-174]

The pure coordination chemistry of porphyrinogen (green axis of Figure I.3) spans the periodic table:[175] its complexes with alkalis[176,177] and alkaline-earths,[177,178] p-block elements,[179] early and late transition metals,[180-188] as well as lanthanides[189-193] and actinides[194-196] have been characterized. This very wide range of coordination abilities stems from the ability of pyrroles to tilt relative to the central metal, thereby change their hapticity towards it and adjust the overall electron donation to its needs. In $\eta^1$ mode, the pyrrole anion is a weak $\pi$ donor because the $\pi$ pair of electrons on N participates in the ring's aromaticity; it is, however, strong donor of a $\sigma$ pair, and the combination of four negative charges within the porphyrinogen macrocycle enhances that property. By tilting to $\eta^3$ and $\eta^5$, each pyrrole can become a four- or six-electron

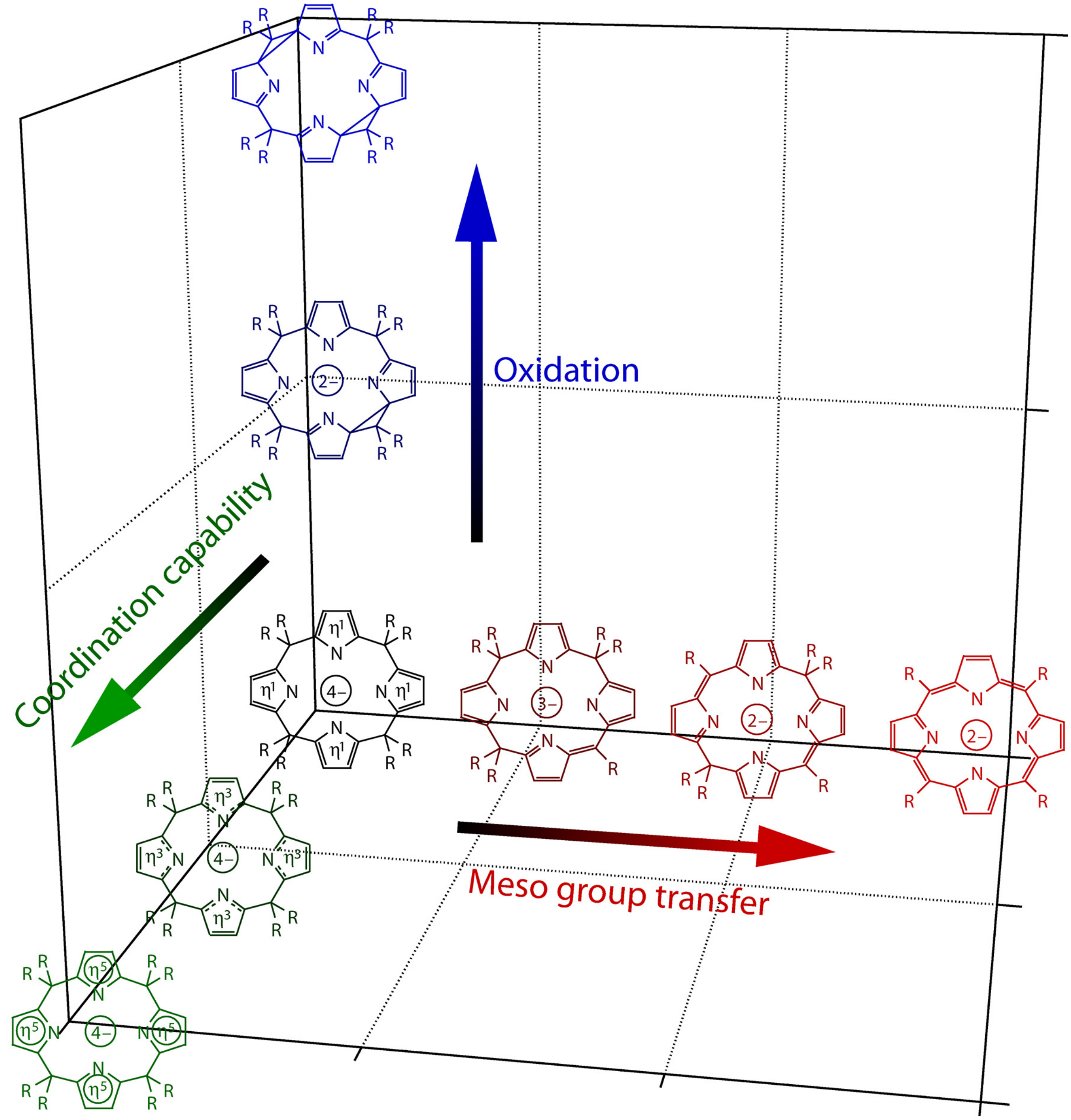
Oxidation
Coordination capability
Meso group transfer
2–
4–
3–
2–
2–
4–
4–
η1
η3
η5
N
R

**Figure I.3.** Three lines of reactivity originating from the porphyrinogen structure — pure acid-base, pure redox, and combined (group transfer). The acid-base (green) axis corresponds to donation of increasing numbers of electrons to the central metal as pyrroles change hapticity. The redox (blue) axis witnesses the formation of C—C bonds between pyrrole α-carbons at each two-electron oxidation of the macrocycle. The group transfer (red) axis takes porphyrinogen to porphyrin via the stepwise elimination of *meso* alkyl groups.

donor *via* its aromatic π orbitals, in Cp fashion, which enables it to accommodate transition metal ions of low d-electron count.

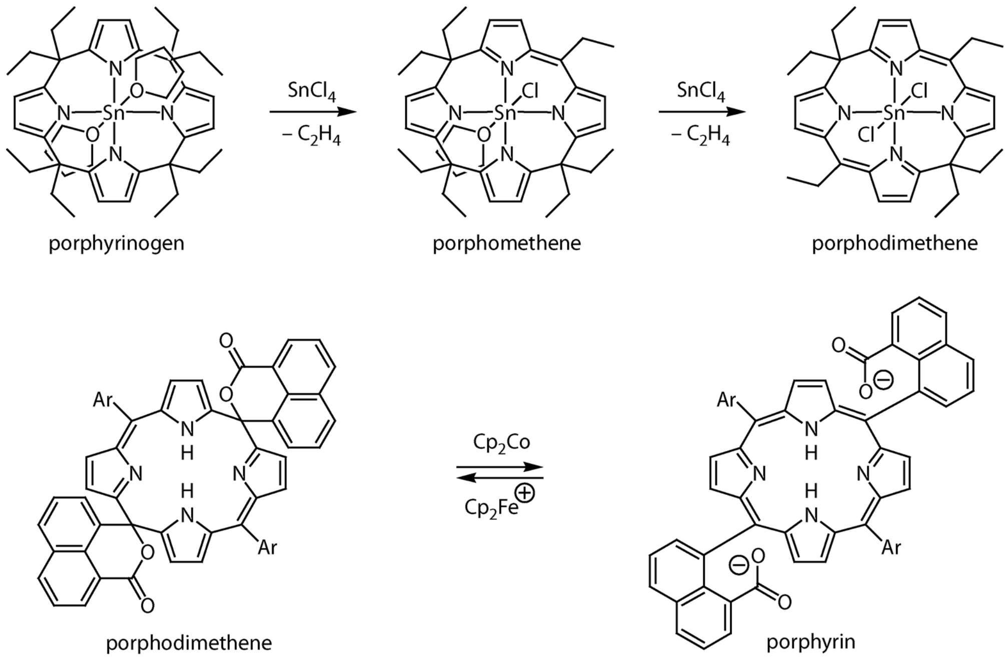

**Scheme I.11.** Stepwise transformation of porphyrinogen to porphyrin. Floriani discovered the oxidative elimination of *meso* ethyl groups as ethylene (upper panel).[179] Scott engineered an intramolecular redox-driven lactonization at the *meso* positions.[199] Ar represents one of several aryl groups (3,4,5-tris(methoxy)phenyl, 2,4,6-trimethylphenyl, 3,5-bis(*tert*butyl)phenyl).

The red branch of Figure I.3, that is, the stepwise oxidation of porphyrinogen to porphyrin with elimination of *meso* substituents, was achieved in a controlled, stepwise fashion by Floriani[179,197,198] and Scott (Scheme I.11).[199-201] The first two steps could be performed by oxidation of tin(IV) octaethylporphyrinogen bis(solvate) with controlled amounts of tin tetrachloride, resulting in the elimination of *meso* ethyl groups as ethylene. The last step took place from a *meso* carboxylate-functionalized porphyrin, which upon oxidation yields lactonization at the *meso* position.

Those "red branch" transformations have an inherent redox component, but because they involve the loss of a group, they are not reversible (unless they are made intramolecular by tethering the leaving group to the macrocycle), therefore they are not amenable to participating in a genuine ligand-based redox reservoir. For that purpose, the "blue" axis of Figure I.3 is more suitable: on this line of transformations, pure ET events (in pairs) are accommodated purely by internal electronic reorganization, without addition or loss of any nuclei. As shown by Floriani, metal porphyrinogens will upon oxidation by two units form an intramolecular C—C bond as a result of coupling between an adjacent pair of neighboring pyrroles, with the formation of an unusual bis-spiro-cyclopropane.[202-207]

## I.3.b. Goals

Because oxidized forms of porphyrinogen have typically been isolated as complexes of transition metal ions bearing axial ligands and with polynuclear metal-halo clusters (or otherwise redox- and spectroscopically active entities) as counter-ions,[202-208] little is known of their properties apart from their solid-state structures. No electrochemical data are available, but for the fully protonated molecule: in $CH_2Cl_2$, it displays a first reversible wave corresponding to injection of a single hole into the $\pi$ system of a pyrrole, followed by an irreversible wave attributed to the formation of the cyclopropane bond accompanied by loss of $H^+$.[209] The structures of oxidized porphyrinogens have not been confirmed in solution by NMR because of the paramagnetism of the central ions. Their UV-vis absorptions have always been overwhelmed by those of the counter-ions, therefore their electronic structures have not been investigated. Perhaps most importantly, no reaction has been reported that makes use of an oxidized porphyrinogen as the oxidizing agent.

Consequently, this thesis will attempt to describe the electronic and redox properties of metalloporphyrinogens from first principles. More specifically, the following points will be addressed. When coordinating a redox-inert metal cation,

1. what oxidation states are available to porphyrinogen;
2. are solid-state structures maintained in solution;
3. what are the electronic structures of oxidized porphyrinogens, how can the redox-active C—C bond be described; and
4. can porphyrinogen complexes of redox-inert metal cations undergo typical redox reactions such as oxidative additions ?

Further, how is porphyrinogen affected when coordinating a redox-active central metal, that is,

5. what overall oxidation states are available to the overall entity;

6. what are the structures in the solid and solution states;
7. can overall OSs be separated into well-defined individual OSs for the metal and for the ligand, respectively, in other words, what are the electronic structures;
8. what is the redox reactivity of such oxidized porphyrinogens: can they behave as multielectron agents and can they be selective for multielectron pathways over single-electron transfers ?

To answer these questions, synthetic routes will be needed to afford metalloporphyrinogens in various oxidation states with redox-inactive and spectroscopically silent counter-ions and axial ligands. Electrochemistry will provide information on available oxidation states and their stabilities. Structural data will be obtained by diffraction methods and NMR. Electronic structures will be probed by a variety of spectroscopic techniques. Finally, theoretical investigations will be conducted by density functional methods.

## I.4. References

1 *Comprehensive Coordination Chemistry II*; McCleverty, J.; Meyer, T. J., eds.; Elsevier: Oxford, 2004.

2 For example Werner, A. *Ber.* **1911**, *44*, 1887-1898.

3 Bethe, H. *Ann. Physik*, **1929**, *3*, 133-208.

4 Lewis, G. N. *J. Franklin Institute* **1938**, *226*, 293-313.

5 Cobble, J. W.; Adamson, A. W. *J. Am. Chem. Soc.* **1950**, *72*, 2276-2278.

6 Lewis, W. B.; Coryell, C. D.; Irvine, J. W., Jr. *J. Chem. Soc., Abstracts* **1949**, S386-S392.

7 Betts, R. H.; Gilmour, H. S. A.; Leigh, R. K. *J. Am. Chem. Soc.* **1950**, *72*, 4978-4980.

8 Ibers, J. A.; Davidson, N. *J. Am. Chem. Soc.* **1951**, *73*, 476-478.

9 Bonner, N. A.; Hunt, J. P. *J. Am. Chem. Soc.* **1952**, *74*, 1866.

10 Sheppard, J. C.; Wahl, A. C. *J. Am. Chem. Soc.* **1953**, *75*, 5133-5134.

11 Cohen, D.; Sullivan, J. C.; Hindman, J. C. *J. Am. Chem. Soc.* **1954**, *76*, 352-354.

12 George, P.; Irvine, D. H. *J. Chem. Soc., Abstracts* **1954**, 587-593.

13 Baker, B. R.; Basolo, F.; Neumann, H. M. *J. Phys. Chem.* **1959**, 63, 371-378.

14 Dodson, R. W. *J. Am. Chem. Soc.* **1950**, *72*, 3315-3316.

15 Harbottle, G.; Dodson, R. W. *J. Am. Chem. Soc.* **1951**, *73*, 2442-2447.

16 Gryder, J. W.; Dodson, R. W. J. Am. Chem. Soc. **1951**, *73*, 2890-2895.

17 Hudis, J.; Dodson, R. W. *J. Am. Chem. Soc.* **1956**, *78*, 911-913.

18 Sutin, N.; Rowley, J. K.; Dodson, R. W. *J. Phys. Chem.* **1961**, *65*, 1248-1252.

19 Taube, H.; Myers, H.; Rich, R. L. *J. Am. Chem. Soc.* **1953**, *75*, 4118-4119.

20 Taube, H; Myers, H. *J. Am. Chem. Soc.* **1954**, *76*, 2103-2111.

21 Taube, H.; King, E. L. *J. Am. Chem. Soc.* **1954**, *76*, 4053-4054.

22 Murmann, R. K.; Taube, H.; Posey, F. A. *J. Am. Chem. Soc.* **1957**, *79*, 262-265.

23 Ogard, A. E.; Taube, H. *J. Am. Chem. Soc.* **1958**, *80*, 1084-1089.

24 Taube, H. *Angew. Chem. Int. Ed. Engl.* **1984**, *23*, 329-339.

25 Franck, J. *Trans. Faraday Soc.* **1926**, *21*, 536-542.

26 Condon, E. U. *Phys. Rev.* **1926**, *28*, 1182-1201.

27 Libby, W. F. *J. Phys. Chem.* **1952**, *56*, 863-868.

28 Weiss, J. *Proc. Roy. Soc. (London)* **1954**, *A222*, 128-141.

29 Marcus, R. A. *J. Chem. Phys.* **1956**, *24*, 966-978.

30 Marcus, R. A. *J. Chem. Phys.* **1957**, *26*, 867-871.

31 Marcus, R. A. *J. Chem. Phys.* **1957**, *26*, 872-877.

32 Marcus, R. A. *Angew. Chem. Int. Ed. Engl.* **1993**, *32*, 1111-1121.

33 Hush, N. S. *Trans. Faraday Soc.* **1961**, *57*, 557-580.

34 Weissman, S. I. *J. Am. Chem. Soc.* **1958**, *80*, 6462-6463.

35 Isied, S. S.; Taube, H. *J. Am. Chem. Soc.* **1973**, *95*, 8198-8200.

36 Magnuson, R. H.; Taube, H. *J. Am. Chem. Soc.* **1972**, *94*, 7213-7214.

37 Tom, G. M.; Creutz, C.; Taube, H. *J. Am. Chem. Soc.* **1974**, *96*, 7827-7828.

38 Tom, G. M.; Taube, H. *J. Am. Chem. Soc.* **1975**, *97*, 5310-5311.

39 Fischer, H.; Tom, G. M.; Taube, H. *J. Am. Chem. Soc.* **1976**, *98*, 5512-5517.

40 Creutz, C.; Kroger, P.; Matsubara, T.; Netzel, T. L.; Sutin, N. *J. Am. Chem. Soc.* **1979**, *101*, 5442-5444.

41 Hush, N. S. *Progr. Inorg. Chem.* **1967**, *8*, 391-444.

42 Hurst, J. K. *J. Am. Chem. Soc.* **1976**, *98*, 4001-4003.

43 Halpern, J.; Legare, R. J.; Lumry, R. *J. Am. Chem. Soc.* **1963**, *85*, 680-682.

44 Wherland, S.; Gray, H. B. *Proc. Nat. Acad. Sci.* **1976**, *73*, 2950-2954.

45 Cummins, D.; Gray, H. B. *J. Am. Chem. Soc.* **1977**, *99*, 5158-5167.

46 Mauk, A. G.; Gray, H. B. *Biochem. Biophys. Res. Commun.* **1979**, *86*, 206-210.

47 Margalit, R.; Kostic, N. M.; Che, C.-M.; Blair, D. F.; Chiang, H.-J.; Pecht, I.; Shelton, J. B.; Shelton, J. R.; Schroeder, W. A.; Gray, H. B. *Proc. Nat. Acad. Sci.* **1984**, *81*, 6554-6558.

48 Winkler, J. R.; Nocera, D. G.; Yocom, K. M.; Bordignon, E.; Gray, H. B. *J. Am. Chem. Soc.* **1982**, *104*, 5798-57800.

49 Makinen, M. W.; Schichman, S. A.; Hill, S. C.; Gray, H. B. *Science* **1983**, *222*, 929-931.

50 Nocera, D. G.; Winkler, J. R.; Yocom, K. M.; Bordignon, E.; Gray, H. B. *J. Am. Chem. Soc.* **1984**, *106*, 5145-5150.

51 McLendon, G. L.; Winkler, J. R.; Nocera, D. G.; Mauk, M. R.; Mauk, A. G.; Gray, H. B. *J. Am. Chem. Soc.* **1985**, *107*, 739-740.

52 Creutz, C.; Sutin, N. *J. Am. Chem. Soc.* **1977**, *99*, 241-243.

53 Irvine, M. P.; Harrison, R. J.; Beddard, G. S.; Leighton, P.; Sanders, J. K. M. *Chem. Phys.* **1986**, *104*, 315-324.

54 Fox, L. S.; Kozik, M.; Winkler, J. R.; Gray, H. B. *Science* **1990**, *247*, 1069-1071.

55 Part III of the following paper reviews the theory and experimental data concerning ET, particularly in biological system, Part IV describes PCET, and Part V its importance in ribonucleotide reductase: Stubbe, J.; Nocera, D. G.; Yee, C. S.; Chang, M. C. Y. *Chem. Rev.* **2003**, *103*, 2167-2201.

56 Cukier, R. I.; Nocera, D. G. *Annu. Rev. Phys. Chem.* **1998**, *49*, 337-369.

57 Damrauer, N. H.; Hodgkiss, J. M.; Rosenthal, J.; Nocera, D. G. *J. Phys. Chem. B* **2004**, *108*, 6315-6321.

58 Mayer, J. M. *Ann. Rev. Phys. Chem.* **2004**, *55*, 363-390.

59 Hammes-Schiffer, S. *Acc. Chem. Res.* **2001**, *34*, 273-281.

60 Hammes-Schiffer, S.; Iordanova, N. *Biochim. Biophys. Acta - Bioenergetics* **2004**, *1655*, 29-36.

61 Hodgkiss, J. M.; Damrauer, N. H.; Pressé, S.; Rosenthal, J. R.; Nocera, D. G. *J. Phys. Chem.*, submitted.

62 Mader, E. A.; Larsen, A. S.; Mayer, J. M. *J. Am. Chem. Soc.* **2004**, *126*, 8066-8067.

63 Aubert, C.; Vos, M. H.; Mathis, P.; Eker, A. P. M.; Brettel, K. *Nature* **2000**, *405*, 586-590.

64 Radmer, R., Kok, B. *Ann. Rev. Biochem.* **1975**, *44*, 409-433.

65 Noy, D.; Moser, C. C.; Dutton, L. *Biochim. Biophys. Acta – Bioenergetics* **2006**, *1757*, 90-105.

66 Dutton, P. L.; Chen, X.; Page, C. C.; Huang, S.; Ohnishi, T.; Moser, C. C. *NATO ASI Series, C* **1998**, *512*, 3-8.

67 Link, T. A. *Studies Phys. Theor. Chem.* **1992**, *78*, 197-217.

68 Groves, J. T.; Kruper, W. J., Jr. *J. Am. Chem. Soc.* **1979**, *101*, 7613-7615.

69 Holm, R. H. *Chem. Rev.* **1987**, *87*, 1401-1449.

70 Mao, S. S.; Holler, T. P.; Yu, G. X.; Bollinger, J. M.; Booker, S.; Johnston, M. I.; Stubbe, J. *Biochem.* **1992**, *31*, 9733-9743.

71 Katsuki, T. *Adv. Synth. Cat.* **2002**, *344*, 131-147.

72 Palucki, M.; McCormick, G. J.; Jacobsen, E. N. *Tet. Lett.* **1995**, *36*, 5457-5460.

73 Kolb, H. C.; Vannieuwenhze, M. S.; Sharpless, K. B. *Chem. Rev.* **1994**, *94*, 2483-2547.

74 Miyaura, N.; Suzuki, A. *Chem. Rev.* **1995**, *95*, 2457-2483.

75 Laplaza, C. E.; Johnson, M. J. A.; Peters, J. C.; Odom, A. L.; Kim, E.; Cummins, C. C.; George, G. N.; Pickering, I. J. *J. Am. Chem. Soc.* **1996**, *118*, 8623-8638.

76 Schrock, R. R. *Acc. Chem. Res.* **2005**, *38*, 955-962.

77 Radmer, R.; Kok, B. *Ann. Rev. Biochem.* **1975**, *44*, 409-433.

78 Peloquin, J. M.; Britt, R. D. *Biochim. Biophys. Acta – Bioenergetics* **2001**, *1503*, 96-111.

79 Britt, R. D.; Campbell, K. A.; Peloquin, J. M.; Gilchrist, M. L.; Aznar, C. P.; Dicus, M. M.; Robblee, J.; Messinger, J. *Biochim. Biophys. Acta – Bioenergetics* **2004**, *1655*, 158-171.

80 Iwata, S.; Barber, J. *Curr. Opin. Struct. Biol.* **2004**, *14*, 447-453.

81 Soper, J. D.; Mayer, J. M. *J. Am. Chem. Soc.* **2003**, *125*, 12217-12229.

82 Baik, M. H.; Newcomb, M.; Friesner, R. A.; Lippard, S. J. *Chem. Rev.* **2003**, *103*, 2385-2419.

83 Watanabe, Y. in *The Porphyrin Handbook*; Kadish, K. M., Smith, K. M.; Guilard, R., eds.; Academic Press: New York, 2000; Vol. 4, pp 97-118.

84 *Cytochrome P450*, 2nd ed; Ortiz de Montellano, P. R., ed.; Plenum Press: New York, 1995.

85 Harischandra, D. N.; Zhang, R.; Newcomb M. *J. Am. Chem. Soc.* **2005**, *127*, 13776-13777.

86 Wagner, W.-D.; Nakamoto, K. *J. Am. Chem. Soc.* **1989**, *111*, 1590-1598.

87 Aliaga-Alcalde, N.; DeBeer George, S.; Mienert, B.; Bill, E.; Wieghardt, K.; Neese, F. *Angew. Chem. Int. Ed.* **2005**, *44*, 2908-2912.

88 Richter-Addo, G. B.; Legzdins, P. *Metal Nitrosyls*; Oxford University Press: New York, 1992.

89 Mu, X. H.; Kadish, K. M. *Inorg. Chem.* **1988**, *27*, 4120-4125.

90 Ford, P. C.; Lorković, I. M. *Chem. Rev.* **2002**, *102*, 993-1017.

91 Scott, N. D.; Walker, J. F.; Hansley, V. L. *J. Am. Chem. Soc.* **1936**, *58*, 5442-5444.

92 Kubo, H.; Hirano, M.; Komiya, S. *J. Organomet. Chem.* **1998**, *556*, 89-95.

93 Brennessel, W. W.; Ellis, J. E.; Pomije, M. K.; Sussman, V. J.; Urnezius, E.; Young, V. G., Jr. *J. Am. Chem. Soc.* **2002**, *124*, 10258-10259.

94 Engelhardt, L. M.; Harvey, S.; Raston, C. L.; White, A. H. *J. Organomet. Chem.* **1988**, *341*, 39-51.

95 Sitzmann, H.; Walter, M. D.; Wolmershauser, G. *Angew. Chem. Int. Ed.* **2002**, *41*, 2315-2316.

96 Evans, W. J.; Nyce, G. W.; Ziller, J. W. *Angew. Chem. Int. Ed.* **2000**, *39*, 240-242.

97 Diaconescu, P. L.; Cummins, C. C. *J. Am. Chem. Soc.* **2002**, *124*, 7660-7661.

98 Cotton, F. A.; Edwards, W. T. *J. Am. Chem. Soc.* **1968**, *90*, 5412-5417.

99 Reingold, J. A.; Virkaitis, Ku. L.; Carpenter, G. B.; Sun, S.; Sweigart, D. A.; Czech, P. T.; Overly, K. R. *J. Am. Chem. Soc.* **2005**, *127*, 11146-11158.

100 Stoll, M. E.; Belanzoni, P.; Calhorda, M. J.; Drew, M. G. B.; Felix, V.; Geiger, W. E.; Gamelas, C. A.; Goncalves, I. S.; Romao, C. C.; Veiros, L. F. *J. Am. Chem. Soc.* **2001**, *123*, 10595-10606.

101 Inagaki, A.; Takaya, Y.; Takemori, T.; Suzuki, H.; Tanaka, M.; Haga, M. *J. Am. Chem. Soc.* **1997**, *119*, 625-626.

102 Merkert, J.; Nielson, R. M.; Weaver, M. J.; Geiger, W. E. *J. Am. Chem. Soc.* **1989**, *111*, 7084-7087.

103 Nielson, R. M.; Weaver, M. J. *Organometallics* **1989**, 8, 1636-1643.

104 Bowyer, W. J.; Merkert, J. W.; Geiger, W. E.; Rheingold, A. L. *Organometallics* **1989**, *8*, 191-198.

105 Wonga, W. W. H.; Curiela, D.; Laib, S.-W.; Drewc, M. G. B.; Beer, P. D. *Dalton Trans.* **2005**, 774-781.

106 Denuault, G.; Gale, P. A.; Hursthouse, M. B.; Light, M. E.; Warriner, C. N. *New J. Chem.* **2002**, *26*, 811-813.

107 Siemeling, U. *Z. Anorg. Allg. Chem.* **2005**, *631*, 2957-2966.

108 Guerro, M.; Roisnel, T.; Pellon, P.; Lorcy, D. *Inorg. Chem.* **2005**, *44*, 3347-3355.

109 Blower, M. A.; Bryce, M. R.; Devonport, W. *Adv. Mat.* **1996**, *8*, 63-65.

110 Loosli, C.; Jia, C.; Liu, S.-X.; Haas, M.; Dias, M.; Levillain, E.; Neels, A.; Labat, G.; Hauser, A.; Decurtins, S. *J. Org. Chem.* **2005**, *70*, 4988-4992.

111 Nielsen, K. A.; Cho, W.-S.; Lyskawa, J.; Levillain, E.; Lynch, V. M.; Sessler, J. L.; Jeppesen, J. O. *J. Am. Chem. Soc.* **2006**, *128*, 2444-2451.

112 Schrauzer, G. N.; Mayweg, V. P. *J . Am. Chem. Soc.* **1962**, *84*, 3221.

113 Schrauzer, G. N.; Mayweg, V. P. *J. Am. Chem. Soc.* **1965**, *87*, 3585-3592.

114 Davison, A.; Edelstein, N.; Holm, R. H.; Maki, A. H. *J. Am. Chem. Soc.* **1963**, *85*, 2029-2030.

115 Davison, A.; Edelstein, N.; Holm, R. H.; Maki, A. H. *J. Am. Chem. Soc.* **1963**, *85*, 3049-3050.

116 Davison, A.; Edelstein, N.; Holm, R. H.; Maki, A. H. *Inorg. Chem.* **1964**, *3*, 814-823.

117 Davison, A.; Edelstein, N.; Holm, R. H.; Maki, A. H. *J. Am. Chem. Soc.* **1964**, *86*, 2799-2805.

118 Maki, A. H.; Edelstein, N.; Davison, A.; Holm, R. H. *J. Am. Chem. Soc.* **1964**, *86*, 4580-4587.

119 Davison, A.; Edelstein, N.; Holm, R. H.; Maki, A. H. *Inorg. Chem.* **1963**, *2*, 1227-1232.

120 Davison, A.; Edelstein, N.; Holm, R. H.; Maki, A. H. *Inorg. Chem.* **1965**, *4*, 55-59.

121 Maki, A. H.; Berry, T. E.; Davison, A.; Holm, R. H.; Balch, A. L. *J. Am. Chem. Soc.* **1966**, *88*, 1080-1082.

122 Holm, R. H.; Balch, A. L.; Davison, A.; Maki, A. H.; Berry, T. E. *J. Am. Chem. Soc.* **1967**, *89*, 2866-2874.

123 Davison, A.; Holm, R. H. *Inorg. Synth.* **1967**, *10*, 8-26.

124 Latham, A. R.; Hascall, V. C.; Gray, H. B. *Inorg. Chem.* **1965**, *4*, 788-792.

125 Billig, E.; Williams, R.; Bernal, I.; Waters, J. H.; Gray, H. B. *Inorg. Chem.* **1964**,*3*, 663-666.

126 Shupack, S. I.; Billig, E.; Clark, R. J. H.; Williams, R.; Gray, H. B. *J. Am. Chem. Soc.* **1964**, *86*, 4594-4602.

127 Gray, H. B.; Billig, E. *J. Am. Chem. Soc.* **1963**, *85*, 2019-2020.

128 Stiefel, E. I.; Waters, J. H.; Billig, E.; Gray, H. B. *J. Am. Chem. Soc.* **1965**, *87*, 3016-3017.

129 Herebian, D.; Ghosh, P.; Chun, H.; Bothe, E.; Weyhermuller, T.; Wieghardt, K. *Eur. J. Inorg. Chem.* **2002**, 1957-1967.

130 Arion, V.; Wieghardt, K.; Weyhermueller, T.; Bill, E.; Leovac, V.; Rufinska, A. *Inorg. Chem.* **1997**, *36*, 661-669.

131 De Bruin, B.; Bill, E.; Bothe, E.; Weyhermueller, T.; Wieghardt, K. *Inorg. Chem.* **2000**, *39*, 2936-2947.

132 Ray, K.; Weyhermueller, T.; Goossens, A.; Craje, M. W. J.; Wieghardt, K. *Inorg. Chem.* **2003**, *42*, 4082-4087.

133 Ghosh, P.; Bill, E.; Weyhermueller, T.; Wieghardt, K. *J. Am. Chem. Soc.* **2003**, *125*, 3967-3979.

134 Min, K. S.; Weyhermueller, T.; Bothe, E.; Wieghardt, K. *Inorg. Chem.* **2004**, *43*, 2922-2931.

135 Bill, E.; Bothe, E.; Chaudhuri, P.; Chlopek, K.; Herebian, D.; Kokatam, S.; Ray, K.; Weyhermueller, T.; Neese, F.; Wieghardt, K. *Chem. Eur. J.* **2005**, *11*, 204-224.

136 Ray, K.; Bill, E.; Weyhermueller, T.; Wieghardt, K. *J. Am. Chem. Soc.* **2005**, *127*, 5641-5654.

137 Blanchard, S.; Neese, F.; Bothe, E.; Bill, E.; Weyhermueller, T.; Wieghardt, K. *Inorg. Chem.* **2005**, *44*, 3636-3656.

138 Ray, K.; Weyhermueller, T.; Neese, F.; Wieghardt, K. *Inorg. Chem.* **2005**, *44*, 5345-5360.

139 Chlopek, K.; Bill, E.; Ueller, T. W.; Wieghardt, K. *Inorg. Chem.* **2005**, *44*, 7087-7098.

140 Kohn, W.; Becke, A. D.; Parr, R. G. *J. Phys. Chem.* **1996**, *100*, 12974-12980.

141 Blackmore, K. J.; Ziller, J. W.; Heyduk, A. F. *Inorg. Chem.* **2005**, *44*, 5559-5561.

142 Groves, J. T.; Haushalter, R. C.; Nakamura, M.; Nemo, T. E.; Evans, B. J. *J. Am. Chem. Soc.* **1981**, *103*, 2884-2886.

143 Dolphin, D.; Forman, A; Borg, D. C.; Fajer, J.; Felton, R. H. *Proc. Nat. Acad. Sci.* **1971**, *68*, 614-618.

144 Felton, R. H.; Dolphin, D.; Borg, D. C.; Fajer, J. *J. Am. Chem. Soc.* **1969**, *91*, 196-198.

145 Fajer, J.; Borg, D. C.; Forman, A.; Dolphin, D.; Felton, R. H. *J. Am. Chem. Soc.* **1970**, *92*, 3451-3459.

146 Ozawa, S.; Watanabe, Y.; Morishima, I. *J. Am. Chem. Soc.* **1994**, *116*, 5832-5838.

147 Renner, M. W.; Buchler, J. W. *J. Phys. Chem.* **1995**, *99*, 8045-8049.

148 Van Caemelbecke, E.; Will, S.; Autret, M.; Adamian, V. A.; Lex, J.; Gisselbrecht, J.-P.; Gross, M.; Vogel, V.; Kadish, K. M. *Inorg. Chem.* **1996**, *35*, 184-192.

149 Cai, S.; Walker, F. A.; Licoccia, S. *Inorg. Chem.* **2000**, *39*, 3466-3478.

150 Simkhovich, L.; Goldberg, I.; Gross, Z. *Inorg. Chem.* **2002**, *41*, 5433-5439.

151 Hilt, G.; Jarbawi, T.; Heineman, W. R.; Steckhan, E. *Chem. Eur. J.* **1997**, *3*, 79-88.

152 Galet, A.; Munoz, M. C.; Agusti, G.; Martinez, V.; Gaspar, A. B.; Real, J. A. *Z. Anorg. Allg. Chem.* **2005**, *631*, 1985-1987.

153 Von Baeyer, J. F. W. A. *Ber.* **1886**, *19*, 2184.

154 Granick, S.; Mauzerall, D. *J. Biol. Chem.* **1958**, *232*, 1119-1140.

155 Mauzerall, D. *J. Am. Chem. Soc.* **1962**, *84*, 2437-2445.

156 Sano, S.; Tanaka, K. *J. Biol. Chem.* **1964**, *239*, PC3109-PC3110.

157 Rothemund, P. *J. Am. Chem. Soc.* **1936**, *58*, 625-627.

158 Rothemund, P. Gage, C. L. *J. Am. Chem. Soc.* **1955**, *77*, 3340-3342.

159 Jacoby, D.; Floriani, C.; Chiesi-Villa, A.; Rizzoli, C. *J. Chem. Soc., Chem. Commun.* **1991**, 220-222.

160 Miyaji, H.; Sato, W.; Sessler, J. L. *Angew. Chem. Int. Ed.* **2000**, *39*, 1777-1780.

161 Gale, P. A.; Hursthouse, M. B.; Light, M. E.; Sessler, J. L.; Warriner, C. N.; Zimmerman, R. S. *Tet. Lett.* **2001**, *42*, 6759-6762.

162 Yoon, D.-W.; Hwang, H.; Lee, C.-H. *Angew. Chem. Int. Ed.* **2002**, *41*, 1757-1759.

163 Woods, C. J.; Camiolo, S.; Light, M. E.; Coles, S. J.; Hursthouse, M. B.; King, M. A.; Gale, P. A.; Essex, J. W. *J. Am. Chem. Soc.* **2002**, *124*, 8644-8652.

164 Blas, J. R.; Marquez, M.; Sessler, J. L.; Luque, F. J.; Orozco, M. *J. Am. Chem. Soc.* **2002**, *124*, 12796-12805.

165 Nielsen, K. A.; Jeppesen, J. O.; Levillain, E.; Becher, J. *Angew. Chem. Int. Ed.* **2003**, *42*, 187-191.

166 Danil De Namor, A. F.; Shehab, M. *J. Phys. Chem. B* **2003**, *107*, 6462-6468.

167 Panda, P. K.; Lee, C.-H. *Org. Lett.* **2004**, *6*, 671-674.

168 Danil de Namor, A. F.; Shehab, M. *J. Phys. Chem. A* **2004**, *108*, 7324-7330.

169 Nielsen, K. A.; Cho, W.-S.; Jeppesen, J. O.; Lynch, V. M.; Becher, J.; Sessler, J. L. *J. Am. Chem. Soc.* **2004**, *126*, 16296-16297.

170 Panda, P. K.; Lee, C.-H. J. Org. Chem. **2005**, *70*, 3148-3156.

171 Custelcean, R.; Delmau, L. H.; Moyer, B. A.; Sessler, J. L.; Cho, W.-S.; Gross, D.; Bates, G. W.; Brooks, S. J.; Light, M. E.; Gale, P. A. *Angew. Chem. Int. Ed.* **2005**, *44*, 2537-2542.

172 Miyaji, H.; Kim, H.-K.; Sim, E.-K.; Lee, C.-K.; Cho, W.-S.; Sessler, J. L.; Lee, C.-H. *J. Am. Chem. Soc.* **2005**, *127*, 12510-12512.

173 Danil de Namor, A. F.; Shehab, M. *J. Phys. Chem. B* **2005**, *109*, 17440-17444.

174 Ji, X. K.; Black, D. S.; Colbran, S. B.; Craig, D. C.; Edbey, K. M.; Harper, J. B.; Willett, G. D. *Tetrahedron* **2005**, *61*, 10705-10712.

175 Floriani, C.; Floriani-Moro, R. in *The Porphyrin Handbook*; Kadish, K. M., Smith, K. M.; Guilard, R., Ed.; Academic Press: New York, 2000; Vol. 3, pp 385-403.

176 Jubb, J.; Jacoby, D.; Floriani, C.; Chiesi-Villa, A.; Rizzoli, C. *Inorg. Chem.* **1992**, *31*, 1306-1308.

177 Bonomo, L.; Solari, E.; Scopelliti, R.; Floriani, C. *Chem. Eur. J.* **2001**, *7*, 1322-1332.

178 Bonomo, L.; Dandin, O.; Solari, E.; Floriani, C.; Scopelliti, R. *Angew. Chem. Int. Ed.* **1999**, *38*, 914-915.

179 Benech, J.-M.; Bonomo, L.; Solari, E.; Scopelliti, R.; Floriani, C. *Angew. Chem. Int. Ed.* **1999**, *38*, 1957-1959.

180 Floriani, C. *Pure Appl. Chem.* **1996**, *68*, 1-8.

181 Bonomo, L.; Solari, E.; Scopelliti, R. ; Floriani, C. *Angew. Chem. Int. Ed.* **2001**, *40*, 2597-2599.

182 Jacoby, D.; Floriani, C.; Chiesi-Villa, A.; Rizzoli, C. *J. Am. Chem. Soc.* **1993**, *115*, 3595-3602.

183 Jacoby, D.; Isoz, S.; Floriani, C.; Schenk, K.; Chiesi-Villa, A.; Rizzoli, C. *Organometallics* **1995**, *14*, 4816-4824.

184 Bonomo, L.; Stern. C. ; Solari, E.; Scopelliti, R. ; Floriani, C. *Angew. Chem. Int. Ed.* **2001**, *40*, 1449-1452.

185 Jacoby, D.; Isoz, S.; Floriani, C.; Chiesi-Villa, A.; Rizzoli, C. *J. Am. Chem. Soc.* **1995**, *117*, 2805-2816.

186 Jacoby, D.; Isoz, S.; Floriani, C.; Chiesi-Villa, A.; Rizzoli, C. *J. Am. Chem. Soc.* **1995**, *117*, 2793-2804.

187 Crescenzi, R.; Solari, E.; Floriani, C.; Re, N.; Chiesi-Villa, A.; Rizzoli, C. *Organometallics* **1999**, *18*, 606-618.

188 Bonomo, L.; Solari, E.; Floriani, C.; Chiesi-Villa, A.; Rizzoli, C. *J. Am. Chem. Soc.* **1998**, *120*, 12972-12973.

189 Campazzi, E.; Solari, E.; Scopelliti, R.; Floriani, C. *Inorg. Chem*. **1999**, *38*, 6240-6245.

190 Campazzi, E.; Solari, E.; Scopelliti, R.; Floriani, C. *Chem. Commun*. **1999**, 1617-1618.

191 Wang, J.; Dick, A. K. J.; Gardiner, M. G.; Yates, B. F.; Peacock, E. J.; Skelton, B. W.; White, A. H. *Eur. J. Inorg. Chem.* **2004**, 1992-1995.

192 Isoz, S.; Floriani, C.; Schenk, K.; Chiesi-Villa, A.; Rizzoli, C. *Organometallics* **1996**, *15*, 337-344.

193 Campazzi, E.; Solari, E.; Floriani, C.; Scopelliti, R. *Chem. Commun.* **1998**, *23*, 2603-2604.

194 Korobkov, I.; Gambarotta, S.; Yap, G. P. A. *Angew. Chem. Int. Ed.* **2002**, *41*, 3433-3436.

195 Korobkov, I.; Gambarotta, S.; Yap, G. P. A. *Angew. Chem. Int. Ed.* **2003**, *42*, 814-818.

196 Korobkov, I.; Aharonian, G.; Gambarotta, S.; Yap, G. P. A. *Organometallics* **2002**, *21*, 4899-4901.

197 Bonomo, L.; Solari, E.; Scopelliti, R.; Floriani, C.; Re, N. *J. Am. Chem. Soc.* **2000**, *122*, 5312-5326.

198 Bonomo, L.; Solari, E.; Martin, G.; Scopelliti, R.; Floriani, C. *Chem. Commun*. **1999**, 2319-2320.

199 Harmjanz, M.; Gill, H. S.; Scott, M. J. *J. Am. Chem. Soc.* **2000**, *122*, 10476-10477.

200 Harmjanz, M.; Gill, H. S.; Scott, M. J. *J. Org. Chem.* **2001**, *66*, 5374-5383.

201 Harmjanz, M.; Božidarević, I.; Scott, M. J. *Org. Lett.* **2001**, *3*, 2281-2284.

202 Floriani, C.; Floriani-Moro, R. in *The Porphyrin Handbook*; Kadish, K. M., Smith, K. M.; Guilard, R., Ed.; Academic Press:New York, 2000; Vol. 3, pp 405-420.

203 Jubb, J.; Floriani, C.; Chiesi-Villa, A.; Rizzoli, C. *J. Am. Chem. Soc.* **1992**, *114*, 6571-6573.

204 De Angelis, S.; Solari, E.; Floriani, C.; Chiesi-Villa, A.; Rizzoli, C. *J. Am. Chem. Soc.* **1994**, *116*, 5691-5701.

205 De Angelis, S.; Solari, E.; Floriani, C.; Chiesi-Villa, A.; Rizzoli, C. *J. Am. Chem. Soc.* **1994**, *116*, 5702-5713.

206 Piarulli, U.; Solari, E.; Floriani, C.; Chiesi-Villa, A.; Rizzoli, C. *J. Am. Chem. Soc.* **1996**, *118*, 3634-3642.

207 Crescenzi, R.; Solari, E.; Floriani, C.; Chiesi-Villa, A.; Rizzoli, C. *J. Am. Chem. Soc.* **1999**, *121*, 1695-1706.

208 Bhattacharya, D.; Dey, S.; Maji, S.; Pal, K.; Sarkar, S. *Inorg. Chem.* **2005**, *44*, 7699-7701.

209 Bucher, C.; Devillers, C. H.; Moutet, J.-C.; Pécaut, J.; Royal, G.; Saint-Amana, E.; Thomas, F. *Dalton Trans.* **2005**, 3620-3631.

# Chapter II

# Electron transfer series of porphyrinogen complexes with redox-inert metal dications — synthesis and structures

Parts of this Chapter have been published:
Bachmann, J.; Nocera, D. G. *J. Am. Chem. Soc.* **2004**, *126*, 2829-2837;
Bachmann, J.; Nocera, D. G. *Inorg. Chem.* **2005**, *44*, 6930-6932.

## II.1. Introduction

The cleanest demonstration of the "non-innocence" of a ligand consists in the isolation of an electron transfer series of its complex with a redox-inert metal ion. The electrochemistry of the complex then furnishes a full thermodynamic characterization. Its spectroscopy enables some description of its electronic structure. Such work was performed early on with magnesium and zinc porphyrins,[1,2] and with nickel, palladium, platinum, zinc and cadmium bis(dithiolene)s.[3-6]

In the tetrapyrrole macrocycle porphyrinogen, it has been shown that one or two cyclopropane rings may be formed from C—C coupling between the $\alpha$-carbons of neighboring pyrroles upon oxidation of the tetrapyrrole — this transformation effectively entails the storage of two or four hole equivalents in the macrocycle ring.[7-12] However, simple characterization similar to that performed on the systems mentioned above is absent from the porphyrinogen literature. Electrochemical and spectroscopic measurements have been obviated by the presence of redox-active central metal ions, axial ligands and/or redox-active polynuclear metal-halide counter-ions in most oxidized porphyrinogens prepared to date. Thus the multielectron redox chemistry of the porphyrinogen framework has remained ill defined.

This Chapter delineates the metallation of porphyrinogen with the redox-inert dications of zinc, magnesium and calcium, and the oxidation of the resulting dianions to yield neutral and dicationic oxidation states in the absence of redox- and spectroscopically active counter-ions and other ligands. Owing to this simplicity, the intrinsic redox properties of porphyrinogen in a homologous $[LM]^{2-}$ / $[L^{\Delta}M]$ / $[L^{\Delta\Delta}M]^{2+}$ series have been unveiled by electrochemistry — $L^{4-}$, $L^{\Delta 2-}$ and $L^{\Delta\Delta}$ represent the reduced, two- and four-electron oxidized porphyrinogen frameworks, respectively. Characteristic structural features are followed spectroscopically (NMR, IR) and structurally (in the solid state). The next Chapter will be concerned with the electronic structure of the same compounds.

Methyl is used as the *meso* substituent in order to prevent undesired oxidative pathways in which a β-hydrogen in close interaction with the central metal initiates the elimination of the *meso* substituent.[13-15]

## II.2. Synthesis

### II.2.a. Metallations

Zinc porphyrinogen $[LZn]^{2-}$ was prepared as its solvated lithium salt by direct reaction

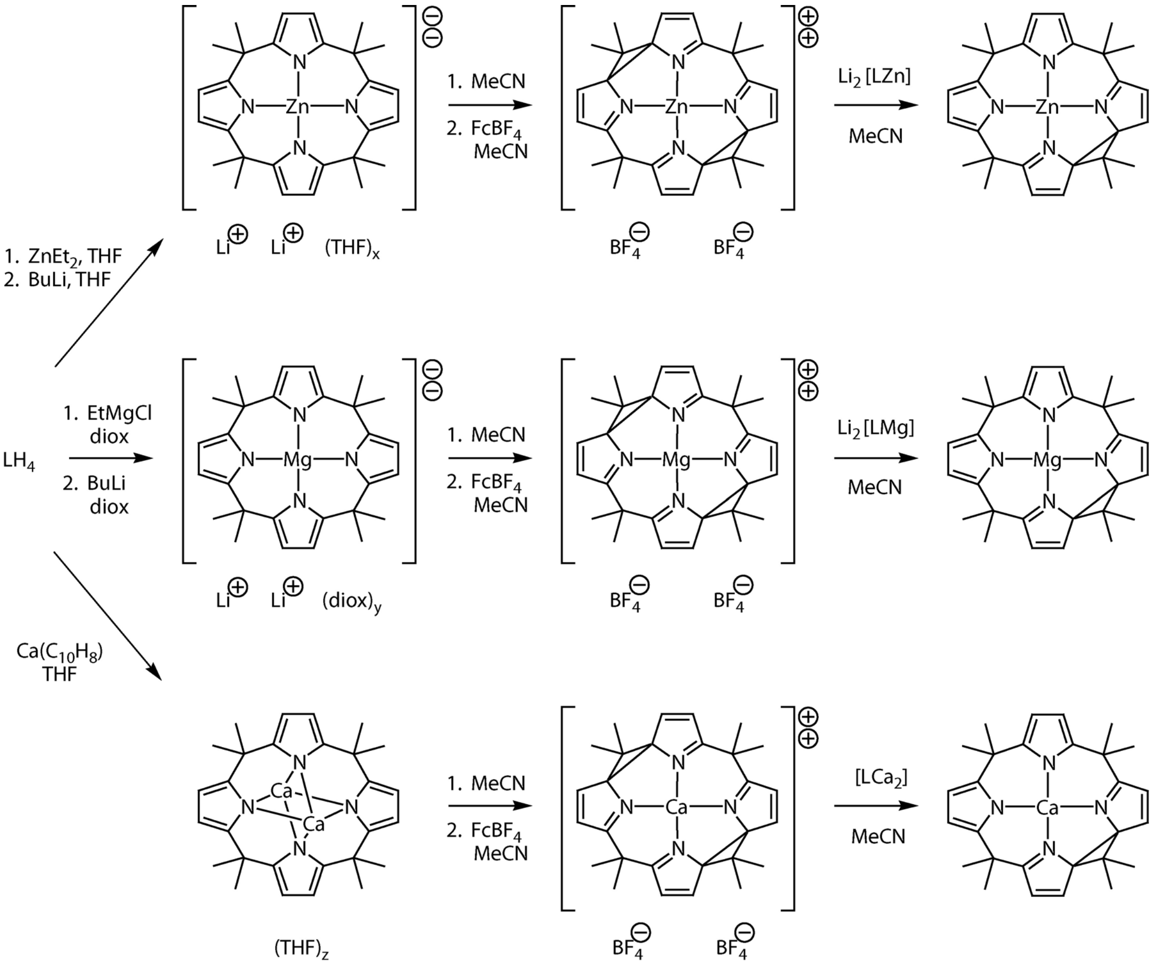
1. $ZnEt_2$, THF
2. BuLi, THF
LH$_4$
1. EtMgCl
diox
2. BuLi
diox
$Ca(C_{10}H_8)$
THF
$Li^+$ $Li^+$ $(THF)_x$
$Li^+$ $Li^+$ $(diox)_y$
$(THF)_z$
1. MeCN
2. $FcBF_4$
MeCN
$BF_4^-$ $BF_4^-$
$Li_2[LZn]$
MeCN
$Li_2[LMg]$
MeCN
$[LCa_2]$
MeCN
N
Zn
Mg
Ca

**Scheme II.1.** Synthesis of electron transfer series of octamethylporphyrinogen complexes of zinc, magnesium and calcium. $Fc^+$ = ferrocenium (bis(cyclopentadienyl)iron(III)) cation; Et = ethyl; Bu = butyl; diox = 1,4-dioxane; $C_{10}H_8$ = naphthalene.

of the free ligand $LH_4$ with BuLi and $ZnEt_2$. A homoleptic dialkylzinc reagent allows for the convenient introduction of the $Zn^{2+}$ ion in a single step from the free base macrocycle. The lithium salt of $[LMg]^{2-}$ was obtained by reaction of diethylmagnesium, generated *in situ* from ethylmagnesium chloride in 1,4-dioxane, and butyllithium with $LH_4$. In the case of calcium, the preference of the constrained doubly oxidized macrocycle, $L^{\Delta\Delta}$, for small cations forced us to avoid $Li^+$ altogether and prepare $[LCa_2]$ from $LH_4$ and activated calcium.[16]

## II.2.b. Oxidations

The fully oxidized member of the series, $[L^{\Delta\Delta}M]^{2+}$ (M = Mg, Zn, Ca), is readily afforded from the oxidation of $[LM]^{2-}$ (M = Mg, Zn) or $[LCa_2]$ in $CH_3CN$ by four equivalents of ferrocenium tetrafluoroborate, after removal of the ethereal solvent molecules solvating the starting materials. The intermediary oxidation state $[L^{\Delta}M]$ can be obtained from the same starting materials by similar treatment with two equivalents of ferrocenium, however it is most conveniently afforded from the near-quantitative comproportionation of $[L^{\Delta\Delta}M]^{2+}$ and $[LM]^{2-}$ (M = Mg, Zn) or $[LCa_2]$. Scheme II.1 delineates the full synthetic pathway for the three electron transfer series. The success of the comproportionation establishes the reversibility of the redox processes within the three series.

The exact conditions (solvent and counter-ion) of the oxidation are crucial to its success since oxidized porphyrinogens are extremely sensitive to decomposition *via* radical pathways. In particular, oxidation of $[LZn]^{2-}$ with ferrocenium hexafluorophosphate in THF fails to provide $[L^{\Delta\Delta}Zn]^{2+}$. Instead, single crystals grown from the reaction mixture allowed the identification of a decomposition product, the solvated, polymeric salt $Zn(O_2PF_2)_2$ (zinc difluorophosphate), by X-ray diffraction analysis (*cf.* Figure II.1 and Tables II.1 and II.2). Accordingly, the reaction conditions were successfully adapted to the use of the $BF_4^-$ salt of $Fc^+$ in MeCN.

**Table II.1.** Summary of X-ray crystallographic data for $[(THF)_2Zn(O_2PF_2)_2]_\infty$.

| | |
|---|---|
| empirical formula (formula weight) | $C_8H_{16}F_4O_6P_2Zn$ (411.54) |
| $T$ (K) | 193(2) |
| $\lambda$ (Å) | 0.71073 |
| crystal system, space group | Monoclinic, $P2_1/c$ |
| $a$ ; $b$ ; $c$ (Å) | 23.1761(18) ; 12.3983(9) ; 10.5537(8) |
| $\beta$ (deg) | 90.0180(10) |
| $Z$ ; $V$ (Å$^3$) | 8 ; 3032.5(4) |
| crystal size (mm$^3$) | 0.47 × 0.07 × 0.07 |
| Abs. coeff. (mm$^{-1}$) | 1.895 |
| $F$(000) | 1664 |
| $\theta$ range for data collection | 2.41 to 23.27° |
| limiting indices | $-11 \le h \le 11$, $-11 \le k \le 6$, $-15 \le \ell \le 15$ |
| no. of reflns collcd ; no. of ind reflns ($R_{int}$) | 11958 ; 4354 (0.1085) |
| completeness to $\theta = 23.27°$ | 99.6 % |
| refinement method | Full-matrix least-squares on $F^2$ |
| data / restraints / parameters | 4354 / 0 / 379 |
| $R_1$,[a] $wR_2$[b] ($I > 2\sigma(I)$) | 0.0720, 0.1861 |
| $R_1$,[a] $wR_2$[b] (all data) | 0.0883, 0.1975 |
| GOF[c] on $F^2$ | 1.197 |
| largest diff. peak and hole | 0.868 and –0.558 eÅ$^{-3}$ |

[a] $R_1 = \Sigma||F_o| - |F_c||/\Sigma|F_o|$.

[b] $wR_2 = (\Sigma(w(F_o^2 - F_c^2)^2)/\Sigma(w(F_o^2)^2))^{1/2}$.

[c] $GOF = (\Sigma\, w(F_o^2 - F_c^2)^2/(n - p))^{1/2}$,
where $n$ is the number of data and $p$ is the number of parameters refined.

**Table II.2.** Selected geometric parameters for $[(THF)_2Zn(O_2PF_2)_2]_\infty$.

| Distances / Å | | Angles / deg | |
|---|---|---|---|
| Zn(1)—O(3) | 2.056(5) | O(3)–Zn(1)–O(2′) | 175.5(2) |
| Zn(1)—O(2′) | 2.064(5) | O(3)–Zn(1)–O(1) | 91.71(17) |
| Zn(1)—O(1) | 2.068(4) | O(2′)–Zn(1)–O(1) | 88.69(17) |
| Zn(1)—O(4′) | 2.073(4) | O(3)–Zn(1)–O(4′) | 88.39(17) |
| Zn(1)—O(9) | 2.125(5) | O(2)–P(1)–O(1) | 121.6(3) |
| Zn(1)—O(10) | 2.137(5) | O(2)–P(1)–F(2) | 108.4(3) |
| P(1)—O(2) | 1.452(5) | O(1)–P(1)–F(2) | 107.2(3) |
| P(1)—O(1) | 1.474(4) | O(2)–P(1)–F(1) | 109.9(3) |
| P(1)—F(2) | 1.522(5) | O(1)–P(1)–F(1) | 108.9(3) |
| P(1)—F(1) | 1.529(5) | F(2)–P(1)–F(1) | 98.4(3) |

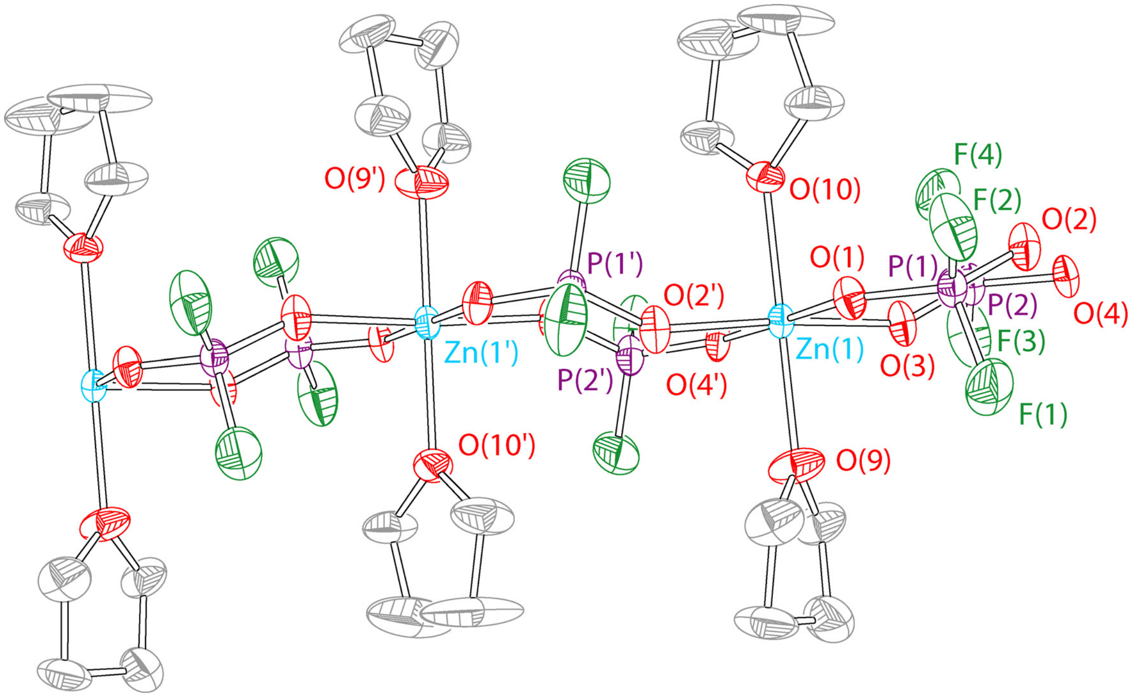

**Figure II.1.** Crystal structure of zinc difluorophosphate. It consists of polymeric chains of THF-solvated $Zn(O_2PF_2)_2$ units with bridging phosphates. The asymmetric unit contains two chemically identical $Zn(O_2PF_2)_2(THF)_2$ units. The Figure represents a segment of chain made out of one such unit and two other repeats related to the first by symmetry. H atoms are omitted for clarity. Thermal ellipsoids are drawn at the 50% probability level. Color coding: Zn, opal blue; P, purple; F, forest green; O, red; C, gray. Selected crystallographic data and geometric parameters are given in Tables II.1 and II.2, respectively.

## II.3. Structures

### II.3.a. Structural information provided spectroscopically

Both the $^1H$ and $^{13}C$ NMR spectroscopies of the THF solvate of $Li_2[LZn]$ in dimethylsulfoxide-$d_6$ (DMSO-$d_6$), displayed in Figure II.2, show a fourfold symmetrical structure, signifying that ion pairing is very loose: the β-pyrrole position gives rise to a single $^1H$ peak, and $^{13}C$ NMR shows two resonances corresponding to the α and β positions of the pyrrole rings. The presence of two distinct methyl lines (both in $^1H$ and $^{13}C$ NMR) corresponds to distinct axial and equatorial *meso* positions in the overall chair conformation of the macrocycle. Chair-chair interconversion at room temperature is signified by broadened methyl peaks. The FWHM (full width at half maximum) of the $^1$H and $^{13}$C signals in DMSO-d$_6$ yields an exchange rate of 35 Hz,

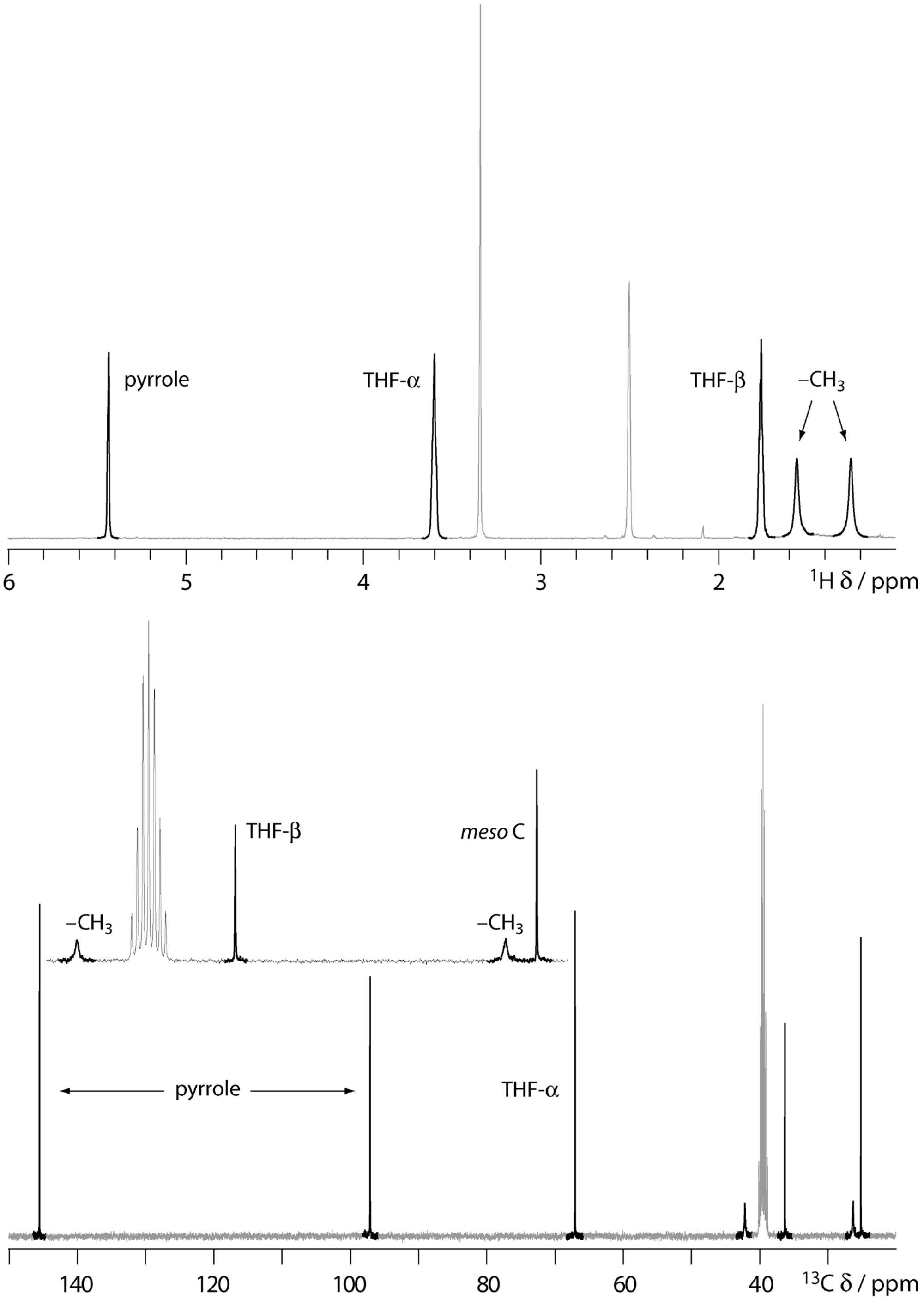

**Figure II.2.** $^1$H and $^{13}$C NMR spectra of Li$_2$(THF)$_4$[LZn] in DMSO-d$_6$ (500 MHz and 100.6 MHz, respectively). Porphyrinogen and THF peaks are highlighted. The inset of the $^{13}$C spectrum is an expansion of the aliphatic area. Note that methyl peaks are broad in both spectra.

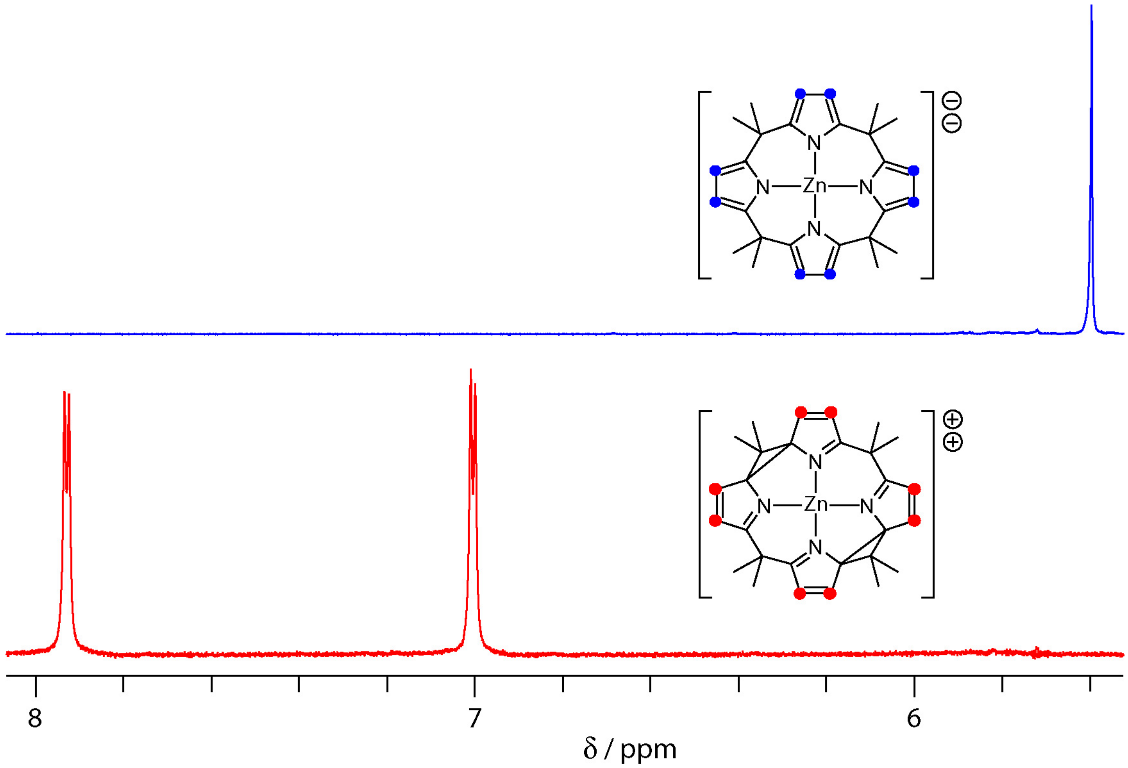

**Figure II.3.** β-Pyrrole region of the $^1$H NMR spectra of $[LZn]^{2-}$ (upper panel, blue) and $[L^{\Delta\Delta}Zn]^{2+}$ (lower panel, red) in $CD_3CN$ (500 MHz). The differences apparent between reduced and oxidized macrocycle are structural (symmetry) and electronic (conjugation).

which increases to ~350 Hz when the measurement is made in $CD_3CN$. In $CD_3CN$, the dioxane solvate of $Li_2[LMg]$ and the MeCN solvate of $[LCa_2]$ show a single $^1$H methyl peak, indicative of even faster solution dynamics.

The symmetry lowering attendant to cyclopropane ring formation upon oxidation to $[L^{\Delta\Delta}M]^{2+}$ is plainly evident in the $^1$H-NMR spectrum of $[L^{\Delta\Delta}Zn](BF_4)_2$ shown in Figure II.3. The single pyrrole peak of $[LZn]^{2-}$ splits into two doublets and the two methyl peaks split into four broadened singlets. In addition, the large downfield shift of the pyrrole signals is indicative of increased conjugation upon macrocycle oxidation. In support of this contention, the proton resonances of porphyrins appear at values similar to those observed here.

Cyclopropane formation is also apparent in the IR spectrum. The C—H stretching vibrations at 3083 cm$^{-1}$ for the pyrrole rings of $[LZn]^{2-}$ shift to 3111 cm$^{-1}$ in $[L^{\Delta\Delta}Zn]^{2+}$. New bands appear at 1050-1150 cm$^{-1}$ and 810 cm$^{-1}$, which we ascribe to the cyclopropane ring;[17] in addition, a band at 1575 $cm^{-1}$ also appears upon oxidation that is consistent with a C=N stretching vibration of the oxidized pyrrole.

## II.3.b. Crystal structures

The structure of [$L^{\Delta}Zn(NCMe)$] is shown on the left panel of Figure II.4 (crystallographic data and selected geometric measurements are given in Tables II.3 and II.4, respectively). The central $Zn^{2+}$ ion displays a distorted square pyramidal coordination geometry, with the square base defined by the four pyrrole nitrogens of the macrocycle and the axial site capped with a nitrogen from coordinating $CH_3CN$. The central $Zn^{2+}$ ion sits above the $N_4$ basal plane, forcing the macrocycle into a bowl conformation that is similar to the macrocyclic ring of $LH_4$ porphyrinogens (calix[4]pyrroles) hydrogen-bonded to an anionic guest.[18-24] The most striking structural characteristic of the macrocycle is that it effectively comprises the fused halves of a reduced and an oxidized porphyrinogen. The oxidized dipyrrole subunit is more constrained due to the presence of the cyclopropane, which forces the coordinating nitrogens into closer proximity to each other. The N⋯N distance of the cyclopropane-bridged pyrroles is only 2.69 Å, whereas the N⋯N distance between the methylene-bridged pyrroles is 3.01 Å. The cyclopropane is, within uncertainties, an equilateral triangle, with a $C^{\alpha}$–$C^{meso}$–$C^{\alpha}$ angle of 60.1(3)° and lengths of 1.544(7) Å and 1.534(6) Å for $C^{\alpha}$—$C^{meso}$ and 1.547(7) Å for $C^{\alpha}$—$C^{\alpha}$. This latter distance is significantly compressed relative to the 2.54 Å distance between the $C^{\alpha}$ of the pyrroles on the opposite side of the macrocycle. The presence of a cyclopropane ring causes changes in the N—$C^{\alpha}$ distances as well. Those of the pyrroles on the reduced side of the macrocycle are equivalent (d(N—$C^{\alpha}$) = 1.377 ± 0.008 Å) whereas the oxidized pyrroles exhibit a marked asymmetry arising from alternating single (d(N—$C^{\alpha}$) = 1.442 ± 0.003 Å) and double bonds (d(N—$C^{\alpha}$) = 1.299 ± 0.002 Å).

The difference between the two halves of the macrocycle is also reflected in the primary coordination sphere of the $Zn^{2+}$ ion. The reduced dipyrrole half of the macrocycle appears to formally carry the negative charge of the dianionic ligand, as evidenced by compressed Zn—N bond lengths of 2.029 Å and 2.019 Å. Conversely, the oxidized, neutral half of the macrocycle displays longer Zn—N bonds of 2.212(4) and

2.237(4) Å; these distances are even longer (Δd ~ 0.1 Å) than those observed in neutral chelating bipyridine complexes of $Zn^{2+}$.[25]

With those structural differences between the two sides of the porphyrinogen, the macrocycle can be described as composed of two ligands within one, in which an

**Table II.3.** Summary of X-ray crystallographic data for $[L^{\Delta}M(NCMe)] \bullet CH_2Cl_2$, M = Zn, Mg.

| | M = Zn | M = Mg |
|---|---|---|
| empirical formula | $C_{31}H_{37}Cl_2N_5Zn$ | $C_{31}H_{37}Cl_2N_5Mg$ |
| formula weight | 615.93 | 574.87 |
| $T$ (K) | 193(2) | 193(2) |
| $\lambda$ (Å) | 0.71073 | 0.71073 |
| crystal system | Triclinic | Triclinic |
| space group | $P\overline{1}$ | $P\overline{1}$ |
| $a$ (Å) | 10.3850(8) | 10.4274(7) |
| $b$ (Å) | 10.6155(9) | 10.6231(7) |
| $c$ (Å) | 14.4068(12) | 14.3549(10) |
| $\alpha$ (deg) | 81.8540(10) | 81.9710(10) |
| $\beta$ (deg) | 85.3500(10) | 85.0730(10) |
| $\gamma$ (deg) | 73.086(2) | 73.5010(10) |
| $Z$ | 2 | 2 |
| $V$ (Å$^3$) | 1502.9(2) | 1507.90(18) |
| crystal size (mm$^3$) | 0.20 × 0.10 × 0.04 | 0.44 × 0.21 × 0.08 |
| Abs. coeff. (mm$^{-1}$) | 1.024 | 0.265 |
| $F$(000) | 644 | 608 |
| $\theta$ range for data coll. | 2.44 to 23.25° | 2.01 to 23.29° |
| limiting indices | $-11 \leq h \leq 11$<br>$-11 \leq k \leq 6$<br>$-15 \leq \ell \leq 15$ | $-11 \leq h \leq 10$<br>$-11 \leq k \leq 11$<br>$-15 \leq \ell \leq 15$ |
| no. of reflns collcd | 6891 | 7845 |
| no. of ind reflns ($R_{int}$) | 4253 (0.0627) | 4327 (0.0504) |
| completeness to $\theta_{max}$ | 98.6% | 99.7 % |
| refinement method | Full-matrix least-squares on $F^2$ | Full-matrix least-squares on F2 |
| data / restraints / params | 4253 / 0 / 362 | 4327 / 0 / 362 |
| $R_1$,[a] $wR_2$[b] ($I > 2\sigma(I)$) | 0.0609, 0.1140 | 0.0928, 0.2700 |
| $R_1$,[a] $wR_2$[b] (all data) | 0.0861, 0.1227 | 0.1104, 0.2899 |
| GOF[c] on $F^2$ | 1.071 | 1.028 |
| largest diff. peak, hole | 0.641, −0.469 eÅ$^{-3}$ | 0.690, −1.222 eÅ$^{-3}$ |

[a] $R_1 = \Sigma||F_o - |F_c||/\Sigma|F_o|$.

[b] $wR_2 = (\Sigma(w(F_o^2 - F_c^2)^2)/\Sigma(w(F_o^2)^2))^{1/2}$.

[c] $GOF = (\Sigma\, w(F_o^2 - F_c^2)^2/(n - p))^{1/2}$,
where $n$ is the number of data and $p$ is the number of parameters refined.

anionic dipyrrole is doubly strapped to a two-electron oxidized dipyrrole. Therefore, this oxidation state can be considered a genuine case of two-electron mixed valency. This line of analysis is further developed in Chapter III.

**Table II.4.** Selected geometric parameters for [L$^{\Delta}$M(NCMe)] • $CH_2Cl_2$, M = Zn, Mg.

|  | M = Zn |  | M = Mg |  |
|---|---|---|---|---|
| Distances / Å |  |  |  |  |
| M—$N_{red}$ | 2.019(4) | 2.029(4) | 2.076(4) | 2.080(4) |
| M—$N_{ox}$ | 2.212(4) | 2.237(4) | 2.193(4) | 2.194(4) |
| $(C^{\alpha}—C^{\alpha})_{ox}$ | 1.547(7) |  | 1.562(7) |  |
| $(C^{meso}—C^{\alpha})_{ox}$ | 1.544(7) | 1.534(6) | 1.528(7) | 1.529(7) |
| $N_{red}—C^{\alpha}$ | 1.369(6) | 1.385(6) | 1.379(6) | 1.388(6) |
|  | 1.387(6) | 1.379(6) | 1.372(6) | 1.377(6) |
| $N_{ox}=C^{\alpha}$ | 1.301(6) | 1.298(6) | 1.302(6) | 1.300(6) |
| $N_{ox}—C^{\alpha}$ | 1.440(6) | 1.445(6) | 1.443(6) | 1.443(6) |
| Angles / deg |  |  |  |  |
| $N_{ox}$–M–$N_{ox}$ | 74.35(14) |  | 75.77(15) |  |
| $N_{red}$–M–$N_{red}$ | 95.92(15) |  | 93.25(16) |  |
| $(C^{\alpha}–C^{meso}–C^{\alpha})_{ox}$ | 60.3(3) |  | 61.4(3) |  |

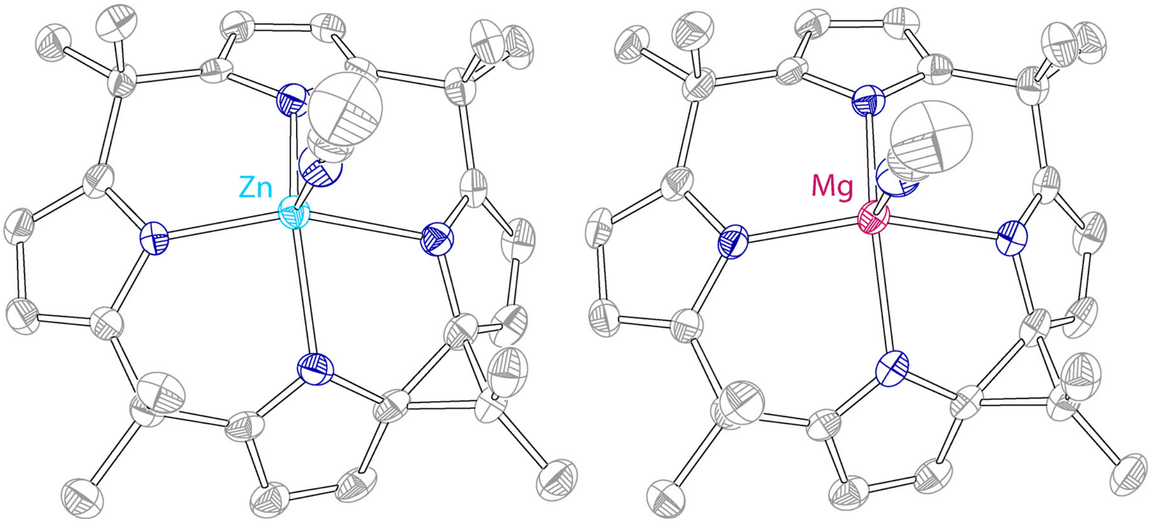

**Figure II.4.** Crystal structures of [L$^{\Delta}$M(NCMe)] • $CH_2Cl_2$, M = Zn, Mg. An uncoordinated solvent molecule and H atoms are omitted for clarity. Thermal ellipsoids are drawn at the 50% probability level. Color coding: Zn, opal blue; Mg, raspberry red; N, blue; C, gray.

The crystal structure of [$L^{\Delta}$Mg(NCMe)], (right side of Figure II.4) is in the same space group and with the same co-crystallized solvent molecule as observed for [$L^{\Delta}$Zn(NCMe)]. More striking, the geometric parameters of the organic periphery in [$L^{\Delta}$Mg(NCMe)] and [$L^{\Delta}$Zn(NCMe)] are identical within uncertainty. The only significant structural difference between the two is in the position of the metal dication within the macrocycle. Whereas both $Mg^{2+}$ and $Zn^{2+}$ lie closer to the dipyrrole dianion than to the oxidized dipyrrole, $Zn^{2+}$ is displaced further from the central core: $d_{avg}(M–N_{red})$ = 2.08 Å (M = Mg) *vs* 2.02 Å (M = Zn). The positional difference between Zn and Mg is inversely related to the ionic radius ($r_{Mg^{2+}}$ = 0.86 Å and $r_{Zn^{2+}}$ = 0.88 Å)[26] and seems to be linked to the pocket size of the two dipyrrole halves. As noted above, the coordinating nitrogens of the dipyrrole dianion are considerably farther apart than those of the oxidized dipyrrole, which are strapped by the base of the cyclopropane. The confluence of the larger pocket size on the reduced side of the macrocycle and smaller pocket size on the oxidized side of the macrocycle appears to effectively “push” the larger cation away from the oxidized dipyrrole and into the dipyrrole dianion. This rationale is also consistent with data from the related $d^7$-$d^9$ octaethylporphyrinogen series [$^{Et}L^{\Delta}$M], M = Co, Ni, Cu, reported by Floriani,[9,10] in which the metal ion lies in a roughly square planar geometry: Ni(II) is the most centrally situated of the three ions, followed by Co(II) and Cu(II). We note, however, that the behavior of non-spherically symmetric ions is less straightforward to interpret because of the influences of covalent bonding, geometric preferences and spin states. Indeed, essentially purely electrostatic bonding in [$L^{\Delta}$Mg(NCMe)] and [$L^{\Delta}$Zn(NCMe)] translates into much larger differences in M—N bond lengths.

## II.4. Electrochemistry

The left panel of Figure II.5 shows the differential pulse voltammograms (DPV) measured on a THF solution of $[LZn]^{2-}$. In the anodic scan, two waves are observed at +0.21 and +0.63 V *vs* NHE. The same DPV waves are obtained when solutions of $[L^{\Delta\Delta}Zn]^{2+}$ are scanned in a cathodic direction. Therefore, they correspond to the $[LZn]^{2-}$

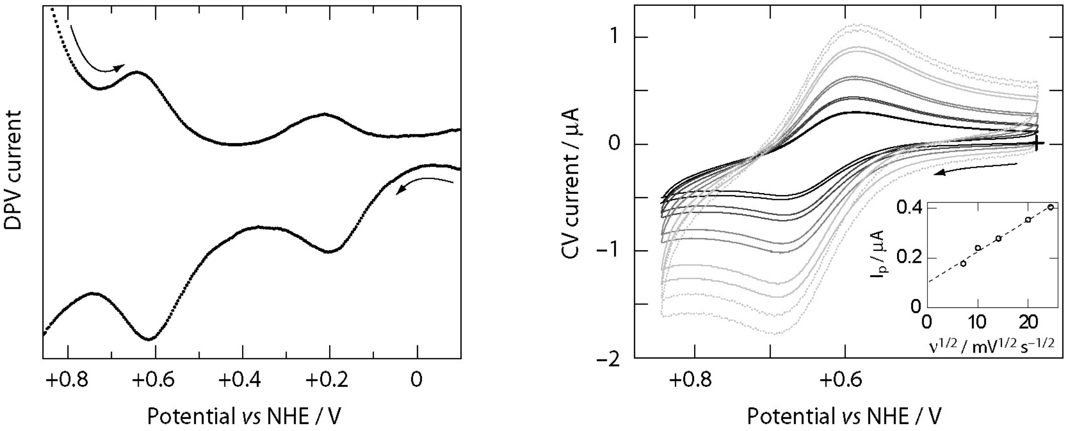

**Figure II.5.** Electrochemistry of zinc porphyrinogen. Left, DPV traces of $10^{-4}$ M $Li_2[LZn]$ in 0.01 M $Bu_4NPF_6$ / THF (scan rate 20 mV/s, pulse amplitude 50 mV, sample width 17 mV, pulse width 50 ms, pulse period 200 ms, quiet time 2 s; an offset has been subtracted). Right, CV traces of $10^{-3}$ M $[L^{\Delta\Delta}Zn](BF_4)_2$ in 0.04 M $Bu_4NBPh_4$ / MeCN; the runs are recorded at scan rates between 50 mV/s (black) and 600 mV/s (dotted light gray). Inset: plot of the anodic peak current $I_p$ *vs* the square root of the scan rate ν, with linear fit.

/ $[L^{\Delta}Zn]$ and $[L^{\Delta}Zn]$ / $[L^{\Delta\Delta}Zn]^{2+}$ couples, respectively, which establishes a 0.42-V stability window for $[L^{\Delta}Zn]$ with respect to disproportionation.

Moreover, the cyclic voltammetric (CV) trace of the $[L^{\Delta\Delta}Zn]^{2+}$ / $[L^{\Delta}Zn]$ couple in MeCN (right panel of Figure II.5) is consistent with the reversibility of redox transformations observed on the preparative scale: plots of the cathodic and anodic currents *vs* $\nu^{1/2}$ (scan rate $50 \leq \nu \leq 600$ mV $s^{-1}$) are linear (inset). The separation between anodic and cathodic CV current maxima is close to one half of the peak-to-peak separation observed for ferrocene in the same conditions, further substantiating the two-electron nature of the redox event.

## II.5. Conclusions

The oxidation-reduction chemistry of a porphyrinogen framework has been unveiled by synthesizing the macrocycle in the absence of redox-active metal, axial ligand and counter-ions. Porphyrinogen complexes of spherical metal dications react in two discrete and reversible two-electron steps, with the concomitant formation of two C—C bonds between the α carbons of adjacent pyrroles. Each cyclopropane thus formed is a two-equivalent redox reservoir within the porphyrinogen framework. The series of three oxidation states spanning reduced $[LM]^{2-}$ and oxidized $[L^{\Delta\Delta}M]^{2+}$ encompasses an overall four-electron transformation. The cyclopropane C—C bond that supports the redox activity of the ligand carries distinct signatures in IR and NMR spectroscopies, and its strength, demonstrated structurally, stabilizes the oxidation of the pyrrolic $\pi$ system at relatively low potential. Both the two-electron redox steps of porphyrinogen and the localization of the redox equivalents in a single, structurally well-defined bond are unique among all redox-active organic compounds, such as tetrathiafulvalene,[27] fullerenes,[28] viologens,[29] quinones,[30] phenols,[31] all of which stabilize one hole or electron, and sometimes a second one, by delocalization in an aromatic system, with limited structural rearrangement — the sulfide / disulfide couple being a prominent exception.

Structurally, the intermediary $[L^{\Delta}M]$ macrocycle consists of a dipyrrole that is doubly strapped to a two-electron oxidized (cyclopropane bridged) dipyrrole neighbor. From this standpoint, it may be described as the two-electron mixed-valent intermediary of the homologous multielectron series. Further, the $L^{\Delta 2-}$ macrocycle is sufficiently rigid that moderate changes in the size of the central $M^{2+}$ do not affect the organic periphery structurally. Instead, the position of the metal ion within the asymmetric macrocyclic ligand must vary according to its size.

## II.6. Experimental section

### II.6.a. Synthesis

*Materials*

All compounds were handled, reactions were performed, and analytical samples were prepared under inert atmosphere using standard Schlenk, dry-box and vacuum-line techniques. Solvents were purchased from VWR Scientific Products and purified using a Braun solvent purification system or using standard solvent purification techniques.[32] Deuterated solvents were purchased from Cambridge Isotope

Laboratories, degassed, dried and distilled by procedures similar to those used for non-isotopically enriched solvents. Technical grade ferrocenium tetrafluoroborate ($FcBF_4$) was purchased from Aldrich, dissolved in acetonitrile and dried over calcium hydride at room temperature; the solvent was degassed and the solid was precipitated with diethylether, collected by filtration and dried *in vacuo*. Other reagents were purchased from Aldrich or Alfa Aesar or Strem Chemicals and used as received. Elemental analyses were conducted at H. Kolbe Mikroanalytisches Laboratorium (Mühlheim a. d. Ruhr, Germany). Electrospray mass spectrometric analyses were conducted at the Mass Spectrometry Facility at the University of Illinois at Urbana-Champaign with a ±0.2 uncertainty on *m/z*.

*Synthesis of* $Li_2(THF)_x[LZn]$

A 10.0-g (23.3 mmol) sample of $LH_4$ was dissolved in 200 mL of THF and a 2.89-M hexane solution of BuLi (46.7 mmol) was added dropwise and under stirring followed by the dropwise addition of a 1.0 M hexane solution of $ZnEt_2$ (23.3 mmol). The light yellow solution was refluxed gently overnight, cooled to room temperature and then to –80 °C to induce crystallization of a white solid, which was separated from the pale orange supernatant by filtration. *Caution*: The solid material is pyrophoric when exposed to air. The white powder was dried *in vacuo*; its THF content varied from one assay to the next and was assessed by $^1H$ NMR and elemental analysis. Yield: 14.6 g (86% for x = 3). $^1H$ NMR (500 MHz, DMSO-$d_6$, 25 °C): $\delta = 5.43$ (s, 8H, pyrrole), 3.61 (m, 12H, THF-$\beta$), 1.77 (m, 12H, THF-$\alpha$), 1.56 (br, 12H, Me), 1.26 (br, 12H, Me); $^{13}C[^1H]$ NMR (100.6 MHz, DMSO-$d_6$, 25 °C): $\delta = 145.5$ (pyrrole), 97.1 (pyrrole), 67.0 (THF-$\alpha$), 42.2 (br, Me), 36.3 (*meso*-C), 26.3 (br, Me), 25.2 (THF-$\beta$); IR: $\nu_{max}$ / $cm^{-1}$ = 3083 m (pyrrole C–H), 1348 m, 1278 m, 1216 m, 1156 m, 1050 s, 888 m, 761 s, 725 s; Anal. Calcd for $C_{40}H_{56}Li_2N_4O_3Zn$ (x = 3): C, 66.71; H, 7.84; N, 7.78. Found: C, 66.57; H, 8.09; N, 7.86.

*Synthesis of* $[L^{\Delta\Delta}Zn](BF_4)_2$

A sample of $Li_2(THF)_x[LZn]$ (2.99 mmol) was dissolved in 50 mL $CH_3CN$, stirred at 25 °C for 5 min, then evaporated and thoroughly dried *in vacuo*. The solid was then redissolved in 80 mL $CH_3CN$ and added dropwise over a 5-min period to a 20-mL $CH_3CN$ solution of $FcBF_4$ (3.39 g, 11.97 mmol). The deep emerald green solution was stirred at 25 °C for 15 min. The solvent was evaporated to leave a solid residue, which was dried *in vacuo* and re-suspended in 600 mL of $CH_2Cl_2$. The solution was stirred until a fine suspension of the solid was obtained. The mixture was refluxed for 5 min and filtered warm. The green filtrate was evaporated and the remaining solid was dried, re-suspended in 500 mL of hexane, and the mixture was stirred for 1 h at 25 °C. The green solid containing $[L^{\Delta\Delta}Zn](BF_4)_2$ and $FcBF_4$ was separated from the yellow Fc solution by filtration and dried *in vacuo*. Residual $FcBF_4$ was removed by suspending the powder in 60 mL of boiling $CH_2Cl_2$ and slowly adding hexane dropwise until solid beige $[L^{\Delta\Delta}Zn](BF_4)_2$ separated from a green-blue supernatant. The solid was collected by filtration after the suspension was cooled and dried *in vacuo*. Solid $[L^{\Delta\Delta}Zn](BF_4)_2$ was obtained as a light cream powder. Yield 44% (0.88 g). $^1H$ NMR (500 MHz, $CD_3CN$, 25 °C): $\delta = 7.93$ (d, 5.5 Hz, 4H, pyrrole), 7.00 (d, 5.5 Hz, 4H, pyrrole), 2.03 (s, 6H, Me), 1.88 (s, 6H, Me), 1.82 (s, 6H, Me), 1.81 (s, 6H, Me); IR: $\nu_{max}$ / cm$^{-1}$ = 3111 m (pyrrole C–H), 1573 m, 1261 w, 1150 s, 1062 s, 1019 s, 884 m, 814 s, 723 m; Anal. Calcd for $C_{28}H_{32}B_2F_8N_4Zn$: C, 50.68; H, 4.86; N, 8.44; Zn, 9.85. Found: C, 50.42; H, 4.95; N, 8.38; Zn, 9.65. (+)ESI-MS $(M{-}2BF_4^-)^{2+}$ calcd for $C_{28}H_{32}N_4Zn$ *m/z*, 244.1, found 244.3.

*Synthesis of* $[L^{\Delta}Zn]\bullet(CH_2Cl_2)_y$

A sample of $Li_2(THF)_x[LZn]$ (0.137 mmol) was dissolved in 2 mL of $CH_3CN$ and stirred for 5 min at 25 °C. The solvent was evaporated and to the remaining solid, a 5 mL solution of $CH_3CN$ containing an equivalent amount of $L^{\Delta\Delta}Zn(BF_4)_2$ (0.091 g, 0.137 mmol) was added. The resulting orange solution was evaporated to dryness and the solid residue was collected and re-suspended in 3 mL of $CH_2Cl_2$. Insoluble $LiBF_4$ was filtered off and the filtrate was evaporated, yielding $[L^{\Delta}Zn]$ as an orange powder, which was recrystallized from $CH_2Cl_2$ / pentane solvent mixture and dried *in vacuo*. Orange needles of $[L^{\Delta}Zn(CH_3CN)]\bullet CH_2Cl_2$ suitable for X-ray diffraction analysis were obtained from a $CH_2Cl_2$ solution (~0.5 mL) containing a trace amount (~20 μL) of $CH_3CN$ layered with pentane (~2 mL). The bulk product contained a variable amount of cocrystallized $CH_2Cl_2$ from one assay to the next, which was assessed by elemental analysis. Yield: 92% (0.134 g for y = 0.65). IR: $\nu_{max}$ / cm$^{-1}$ = 3090 w (pyrrole C–H), 1568 m, 1353 m, 1278 w, 1218 w, 1155 m, 1103 s, 1055 s, 891 w, 802 m, 771 w, 723 m; Anal. Calcd for

$C_{29.65}H_{33.3}Cl_{1.3}N_4Zn$ (y = 0.65): C, 63.12; H, 6.16; N, 10.28; Zn, 12.00. Found: C, 62.73; H, 5.89; N, 9.92; Zn, 12.43.

*Synthesis of $Li_2$(1,4-dioxane)$_5$[LMg]*

A sample of $LH_4$ (10.0 g, 23.3 mmol) was dissolved in 400 mL of 1,4-dioxane and 23.5 mL of a 2.0-M $Et_2O$ solution (46.7 mmol, 2 equiv) of ethylmagnesium chloride was added. The resulting white suspension was refluxed overnight, the mixture was cooled down to room temperature and filtered and butyllithium (23.5 mL of a 2.0-M pentane solution, 46.7 mmol, 2 equiv) was added to the filtrate and the mixture was again refluxed overnight. The mixture was then cooled to room temperature and the product was collected by filtration and dried. Yield: 10.98 g (50%). The solid was then recrystallized from 1,4-dioxane. $^1H$ NMR (500 MHz, $CD_3CN$): $\delta$ = 5.66 (s, 8H, pyrrole), 3.62 (s, 40H, dioxane), 1.49 (s, 24H, Me). Anal. Calcd for $C_{48}H_{72}Li_2MgN_4O_{10}$: C, 63.82; H, 8.04; N, 6.21. Found: C, 63.73; H, 7.94; N, 6.15.

*Synthesis of $[L^{\Delta\Delta}Mg](BF_4)_2$.*

Two separate 10-mL MeCN solutions of $LMgLi_2(diox)_5$ (0.48 g, 0.53 mmol) and $FcBF_4$ (0.60 g, 2.11 mmol, 4 equiv.) were prepared. The former was added dropwise to the latter, and the combined green solution was evaporated and dried in vacuum. The solid residue was triturated in 200 mL of boiling $CH_2Cl_2$ and the resulting suspension was filtered. The filtrate was evaporated and dried, then triturated in 200 mL hexanes, filtered and dried again. The off-white (greenish) powder was recrystallized from $CH_2Cl_2$ (80 mL)/hexanes (30 mL). Yield: 0.09 g (30%). $^1H$ NMR (500 MHz, $CD_3CN$): $\delta$ = 7.88 (d, 5 Hz, 4H, pyrrole), 6.96 (d, 5 Hz, 4H, pyrrole), 2.01 (s, 6H, Me), 1.86 (s, 6H, Me), 1.84 (s, 6H, Me), 1.80 (s, 6H, Me). Anal. Calcd for $C_{28}H_{32}N_4MgB_2F_8$: C, 54.00; H, 5.18; N, 9.00. Found: C, 53.73; H, 5.24; N, 8.79.

*Synthesis of $[L^{\Delta}Mg]$*

A sample of $Li_2(diox)_5[LMg]$ (121 mg, 0.134 mmol) was dissolved in 3 mL of MeCN and added to powdered $[L^{\Delta\Delta}Mg](BF_4)_2$ (76 mg, 0.134 mmol). The resulting vermilion red solution was evaporated. The remaining solid residue was triturated in 3 mL of $CH_2Cl_2$ and the white salt was filtered off and the filtrate evaporated and dried to give 120 mg (100%) of crude material. Single crystals of X-ray quality were grown by vapor diffusion of toluene (~2 mL) into a concentrated $CH_2Cl_2$ solution (~0.5 mL) of the product that was spiked with MeCN (~20 μL); diffraction data showed that the acetonitrile adduct [$L^{\Delta}$Mg(NCMe)]•$CH_2Cl_2$ was obtained.

*Preparation of activated calcium*

Calcium iodide (12.03 g, 40.93 mmol), naphthalene (10.49 g, 81.85 mmol, 2 equiv.) and lithium metal (0.568 g, 81.85 mmol, 2 equiv.) were mixed in 100 mL THF and the mixture was stirred at room temperature overnight. The black suspension was filtered and dried under vacuum on the frit at room temperature. The solid was transferred to a high-vacuum flask and further dried overnight under 10 μTorr at 140°C. Yield: 4.99 g (72%) of black $Ca(C_{10}H_8)_{0.98}$. Anal. Calcd for $C_{9.80}H_{7.84}Ca$: C, 71.07; H, 4.78; Ca, 24.15. Found: C, 71.08; H, 4.71; Ca, 24.37.

*Synthesis of $LCa_2(NCMe)_4$*

Activated calcium (1.94 g, 11.53 mmol) and $LH_4$ (2.47 g, 5.77 mmol, 0.5 equiv.) were mixed in THF and refluxed overnight. The colorless solution was cooled to room temperature, then cooled further to –80°C and maintained at that temperature for 2 hr. The white precipitate was filtered cold, dried, recrystallized from toluene (100 mL)/MeCN (200 mL) and dried in vacuum. Yield: 1.02 g (27%). $^1$H NMR (500 MHz, THF-$d_8$): δ = 5.89 (s, 8H, pyrrole), 1.95 (s, 12H, MeCN), 1.31 (s, 24H, Me).

*Synthesis of [$L^{\Delta\Delta}$Ca]($BF_4$)$_2$*

A 5-mL toluene suspension of $LCa_2(NCMe)_4$ (0.48 g, 0.71 mmol) was added dropwise to a 20-mL MeCN solution of $FcBF_4$ (0.62 g, 2.28 mmol, 4 equiv). The resulting green solution was evaporated and dried under vacuum. The solid was triturated in 30 mL of $CH_2Cl_2$ for 20 min., filtered, and resuspended in 300 mL of $CH_2Cl_2$, which was then brought to reflux. The warm suspension was filtered and the product was precipitated from the filtrate by dropwise addition of 100 mL of hexanes. The white powder was filtered and dried in vacuum. Yield: 0.13 g (37%). $^1$H NMR (500 MHz, $CD_3CN$): δ = 7.73 (d, 5 Hz, 4H, pyrrole), 6.81 (d, 5 Hz, 4H, pyrrole), 2.00 (s, 6H, Me), 1.87 (s, 6H, Me), 1.80 (s, 6H, Me), 1.79 (s, 6H, Me). Anal. Calcd for [$L^{\Delta\Delta}$Ca]($BF_4$)$_2$·0.3$CH_2Cl_2$,

$C_{28.3}H_{32.6}N_4CaB_2F_8Cl_{0.6}$: C, 51.19; H, 4.95; N, 8.44; Ca, 6.02. Found: C, 51.54; H, 4.82; N, 8.30; Ca, 6.08.

*Synthesis of [L$^{\Delta}$Ca]*

A 5-mL MeCN suspension of [L$^{\Delta\Delta}$Ca]$(BF_4)_2$ (90 mg, 0.13 mmol) was added to a 5-mL MeCN solution of $LCa_2(NCMe)_4$ (86 mg, 0.13 mmol) under stirring. The brown mixture was stirred for 10 min. at r. t., then evaporated and dried in vacuum. The solid residue was triturated in 3 mL $CH_2Cl_2$ and filtered, then the filtrate was evaporated and dried. The product was recrystallized by liquid-liquid diffusion of pentane into a concentrated $CH_2Cl_2$ solution. Yield: 110 mg (88%). Anal. Calcd for [L$^{\Delta}$Ca]·0.18$CH_2Cl_2$, $C_{28.18}H_{32.36}N_4CaCl_{0.36}$: C, 70.55; H, 6.80; N, 11.69; Ca, 8.34. Found: C, 70.88; H, 6.46; N, 11.25; Ca, 8.26.

## II.6.b. Spectroscopy

IR spectra of samples in nujol mulls were collected on a Perkin-Elmer 2000 FTIR spectrometer. $^1$H and $^{13}$C NMR spectra were recorded at the MIT Department of Chemistry Instrumentation Facility (DCIF) on a Varian Inova-500 or a Bruker Avance-400 spectrometer at 20 °C.

## II.6.c. Electrochemistry

Electrochemistry was performed with a standard three-electrode configuration using a CV-50W potentiostat (Bioanalytical Systems). The working electrode was Pt, the auxiliary electrode was a Pt wire and the reference was an Ag/$AgNO_3$ electrode, which was externally referenced to the $Fc^+/Fc$ couple ($E^o(Fc^+/Fc) = 0.65$ V (in $CH_3CN$) and 0.69 V (in THF) vs NHE).[33]

## II.6.d. Crystallography

*Data collection and reduction*

Crystals were coated with Paratone N oil and mounted on a glass fiber. X-ray diffraction data were collected at –80 °C on a Siemens three-circle diffractometer equipped with a CCD detector, using the Mo K$\alpha$ radiation, selected by a graphite monochromator. The data were integrated to $hk\ell$-intensity and the final unit cell calculated using the SAINT v.4.050 program from Siemens. Solution and refinement were performed with the SHELXTL v.5.03 suite of programs developed by G. M. Sheldrick and Siemens Industrial Automation, 1995. No absorption correction was performed.

*X-ray crystal structure of* $[(THF)_2Zn(O_2PF_2)_2]_\infty$

A colorless needle was grown from a concentrated benzene / THF solution of the $Li_2[LZn]$ / $FcPF_6$ / THF reaction after removal of the undissolved salts, evaporation, triturating in hexanes, then filtration and drying *in vacuo*. The structure was solved by direct methods; the least-squares refinement converged normally (with hydrogen atoms placed at calculated positions using a standard riding model and refined isotropically). The asymmetric unit contains two chemically identical $[(THF)_2Zn(O_2PF_2)_2]$ monomers that are not bonded to each other.

*X-ray crystal structure of* $[L^{\Delta}Zn(CH_3CN)]\bullet CH_2Cl_2$

A bright orange crystal was grown by layering pentane onto a concentrated $CH_2Cl_2$ solution of $[L^{\Delta}Zn]$ spiked with MeCN. The structure was solved by the Patterson method; the least-squares refinement converged normally (with hydrogen atoms placed at calculated positions using a standard riding model and refined isotropically).

*X-ray crystal structure of* $[L^{\Delta}Mg(CH_3CN)]\bullet CH_2Cl_2$

A bright vermilion red crystal was grown by layering pentane onto a concentrated $CH_2Cl_2$ solution of $[L^{\Delta}Mg]$ spiked with MeCN. The structure was solved by direct methods; the least-squares refinement converged normally (with hydrogen atoms placed at calculated positions using a standard riding model and refined isotropically).

## II.7. References

1 Felton, R. H.; Dolphin, D.; Borg, D. C.; Fajer, J. *J. Am. Chem. Soc.* **1969**, *91*, 196-198.

2 Fajer, J.; Borg, D. C.; Forman, A.; Dolphin, D.; Felton, R. H. *J. Am. Chem. Soc.* **1970**, *92*, 3451-3459.

3 Schrauzer, G. N.; Mayweg, V. P. *J. Am. Chem. Soc.* **1965**, *87*, 3585-3592.

4 Davison, A.; Edelstein, N.; Holm, R. H.; Maki, A. H. *J. Am. Chem. Soc.* **1963**, *85*, 2029-2030.

5 Maki, A. H.; Berry, T. E.; Davison, A.; Holm, R. H.; Balch, A. L. *J. Am. Chem. Soc.* **1966**, *88*, 1080-1082.

6 Holm, R. H.; Balch, A. L.; Davison, A.; Maki, A. H.; Berry, T. E. *J. Am. Chem. Soc.* **1967**, *89*, 2866-2874.

7 Floriani, C.; Floriani-Moro, R. in *The Porphyrin Handbook*; Kadish, K. M., Smith, K. M.; Guilard, R., Ed.; Academic Press:New York, 2000; Vol. 3, pp 405-420.

8 Jubb, J.; Floriani, C.; Chiesi-Villa, A.; Rizzoli, C. *J. Am. Chem. Soc.* **1992**, *114*, 6571-6573.

9 De Angelis, S.; Solari, E.; Floriani, C.; Chiesi-Villa, A.; Rizzoli, C. *J. Am. Chem. Soc.* **1994**, *116*, 5691-5701.

10 De Angelis, S.; Solari, E.; Floriani, C.; Chies-Villa, A.; Rizzoli, C. *J. Am. Chem. Soc.* **1994**, *116*, 5702-5713.

11 Piarulli, U.; Solari, E.; Floriani, C.; Chiesi-Villa, A.; Rizzoli, C. *J. Am. Chem. Soc.* **1996**, *118*, 3634-3642.

12 Crescenzi, R.; Solari, E.; Floriani, C.; Chiesi-Villa, A.; Rizzoli, C. *J. Am. Chem. Soc.* **1999**, *121*, 1695-1706.

13 Benech, J.-M.; Bonomo, L.; Solari, E.; Scopelliti, R.; Floriani, C. *Angew. Chem. Int. Ed.* **1999**, *38*, 1957-1959.

14 Bonomo, L.; Solari, E.; Scopelliti, R.; Floriani, C.; Re, N. *J. Am. Chem. Soc.* **2000**, *122*, 5312-5326.

15 Bonomo, L.; Solari, E.; Martin, G.; Scopelliti, R.; Floriani, C. *Chem. Commun.* **1999**, 2319-2320.

16 Bonomo, L.; Dandin, O.; Solari, E.; Floriani, C.; Scopelliti, R. *Angew. Chem. Int. Ed.* **1999**, *38*, 913-915.

17 *Handbook of Data on Common Organic Compounds*; Lide, D. R., Milne, G. W. A., Eds.; CRC Press: Boca Raton, FL, 1995; Vol. I.

18 Gale, P. A.; Sessler, J. L.; Král, V.; Lynch, V. J. *J. Am. Chem. Soc.* **1996**, *118*, 5140-5141.

19 Anzenbacher, P., Jr.; Jursíková, K.; Lynch, V. M.; Gale, P. A.; Sessler, J. L. *J. Am. Chem. Soc.* **1999**, *121*, 11020-11021.

20 Miyaji, H.; Sato, W.; Sessler, J. L. *Angew. Chem. Int. Ed.* **2000**, *39*, 1777-1780.

21 Sessler, J. L.; Anzenbacher, P., Jr.; Miyaji, H.; Jursíková, K.; Bleasdale, E. R. Gale, P. A. *Ind. Eng. Chem. Res.* **2000**, *39*, 3471-3478.

22 Blás, J. R.; Márquez, M.; Sessler, J. L.; Luque, J.; Orozco, M. *J. Am. Chem. Soc.* **2002**, *124*, 12796-12805.

23 Nielsen, K. A.; Jeppesen, J. O.; Levillain, E.; Becher, J. *Angew. Chem. Int. Ed.* **2003**, *42*, 187-191.

24 Yoon, D.-W.; Hwang, H.; Lee, C.-H. *Angew. Chem. Int. Ed.* **2002**, *41*, 1757-1759.

25 Liu, M.; Arora, S. K. *Acta Cryst. C* **1993**, *49*, 372-374.

26 Shannon, R. D. *Acta Crystallogr.* **1976**, *A32*, 751-767.

27 Bendikov, M.; Wudl, F.; Perepichka, D. F. *Chem. Rev.* **2004**, *104*, 4891-4945.

28 Boulas, P. L.; Gómez-Kaifer, M.; Echegoyen, L. *Angew. Chem. Int. Ed.* **1998**, *37*, 216-247.

29 Bird, C. L.; Kuhn, A. T. *Chem. Soc. Rev.* **1981**, *10*, 49-82.

30 Stradins, J.; Turovska, B.; Glezer, V. *Bioelectrochem. Bioenergetics* **1993**, *32*, 1-13.

31 Hoganson, C. W.; Tommos, C. *Biochim. Biophys. Acta* **2004**, *1655*, 116-122.

32 Armarego, W. L. F.; Perrin, D. D. *Purification of Laboratory Chemicals*; 4th ed.; Butterworth-Heinmann: Oxford, 1996.

33 Connelly, N. G.; Geiger, W. E. *Chem. Rev.* **1996**, *96*, 877-910.

# Chapter III

# Electron transfer series of porphyrinogen complexes with redox-inert metal dications — electronic structures

Parts of this Chapter have been published:
Bachmann, J.; Nocera, D. G. *J. Am. Chem. Soc.* **2004**, *126*, 2829-2837;
Bachmann, J.; Nocera, D. G. *Inorg. Chem.* **2005**, *44*, 6930-6932.

## III.1. Mixed valency in a variety of flavors and colors

Mixed valency in molecular compounds is typically accommodated at metal centers the formal oxidation states of which differ by a single electron (Scheme III.1, left).[1-4] In these complexes, reactivity is confined to *single* electron oxidations and reductions of the constituent $M^n$ and $M^{n+1}$ centers, respectively.[5-10] As an extrapolation from this one-electron formalism, it has been shown that two-electron mixed valency of bimetallic cores (Scheme III.1, center) provides an entry into a *multi*electron oxidation-reduction chemistry. Redox cooperativity may be established between the individual metal centers of a $M^n\cdots M^{n+2}$ mixed-valent core; two-electron oxidations may be promoted at a $M^{n+2}$ center and two-electron reductions at a $M^n$ center.[11-14] Those successes in using $M^n\cdots M^{n+2}$ species to drive two- and four-electron transformations along ground- and excited-state pathways establish the utility of two-electron mixed valency as a useful design concept in the development of multielectron reaction schemes.

Two-electron mixed valency has heretofore been restricted to a metal core. Metal-to-metal charge transfer excitation[15-18] or internal disproportionation of a symmetric $M^{n+1}\cdots M^{n+1}$ bimetallic core will yield a $M^n\cdots M^{n+2}$ species.[11,13,19] For either approach, the ligand framework is crucial for stabilizing the two-electron mixed-valent core with respect to its symmetric congener,[11,13,20,21] but it is not directly involved in the redox chemistry. Nevertheless, the active participation of ligands in the redox transformations of some metal complexes (detailed in Chapter I)[22-25] suggests the antithetical approach to two-electron mixed valency wherein a ligand framework, as opposed to a bimetallic core, is exploited as the electron/hole reservoir. In particular, the redox chemistry of octamethylporphyrinogen complexes of redox-inert, spherical metal dications, delineated in Chapter II, supports an intermediary oxidation state $[L^{\Delta}M]$ (Scheme III.1, right) which *(a)* is stable with respect to disproportionation to its redox-extreme congeners $[LM]^{2-}$ and $[L^{\Delta\Delta}M]^{2+}$ and *(b)* displays the structural properties of mixed valency — two-electron oxidation of a dipyrrole moiety translating into a C—C bond between the $\alpha$-carbons of neighboring pyrroles.

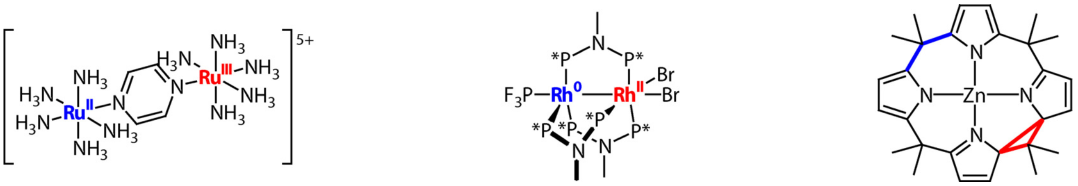

**Scheme III.1.** Three flavors of mixed valency — the juxtaposition of two moieties only differing in their oxidation state. The Creutz-Taube ion (left) is the prototypical example of dinuclear $M^{n}\cdots M^{n+1}$ mixed valency. A rare metal-based *two-electron* mixed-valent system is shown in the middle (Heyduk and Nocera; P* = $PF_2$). The present work explores *ligand-based* two-electron mixed valency in the system depicted at the right.

This Chapter therefore seeks to achieve a description of the particular type of mixed valency observed in porphyrinogen complexes — ligand-based and characterized by a two-electron inequivalency between redox centers. Its main spectroscopic handle is its visible intervalence charge transfer (IVCT). IVCT was defined within both theoretical[26-28] and experimental[29] frameworks soon after mixed valency was observed to give rise to an intense visible absorption in molecules[30] and solids.[31] The intensity and energy of IVCT in these systems depends on the electronic and structural properties of the bridge linking the mixed-valent metal centers.[32-35] To date, occurrence of IVCT has been documented mostly between metals that differ by one in their formal oxidation state.

## III.2. Origin of a visible color

### III.2.a. UV-vis spectra

The two-electron mixed-valent nature of the $L^{\Delta 2-}$ macrocycle is evident visually from its color: $[LZn]^{2-}$ and $[L^{\Delta\Delta}Zn]^{2+}$ are white or off-white powders, but their comproportionation to $[L^{\Delta}Zn]$ yields an intense orange color.

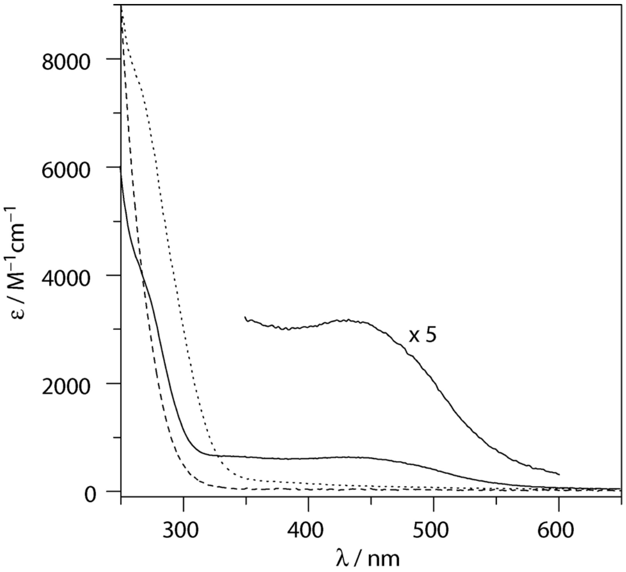

**Figure III.1.** UV-vis absorption spectra of $Li_2(THF)_x[LZn]$ (– – –) in THF and of $[L^{\Delta}Zn(CH_3CN)]$ (—) and $[L^{\Delta\Delta}Zn](BF_4)_2$ (- - -) in $CH_3CN$. The inset shows a ×5 magnification of the absorption profile of $[L^{\Delta}Zn(CH_3CN)]$ in the visible spectral region.

*Choice of solvents*

Figure III.1 shows the absorption spectra for the three compounds of the series. The spectra of $[L^{\Delta\Delta}Zn]^{2+}$ and $[L^{\Delta}Zn]$ are recorded in $CH_3CN$ whereas that of $[LZn]^{2-}$ is recorded in THF. This choice of solvents is dictated by the solution chemistry of the compounds. Acetonitrile solutions of $[LZn]^{2-}$ exhibit a near-UV absorption band the energy ($\lambda_{max}$ = 300-400 nm) and intensity of which are concentration dependent; the band vanishes in the spectrum of the compound in THF. We attribute this behavior to cation-promoted aggregation of the macrocycle, which is suppressed when the $Li^+$ cation is solvated by THF. Consistent with this tenet, similar behavior may be reproduced for the absorption spectrum of the $Li^+$ salt of deprotonated pyrrole (prepared by reacting pyrrole with butyllithium). In the case of $[L^{\Delta\Delta}Zn]^{2+}$ and $[L^{\Delta}Zn]$, the insufficient stability of the compounds in THF prevents us from measuring absorption data in this solvent. However, $CH_3CN$ is a viable solvent for these compounds since they do not possess any counter-cations.

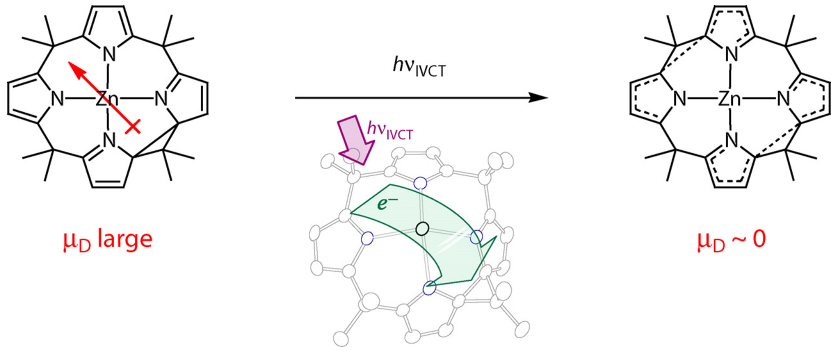

**Figure III.2.** A simplified representation of the IVCT in [L$^{\Delta}$Zn], and its consequence on the molecular dipole $\mu_D$. In effect, the transfer of an electron across the complex upon photoexcitation rearranges charges in a more symmetrical manner.

*Spectral comparison*

The absorption profiles (Figure III.2) of the fully reduced and oxidized members, [LZn]$^{2-}$ and [L$^{\Delta\Delta}$Zn]$^{2+}$, are similar, unremarkable and in line with their colorless appearance. A rising absorption into the UV spectral region is consistent with the presence of a strongly absorbing $\pi \rightarrow \pi^*$ transition of pyrrole at high energy ($\lambda_{max}$ = 208 nm).[36] The UV spectral region of [L$^{\Delta}$Zn] is also dominated by the rising absorption edge of the $\pi \rightarrow \pi^*$ transition of the constituent pyrroles. However, its visible region is dominated by a broad absorption the maximum of which is observed at 430 nm in $CH_3CN$. Given the mixed-valent nature of [L$^{\Delta}$Zn], it is appealing to assign this visible absorption to an intervalence charge transfer (IVCT), that is, the photoinduced evolution of the system from its asymmetric ground state (one reduced and one oxidized dipyrrole) to a symmetrical excited state (two dipyrrole radical anions). In simple terms, it would correspond to the transfer of an electron from the HOMO localized on the reduced dipyrrole across the macrocycle into the LUMO localized on its oxidized counterpart (Figure III.2)

*Solvent dependence*

The validity of the IVCT assignment can be tested experimentally. Juxtaposed reduced and oxidized dipyrrole units engender a large dipole moment in the ground electronic state of the [L$^{\Delta}$Zn] complex. The dipole should be alleviated by the electron redistribution accompanying IVCT excitation — in a limiting resonance form of the IVCT excited state, the dipole will be annihilated. Thus, polar solvents should stabilize the ground state of [L$^{\Delta}$Zn] relative to its lowest energy IVCT excited state. As the static dielectric constant of the solvent is decreased, the ground state should be destabilized, engendering a decreased HOMO-LUMO gap. Atypical of most charge transfer transitions, the energy of the IVCT transition of [L$^{\Delta}$Zn] should therefore blue-shift as the polarity of the solvent increases. Experimental data taken in acetonitrile, dichloromethane and toluene validate this prediction, and thereby confirm the IVCT nature of the transition.

## III.2.b. Theoretical description

*Singlet state*

The electronic structure of [L$^{\Delta}$Zn] was examined further by DFT calculations. Figure III.3 displays the color-coded energy levels and representations of the frontier Kohn-Sham[37] molecular orbitals. The most striking feature of the energy level diagram is the clear-cut division of orbital parentage between oxidized and reduced sides of the ligand. The highest-energy occupied molecular orbitals are localized on the reduced half of the macrocycle whereas the lowest-energy unoccupied orbitals are localized on its oxidized half. The Zn d orbitals lie very deep in the MO diagram (HOMO–29 to HOMO–33) and effectively do not contribute to the frontier MOs. The HOMO to HOMO–4 (blue) are the **A**- and **B**-type orbitals (according the nomenclature of Scheme III.2) of the pyrroles on the reduced side of the porphyrinogen. An orbital pair arises from the in-phase and out-of-phase interaction of orbitals on individual pyrroles along the C$^{\alpha}$—C$^{\alpha}$ axis of the dipyrrole subunit. The weak interaction between pyrrole subunits on the reduced side of the porphyrinogen, indicated by the small energy difference of 0.15 eV for in-phase and out-of-phase linear combinations, is consistent with the long C$^{\alpha}$—C$^{\alpha}$ distance. The MOs formed from the equivalent $\pi$ orbital set of

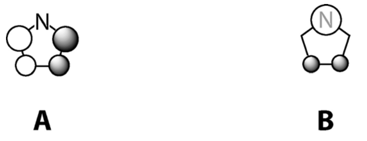

**Scheme III.2.** Schematic representation of the highest occupied $\pi$ orbitals of the pyrrolyl anion (corresponding to the $e_1''$ orbitals of $D_{5h}$ cyclopentadienyl). The nodal plane containing the nuclei is not displayed in this top view.

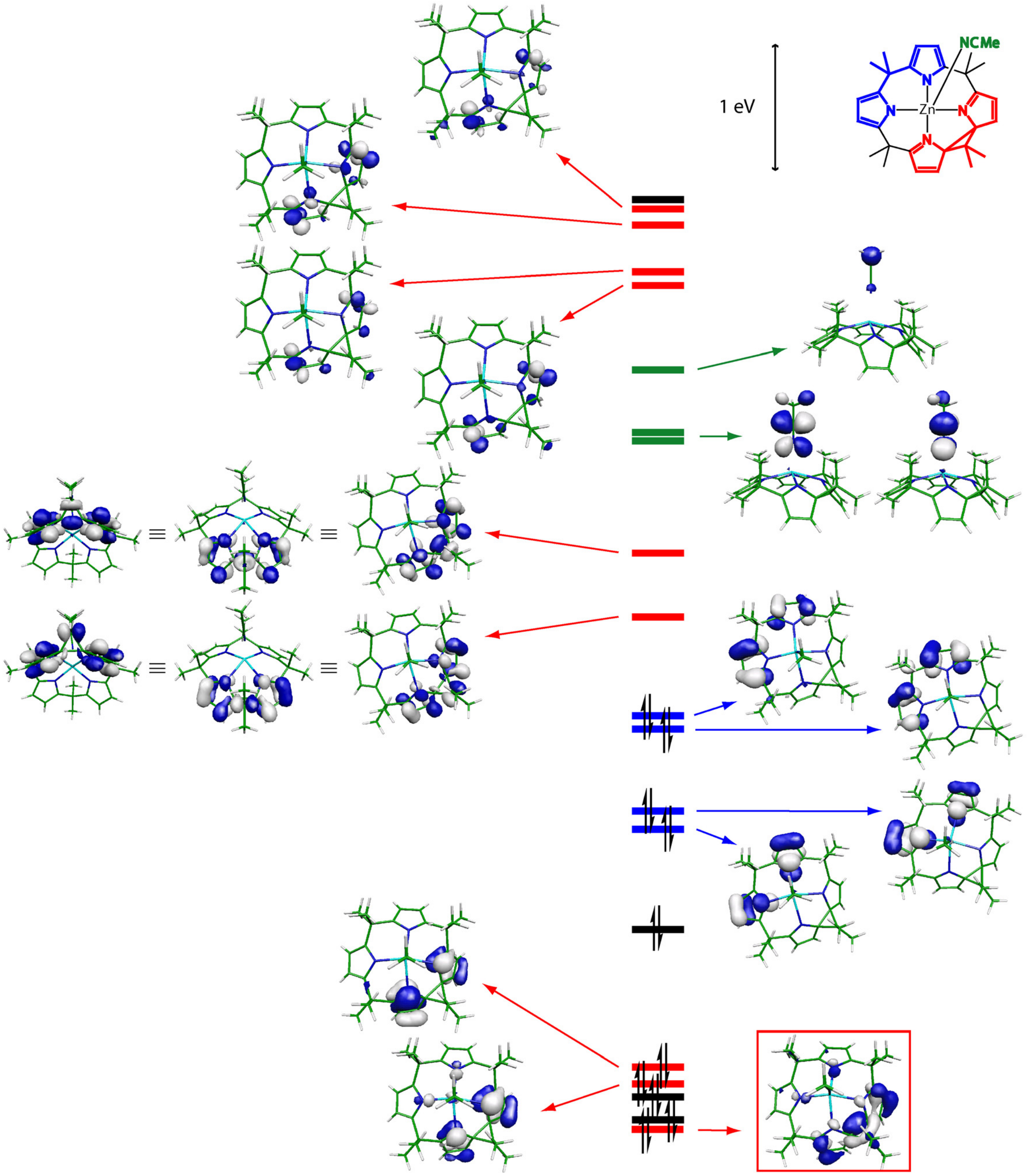

**Figure III.3.** Computed Kohn-Sham MO diagram of [L$^{\Delta}$Zn(NCMe)] in the gas phase. The colors of the energy levels code for the parentage of the corresponding orbitals: green, acetonitrile; blue, reduced dipyrrole π system; red, oxidized dipyrrole π system; black, σ framework of the porphyrinogen. The orbital framed in red carries the C$^{\alpha}$—C$^{\alpha}$ bond within the oxidized dipyrrole. The representations of the LUMO and LUMO+1 are repeated for clarity in two different orientations, after removal of the coordinated MeCN.

pyrroles on the oxidized half of the porphyrinogen (red) also appear as pairs corresponding to $C^{\alpha}$—$C^{\alpha}$ bonding and antibonding combinations. The HOMO–6 / HOMO–5 orbitals are composed of **B** orbitals that are effectively insulated from each other by the absence of electron density at $C^{\alpha}$. The HOMO–6 and HOMO–5 are more stable than their **B**-type counterparts on the reduced dipyrrole ($\Delta E$ = E(HOMO–6 / –5) – E(HOMO–2 / –3) ≈ –2 eV) owing to the greater electronegative character of the oxidized half of the macrocycle. In the **A**-type derived MO pair on the oxidized pyrrole, the $sp^3$ character of $C^{\alpha}$ causes the pyrrole rings of the oxidized subunit to assume an orientation nearly perpendicular to the plane of the cyclopropane ring. This stereochemistry causes an antibonding interaction between pπ(pyrrole) and pσ(cyclopropane bridgehead) orbitals that is sufficiently destabilizing to place the $e_1''$-type MOs at the LUMO / LUMO+1 position, as displayed by Figure III.4.

As a result, the frontier MO set (Figure III.3) exhibits a LUMO localized on the oxidized half of the porphyrinogen and a HOMO localized on the reduced half of the

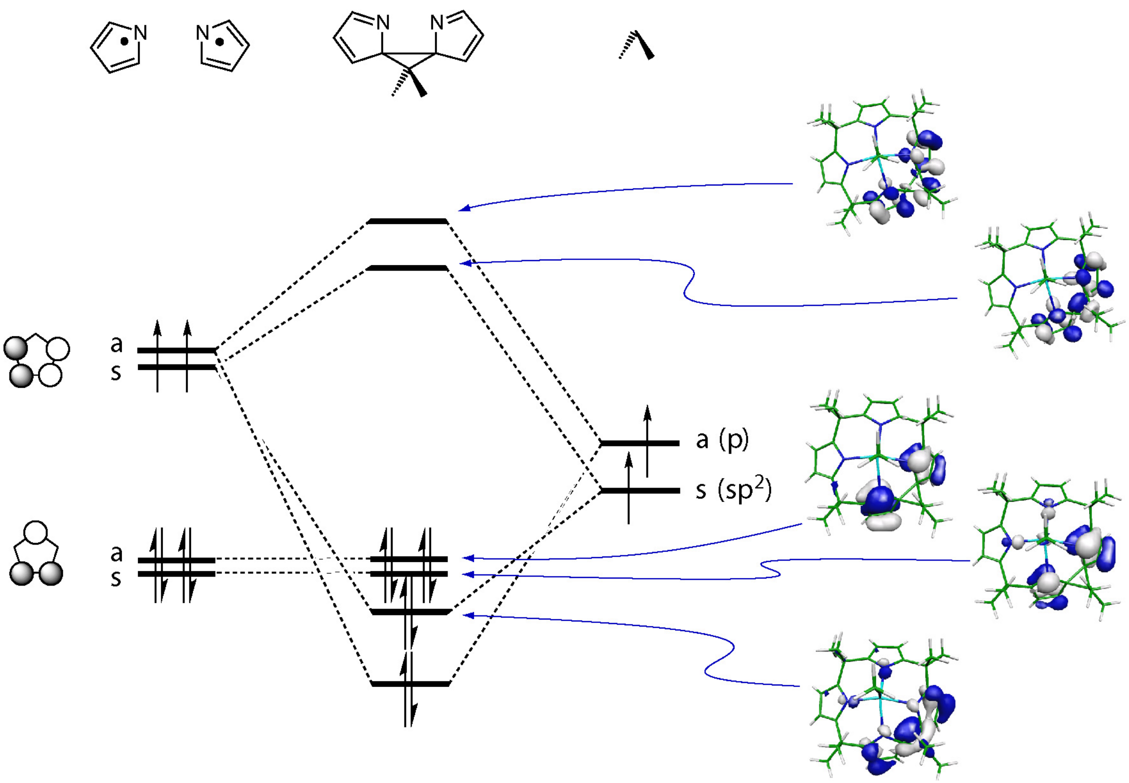

**Figure III.4.** A simplified description of the orbital interactions leading to the MO structure of the oxidized (neutral) dipyrromethane unit. The labels a and s describe the symmetry of each orbital with respect to the plane containing the C atoms of the dimethylmethylene fragment.

porphyrinogen. The MO diagram therefore nicely accounts for the IVCT assignment of the lowest energy absorption band of [L$^{\Delta}$Zn]. TD-DFT indicates that several IVCT transitions may arise within this manifold, qualitatively explaining the breadth of the charge transfer transition.

Other notable highlights of the MO diagram include the HOMO–9, which is framed in Figure III.3. The orbital embodies the antithesis of the interaction that leads to the LUMO. Specifically, the **A** orbitals on the oxidized dipyrrole are bonding with respect to the cyclopropane bridgehead, engendering a very stable MO which carries most of the C$^{\alpha}$—C$^{\alpha}$ bonding interaction (*cf.* Figure III.4). The pyrrole $\pi$ orbitals of higher nodal structure ($e_2''$-type when described in terms of $D_{5h}$ cyclopentadienyl MOs) contribute to unoccupied MOs that lie to higher energy. On the oxidized dipyrrole half of the porphyrinogen, the $e_2''$-type derived MOs are energetically proximate to the LUMO (LUMO+5 to LUMO+8); the MO's involving the $e_2''$-type orbitals on the reduced half of the porphyrinogen are very high in energy and not shown. The MOs involving the $CH_3CN$ are unremarkable and have little effect on the structure and spectroscopy of the [L$^{\Delta}$Zn] complex.

The Mulliken charge analysis of the porphyrinogen framework confirms the consequence of dipyrrole oxidation on coordination properties observed experimentally in the crystal structure of [L$^{\Delta}$Zn(NCMe)] (Chapter II). The N atoms of the oxidized dipyrrole bear significantly less negative charge (–0.42 charge units) than those of the reduced dipyrrole (–0.50 and –0.51, respectively), although all pyrrole N atoms are clearly more negative than that of the axially ligated acetonitrile N (–0.23). A very large dipole moment of 11.9 Debye is calculated for the ground state molecule (in the gas phase), which underscores the influence of solvation on the energy of IVCT noted above.

### *Triplet state*

Geometry optimization of [L$^{\Delta}$Zn(NCMe)] in the triplet state yields a good picture of the structure of the molecule after excitation, if it were to perform intersystem crossing and vibrational relaxation in the triplet well. It also gives a measure of the strength of the redox-active C—C bond. The triplet is compared to the

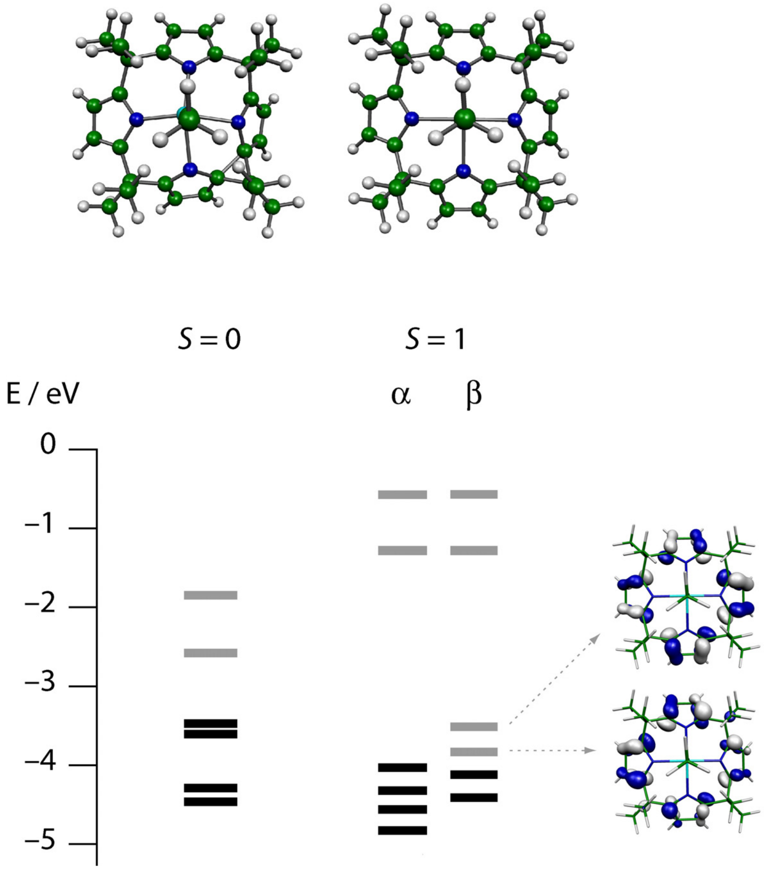

**Figure III.5.** Comparison of computed singlet and triplet states of neutral zinc porphyrinogen. Top, ball-and-stick representations of the optimized structures; below, Kohn-Sham MO diagrams (black, occupied; gray, virtual). The triplet is unrestricted and therefore features two distinct sets of spinors for α and β electrons; its two SOMOs are depicted on the right.

**Table III.1.** Comparison of structural and electronic parameters for computed singlet and triplet states of $[L^{\Delta}Zn(NCMe)]$.

| | $S = 0$ | $S = 1$ |
|---|---|---|
| Diametrically opposed $C^{\alpha}\cdots C^{\alpha}$ distances / Å | 1.63 | 2.38 |
| | 2.55 | 2.41 |
| Mulliken charges on coordinated N atoms | −0.50 | −0.48 |
| | −0.50 | −0.48 |
| | −0.43 | −0.47 |
| | −0.43 | −0.47 |

singlet in Figure III.5 and Table III.1. The most obvious feature of the triplet is its symmetry, apparent in the metrics and charges of the macrocycle. In the triplet, one electron has been transferred from the reduced dipyrrole into its oxidized counterpart, and the two highest-lying electrons are now evenly distributed over all four pyrrole rings — both SOMOs are completely delocalized. There are no clear $C^{\alpha}\cdots C^{\alpha}$ bonding interactions, although $C^{\alpha}\cdots C^{\alpha}$ distances are somewhat compressed (2.4 Å) relative to the nonbonded $C^{\alpha}\cdots C^{\alpha}$ distances (2.6 Å) in the singlet structure. The charges on the four N atoms are equivalent (–0.48±0.01, instead of –0.50±0.01 and –0.43±0.01 observed in the singlet), and consequently, the Zn—N bond lengths are equal. The most unexpected property of the computed triplet state is its low energy: in internal energy terms, and if differences in zero-point energy are neglected, the triplet is computed to only lie less than 5 kJ/mol above the singlet. This means that the energy gained by pairing up two electrons in a strongly bonding orbital in the singlet is mostly compensated by unfavorable strains in the spiro-cyclopropane formed. A weak $C^{\alpha}$—$C^{\alpha}$ bond (even though structurally short) is likely to be the reason for the relatively low redox potential necessary to oxidize metal porphyrinogens, and for the observed propensity of oxidized porphyrinogen complexes to undergo decomposition *via* radical pathways.

A magnetic measurement by Evans method[38,39] on a MeCN solution of $[L^{\Delta}Zn]$ is consistent with the presence of a small amount of triplet state in equilibrium with the singlet ground state. At 20°C, a 49-mM concentration of $[L^{\Delta}Zn]$ causes the Larmor frequency of a dissolved standard to shift by 0.031 ppm (relative to an internal reference). Thus the observed overall molar paramagnetic susceptibility of $[L^{\Delta}Zn]$ is calculated to be $\chi^{p}_{obs} = +110\cdot10^{-6}$ (in cgs units), to be compared to the value of $\chi^{p}_{calc} = +3400\cdot10^{-6}$ expected for an organic triplet diradical ($g = 2$, $S = 1$). Given the additive property of magnetic susceptibilities, the ratio corresponds to the fraction of $[L^{\Delta}Zn]$ that exists as a triplet, 3%. From there, a difference in Gibbs free energy of $\Delta G = 8.5$ kJ/mol is obtained between $^{1}[L^{\Delta}Zn]$ and $^{3}[L^{\Delta}Zn]$; the differences in structural symmetry and spin degeneracy correspond to an entropic difference of $\Delta S = R\cdot(\ln4 + \ln3)$, yielding in enthalpic terms (and in internal energy, if the change in volume is neglected) $\Delta H = 15$ kJ/mol $= \Delta U$, in reasonable agreement to the value computed by DFT methods. The larger singlet-triplet gap obtained experimentally is consistent with the additional stabilization of the strongly dipolar singlet state in the dielectric medium of the solvent.

# III.3. Structural tuning of the IVCT

*Experimental observations*

The visible color of the mixed-valent [L$^{\Delta}$M] state is sensitive to the nature of M$^{2+}$: [L$^{\Delta}$Mg] is vermilion red, whereas [L$^{\Delta}$Zn] is orange and [L$^{\Delta}$Ca] yellow. The UV-visible absorption spectra of Figure III.6 clearly display the corresponding blue-shift of the first absorption maximum (due to IVCT): [L$^{\Delta}$Mg] ($E = 21000$ cm$^{-1}$) < [L$^{\Delta}$Zn] ($E = 24800$ cm$^{-1}$) < [L$^{\Delta}$Ca] ($E = 37000$ cm$^{-1}$).[a] Because Mg$^{2+}$, Zn$^{2+}$ and Ca$^{2+}$ are similarly closed-shell spherical dications and their orbitals do not participate in the frontier MOs of [L$^{\Delta}$M] (as described above), no difference in the electronic properties of the three metal ions can account for the trend in absorption energies. Instead, variations in ionic radii give rise to well-defined *structural* differences in [L$^{\Delta}$M(NCMe)] (*c.f.* Chapter II). The position of M$^{2+}$ along the axis linking the centers of the reduced (dianionic) and oxidized (neutral) dipyrrole changes depending on its size. Consequently, the size of M$^{2+}$ can be expected to modulate the ground-state molecular dipole. Given that the dipole is drastically diminished in the excited state, the size of M$^{2+}$ should be reflected in the energy of the IVCT, which is indeed observed experimentally.

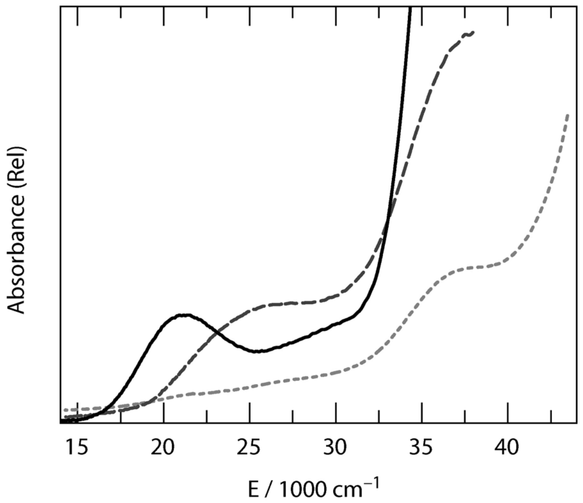

**Figure III.6.** UV-visible absorption spectra of [L$^{\Delta}$Mg] (—), [L$^{\Delta}$Zn] (– –) and [L$^{\Delta}$Ca] (---) in $CH_2Cl_2$. The ordinate is an arbitrary absorbance scale.

---

[a] From fits of the experimental traces to sums of Gaussians.

### *Theory*

Electronic consequences of the structural differences between the two sides are described in a more quantitative fashion by DFT calculations. Comparison of the MO diagram of [$L^{\Delta}$Mg(NCMe)] (for which crystallographic data are also available) with that of [$L^{\Delta}$Zn(NCMe)] presented above, shows a completely conserved general picture. However, the difference in dication position between the dipyrroles is also manifested in the computed dipole moment of the molecules. Movement of the dication closer to the dipyrrole dianion does diminish the dipole of [$L^{\Delta}$M(NCMe)], as expected: $\mu_D$ = 11.9 D for M = Zn, and $\mu_D$ = 12.4 D for M = Mg. The HOMO-LUMO gap reflects the intensity of the ground-state dipole: it is computed be 0.82 eV for M = Zn and 0.72 eV for M = Mg. The smaller energy gap obtained for M = Mg relative to M = Zn arises from both a destabilization of the HOMO (+0.05 eV) and a stabilization of the LUMO (–0.05 eV). This result is consistent with simple electrostatic consideration of the position of the dication between the dipyrrole halves of the molecule. The MOs localized on the dipyrrole dianion will be stabilized as the dication moves toward it; at the same time, those on the oxidized dipyrrole will be destabilized as the electropositive metal center is moved further away.

### *X-ray photoelectron spectroscopy*

A series of photoelectron measurements were performed with the goal of obtaining a direct experimental handle on the energies of the HOMOs of [$L^{\Delta}$M] (M = Mg, Zn, Ca). However, the X-ray photoelectron (XPS) spectrometer at MIT's Center for Materials Science and Engineering (a Kratos AXIS) lacks the fine resolution needed to observe the frontier orbitals. Only an instrument equipped with a UV source would be capable of furnishing the desired information. However, consideration of the peaks corresponding to the core orbitals provides a qualitative confirmation of the elemental analyses of the three compounds and of the similarity of their organic frameworks.

## III.4. Excited state dynamics

Transient absorption (TA) spectroscopy can provide further insight into the nature and dynamics of an excited state by recording an absorption signal at a given time after a "pump" light pulse. A picosecond single-wavelength kinetic trace recorded within the ground-state absorption envelope of [$L^{\Delta}$Mg] is shown in Figure III.7. The signal is negative, corresponding to the depletion of ground state population by the pump pulse. An initial spike with a lifetime on the order of 1 ps and due to nonlinear phenomena caused by the overlap of the pump and probe beams at t = 0 is always observed, and does not require consideration. The bleach then decays on a 10- to 20-ps timescale. No signal is observed upon probing at 806 nm.

Thus, a measurable population of [$L^{\Delta}$Mg] is excited upon irradiation. However, no indication of a genuine excited-state absorption (positive signal), which may be expected at long wavelengths originating from the "diradical" excited state, could be seen at 806 nm. Moreover, the excited state relaxes down to the ground state very quickly, within the timescale of atomic motions, presumably *via* vibrational cooling.[40,41]

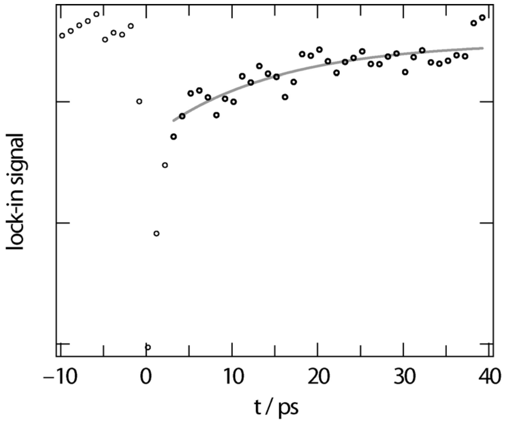

**Figure III.7.** TA signal of [$L^{\Delta}$Mg] in $CH_2Cl_2$. Circles are the experimental data points, and the gray trace a monoexponential fit to the decay; data points considered for the fit are bolded. $\lambda_{exc}$ = 490 nm; $\lambda_{probe}$ = 470 nm; $\tau$ = 14 ps ($R^2$ = 0.74).

# III.5. Conclusions

Spectroscopy and theory show that the mixed-valent formulation of [$L^{\Delta}M$] is not limited to formal and structural criteria: it is substantiated by a visible IVCT transition.

*Relevance to reaction chemistry*

Several similarities between ligand-based and metal-based approaches to two-electron mixed valency are evident. For both approaches, (1) the two-electron mixed-valent intermediate is the linchpin that couples the two-electron chemistry of the individual redox centers (dipyrroles in the case of porphyrinogen, metal centers in the case of the dinuclear complexes), (2) the two-electron mixed-valent compound is the structural composite of the symmetric oxidized and reduced congeners, and (3) the frontier molecular orbitals and corresponding lowest energy electronic transitions are confined to the two-electron mixed-valent core.[42] Despite these similarities, the ligand-based approach to two-electron mixed valency differs from that of a metal-based approach in one important aspect. Because coordination geometry is inextricably linked to metal oxidation state, two-electron/hole storage in the metal-based approach *must* be accompanied by alterations of the primary coordination sphere. Conversely, in the approach described here, two-electron/hole storage occurs in the macrocycle periphery, decoupled from the acid-base chemistry of the metal. This orthogonalization between redox storage and small molecule coordination sites offers a new design element for using two-electron mixed valency to promote multielectron reactivity.

*Relevance to the fundamental nature of mixed valency*

The IVCT transition in [$L^{\Delta}M$] is sensitive to the bridge intervening between the redox termini. Heretofore, such bridge effects have mostly been described in metal-based one-electron mixed valency, the bridge typically being a ligand that connects the metal ions. Changes in the bridge cause variations in electronic coupling as well as distance, and the IVCT energy is consequently related to the bridge in a complex way.[34,43-45] This is not the case for this system: the IVCT depends on a single structural parameter, the position of the central metal between the redox termini.

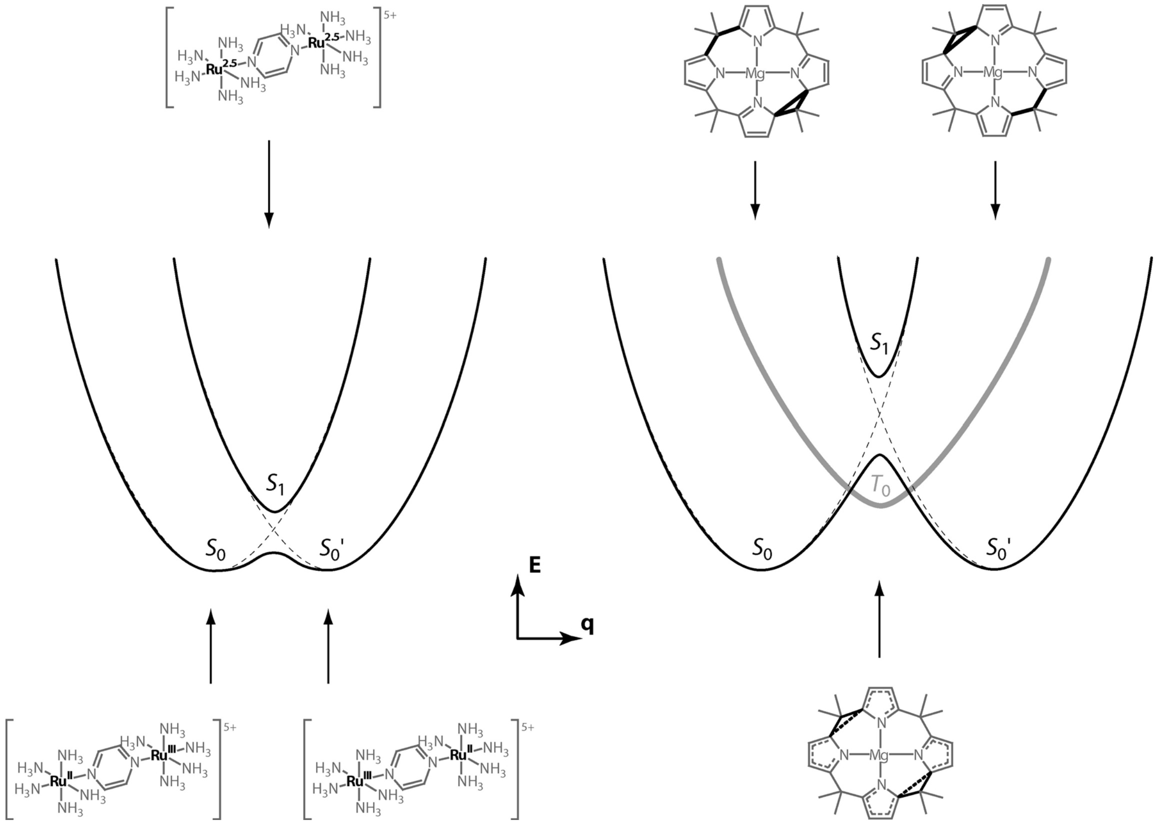

**Figure III.8.** Fundamental differences between one- and two-electron mixed valency and their respective IVCT states. The examples of a diruthenium (II/III) system and of neutral magnesium porphyrinogen are displayed in their respective mixed-valent and valence-symmetric (IVCT) states. The curves represent the electronic energy E of certain states with respect to a collective nuclear coordinate q (in the diruthenium example, q is mainly the ratio between the Ru—N distances on the left and those on the right; in the porphyrinogen case, it mostly represents the ratio between the two diametrically opposed $C^{\alpha}$—$C^{\alpha}$ distances). Thin dashed curves are the diabatic states, and thicker, solid ones represent the result of their interaction: a mixed-valent ground state ($S_0$, equivalent to $S_0'$) and a valence-symmetric (IVCT) excited state, $S_1$. The two-electron case is more involved due to the existence of a valence-symmetric triplet state $T_0$ (thicker gray curve).

The unique characteristics of the redox centers — their being ligand-based and deriving their mixed valency from a two-electron inequivalency — bears consequences on the IVCT state. Experimentally, the IVCT state in the porphyrinogen system is found to be significantly higher in energy (in the UV or visible instead of the NIR) and longer-lived (by an order of magnitude) than “traditional” one-electron mixed-valent compounds of the type $Ru^{II}\cdots Ru^{III}$ (within the limited set of data available, mostly on non-symmetric systems).[46,47] Figure III.8 shows the difference in the nature of the IVCT state between the two types of mixed valency. On the left, IVCT excitation of a one-electron mixed-valent system initially yields the valence-symmetric state $S_1$, which is not observed and very quickly decays into either one of the mixed-valent wells ($S_0$ or $S_0'$). If the two wells are chemically and spectroscopically distinct, then back-ET from the less stable well ($S_0'$) into the first (the ground state, $S_0$) can be resolved on the 1-ps timescale.[46,47] On the right, the consideration of two mobile electrons instead of just one introduces an additional state available to the system, namely the triplet (in gray). Because of Pauli repulsions, the triplet only exists when the two electrons reside on opposite sides of the macrocycle, that is to say, it only exists as a valence-symmetric state, $T_0$. Hence, the [$L^{\Delta}M$] system has, in addition to both equivalent (and undistinguishable) mixed-valent (singlet) ground states $S_0$ and $S_0'$, a relatively stabilized valence-symmetric triplet state $T_0$, attainable from the fleeting singlet IVCT state $S_1$ *via* intersystem crossing (ISC).

This qualitative description of the system accounts for the experimental observations. In this picture, the high energy of the IVCT transition is due to the large Δq between symmetrically related mixed-valent ground states (in other words, to a large structural reorganization upon C—C bond formation and breaking), and the relatively slow decay of the observed transient may follow from the stability of the valence-symmetric triplet $T_1$ state.

# III.6. Experimental section

## III.6.a. Physical measurements

*Electronic spectroscopy*

UV-vis-NIR solution absorption spectra were recorded between 220 and 1800 nm on a Cary-17 spectrophotometer modified by On-Line Instrument Systems (OLIS) to include computer control or a Spectral Instruments 440 Model spectrophotometer.

*Magnetic measurement*

The magnetic properties of [$L^{\Delta}Zn$] were measured in solution by Evans method.[38,39] A solvent mixture was prepared from 200 μL of $C_6H_6$ and 4 mL of $CD_3CN$. A sample of [$L^{\Delta}Zn$] (12 mg) was dissolved in 0.5 mL of solvent and transferred into an NMR tube enclosing a glass insert containing pure solvent. In $^1$H NMR at $\nu_0 = 500$ MHz, the $C_6H_6$ peaks from the insert and the [$L^{\Delta}Zn$] solution were separated by 0.051 ppm, whereas a separation of 0.020 ppm was measured for a blank prepared in the same manner but in the absence of [$L^{\Delta}Zn$]. The specific magnetic susceptibility of [$L^{\Delta}Zn$] is calculated in cgs units from the shift $\Delta\nu/\nu_0 = 0.031 \cdot 10^{-6}$ by the equation,

$$\chi = \chi_0 + \frac{3000}{4\pi} \cdot \frac{\Delta\nu / \nu_0}{c \cdot M} = -0.37 \cdot 10^{-6}$$

where the molar concentration $c = 4.9 \cdot 10^{-2}$, the molecular mass $M = 490$ and the magnetic susceptibility of the solvent $\chi_0 = -0.68 \cdot 10^{-6}$.[48] After conversion to a molar scale, the observed paramagnetic susceptibility $\chi^{p}_{obs}$ is obtained by subtraction of the diamagnetic contribution $\chi^{d}$, evaluated from Pascal's constants ($\chi^{d} = -294 \cdot 10^{-6}$),[49]

$$\chi_M = \chi \cdot M \qquad \Rightarrow \qquad \chi^{p}_{obs} = \chi_M - \chi^{d} = +112 \cdot 10^{-6}$$

The molar paramagnetic susceptibility $\chi^{p}_{calc}$ expected to arise from an organic triplet diradical (S = 1, $g = 2$) can be calculated from the effective magnetic moment $\mu_{eff}$,

$$\mu_{eff} = g\sqrt{S(S+1)} = 2.828\sqrt{\chi^{p}_{calc} \cdot T} \qquad \Rightarrow \qquad \chi^{p}_{calc} = +3410 \cdot 10^{-6}$$

at $T = 293$ K. Consequently, the fraction of $^3$[$L^{\Delta}Zn$] contributing to the observed magnetism is $\chi^{p}_{obs} / \chi^{p}_{calc} = 0.03$.

## III.6.b. Computational methods

Time-dependent density functional theory calculations (TD-DFT)[50,51] were performed using the Amsterdam Density Functional (ADF2002.02) program[52,53] on a home-built Linux cluster comprising sixty Intel processors organized in groups of twelve running in parallel. The generalized gradient approximation (GGA) was used as implemented in ADF by the LB94 functional,[54] allowing an accurate description of the asymptotic density behavior. A basis set of quadruple-ζ Slater-type functions augmented by triple polarization (ET-QZ3P) was used for all atoms, without frozen core approximation. The geometry was set at that observed in the corresponding experimental crystal structure, with uncoordinated solvents removed; spin restriction was applied. Ten excitation energies were computed by the Davidson procedure.[55]

Static molecular orbital pictures were obtained by single point calculations at a less heavy level (GGA Becke88 for exchange,[56] Perdew-Wang91 for correlation,[57] with TZ2P with frozen cores). Orbitals were visualized using the Molekel software.[58,59]

Full geometry optimizations were performed in the singlet and the triplet states with GGA-B88x/PW91c-TZ2P. The singlet geometry is not significantly different from the experimental solid-state structure. Spin restriction was lifted for the triplet; in the singlet, it was checked that spin restriction did not affect the results. The relative energies quoted in the text are gas-phase internal energies at 0 K, without consideration of zero-point energies.

### III.6.c. Transient absorption spectroscopy

Samples for transient absorption spectroscopy were contained in a 2-mm pathlength high-vacuum cell and prepared to yield an optical density of ~0.5 at the excitation wavelength. The setup used for ultrafast transient absorption experiments was described previously.[60] In brief, the pulsed 806-nm output (~150 fs-wide pulse) of a regeneratively amplified Ti-Sapphire laser system was separated into two beams. The weaker component was focused into either a sapphire or a calcium fluoride substrate to generate the broadband probe pulse. The major component was either frequency-doubled to 403 nm, or tuned throughout the visible range with an optical parametric amplifier, then propagated along a computer-controlled optical delay-line to furnish time resolution. The excitation energy was set to ~5 μJ/pulse, and both beams were spatially overlapped on the sample; the pump beam was then blocked, and the probe was spectrally resolved in a monochromator. Transient spectra were recorded with a CCD camera and derived using a ‘negative time’ reference spectrum; single-wavelength kinetics were obtained with a lock-in amplified photodiode detector.

## III.7. References

1 Taube, H. *Angew. Chem. Int. Ed. Engl.* **1984**, *23*, 329-339.

2 Creutz, C. *Prog. Inorg. Chem.* **1983**, *30*, 1-73.

3 *Mixed Valency System: Applications in Chemistry, Physics and Biology*; Prassides, K., Ed.; NATO ASI Series C: Mathematical and Physical Sciences 343; Kluwer Academic: Dordrecht, 1991.

4 Schatz, P.N. In *Inorganic Electronic Structure and Spectroscopy*; Solomon, E. I., Lever, A. B. P., Eds.; Wiley-Interscience: New York, 1999; Vol. 2, pp 175-226.

5 Ito, T.; Hamaguchi, T.; Nagino, H.; Yamaguchi, T.; Kido, H.; Zavarine, I. S.; Richmond, T.; Washington, J.; Kubiak, C. P. *J. Am. Chem. Soc.* **1999**, *121*, 4625-4632.

6 Ito, T.; Hamaguchi, T.; Nagino, H.; Yamaguchi, T.; Washington, J.; Kubiak, C. P. *Science* **1997**, *277*, 660-663.

7 Vahrenkamp, H.; Geiss, A.; Richardson, G. N. *J. Chem. Soc., Dalton Trans.* **1997**, 3643-3651.

8 Balzani, V.; Juris, A.; Venturi, M.; Campagna, S.; Serroni, S. *Chem. Rev.* **1996**, *96*, 759-833.

9 Kunkely, H.; Pawlowski, V.; Vogler, A. *Inorg. Chim. Acta* **1994**, *225*, 327-330.

10 Vogler, A.; Osman, A. H.; Kunkely, H. *Coord. Chem. Rev.* **1985**, *64*, 159-173.

11 Heyduk, A. F.; Macintosh, A. M.; Nocera, D. G. *J. Am. Chem. Soc.* **1999**, *121*, 5023-5032.

12 Odom, A. L.; Heyduk, A. F.; Nocera, D. G. *Inorg. Chim. Acta.* **2000**, *297*, 330-337.

13 Heyduk, A. F.; Nocera, D. G. *J. Am. Chem. Soc.* **2000**, *122*, 9415-9426.

14 Heyduk, A. F.; Nocera, D. G. *Science* **2001**, *293*, 1639-1641.

15 Engebretson, D. S.; Zaleski, J. M.; Leroi, G. E.; Nocera, D. G. *Science*, **1994**, *265*, 759-762.

16 Engebretson, D. S.; Graj, E.; Leroi, G. E.; Nocera, D. G. *J. Am. Chem. Soc.* **1999**, *121*, 868-869.

17 Pistorio, B. J.; Nocera, D. G. *Chem. Commun.* **1999**, 1831-1832.

18 Cotton, F. A.; Nocera, D. G. *Acc. Chem. Res.* **2000**, *33*, 483-490.

19 Heyduk, A. F.; Nocera, D. G. *Chem. Commun.* **1999**, 1519-1520.

20 Manke, D. R.; Nocera, D. G. *Inorg. Chem.* **2003**, *42*, 4431-4436.

21 Hsu, T. L. C.; Helvoigt, S. A.; Partigianoni, C. M.; Turró C.; Nocera, D. G. *Inorg. Chem.* **1995**, *34*, 6186-6190.

22 Davison, A.; Edelstein, N.; Holm, R. H.; Maki, A. H. *Inorg. Chem.* **1963**, *2*, 1227-1232.

23 Pierpont, C. G.; Lange, C. W. *Prog. Inorg. Chem.* **1994**, *41*, 331-442

24 Wang, K.; Stiefel, E. I. *Science* **2001**, *291*, 106-109.

25 Herebian, D.; Bothe, E.; Neese, F.; Weyhermueller, T.; Wieghardt, K. *J. Am. Chem. Soc.* **2003**, *125*, 9116-9128 and references therein.

26 Allen, G. C.; Hush, N. S. *Prog. Inorg. Chem.* **1967**, *8*, 357-389.

27 Hush, N. S., *Prog. Inorg. Chem.* **1967**, *8*, 391-444.

28 Robin, M. B.; Day, P. *Adv. Inorg. Chem. Radiochem.* **1967**, *10*, 247-422.

29 Tom, G. M.; Creutz, C.; Taube, H. *J. Am. Chem. Soc.* **1974**, *96*, 7827-7828.

30 Klotz, I. M.; Czerlinski, G. H.; Fiess, H. A. *J. Am. Chem. Soc.* **1958**, *80*, 2920-2923.

31 Day, P.; Smith, D. W. *J. Chem. Soc. A* **1967**, *7,* 1045-1046.

32 Kaim, W.; Klein, A.; Glockle, M. *Acc. Chem. Res.* **2000**, *33*, 755-763.

33 Londergan, C. H.; Kubiak, C. P. *Chem. Eur. J.* **2003**, *9*, 5962-5969.

34 Demadis, K. D.; Hartshorn, C. M.; Meyer, T. J. *Chem. Rev.* **2001**, *101*, 2655-2685.

35 Creutz, C. *Prog. Inorg. Chem.* **1983**, *30*, 1-73.

36 Perkampus, H.-H. *UV-VIS Atlas of Organic Compounds*; VCH Verlagsgesellshaft: Weinheim, 1992.

37 Kohn, W.; Becke, A. D.; Parr, R. G. *J. Phys. Chem.* **1996**, *100*, 12974-12980.

38 Evans, D. F. *J. Chem. Soc.*, **1959**, 2003-2005.

39 Sur, S. K. *J. Magnet. Res.* **1989**, *82*, 169-173.

40 Mizutani, Y.; Kitagawa, T. *Science* **1997**, *278*, 443-446.

41 Kholodenko, Y.; Volk, M.; Gooding, E.; Hochstrasser, R. M. *Chem. Phys.* **2000**, *259*, 71-87.

42 Kadis, J.; Shin, Y.-g. K.; Dulebohn, J. I.; Ward, D. L.; Nocera, D. G. *Inorg. Chem.* **1996**, *35*, 811-817.

43 Lambert, C.; Risko, C.; Coropceanu, V.; Schelter, J.; Amthor, S.; Gruhn, N. E.; Durivage, J. C.; Bredas, J.-L. *J. Am. Chem. Soc.* **2005**, *127*, 8508-8516.

44 Brunschwig, B. S.; Creutz, C.; Sutin, N. *Chem. Soc. Rev.* **2002**, *31*, 168-184.

45 Barbara, P. F.; Meyer, T. J.; Ratner, M. A. *J. Phys. Chem.* **1996**, *100*, 13148-13168.

46 Doorn, S. K.; Dyer, R. B.; Stoutland, P. O.; Woodruff, W. H. *J. Am. Chem. Soc.* **1993**, *115*, 6398-6405.

47 Macpherson, B. P.; Bernhardt, P. V.; Hauser, A.; Pages, S.; Vauthey, E. *Inorg. Chem.* **2005**, *44*, 5530-5536.

48 Weast, R. D., Ed., *Handbook of Chemistry and Physics*; CRC Press: Cleveland, 1974; 55th ed., p. E121.

49 Girerd, J.-J; Journaux, Y. in *Physical Methods in Bioinorganic Chemistry*; Que, L., Jr., Ed.; University Science Books: Sausalito, CA, 2000; p. 324.

50 van Gisbergen, S. J. A.; Kootstra, F.; Schipper, P. R. T.; Gritsenko, O. V.; Snijders, J. G.; Baerends, E. J. *Phys. Rev. A* **1998**, *57*, 2556-2571.

51 Jamorski, C.; Casida, M. E.; Salahub, D. R. *J. Chem. Phys.* **1996**, *104*, 5134-5147.

52 te Velde, G.; Bickelhaupt, F. M.; van Gisbergen, S. J. A.; Fonseca Guerra, C.; Baerends, E. J.; Snijders, J. G.; Ziegler, T. *J. Comput. Chem.* **2001**, *22*, 931-967.

53 Fonseca Guerra, C.; Snijders, J. G.; te Velde, G.; Baerends, E. J. *Theor. Chem. Acc.* **1998**, *99*, 391- 403.

54 van Leeuwen, R.; Baerends, E. J. *Phys. Rev. A* **1994**, *49*, 2421-2431.

55 van Gisbergen, S. J. A.; Snijders, J. G.; Baerends, E. J. *Comput. Phys. Commun.* **1999**, *118*, 119- 138.

56 Becke, A. D. *Phys. Rev. A* **1988**, *38*, 3098-3100.

57 Perdew, J. P.; Chevary, J. A.; Vosko, S. H.; Jackson, K. A.; Pederson, M. R.; Singh, D. J.; Fiolhais, C. *Phys. Rev. B* **1992**, *46*, 6671-6687.

58 Molekel v.4.2/3, Flükiger, P.; Lüthi, H. P.; Portmann, S.; Weber, J., Swiss Center for Scientific Computing, Manno (Switzerland), 2000-2002.

59 Portmann, S.; Lüthi, H. P. *Chimia* **2000**, *54*, 776-770.

60 Hodgkiss, J. M.; Chang, C. C.; Pistorio, B. J.; Nocera, D. G. *Inorg. Chem.* **2003**, *42*, 8270-8277.

## Chapter IV

# Reactivity of porphyrinogen complexes of redox-inactive $d^0$ and $d^{10}$ metal ions

## IV.1. Introduction

That porphyrinogen complexes of alkaline-earth and zinc dications can be prepared in three oxidation states (Chapter II) proves the redox abilities of the tetrapyrrole ligand; it also enables one to study the electronic structures of the macrocycle (Chapter III). Essentially, this transposes the bulk of the work performed on electron transfer series of dithiolene-related complexes[1-4] into the porphyrinogen realm. Application of “non-innocent” ligands in chemistry, however, will require that their metal complexes perform more involved transformations, for instance atom and group transfers. The paucity of such examples in the published literature (to date limited to galactose oxidase mimics,[5-8] an iron diimine complex active towards some organometallic transformations,[9,10] and an oxidative addition to a Zr(IV) center)[11] invites more effort to be spent in the area.

This Chapter is concerned with the small-molecule redox chemistry of reduced $Zn^{2+}$ and $Zr^{IV}$ porphyrinogens. The preparation of *meso*-octabenzylporphyrinogen and the coordination properties of zirconium porphyrinogen are described in its first part. The shorthand notation $L^{4-}$ designates the octamethylporphyrinogen tetraanion, and ${}^{Ph}L^{4-}$ the octabenzyl version of the ligand.

## IV.2. A new porphyrinogen ligand

Octamethylporphyrinogen was selected as the preferred ligand for the study of the fundamental properties of oxidized metal porphyrinogen complexes because of its simplicity and the lack of potentially reactive β-H atoms on the *meso* substituents. Its main drawbacks are its poor crystallinity and the limited solubility of its ionic metal complexes in all but very polar solvents. Therefore, we set out to design a porphyrinogen macrocycle that would overcome those constraints while maintaining the absence of β-hydrogens in the vicinity of the central metal. In order for the condensation reaction to proceed to the cyclic tetramer, the ketone must be sufficiently electrophilic for two pyrroles to react subsequently at the same carbon, and preferably symmetrical in order to prevent the complications associated with the possible formation of several isomers in a mixture. Work from Sessler's group indicates that ketones directly substituted by aryl groups are poor starting materials.[12,13] Cyclic aliphatic ketones, however, have been used successfully,[14,15] and substituted cyclohexanones are reasonable candidates as starting materials for our purposes.

## IV.2.a. From 4-*tert*butylcyclohexanone

The acid-catalyzed reaction between pyrrole and 4-*tert*butylcyclohexanone proceeds in a manner similar to that between pyrrole and acetone, with a strong exothermicity and the precipitation of a white solid. ESI-MS of the isolated product shows the exclusive presence of a compound of mass 813 amu, corresponding to the desired *meso*-tetrakis(3'-*tert*butylpent-1',5'diyl)porphyrinogen. However, its $^1$H NMR indicates that it is a mixture of distinct, non-interconverting products giving rise to sharp peaks. This behavior is indicative of a mixture of stereoisomers: the starting ketone is prochiral, and the precipitation process is not selective, most likely yielding the four diastereomers displayed in Scheme IV.1 in approximately statistical ratios.

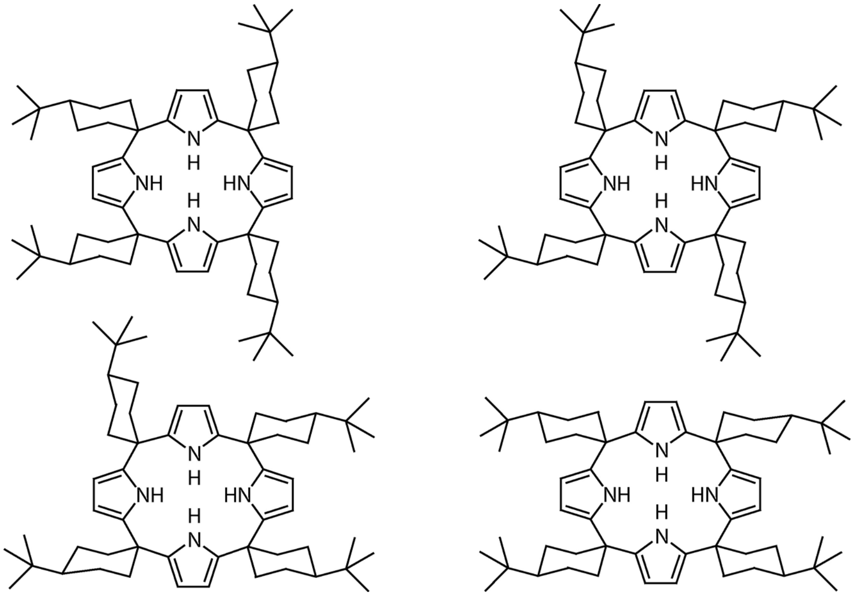

**Scheme IV.1.** Diastereomers of *meso*-tetrakis(3'-tertbutylpentan-1',5'-diyl)porphyrinogen.

## IV.2.b. From 3,3,5,5-tetramethylcyclohexanone

When 4-*tert*butylcyclohexanone is replaced with 3,3,5,5-tetramethylcyclohexanone, the condensation reaction does not occur spontaneously upon addition of the acid catalyst. A short period of heating, however, yields a white precipitate similar in appearance to those obtained in the preparations of octaalkylporphyrinogens. Analysis of the solid indicates that it is composed of a single, non-porphyrinogenic species characterized by a mass / charge ratio $m/z$ = 339.29 and by $^1$H NMR signals at $\delta$ = 8.27 (br, 1H), 6.15 (d, 2H), 5.60 (s, 2H), 2.11 (s, 4H), 1.43 (s, 4H), 1.12 (s, 12H), and 1.04 ppm (s, 12H). Its crystal structure, shown in Figure IV.1, is consistent with the analytical data. The product is 2,5-bis(3′,3′,5′,5′-tetramethylcyclohex-1′-enyl)pyrrole

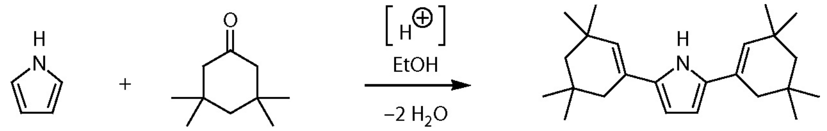

**Scheme IV.2.** Condensation of pyrrole with a bulky ketone.

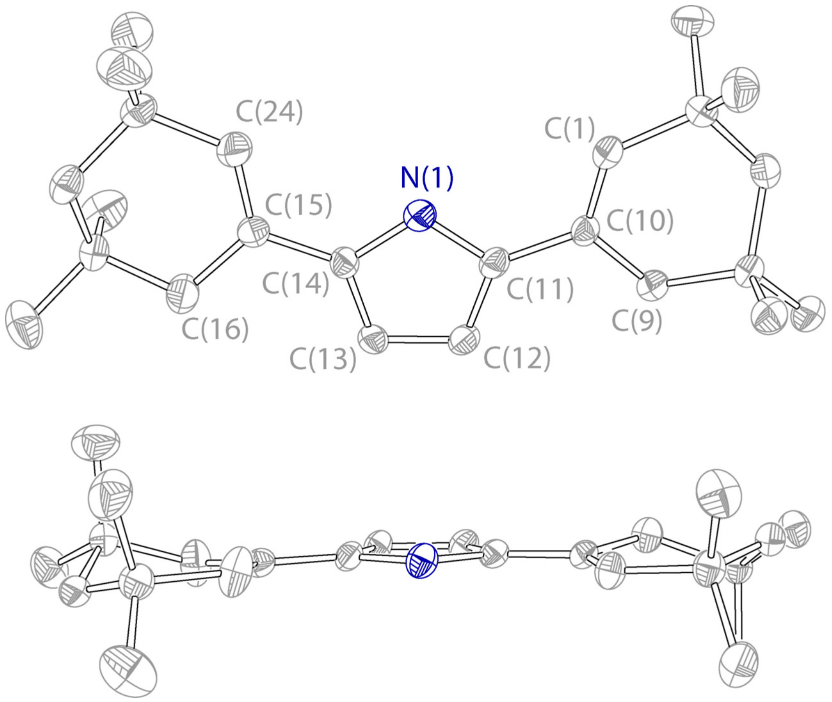

**Figure IV.1.** Crystal structure of 2,5-bis(3′,3′,5′,5′-tetramethylcyclohex-1′-enyl)pyrrole, top and side views. H atoms are omitted. Thermal ellipsoids are drawn at the 50% probability level. Color coding: N, blue; C, gray.

(Scheme IV.2). Thus, steric protection of the ketone at its 3 and 5 positions sufficiently reduces its electrophilic reactivity that after reaction with a first pyrrole, elimination of water becomes favored with respect to further substitution.

**Table IV.1.** Summary of X-ray crystallographic data for 2,5-bis(3′,3′,5′,5′-tetramethylcyclohex-1′-enyl)pyrrole.

| | |
|---|---|
| empirical formula (formula weight) | $C_{24}H_{37}N$ (339.55) |
| $T$ (K) | 100(2) |
| $\lambda$ (Å) | 0.71073 |
| crystal system, space group | Monoclinic, $P2_1/n$ |
| $a$ ; $b$ ; $c$ (Å) | 5.7754(4) ; 23.5817(15) ; 15.4218(10) |
| $\beta$ (deg) | 91.5620(10) |
| $Z$ ; $V$ (Å$^3$) | 4 ; 2099.6(2) |
| crystal size (mm$^3$) | 0.12 × 0.04 × 0.04 |
| abs. coeff. (mm$^{-1}$) | 0.061 |
| $F$(000) | 752 |
| $\theta$ range for data collection | 1.58 to 23.26° |
| limiting indices | $-6 \leq h \leq 6, -25 \leq k \leq 26, -17 \leq \ell \leq 13$ |
| no. of reflns collcd ; no. of ind. reflns ($R_{int}$) | 10159 ; 3029 (0.0889) |
| completeness to $\theta = 23.26°$ | 100.0 % |
| refinement method | Full-matrix least-squares on $F^2$ |
| data / restraints / parameters | 3029 / 0 / 238 |
| $R_1$,[a] $wR_2$[b] ($I > 2\sigma(I)$) | 0.0527, 0.1306 |
| $R_1$,[a] $wR_2$[b] (all data) | 0.0655, 0.1410 |
| GOF[c] on $F^2$ | 1.036 |
| largest diff. peak and hole | 0.434 and −0.269 eÅ$^{-3}$ |

[a] $R_1 = \Sigma||F_o| - |F_c||/\Sigma|F_o|$.
[b] $wR_2 = (\Sigma(w(F_o^2 - F_c^2)^2)/\Sigma(w(F_o^2)^2))^{1/2}$.
[c] $\text{GOF} = (\Sigma\ w(F_o^2 - F_c^2)^2/(n - p))^{1/2}$,
where $n$ is the number of data and $p$ is the number of parameters refined.

**Table IV.2.** Selected bond lengths (Å) for 2,5-bis(3′,3′,5′,5′-tetramethylcyclohex-1′-enyl)pyrrole.

| | | | |
|---|---|---|---|
| N(1)—C(14) | 1.381(3) | C(1)—C(10) | 1.339(3) |
| N(1)—C(11) | 1.384(3) | C(15)—C(24) | 1.344(3) |
| C(11)—C(12) | 1.375(3) | C(9)—C(10) | 1.501(3) |
| C(13)—C(14) | 1.374(3) | C(15)—C(16) | 1.477(3) |
| C(12)—C(13) | 1.405(3) | C(10)—C(11) | 1.462(3) |
| | | C(14)—C(15) | 1.461(3) |

In the crystal structure, the double C=C bond within each cyclic $C_6$ substituent is evident from its shorter bond length ($d_{avg}$(C(15)—C(24), C(10)—C(1)) = 1.34 Å, whereas $d_{avg}$(C(15)—C(16), C(10)—C(9)) = 1.49 Å) and its planarity (obvious in the front view in Figure IV.1), which causes the cyclohexenyls to assume a half-chair conformation. The ene moieties are coplanar with the pyrrole ring, and are oriented *syn* relative to the pyrrolic N.

## IV.2.c. From dibenzylketone

The carbonyl functionality of dibenzylketone is not directly substituted by an aryl, therefore it can be expected to remain sufficiently reactive. Moreover, it is not prochiral and maintains plenty of space for attack of the nucleophile (the pyrrole). The acid-catalyzed reaction of dibenzylketone with pyrrole does not result in exothermicity as expected; instead, it quickly turns a very deep red color indicative of oxidation and oligomerization of pyrrole, which worsens upon heating. It was found, however, that accurate control over the purity of the materials in the reaction mixture allows one to obtain the desired *meso*-octabenzylporphyrinogen, albeit in low yield. The synthesis of octamethylporphyrinogen proceeds to near-quantitative yields without any influence by the presence of air or of brown impurities in the pyrrole starting material. In contrast to this, in the preparation of octabenzylporphyrinogen, the reaction of freshly distilled pyrrole with pure dibenzylketone in degassed methanol under dinitrogen yields 11% of isolable desired product, whereas the yield drops drastically (to 0-4%) as soon as the purity conditions are less optimal.

The crystal structure of octabenzylporphyrinogen, $^{Ph}LH_4$, is displayed in Figure IV.2. In the absence of a hydrogen-bond acceptor host, the porphyrinogen skeleton adopts an alternate (“up-down-up-down”) conformation of the pyrroles. Axial benzyl substituents are folded above and below the macrocycle, whereas equatorial benzyls reach outwards.[a]

---

[a] Substituents pointing in directions approximately perpendicular to the macrocyclic plane and within it are denoted axial and equatorial, respectively.

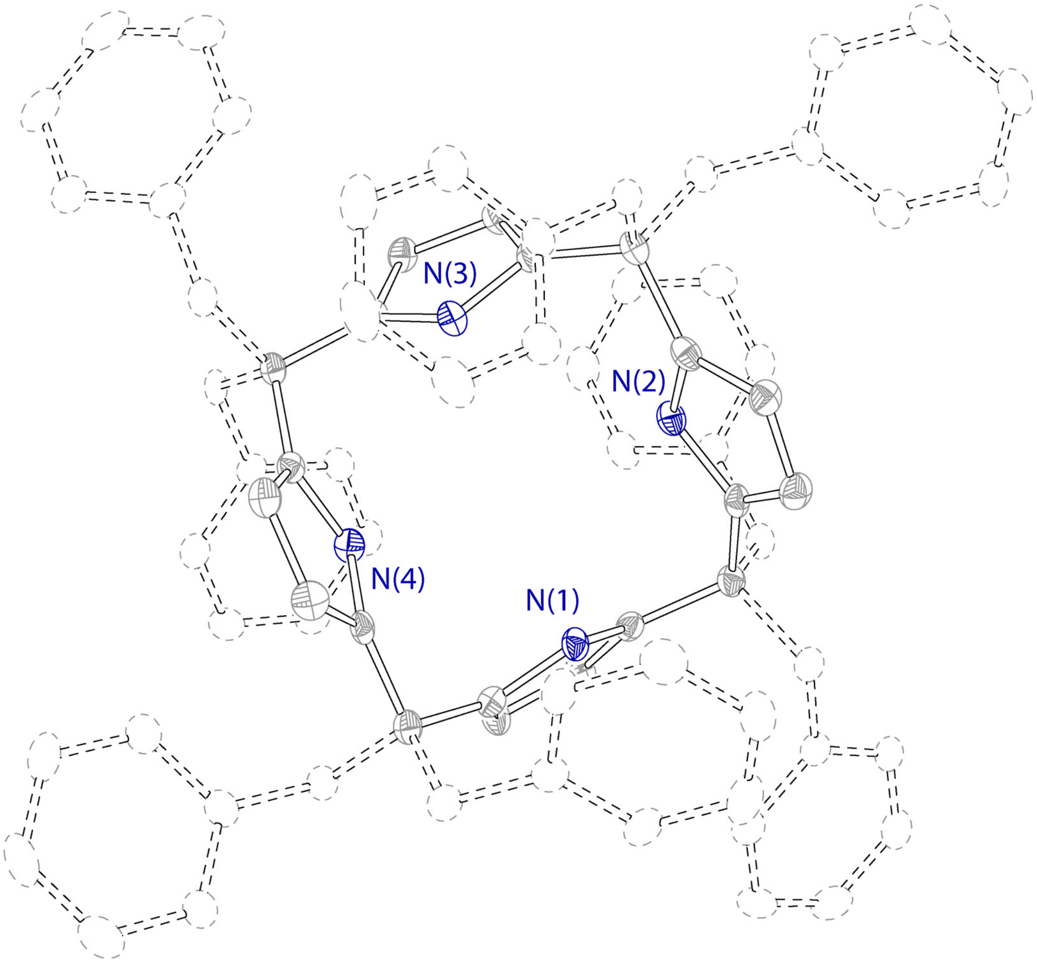

**Figure IV.2.** Crystal structure of octabenzylporphyrinogen, $^{Ph}LH_4$. The porphyrinogen backbone is drawn in full ellipsoids and solid bonds, whereas the *meso* benzyl substituents are in open ellipsoids and dotted bonds. H atoms and lattice toluene solvent molecules are omitted. Thermal ellipsoids are drawn at the 50% probability level. Color coding: N, blue; C, gray.

# IV.3. Zirconium porphyrinogen

## IV.3.a. Coordination chemistry

*Preparation*

Zirconium octaethylporphyrinogen was previously prepared from the reaction of the corresponding tetralithiated ligand with a Zr(IV) halide.[16] However, the ready availability of homoleptic zirconium(IV) amides furnishes a direct route to

**Table IV.3.** Summary of X-ray crystallographic data for *meso*-octabenzylporphyrinogen, $^{Ph}LH_4 \bullet$ 4 PhMe.

| | |
|---|---|
| empirical formula (formula weight) | $C_{104}H_{100}N_4$ (1405.88) |
| $T$ (K) | 100(2) |
| $\lambda$ (Å) | 0.71073 |
| crystal system, space group | Monoclinic, $P2_1/c$ |
| $a$ ; $b$ ; $c$ (Å) | 18.5272(7) ; 23.1094(8) ; 193911(7) |
| $\beta$ (deg) | 107.3970(10) |
| $Z$ ; $V$ (Å$^3$) | 4 ; 7922.6(5) |
| crystal size (mm$^3$) | $0.10 \times 0.08 \times 0.05$ |
| Abs. coeff. (mm$^{-1}$) | 0.067 |
| $F$(000) | 3008 |
| $\theta$ range for data collection | 1.15 to 23.27° |
| limiting indices | $-19 \le h \le 20, -25 \le k \le 14, -21 \le \ell \le 21$ |
| no. of reflns collcd ; no. of ind. reflns ($R_{int}$) | 38509 ; 11382 (0.1011) |
| completeness to $\theta$ = 23.27° | 99.9 % |
| refinement method | Full-matrix least-squares on $F^2$ |
| data / restraints / parameters | 11382 / 0 / 992 |
| $R_1$,[a] $wR_2$[b] ($I > 2\sigma(I)$) | 0.0568, 0.1224 |
| $R_1$,[a] $wR_2$[b] (all data) | 0.1017, 0.1452 |
| GOF[c] on $F^2$ | 1.046 |
| largest diff. peak and hole | 0.330 and −0.341 eÅ$^{-3}$ |

[a] $R_1 = \Sigma||F_o - |F_c||/\Sigma|F_o|$.

[b] $wR_2 = (\Sigma(w(F_o^2 - F_c^2)^2)/\Sigma(w(F_o^2)^2))^{1/2}$.

[c] GOF $= (\Sigma\, w(F_o^2 - F_c^2)^2/(n - p))^{1/2}$, where $n$ is the number of data and $p$ is the number of parameters refined.

zirconium(IV) porphyrinogens from the protonated free ligand. The reaction was found to be unexpectedly slow, only occurring in boiling THF over the time scale of hours. Under similar conditions, tetrakis(dimethylamido)titanium does not react with $LH_4$: overnight heating of the reagents in boiling DME results in no reaction. Both the octamethyl and octabenzyl versions of zirconium(IV) porphyrinogen, $LZr^{IV}(NHMe_2)(THF)$ and $^{Ph}LZr^{IV}(NHMe_2)(THF)$, are obtained from $(Me_2N)_4Zr$ under similar conditions.

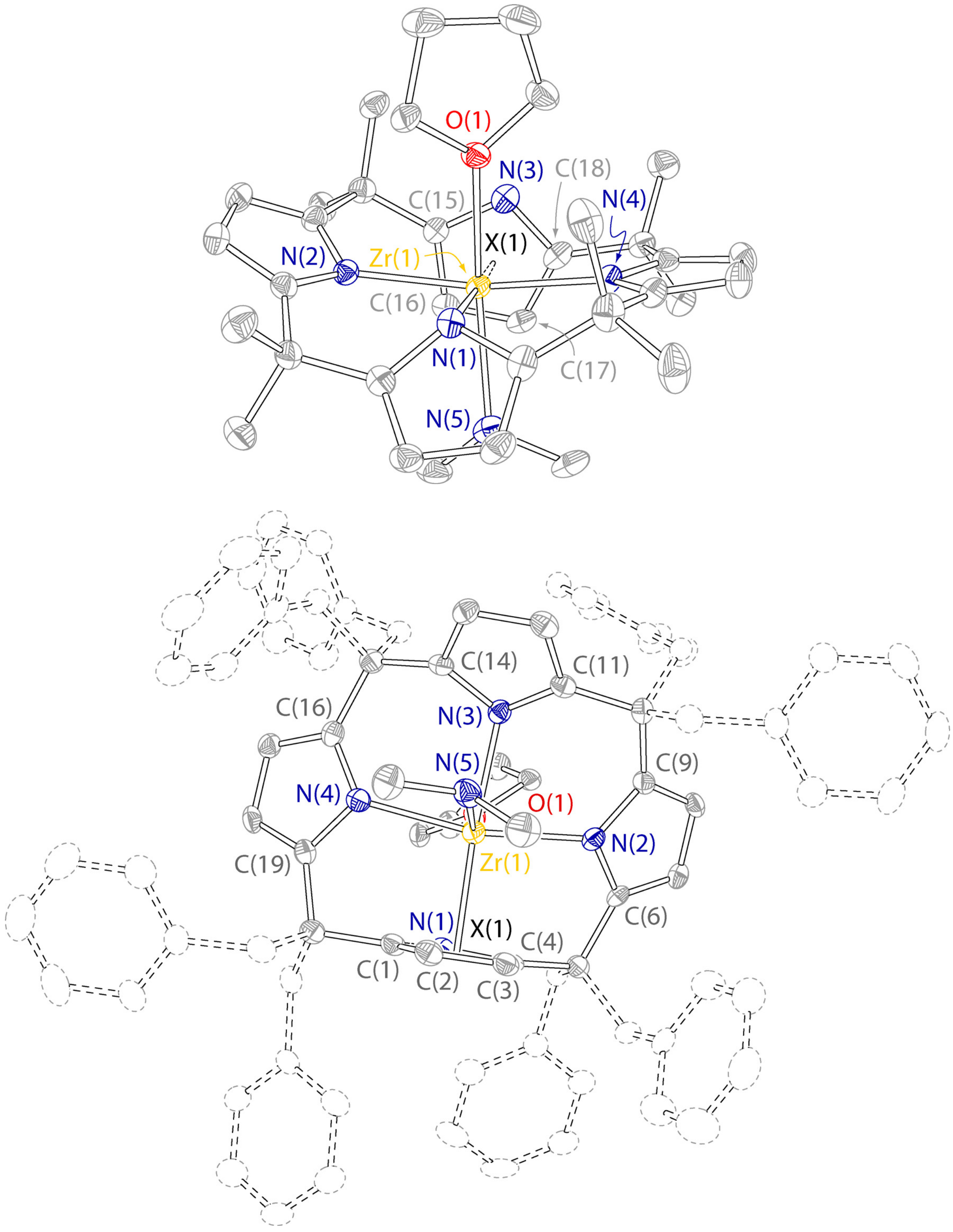
O(1)
N(3)
C(18)
N(4)
C(15)
X(1)
Zr(1)
N(2)
C(16)
N(1)
C(17)
N(5)
C(14)
C(11)
C(16)
N(3)
C(9)
N(5)
O(1)
N(4)
N(2)
Zr(1)
C(19)
C(6)
N(1)
X(1)
C(4)
C(1)
C(2)
C(3)

**Figure IV.3.** Crystal structures of Zr(IV) octamethyl- and octabenzylporphyrinogen, $\mathrm{LZr^{IV}(NHMe_2)(THF)}$ (top) and $\mathrm{^{Ph}LZr^{IV}(NHMe_2)(THF)}$ • THF (bottom). H atoms and uncoordinated solvents are omitted. Thermal ellipsoids are drawn at the 50% probability level; *meso* benzyl substituents are in open ellipsoids and dotted bonds. Color coding: Zr, yellow; N, blue; O, red; C, gray.

Their solid-state structures are displayed in Figure IV.3 and their crystallographic data and selected metric parameters are compared in Tables IV.4 and IV.5. The inorganic core is very similar in both structures. Zr assumes a pseudo-octahedral coordination by three $\eta^1$ pyrrole nitrogens, one $\eta^5$ pyrrole (its centroid considered as a ligand for geometry considerations), a dimethylamine and a THF solvent molecule. Both axial ligands are tightly bound, because they are not removed by recrystallization or prolonged application of vacuum. They are somewhat labile, however, as evidenced by their broadened $^1$H NMR peaks. The most dramatic feature of the structures is the $\eta^5$, "cyclopentadienyl-type" coordination of one pyrrole to the strongly Lewis acidic Zr center. The pyrrole plane is almost perfectly perpendicular to the Zr—X axis (where X designates the centroid), with Zr–X–N and Zr–X–C angles comprised between 88 and 92° and between 83 and 95° in the methyl and benzyl versions, respectively. The strain imposed by the $\eta^5$ pyrrole on the macrocycle translates into marked deviations of the other three pyrroles from their usual

**Table IV.4.** Comparison of selected metric parameters for the octamethyl and octabenzyl porphyrinogens of zirconium(IV), $LZr^{IV}(NHMe_2)(THF)$ and $^{Ph}LZr^{IV}(NHMe_2)(THF) \cdot THF$.

| $LZr^{IV}(NHMe_2)(THF)$ | | $^{Ph}LZr^{IV}(NHMe_2)(THF) \cdot THF$ | |
|---|---|---|---|
| Distances / Å | | | |
| Zr(1)—X(1) | 2.247 | Zr(1)—X(1) | 2.239 |
| Zr(1)—N(3) | 2.485(2) | Zr(1)—N(1) | 2.412(3) |
| Zr(1)—C(15) | 2.495(3) | Zr(1)—C(1) | 2.500(4) |
| Zr(1)—C(16) | 2.538(3) | Zr(1)—C(4) | 2.502(4) |
| Zr(1)—C(17) | 2.566(3) | Zr(1)—C(3) | 2.614(4) |
| Zr(1)—C(18) | 2.543(3) | Zr(1)—C(2) | 2.626(4) |
| Zr(1)—N(4) | 2.211(2) | Zr(1)—N(4) | 2.197(3) |
| Zr(1)—N(2) | 2.223(2) | Zr(1)—N(2) | 2.205(3) |
| Zr(1)—N(1) | 2.247(2) | Zr(1)—N(3) | 2.231(3) |
| Zr(1)—N(5) | 2.394(2) | Zr(1)—N(5) | 2.386(4) |
| Zr(1)—O(1) | 2.3059(18) | Zr(1)—O(1) | 2.320(3) |
| Angles / deg | | | |
| N(1)–Zr(1)–N(2) | 80.69(8) | N(3)–Zr(1)–N(2) | 80.92(12) |
| N(1)–Zr(1)–N(3) | 155.52(8) | N(3)–Zr(1)–N(1) | 154.80(12) |
| N(1)–Zr(1)–N(4) | 87.45(8) | N(3)–Zr(1)–N(4) | 86.33(12) |
| N(1)–Zr(1)–N(5) | 77.48(9) | N(3)–Zr(1)–N(5) | 77.38(12) |
| N(1)–Zr(1)–O(1) | 81.80(7) | N(3)–Zr(1)–O(1) | 79.66(11) |

**Table IV.5.** Summary of X-ray crystallographic data for the octamethyl and octabenzyl porphyrinogens of zirconium(IV), $LZr^{IV}(NHMe_2)(THF)$ and $^{Ph}LZr^{IV}(NHMe_2)(THF) \cdot THF$.

| | $LZr^{IV}(NHMe_2)(THF)$ | $^{Ph}LZr^{IV}(NHMe_2)(THF) \cdot THF$ |
|---|---|---|
| empirical formula | $C_{34}H_{47}N_5OZr$ | $C_{86}H_{87}N_5O_2Zr$ |
| formula weight | 632.99 | 1313.83 |
| $T$ (K) | 100(2) | 100(2) |
| $\lambda$ (Å) | 0.71073 | 0.71073 |
| crystal system, space group | Monoclinic, $C2/c$ | Monoclinic, $P2_1/c$ |
| $a$ (Å) | 19.8193(11) | 21.932(5) |
| $b$ (Å) | 17.7496(10) | 10.945(2) |
| $c$ (Å) | 18.6897(11) | 28.308(6) |
| $\beta$ (deg) | 109.9060(10) | 97.648(5) |
| $Z$ ; $V$ (Å$^3$) | 8 ; 6181.9(6) | 4 ; 6735(2) |
| crystal size (mm$^3$) | $0.08 \times 0.05 \times 0.05$ | $0.50 \times 0.40 \times 0.05$ |
| Abs. coeff. (mm$^{-1}$) | 0.391 | 0.218 |
| $F(000)$ | 2672 | 2776 |
| $\theta$ range for data collection | 1.58 to 23.27° | 0.94 to 23.35° |
| limiting indices | $-21 \leq h \leq 22$ | $-24 \leq h \leq 24$ |
| | $-17 \leq k \leq 19$ | $-12 \leq k \leq 12$ |
| | $-20 \leq \ell \leq 20$ | $-31 \leq \ell \leq 31$ |
| no. of reflns collcd | 14952 | 72744 |
| no. of ind. reflns ($R_{int}$) | 4449 (0.0584) | 9733 (0.1402) |
| completeness to $\theta_{max}$ | 99.9 % | 99.4 % |
| refinement method | Full-matrix least-squares on $F^2$ | |
| data / restraints / parameters | 4449 / 0 / 558 | 9733 / 10 / 850 |
| $R_1$,[a] $wR_2$[b] ($I > 2\sigma(I)$) | 0.0319, 0.0743 | 0.0472, 0.0959 |
| $R_1$,[a] $wR_2$[b] (all data) | 0.0411, 0.0791 | 0.0949, 0.1141 |
| GOF[c] on $F^2$ | 1.041 | 0.904 |
| largest diff. peak and hole | 0.525 and −0.254 eÅ$^{-3}$ | 0.708 and −0.418 eÅ$^{-3}$ |

[a] $R_1 = \Sigma||F_o - |F_c||/\Sigma|F_o|$.

[b] $wR_2 = (\Sigma(w(F_o^2 - F_c^2)^2)/\Sigma(w(F_o^2)^2))^{1/2}$.

[c] $GOF = (\Sigma\, w(F_o^2 - F_c^2)^2/(n - p))^{1/2}$, where $n$ is the number of data and $p$ is the number of parameters refined.

"horizontal" geometry (that is, a geometry in which the pyrrole plane contains the Zr—N axis): the plane of the pyrrole *trans* to the $\eta^5$ pyrrole deviates from "horizontality" by 48 and 46°, respectively, in the methyl and benzyl derivatives. In contrast to this, in Floriani's octaethylporphyrinogen zirconium-THF, the absence of a second axial ligand causes two pyrroles to bind $\eta^5$ to Zr(IV), which relieves the strain on the macrocycle.[16]

*Reaction with water*

Crystals grown from a solution of LZr$^{IV}$(NHMe$_2$)(THF) in wet solvents yielded the adduct between one water molecule and two zirconium porphyrinogen entities, [HLZr$^{IV}$]$_2$O (Figure IV.4 and Tables IV.6 and IV.7). In this compound, the water molecule has been cleaved to its acid-base components, an oxo, which coordinates in a bridging fashion between two Zr centers, and two protons, which protonate the $\alpha$ position of two porphyrinogen pyrroles. $\alpha$-Protonation is established unambiguously by the pyramidalization that distinguishes one $\alpha$-C from the seven other, planar $\alpha$ positions within the same macrocycle. Bond lengths within the protonated pyrroles are also affected, as witnessed by lengthened C$^{\alpha}$—C$^{\beta}$ distances: for example, C(8)—C(9) = 1.482(4) Å, whereas in the adjacent pyrrole C(1)—C(2) = 1.365(4). The macrocycle

**Table IV.6.** Summary of X-ray crystallographic data for [HLZr$^{IV}$]$_2$O.

| | |
|---|---|
| empirical formula (formula weight) | $C_{56}H_{66}N_8OZr_2$ (1049.61) |
| $T$ (K) | 100(2) |
| $\lambda$ (Å) | 0.71073 |
| crystal system, space group | Monoclinic, *C*2/*c* |
| *a* ; *b* ; *c* (Å) | 42.064(2) ; 12.5032(6) ; 19.0221(9) |
| $\beta$ (deg) | 101.0830(10) |
| *Z* ; *V* (Å$^3$) | 8 ; 9817.9(8) |
| crystal size (mm$^3$) | 0.12 × 0.09 × 0.04 |
| Abs. coeff. (mm$^{-1}$) | 0.474 |
| *F*(000) | 4368 |
| $\theta$ range for data collection | 0.99 to 23.27° |
| limiting indices | $-41 \le h \le 46$, $-11 \le k \le 13$, $-21 \le \ell \le 19$ |
| no. of reflns collcd ; no. of ind. reflns ($R_{int}$) | 23488 ; 7051 (0.0629) |
| completeness to $\theta$ = 23.27° | 99.8 % |
| refinement method | Full-matrix least-squares on $F^2$ |
| data / restraints / parameters | 7051 / 0 / 620 |
| $R_1$,[a] $wR_2$[b] ($I > 2\sigma(I)$) | 0.0310, 0.0735 |
| $R_1$,[a] $wR_2$[b] (all data) | 0.0377, 0.0774 |
| GOF[c] on $F^2$ | 1.051 |
| largest diff. peak and hole | 0.472 and −0.339 eÅ$^{-3}$ |

[a] $R_1 = \Sigma||F_o| - |F_c||/\Sigma|F_o|$.

[b] $wR_2 = (\Sigma(w(F_o^2 - F_c^2)^2)/\Sigma(w(F_o^2)^2))^{1/2}$.

[c] $GOF = (\Sigma\, w(F_o^2 - F_c^2)^2/(n - p))^{1/2}$,
where *n* is the number of data and *p* is the number of parameters refined.

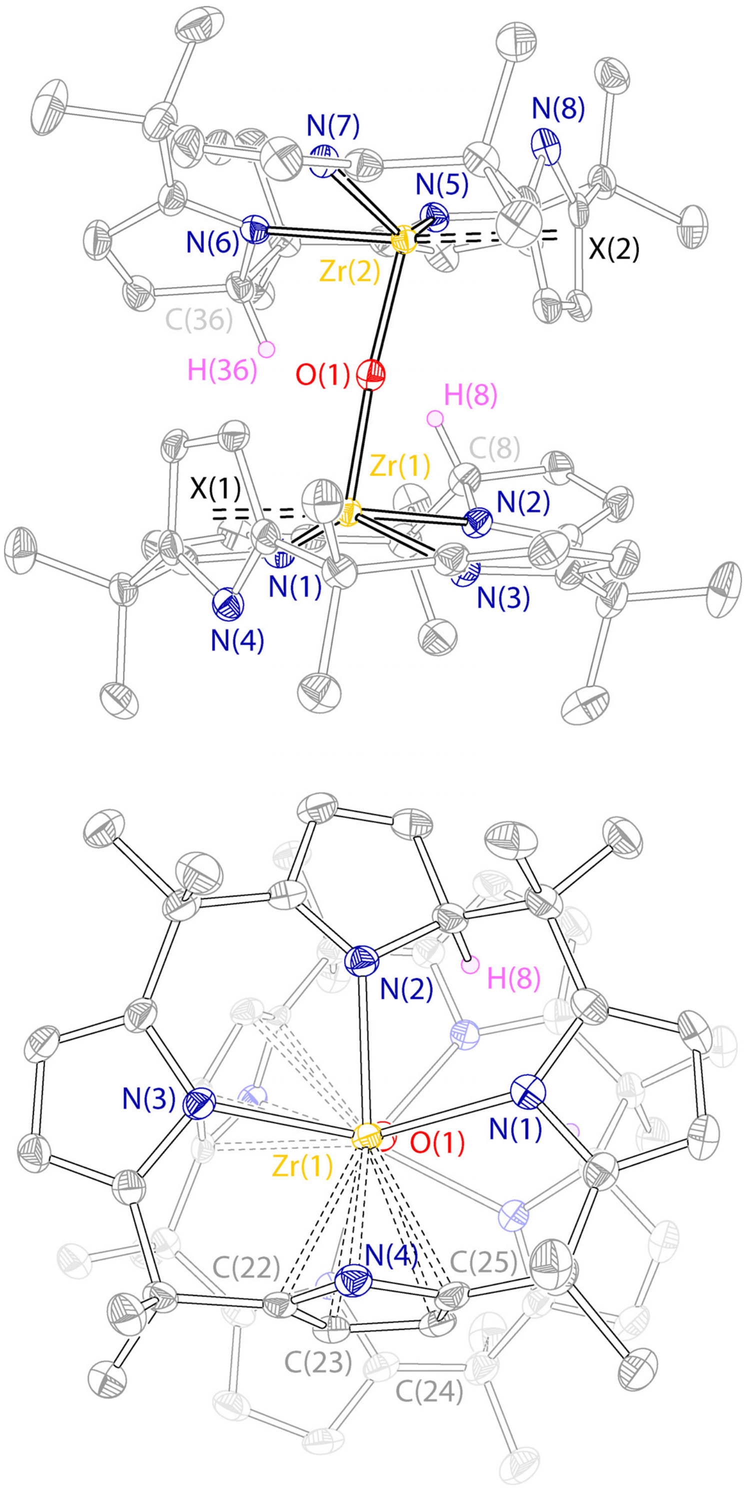
N(7)
N(8)
N(5)
N(6)
Zr(2)
X(2)
C(36)
H(36)
O(1)
H(8)
C(8)
Zr(1)
X(1)
N(2)
N(1)
N(3)
N(4)
N(2)
H(8)
N(3)
N(1)
O(1)
Zr(1)
C(22)
N(4)
C(25)
C(23)
C(24)

**Figure IV.4.** Crystal structure of $[\mathrm{HLZr^{IV}}]_2\mathrm{O}$, side and top views. For clarity, the bonds to Zr are bolded in the side view, and one porphyrinogen is drawn in faded colors in the top view. H atoms are omitted except for the protons at $C^{\alpha}$. Thermal ellipsoids are drawn at the 50% probability level. Color coding: Zr, yellow; N, blue; O, red; C, gray; H, pink. X labels correspond to the centroids of the $\eta^5$ pyrroles. $L^{4-}$ = *meso*-octamethylporphyrinogen.

maintains a coordination geometry not unlike that observed in the absence of water, with one $\eta^5$ pyrrole *trans* to the protonated pyrrole and three $\eta^1$ pyrroles, all three of which display a tilt relative to the Zr—N axis. Unlike in $LZr^{IV}(NHMe_2)(THF)$, however, the three coordinating N atoms and the centroid X do not define a plane; instead, the nitrogens of the pyrroles flanking the $\eta^5$ pyrrole lie above the roughly straight X—Zr—N axis. Thus, with the loss of the axial ligand *trans* to the oxo, the NNNXO coordination polyhedron around Zr is best described as a trigonal bipyramid, with the $\eta^5$ pyrrole and the protonated pyrrole as the axial ligands (N(2)–Zr(1)–X(1) = 176°), and the remaining pyrroles occupying the equatorial plane along with the oxo, with angles O(1)–Zr(1)–N(3) = 108°, O(1)–Zr(1)–N(1) = 103°, and N(3)–Zr(1)–N(1) = 139°. The μ-oxo bridge deviates from linearity slightly, with Zr(1)–O(1)–Zr(2) = 169°. Relative to the Zr···Zr axis, the porphyrinogens are staggered, with a 42° dihedral angle for

**Table IV.7.** Selected metric parameters for $[HLZr^{IV}]_2O$.

| Distances / Å | | | |
|---|---|---|---|
| Zr(1)—O(1) | 1.9362(18) | Zr(2)—O(1) | 1.9363(18) |
| Zr(1)—N(3) | 2.221(2) | Zr(2)—N(7) | 2.218(2) |
| Zr(1)—N(1) | 2.228(2) | Zr(2)—N(5) | 2.222(2) |
| Zr(1)—N(2) | 2.315(2) | Zr(2)—N(6) | 2.304(2) |
| Zr(1)—N(4) | 2.382(2) | Zr(2)—N(8) | 2.405(2) |
| Zr(1)—C(22) | 2.477(3) | Zr(2)—C(53) | 2.466(3) |
| Zr(1)—C(25) | 2.481(3) | Zr(2)—C(50) | 2.481(3) |
| Zr(1)—C(24) | 2.609(3) | Zr(2)—C(52) | 2.581(3) |
| Zr(1)—C(23) | 2.621(3) | Zr(2)—C(51) | 2.604(3) |
| Zr(1)—X(1) | 2.218 | Zr(2)—X(2) | 2.212 Å |

| Angles / deg | | | |
|---|---|---|---|
| Zr(1)–O(1)–Zr(2) | 169.17(11) | | |
| O(1)–Zr(1)–N(3) | 107.50(8) | O(1)–Zr(2)–N(7) | 107.00(8) |
| O(1)–Zr(1)–N(1) | 103.01(8) | O(1)–Zr(2)–N(5) | 104.29(8) |
| N(3)–Zr(1)–N(1) | 139.44(8) | N(7)–Zr(2)–N(5) | 138.51(8) |
| O(1)–Zr(1)–N(2) | 81.90(8) | O(1)–Zr(2)–N(6) | 82.16(7) |
| N(3)–Zr(1)–N(2) | 79.02(8) | N(7)–Zr(2)–N(6) | 79.75(8) |
| N(1)–Zr(1)–N(2) | 79.53(8) | N(5)–Zr(2)–N(6) | 78.25(8) |
| O(1)–Zr(1)–X(1) | 102.5 | O(1)–Zr(2)–X(2) | 103.0 |
| N(1)–Zr(1)–X(1) | 99.3 | N(5)–Zr(2)–X(2) | 100.1 |
| N(3)–Zr(1)–X(1) | 99.5 | N(7)–Zr(2)–X(2) | 98.6 |
| N(2)–Zr(1)–X(1) | 175.6 | N(6)–Zr(2)–X(2) | 174.8 |

N(4)–Zr(1)···Zr(2)–N(9).Thus, $LZr^{IV}$ can be considered as a bifunctional "carrier" of $H_2O$ in organic medium (in the form $(HLZr^{IV})_2O$). Octaethylporphyrinogen Zr(IV) has been shown to behave as such a carrier for NaH, KH and LiR (R = Me, tBu) — in the form of a dimer, a tetramer and a monomer, respectively.[17,18] The difference between the two cases is in the nature of the cationic entity and its bonding mode to the pyrroles. The $H^+$ in $(HLZr^{IV})_2O$ is σ-bonded to an α-C, whereas $Li^+$, $Na^+$ and $K^+$ in the octaethylporphyrinogen complexes require $\eta^5$ coordination to a pyrrole.

## IV.3.b. Redox chemistry

Exposure of $LZr^{IV}(NHMe_2)(THF)$ to air, in the solid state and in solution, results in decomposition. So do its reactions with stoichiometric or excess $^1O_2$[b] or $^3O_2$ (in the presence or absence of $Me_3SiCl$), with $Me_3NO$, with $XeF_2$ and with $PhICl_2$. However, upon addition of $Me_3NO$ to a mixture of $LZr^{IV}(NHMe_2)(THF)$ and $Me_3SnCl$ in ethereal solvent, a pink-red mixture is obtained which strongly fluoresces in solution at room temperature (Figure IV.5). The excitation spectrum shows two vibronic bands within the electronic envelope, with a frequency of approximately $\nu = 1100\ cm^{-1}$ in the electronic excited state; the lack of vibronic structure in the emission spectrum indicates that the energy of the corresponding vibrational mode is even higher in the ground state. A very small Stokes shift of 12 nm ($350\ cm^{-1}$) is apparent, similar to those observed for difluoroboron-dipyrromethene dyes in various solvents[19] and an order of magnitude smaller than those of a variety of metalloporphyrins.[20] These characteristics indicate that the emissive species is structurally rigid, with insignificant geometric rearrangement upon photoexcitation — in other words, it is not a porphyrinogen. Most likely, the porphyrinogen skeleton has been cleaved by electrophilic attack at the sensitive α-C to yield dipyrromethane-type structures, as observed by Floriani in the oxygenation of octaethyporphyrinogen Zr(IV) by benzaldehyde.[21]

---

[b] Obtained *in situ* from $^3O_2$ in the presence of irradiated anthracene sensitizer.

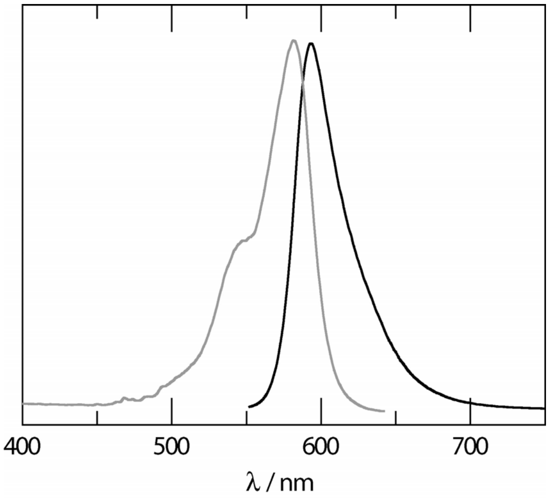

**Figure IV.5.** Fluorescence in toluene solution of an oxidation product of $LZr^{IV}(NHMe_2)(THF)$ by $Me_3NO$ in the presence of $Me_3SnCl$. Black, emission spectrum upon excitation at 545 nm; gray, excitation spectrum for emission at 650 nm. The signal is on an arbitrary scale. $L^{4-}$ = *meso*-octamethylporphyrinogen.

In stark contrast to the decomposition of zirconium(IV) octamethylporphyrinogen $LZr^{IV}(NHMe_2)(THF)$ in air to a brown solid, the octabenzyl version $^{Ph}LZr^{IV}(NHMe_2)(THF)$ immediately turns to an intense red color upon exposure to air, both as a solid and in solution. The same color is obtained under more controlled conditions in the reaction of $^{Ph}LZr^{IV}(NHMe_2)(THF)$ with a stoichiometric amount of $O_2$ or $XeF_2$.[c] However, upon isolation form the crude reaction mixture, the red product is slowly converted to an orange and/or brown color, most likely indicative of uncontrolled decomposition. As in the above paragraphs, this behavior is to be attributed most likely to partial cleavage of the porphyrinogen macrocycle, a process that is assisted by the very oxo- and halophilic Zr(IV) center and occurs in consecutive steps that are not easily separated. Attempts to crystallize the product directly from the reaction mixture yielded crystals that diffracted X-rays weakly.

---

[c] Neither $Zr(NMe_2)_4$ nor $^{Ph}LH_4$ give rise to any hue of red when exposed to either $O_2$ or $XeF_2$.

## IV.4. Reaction of zinc porphyrinogen with $CO_2$

Exposure of a colorless acetonitrile or THF solution of $Li_2(solv)_x$ [LZn] to a $CO_2$ atmosphere causes the solution to turn red immediately. The UV-vis absorption spectrum in THF shows a broad visible band with $\lambda_{max} = 495$ nm. The IR spectrum does not display any signal clearly indicative of free CO (2140 cm$^{-1}$), $CO_3^{2-}$ (1450 cm$^{-1}$), or $H_2CO$ (1740, 1500 and 1170 cm$^{-1}$); the most conspicuous bands that appear upon reaction with $CO_2$ are at 3344, 1639 and 1622 cm$^{-1}$ (assignable to C=C and C=N stretches), 1261 and 804 cm$^{-1}$. The product eluded structural characterization.

From the very limited amount of experimental evidence available, it is clear that *(a)* $CO_2$ reacts with $Li_2$ [LZn], *(b)* the $[LZn]^{2-}$ unit is oxidized to a species containing the mixed-valent ligand $L^{\Delta 2-}$, but not the neutral [$L^{\Delta}$Zn], and *(c)* deoxygenation of $CO_2$ to CO does not occur. Thus, the most likely hypothesis is that two $CO_2$ molecules are reduced and coupled by $[LZn]^{2-}$ to yield the oxalate dianion, $C_2O_4^{2-}$. Precedents for well-defined $CO_2$ reduction by non-organometallic molecular species include its conversion to CO by “iron(0) porphyrins” ($E \le -1.5$ V),[22] to formate ($HCO_2^-$) by a neutral $Ir_2^0$ core held by bridging bis(isocyanato) ligands ($E < -1.3$ V),[23] to oxalate by two equivalents of a bis(cyclopentadienyl)samarium(II) solvate ($E \approx -2$ V),[24] to oxalate by a formally “Ni(I)-macrocycle” anion ($E \le -2$ V),[25] to oxalate by two equivalents of a Cu(I)-macrocycle cation,[26] and to a coordinated and labile “$CO_2^{2-}$“ dianion by a “Co(I) salen”.[27,28] This list calls for two remarks. Firstly, $CO_2$ is usually reduced only by thermodynamically very strong reducing agents, with the notable exception of the Cu(I) system, whereas the $CO_{2(g)}$ / $H_2C_2O_4$ redox couple is at a much more reasonable −0.49 V in standard acidic aqueous conditions.[29] Secondly, the same ambiguity concerning the validity of very low metal oxidation states appears in most cases: porphyrin ligands are well known to be reduced at potentials $E \le -1$ V,[30] the physical ground state of the formal Ni(I) complex of a conjugated macrocycle might well be Ni(II)-ligand radical anion, and the possibility of reducing $M^{II}$-salen complexes to $M^{II}$(salen$^{\bullet -}$) instead of $[M^{I}(salen)]^-$ has been established.[31] Therefore, the hypothesis that the $CO_2$ reduction might be in fact effected by, respectively, the Fe(II) complex of a direduced porphyrin, the Ni(II) complex of a reduced radical macrocycle, and the Co(II) complex of a reduced salen radical,[d] is appealing.

In contrast to the majority of the above examples of $CO_2$ reduction, $Li_2$ [LZn] is a very mild reducing agent (E = +0.21 V), therefore its reaction with $CO_2$ is of relevance to efforts towards the reduction of $CO_2$ at low overpotentials. In mechanistic terms, an intriguing coincidence is found between zinc porphyrinogen and several established $CO_2$-reducing molecular systems (mentioned in the above paragraph) that are likely to feature a reduced macrocyclic ligand: it might suggest that outer-sphere electron transfer from the metal complex reductant to yield $(CO_2)^{\bullet -}$, as opposed to coordination of $CO_2$ to the transition metal ion, is the more favorable first step towards the eventual reduction of $CO_2$.

## IV.5. Conclusions

Zinc and zirconium(IV) porphyrinogen react with redox agents varying in their thermodynamic oxidizing power from $CO_2$ to $XeF_2$. However, in no case was the oxidized metal-porphyrinogen product structurally characterized, and it is more than likely that in most instances the compound initially formed further decays, either *via* radical pathways back to $LH_4$ or $^{Ph}LH_4$, or intramolecularly resulting in the eventual cleavage of the macrocycle. Such behavior is attributed to the poor stability of the "delta" C—C bond that appears upon oxidation with respect to the triplet state in which the bond is broken and two unpaired electrons are delocalized over all four pyrroles (Chapter III).

There is, however, unambiguous evidence that *(a)* the reduced porphyrinogen ligand is able to function as a redox reservoir in reactions involving the interaction of small molecules with the metal, and *(b)* it also maintains acid-base properties. The latter quality can potentially be exploited when it comes to binding several substrates to be further reacted together (see Chapter VIII). It also complicates matters in the sense that the ligand can be attacked instead of the metal center by agents meant for the latter — for example, in the reaction of $LZr^{IV}$ with $XeF_2$, one cannot exclude the possibility of C—F bonds being formed in place of the more thermodynamically favorable $Zr^{IV}$—F bonds.

---

[d] In the salen system, this hypothesis is substantiated by the disappearance of the IR C=N stretches as well as the short Co—N bonds and somewhat long C—N bonds mentioned for M'[(salen)Co], M' = Li, Na.[27,28]

The multifunctional nature of metal-porphyrinogen complexes opens up avenues for the development of novel reaction pathways, but the increase in complexity that it represents means that a challenge needs to be addressed: the challenge is to *control* the site attacked by a given reagent and the nature of its reaction.

## IV.6. Experimental section

### IV.6.a. Synthesis

*Materials and analyses*

All compounds were handled, reactions were performed, and analytical samples were prepared in inert atmosphere using standard Schlenk, dry-box and vacuum-line techniques. Solvents were purchased from VWR Scientific Products and purified using a Braun solvent purification system or using standard solvent purification techniques.[32] Deuterated solvents were purchased from Cambridge Isotope Laboratories, degassed, dried and distilled by procedures similar to those used for non-isotopically enriched solvents. Reagents were purchased from Aldrich or Strem and used as received. Elemental analyses were conducted at H. Kolbe Mikroanalytisches Laboratorium (Mühlheim a. d. Ruhr, Germany). $^1$H-NMR spectra were recorded at the MIT Department of Chemistry Instrumentation Facility (DCIF) on a Varian Inova-500 spectrometer, a Bruker Avance–400 or a Bruker Avance–600. $^1$H NMR chemical shifts are quoted in ppm relative to tetramethylsilane and spectra have been internally calibrated to the monoprotio impurity of the deuterated solvent. ESI-MS was performed at the MIT DCIF on a Bruker Daltonics APEX-IV 4.7 Tesla Fourier Transform Mass Spectrometer.

*Synthesis of* meso-*tetrakis(3′-*tert*butylpent-1,5-diyl)porphyrinogen, isomeric mixture*

Samples of 4-*tert*butylcyclohexanone (3.06 g, 19.8 mmol) and pyrrole (1.33 g, 19.8 mmol) were dissolved in 30 mL of EtOH. $MeSO_3H$ (0.1 mL) was added, which caused the solution to boil violently for 5 min. After cooling, a precipitate was isolated by filtration and dried *in vacuo* to yield 2.55 g (63%) of white powder. $^1H$ NMR of the product in $CDCl_3$ and in $C_6D_6$ showed the presence of several non-interconverting species. (+)-ESI-MS proved that the mixture was composed of different isomers of the same single mass: *m/z* = 835.6599, 813.6772 (calcd for $[M+Na]^+$ 835.6593, for $[M+H]^+$ 813.6774).

*Synthesis of 2,5,-bis(3′,3′,5′,5′-tetramethylcyclohex-1′-enyl)pyrrole*

Samples of 3,3,5,5-tetramethylcyclohexanone (8.91 g, 57.8 mmol) and pyrrole (3.88 g, 57.8 mmol) were dissolved in 40 mL of EtOH. $MeSO_3H$ (0.5 mL) was added and the solution was refluxed for 90 min. After cooling, the reaction mixture was filtered to isolate the precipitate from the red supernatant. After rinsing with fresh EtOH and drying *in vacuo*, 4.4 g (13 mmol, 49%) of off-white pink powder were obtained. The solid was recrystallized from toluene / EtOH to yield a white, light, fibrous solid. $^1H$ NMR (500 MHz, $CDCl_3$): δ/ppm = 8.27 (br s, 1H, NH), 6.15 (d, 2.5 Hz, 2H, pyrrole β), 5.60 (s, 2H, =CH–), 2.11 (s, 4H, $-CH_2-$), 1.43 (s, 4H, $-CH_2-$), 1.12 (s, 12H, $-CH_3$), 1.04 (s, 12H, $-CH_3$). $^{13}C$ NMR (126 MHz, $CDCl_3$): δ = 134.29, 128.03, 125.81, 106.86, 50.52, 40.42, 33.53, 32.59, 31.25, 30.73. Anal. Calcd for $C_{24}H_{37}N$: C, 84.89; H, 10.98; N, 4.13. Found: C, 84.69; H, 11.05; N, 4.08. (+)-ESI-MS: *m/z* = 339.29 (calcd 339.29).

*Synthesis of* meso-*octabenzylporphyrinogen,* $^{Ph}LH_4$

Pyrrole was distilled under a reduced pressure of $N_2$ prior to the reaction and stored under vacuum. Pyrrole (4.70 g, 70.1 mmol) was then dissolved in 30 mL of MeOH and the solution was degassed and maintained under $N_2$. Dibenzylketone (14.74 g, 70.1 mmol) was added and the mixture was gently heated until it was completely dissolved. $MeSO_3H$ (0.3 mL) was added and the clear solution was refluxed for 12 hr. After cooling, the system was opened to air and a slightly orange supernatant was separated from a solid sticking to the walls of the flasks. The solid was redissolved in a minimum amount of boiling toluene and crystallized by addition of MeCN then cooling, to yield 2.0 g (11%) of a white crystalline solid after drying *in vacuo*. $^1$H NMR (400 MHz, $CDCl_3$): δ/ppm = 7.24 to 7.19 (m, 24H, *m*- and *p*-phenyl), 6.85 (dd, 7.4 and 1.5 Hz, 16H, *o*-phenyl), 6.25 (br t, 4 Hz, NH), 5.64 (d, 2.7 Hz, 8H, pyrrole), 2.91 (q, 12.5 Hz, 16H, $-CH_2-$). (+)-ESI-MS: *m/z* = 1059.5413, 1037.5524 (calcd for $[M+Na]^+$ 1059.5341, for $[M+H]^+$ 1037.5522).

*Synthesis of $LZr^{IV}(NHMe_2)(THF)$*

Samples of $Zr(NMe_2)_4$ (0.99 g, 3.7 mmol) and $LH_4$ (1.59 g, 3.7 mmol) were dissolved in 15 mL of THF and refluxed for 3 hr, then the volatiles were removed *in vacuo*. The canary yellow crude solid was redissolved in a minimum of THF and layered with pentane to yield (after drying) 0.61 g of yellow-orange crystals overnight. A second, 0.75-g crop, analytically identical to the first, was obtained from the supernatant to reach a combined yield of 58%. $^1$H NMR (500 MHz, $C_6D_6$): δ/ppm = 6.29 (s, 8H, pyrrole), 3.54 (br s, 4H, α-THF), 3.45 (br s, $NHMe_2$), 1.77 (s, 12H, $-CH_3$), 1.74 (s, 12H, $-CH_3$), 1.39 (br s, 4H, β-THF). Anal. Calcd for $C_{34}H_{47}N_5OZr$: C, 64.51; H, 7.48; N, 11.06. Found: C, 64.68; H, 7.55; N, 10.96.

*Synthesis of $^{Ph}LZr^{IV}(NHMe_2)(THF)$*

Samples of $Zr(NMe_2)_4$ (44 mg, 0.16 mmol) and $^{Ph}LH_4$ (170 mg, 0.16 mmol) were dissolved in 10 mL of THF and refluxed for 3 hr, then the volatiles were removed *in vacuo*. The brown solid was redissolved in a minimum of THF/toluene mixture and layered with pentane to yield (after drying) 125 mg (64%) of yellow-orange crystals after several days. Anal. Calcd for $C_{84}H_{83}N_5O_{1.5}Zr$ ($^{Ph}LZr^{IV}(NHMe_2)(THF)$ • 0.5 THF): C, 78.96; H, 6.55; N, 5.48; Zr, 7.14. Found: C, 78.88; H, 6.50; N, 5.58; Zr, 7.22.

## IV.6.b. X-ray crystal structure determinations

*General technique*

X-ray quality crystals were coated with Paratone N oil and mounted on a glass fiber. X-ray diffraction data were collected on a Siemens diffractometer equipped with a CCD detector, using the Mo Kα radiation, selected by a graphite monochromator. The data were integrated to *hkℓ*-intensity and the final unit cell calculated using the SAINT v.4.050 program from Siemens. Solution and refinement were performed with the SHELXTL v.5.03 suite of programs developed by G. M. Sheldrick and Siemens Industrial Automation, 1995. Least-squares refinements were applied to $F^2$, with hydrogen atoms of organic fragments placed at calculated positions using a standard riding model and refined isotropically. No absorption correction was performed, except where otherwise stated.

*2,5,-Bis(3′,3′,5′,5′-tetramethylcyclohex-1′-enyl)pyrrole*

White crystals were grown by slow evaporation of a concentrated MeCN/THF solution. The structure was solved by direct methods. During refinement, the N-pyrrolic proton was located from the difference map, while other H atoms were placed at calculated positions.

*$^{Ph}LH_4$*

White crystals were grown by cooling a warm, concentrated toluene solution of $^{Ph}LH_4$. The structure was solved by direct methods. During the refinement, four toluene solvent molecules were found in the asymmetric unit; none was disordered.

*$[LZr^{IV}(NHMe_2)(THF)]$*

Yellow crystals were grown from a concentrated solution in THF/toluene/pentane. The structure was solved by Patterson's method; refinement proceeded and converged normally.

*[HLZr$^{IV}$]$_2$O*

Yellow-orange crystals were grown by diffusion of hexane vapor into a solution of [LZr$^{IV}$(NHMe$_2$)(THF)] in wet THF. The structure was solved by direct methods; refinement proceeded and converged normally.

*[H$^{Ph}$LZr$^{IV}$]$_2$O*

Yellow-orange crystals were grown by covering a solution of [LZr$^{IV}$(NHMe$_2$)(THF)] in toluene / THF with a pentane layer. The structure was solved by direct methods; refinement proceeded and converged normally. An empirical absorption correction was applied as implemented by the program SADABS in the SHELX package.

## IV.7. References

1 Schrauzer, G. N.; Mayweg, V. P. *J. Am. Chem. Soc.* **1965**, *87*, 3585-3592.

2 Davison, A.; Edelstein, N.; Holm, R. H.; Maki, A. H. *J. Am. Chem. Soc.* **1963**, *85*, 2029-2030.

3 Maki, A. H.; Berry, T. E.; Davison, A.; Holm, R. H.; Balch, A. L. *J. Am. Chem. Soc.* **1966**, *88*, 1080-1082.

4 Holm, R. H.; Balch, A. L.; Davison, A.; Maki, A. H.; Berry, T. E. *J. Am. Chem. Soc.* **1967**, *89*, 2866-2874.

5 Wang, Y.; DuBois, J. L.; Hedman, B.; Hodgson, K. O.; Stack, T. D. P. *Science* **1998**, *279*, 537-540.

6 Chaudhuri, P.; Hess, M.; Flörke, U.; Wieghardt, K. *Angew. Chem. Int. Ed.* **1998**, *37*, 2217-2220.

7 Chaudhuri, P.; Hess, M.; Weyhermüller, T.; Wieghardt, K. *Angew. Chem. Int. Ed.* **1999**, *38*, 1095-1098.

8 Chaudhuri, P.; Hess, M.; Müller, J.; Hildenbrand, K.; Bill, E.; Weyhermüller, T.; Wieghardt, K. *J. Am. Chem. Soc.* **1999**, *121*, 9599-9610.

9 Bouwkamp, M. W.; Lobkovsky, E.; Chirik, P. J. *J. Am. Chem. Soc.* **2005**, *127*, 9660-9661.

10 Bart, S. C.; Hawrelak, E. J.; Lobkovsky, E.; Chirik, P. J. *Organometallics* **2005**, *24* , 5518-5527.

11 Blackmore, K. J.; Ziller, J. W.; Heyduk, A. F. *Inorg. Chem.* **2005**, *44*, 5559-5561.

12 Sessler, J. L.; Anzenbacher, P.; Miyaji, H.; Jursikova, K.; Bleasdale, E. R.; Gale, P. A. *Ind. Eng. Chem. Res.* **2000**, *39*, 3471-3478.

13 Anzenbacher, P.; Jursikova, K.; Lynch, V. M.; Gale, P. A.; Sessler, J. L. *J. Am. Chem. Soc.* **1999**, *121*, 11020-11021.

14 Bonomo, L.; Solari, E.; Scopelliti, R.; Floriani, C.; Re, N. *J. Am. Chem. Soc.* **2000**, *122*, 5312-5326.

15 Bhattacharya, D.; Dey, S; Maji, S.; Pal, K.; Sarkar, S. *Inorg. Chem.* **2005**, *44*, 7699-7701.

16 Jacoby, D.; Floriani, C.; Chiesi-Villa, A.; Rizzoli, C. *J. Chem. Soc. Chem. Commun.* **1991**, *11*, 790-792.

17 Jacoby, D.; Floriani, C.; Chiesi-Villa, A.; Rizzoli, C. *J. Am. Chem. Soc.* **1993**, *115*, 3595-3602.

18 Jacoby, D.; Isoz, S.; Floriani, C.; Schenk, K.; Chiesi-Villa, A.; Rizzoli, C. *Organometallics* **1995**, *14*, 4816-4824.

19 Qin, W.; Rohand, T.; Baruah, M.; Stefan, A.; Van der Auweraer, M.; Dehaen W.; Boens, N. *Chem. Phys. Lett.* **2006**, *420*, 562-568.

20 Harriman, A. *J. Chem. Soc. Faraday Trans.* **1980**, *76*, 1978-1985.

21 Solari, G.; Solari, E.; Lemercier, G.; Floriani, C.; Chiesi-Villa, A.; Rizzoli, C. *Inorg. Chem.* **1997**, *36*, 2691-2695.

22 Bhugun, I.; Lexa, D.; Savéant, J.-M. *J. Am. Chem. Soc.* **1996**, *118*, 1769-1776.

23 Cheng, S. C.; Blaine, C. A.; Hill, M. G.; Mann, K. R. *Inorg. Chem.* **1996**, *35*, 7704-7708.

24 Evans, W. J.; Seibel, C. A.; Ziller, J. W. *Inorg. Chem.* **1998**, *37*, 770-776.

25 Rudolph, M.; Dautz, S.; Jäger, E.-G. *J. Am. Chem. Soc.* **2000**, *122*, 10821-10830.

26 Farrugia, L. J.; Lopinski, S.; Lovatt, P. A.; Peacock, R. D. *Inorg. Chem.* **2001**, *40*, 558-559.

27 Fachinetti, G.; Floriani, C.; Zanazzi, P. F. *J. Am. Chem. Soc.* **1978**, *100*, 7405-7407.

28 Fachinetti, G.; Floriani, C.; Zanazzi, P. F.; Zanzari, A. R. *Inorg. Chem.* **1979**, *18*, 3469-3475.

29 Brown, T. L.; LeMay, H. E., Jr.; Bursten, B. E. *Chemistry: The Central Science*, 8th ed.; Prentice Hall: New Jersey, 2000.

30 Lin, C.-L.; Fang, M.-Y.; Cheng, S.-H. *J. Electroan. Chem.* **2003**, *531*, 155-162.

31 Azevedo, F.; Freire, C.; Castro, B. *Polyhedron* **2002**, *21*, 1695-1705.

32 Armarego, W. L. F.; Perrin, D. D. *Purification of Laboratory Chemicals*, 4th ed.; Butterworth-Heinmann: Oxford, 1996.

# Chapter V

# Electron transfer series of iron porphyrinogen — synthesis and structures

Parts of this Chapter have been published:

Bachmann, J.; Nocera, D. G. *J. Am. Chem. Soc.* **2005**, *127*, 4730-4743.

# V.1. Introduction

Iron porphyrin, or heme, is a ubiquitous and versatile protein cofactor. By controlling the heme axial coordination and peptidic environment, proteins may tune cofactor reactivity to selectively perform redox-derived functions as varied as single-electron transfer (cytochromes),[1-13] dioxygen coordination and transport (hemoglobin and myoglobin),[14-17] dioxygen activation and substrate oxidation (cytochrome P-450),[18-23] and peroxide and superoxide removal (peroxidases, catalase).[24-26] Accordingly, the redox properties of iron porphyrins have been investigated intensely in isolated cofactors,[27,28] in the environments of *de novo* designed[29-37] and natural proteins,[38-51] and in the context of small molecule substrate activation and catalysis.[52-62] The redox activity of hemes is typically metal centered with the notable exception of compound I, which possesses an iron oxo the oxidizing power of which is augmented by a single oxidizing equivalent stored in the porphyrin macrocycle.[63-67] It is conceivable that further expanding the redox abilities of the macrocycle could broaden the range of transformations achievable at a mononuclear iron complexe — metal-organic redox cooperativity would engender a multielectron chemistry of the "artificial hemes" that is unavailable to native heme cofactors. Therefore, the present Chapter describes the syntheses, structures and redox properties of the available oxidation states of iron porphyrinogen.

Previous Chapters have dealt with porphyrinogen complexes of redox-inert metal ions, and have provided benchmarks for the ligand's redox activity. The additional presence of a redox-active central ion introduces new questions. In particular, the result of the interaction between the one-electron redox couple of the metal and the two-electron redox couples of the ligand is unknown. The range of OSs available to the overall construct might be widened, and the redox stoichiometry of available couples might change. To date, the electrochemical and spectroscopic properties of transition metal porphyrinogen have remained largely unexplored, due principally to the presence of non-innocent counter-ions and axial ligands.[68-73]

This Chapter describes the synthesis of the sodium and tetrafluoroborate salts of porphyrinogen macrocycles containing iron. Owing to the absence of redox-active counter-ions and axial ligands, the oxidation-reduction chemistry of the iron porphyrinogens is unveiled by electrochemistry and the various oxidation states are structurally characterized in the solid state and in solution by paramagnetic NMR. The next Chapter will explore the electronic structures of iron porphyrinogens.

## V.2. Synthesis

### V.2.a. Metallation

Scheme V.1 outlines the syntheses of the iron porphyrinogens that are the focus of this study. Control of the availability of solubilized $FeCl_2$ is essential to obtaining the parent complex $[LFe^{III}]^{-}$ in the absence of iron-based anions. Heterogeneous introduction of the Fe(II) ion into solution with gentle stirring is critical to the success of this chemistry, with $FeCl_2$ beads (–10 mesh) serving as the Fe(II) source. Reaction mixtures containing the deprotonated porphyrinogen macrocycle, $L^{4-}$, and the $FeCl_2$ beads turn the very deep red color that is characteristic of the presence of the $[LFe^{III}]^{-}$ complex after ~1 h. The presumed direct insertion product, $[LFe^{II}]^{2-}$, is oxidized *in situ* to $[LFe^{III}]^{-}$ by $FeCl_2$ (consistent with the observed formation of black Fe metal powder during the reaction). Under the heterogeneous synthesis conditions, $[LFe^{III}]^{-}$ is isolated as the sodium salt. The absence of iron-containing countercations was confirmed by elemental analysis, single-crystal X-ray diffraction analysis, and by Mössbauer spectroscopy.

Complications arise if the iron center is installed into the macrocycle according to established procedures.[70,71] Tetrahydrofuran suspensions of $Na_4L$ charged with $FeCl_2$ *powder* turn deep red within minutes and $[LFe^{III}]^{-}$ is isolable as a salt of $Fe^{II}_2$-based countercations, $[(THF)_4Fe(\mu\text{-}Cl)_2Fe(THF)_4]_{1/2}$ $[(THF)_3Fe(\mu\text{-}Cl)_3Fe(THF)_3]$ $[LFe]_2$ (see Scheme V.1). The very low solubility of $Na_4L$ with respect to $FeCl_2$ in THF presumably leads to a preponderance of Fe(II) in solution during metallation, thereby favoring the

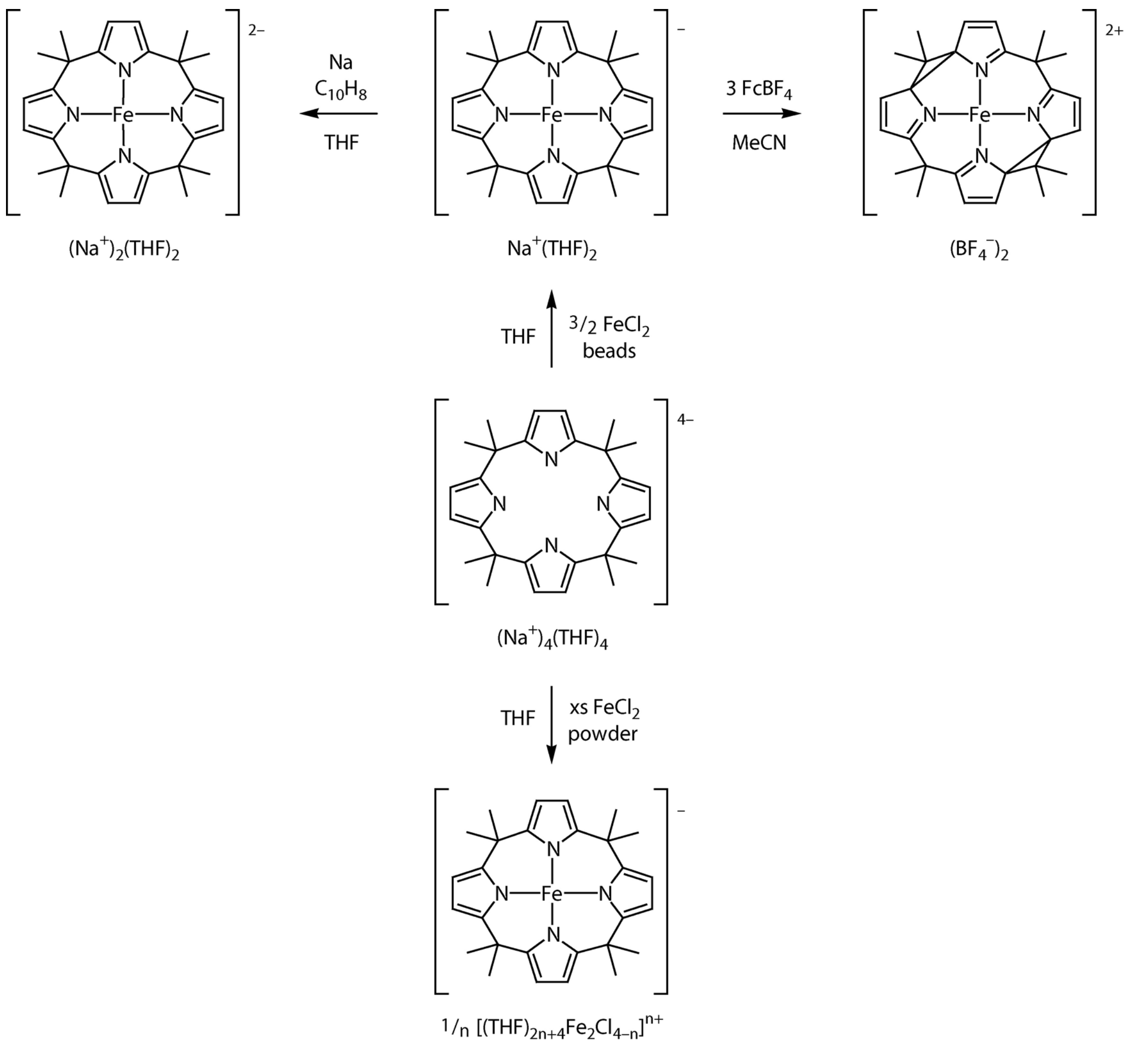
2–
Na
$C_{10}H_8$
THF
$(Na^+)_2(THF)_2$
–
$Na^+(THF)_2$
3 $FcBF_4$
MeCN
2+
$(BF_4^-)_2$
THF
3/2 $FeCl_2$
beads
4–
$(Na^+)_4(THF)_4$
THF
xs $FeCl_2$
powder
–
1/n $[(THF)_{2n+4}Fe_2Cl_{4-n}]^{n+}$
N
Fe

**Scheme V.1.** Preparation of the three oxidation states of iron porphyrinogen. THF = tetrahydrofuran; $Fc^+$ = ferrocenium cation; $C_{10}H_8$ = naphthalene; xs = excess.

formation of the bimetallic cations followed by their subsequent metathesis with the $Na^+$ ion. This wayward chemistry is observed despite a stoichiometric $Na_4L/FeCl_2$ ratio and a slow addition of $FeCl_2$ to solution. Indeed, the only way we found to prevent the buildup of Fe(II) in solution was the utilization of the heterogeneous reaction conditions described in the foregoing paragraph. Given the abundance of $Fe^{n+}$ centers in $[(THF)_4Fe(\mu\text{-}Cl)_2Fe(THF)_4]_{1/2}[(THF)_3Fe(\mu\text{-}Cl)_3Fe(THF)_3][LFe]_2$, different combinations of formal charges for the constituent Fe ions may satisfy the overall charge balance. The oxidation states in this compound are assigned by inspection of its X-ray crystal structure (*cf.* Tables V.1 and V.2 and Figure V.1). The metric parameters of the $[(THF)_3Fe(\mu\text{-}Cl)_3Fe(THF)_3]^{n+}$ complex cation are identical to those of the cation in the

**Table V.1.** Summary of X-ray crystallographic data for $\mathrm{[(THF)_3Fe^{II}(\mu\text{-}Cl)_3Fe^{II}(THF)_3]}$ $\mathrm{[(THF)_4Fe^{II}(\mu\text{-}Cl)_2Fe^{II}(THF)_4]_{1/2}}$ $\mathrm{[LFe^{III}]_2 \bullet 2\ PhCH_3}$.

| | |
|---|---|
| empirical formula (formula weight) | $\mathrm{C_{110}H_{154}Cl_4Fe_5N_8O_{10}}$ (2169.53) |
| $T$ (K) | 193(2) |
| $\lambda$ (Å) | 0.71073 |
| crystal system, space group | Triclinic, $P\overline{1}$ |
| $a$ ; $b$ ; $c$ (Å) | 13.0139(8) ; 15.3786(10) ; 29.1680(19) |
| $\alpha$; $\beta$; $\gamma$ (deg) | 84.7050(10) ; 80.1510(10) ; 69.8640(10) |
| $Z$ ; $V$ (Å$^3$) | 2 ; 5396.5(6) |
| crystal size (mm$^3$) | $0.35 \times 0.18 \times 0.08$ |
| Abs. coeff. (mm$^{-1}$) | 0.816 |
| $F(000)$ | 2296 |
| $\theta$ range for data collection | 2.04 to 23.30° |
| limiting indices | $-14 \leq h \leq 13$, $-17 \leq k \leq 8$, $-32 \leq \ell \leq 32$ |
| no. of reflns collcd ; no. of ind. reflns ($R_{\mathrm{int}}$) | 22060 ; 15256 (0.05875) |
| completeness to $\theta = 23.27°$ | 97.9 % |
| refinement method | Full-matrix least-squares on $F^2$ |
| data / restraints / parameters | 15256 / 0 / 1279 |
| $R_1$,[a] $wR_2$[b] ($I > 2\sigma(I)$) | 0.0987, 0.1812 |
| $R_1$,[a] $wR_2$[b] (all data) | 0.1033, 0.1831 |
| GOF[c] on $F^2$ | 1.429 |
| largest diff. peak and hole | 0.578 and −0.412 eÅ$^{-3}$ |

[a] $R_1 = \Sigma||F_o| - |F_c||/\Sigma|F_o|$.

[b] $wR_2 = (\Sigma(w(F_o^2 - F_c^2)^2)/\Sigma(w(F_o^2)^2))^{1/2}$.

[c] $\mathrm{GOF} = (\Sigma\, w(F_o^2 - F_c^2)^2/(n - p))^{1/2}$,
where $n$ is the number of data and $p$ is the number of parameters refined.

**Table V.2.** Selected geometric parameters for $\mathrm{[(THF)_3Fe^{II}(\mu\text{-}Cl)_3Fe^{II}(THF)_3]}$ $\mathrm{[(THF)_4Fe^{II}(\mu\text{-}Cl)_2Fe^{II}(THF)_4]_{1/2}}$ $\mathrm{[LFe^{III}]_2 \bullet 2\ PhCH_3}$.

| Distances / Å | | Angles / deg | |
|---|---|---|---|
| $\mathrm{[(THF)_3Fe^{II}(\mu\text{-}Cl)_3Fe^{II}(THF)_3]^+}$ | | | |
| $\mathrm{(Fe—Cl)_{avg}}$ | 2.48(±0.05) | $\mathrm{(Cl–Fe–Cl)_{avg}}$ | 86.8(±1.9) |
| $\mathrm{[(THF)_4Fe^{II}(\mu\text{-}Cl)_2Fe^{II}(THF)_4]^{2+}}$ | | | |
| $\mathrm{(Fe—Cl)_{avg}}$ | 2.47(±0.02) | Cl–Fe–Cl | 81.93(7) |
| $\mathrm{[LFe^{III}]^-}$ | | | |
| $\mathrm{(Fe—N)_{av}}$ | 1.903(±0.010) | $\mathrm{(N–Fe–N)_{avg}}$ | 90.0(±0.5) |

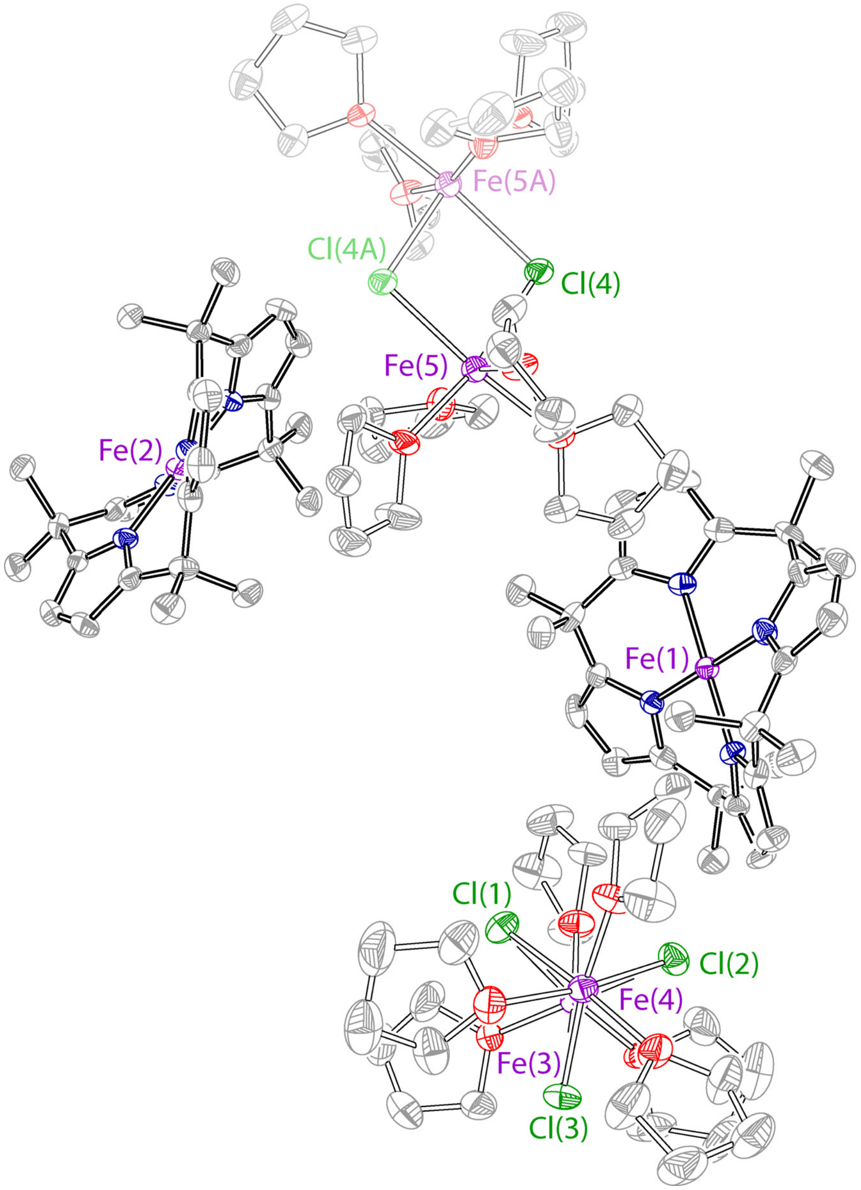

**Figure V.1.** Crystal structure of $[(THF)_3Fe^{II}(\mu\text{-}Cl)_3Fe^{II}(THF)_3]$ $[(THF)_4Fe^{II}(\mu\text{-}Cl)_2Fe^{II}(THF)_4]_{1/2}$ $[LFe^{III}]_2 \cdot 2\ PhCH_3$. The asymmetric unit only contains one half of $[(THF)_4Fe^{II}(\mu\text{-}Cl)_2Fe^{II}(THF)_4]^{2+}$: the second half, generated by symmetry, is represented in faded colors. For clarity, H atoms and lattice solvent molecules are omitted, and bonds within the iron porphyrinogen anions are bolded. Thermal ellipsoids are drawn at the 50% probability level. Color coding: Fe, purple; N, blue; Cl, green; O, red; C, gray. Selected crystallographic data and geometric parameters are given in Tables V.1 and V.2, respectively.

previously reported salt $[(THF)_3Fe^{II}(\mu\text{-}Cl)_3Fe^{II}(THF)_3]$ $[(THF)Sn^{IV}Cl_5]$.[74] Additionally, the metrics of the porphyrinogen anion are identical to those of the crystal structure of $[Na(solv)_2][LFe^{III}]$ (*vide infra*), thus setting an oxidation state of +II for the iron centers in the complex cation $[(THF)_4Fe(\mu\text{-}Cl)_2Fe(THF)_4]^{2+}$.

## V.2.b. Oxidation-reduction

The $[LFe^{III}]^-$ complex serves as the starting material for the other series members. The one-electron reduced counterpart $[LFe^{II}]^{2-}$ is afforded in quantitative yield by the reaction of $[LFe^{III}]^-$ with a stoichiometric or excess amount of sodium naphthalenide. The $Na^+$ ions may be exchanged with tetrabutylammonium using $Bu_4NCl$ in THF.

Alternatively, $[LFe^{III}]^-$ may be oxidized by ferrocenium tetrafluoroborate ($FcBF_4$) in $CH_3CN$. $[L^{\Delta\Delta}Fe^{II}](BF_4)_2$ is obtained as the only isolable iron product, regardless of the $Na[LFe^{III}]/FcBF_4$ ratio. Care was taken in the choice of the starting material. Ethers appear to favor radical processes and exacerbate the subsequent decomposition of the oxidized product. Consequently, $[Na(solv)_2][LFe^{III}]$ where solv = THF was avoided. Three equivalents of $FcBF_4$ are consumed in the reaction as ascertained by recovery of the Fc reduction product; for preparative convenience, three equivalents of $FcBF_4$ were therefore employed for the oxidation. The macrocycle undergoes a selective four-electron oxidation from $L^{4-}$ to $L^{\Delta\Delta}$ while $Fe^{III}$ is reduced to $Fe^{II}$, and under no conditions is a product obtained with the macrocycle oxidized by two electrons (*i.e.*, $L^{\Delta 2-}$). Consistent with this result, $[L^{\Delta\Delta}Fe^{II}]^{2+}$ and $[LFe^{III}]^-$ do not undergo a comproportionation reaction. $[L^{\Delta\Delta}Fe^{II}](BF_4)_2$ does not thermally decompose in the solid state, in acetonitrile solution, or as a dichloromethane suspension at room temperature. However, salt metathesis attempts in dichloromethane with sodium tetraphenylborate caused decomposition on the timescale of dissolution of the reactants, as witnessed by a color change from yellow to brown and the complete loss of the NMR signals of $[L^{\Delta\Delta}Fe^{II}]^{2+}$. For the purpose of growing large single crystals suitable for X-ray analysis, sodium cobalticarborane, $Na[(C_2B_9H_{11})_2Co]$ was employed for salt metathesis, which proceeded very cleanly in $CH_2Cl_2$.

Published work shows that the iron center of $[L^{\Delta\Delta}Fe^{II}]^{2+}$ may be oxidized when chloride is available to coordinate axially, yielding $[L^{\Delta\Delta}Fe^{III}Cl]^{2+}$.[70] The oxidation, however, does not proceed easily in the absence of non-coordinating counter-anions. For instance, treatment of $[L^{\Delta\Delta}Fe^{II}]^{2+}$ with the strongly oxidizing thianthrenium radical cation[75] was accompanied by the disappearance of the deep purple color of the radical cation, but most of the $[L^{\Delta\Delta}Fe^{II}]^{2+}$ starting material was recovered.

## V.3. Electrochemistry

The left panel of Figure V.2 shows the full cyclic voltammogram of $[LFe^{III}]^-$ in $CH_3CN$ (gray trace). Two oxidation-reduction events are observed. Pseudo-reversible electrochemical behavior for the CV process at $E_{½} = -0.57$ V (vs NHE) is indicated by nearly linear plots of the cathodic and anodic currents *vs* $\nu^{½}$ (scan rate $50 \leq \nu \leq 600$ mV s$^{-1}$) (right panel of Figure V.2), and values of 1.2 ± 0.2 for the ratios of the anodic and cathodic peak currents. The redox process at more positive potential is characterized by a significant increase in the current response and an irreversible waveform. As is often the case, a potential for the redox process is afforded by differential pulse voltammetry. An anodically scanning electrode immersed in a $CH_3CN$ solution of $[LFe^{III}]^-$ yields two peaks in the differential pulse voltammogram. The process at $E_p = -0.55$ V (vs NHE) corresponds to the reversible $E_{½} = -0.57$ V wave observed in the cyclic voltammogram. The process at $E_p = 0.77$ V (vs NHE) corresponds to a multielectron reaction; its peak current is ~3 times greater than that of the reversible process. A more accurate measurement of the redox equivalency for both electrode processes is afforded by chronocoulometry. Using the Cottrell equation, plots of Q *vs* $t^{½}$ for potential steps encompassing the $E_p = -0.55$ and $E_p = 0.77$ redox processes yield linear responses with slopes in 1 : 2.7 ratio, consistent with the DPV result. The identities of these two electrode processes are revealed by performing electrochemical experiments on solutions of $[L^{\Delta\Delta}Fe^{II}]^{2+}$: DPV exhibits peaks identical to those displayed in Figure V.2. Taken together, the DPV, CV and chronocoulometric results yield the following electrochemical assignments, which correspond to the redox processes observed on the preparative scale:

$$[\mathrm{LFe^{III}}]^{-} + \mathrm{e^{-}} \rightarrow [\mathrm{LFe^{II}}]^{2-} \qquad E_{½} = -0.57\ \mathrm{V} \qquad (1)$$

$$[\mathrm{L^{\Delta\Delta}Fe^{II}}]^{2+} + 3\,\mathrm{e^{-}} \rightarrow [\mathrm{LFe^{III}}]^{-} \qquad E_{\mathrm{p}} = +0.77\ \mathrm{V} \qquad (2)$$

Peak potential measurements for quasi-reversible and irreversible processes in DPV will be shifted to more negative potentials by an activation overpotential; however, fast cyclic voltammetric scans of the $[\mathrm{L^{\Delta\Delta}Fe^{II}}]^{2+}/[\mathrm{LFe^{III}}]^{-}$ couple indicate that $E_{\mathrm{p}}$ is near $E_{½}$.

The porphyrinogen macrocycle is very electron-donating as reflected by the reduction potential of the iron residing at its core. The reduction potential of reaction (1) is more negative than that of low-potential ferrodoxins (Fd), the ferric forms of which are among the most difficult iron cofactors to reduce in biology, $0 \leq E_{½}(\mathrm{FdFe^{III/II}}) \leq -0.5$ V *vs* NHE.[76] With regard to its porphyrin relatives, however, iron porphyrinogen is ~ 0.5 to 1.3 V more difficult to reduce than heme cofactors (depending on the nature of the axial ligands).

Reaction (2) provides a measure of ligand-centered redox processes. The porphyrinogen can react in two-electron steps with the concomitant formation of a C—C bond between the α carbons of adjacent pyrroles; each cyclopropane thus

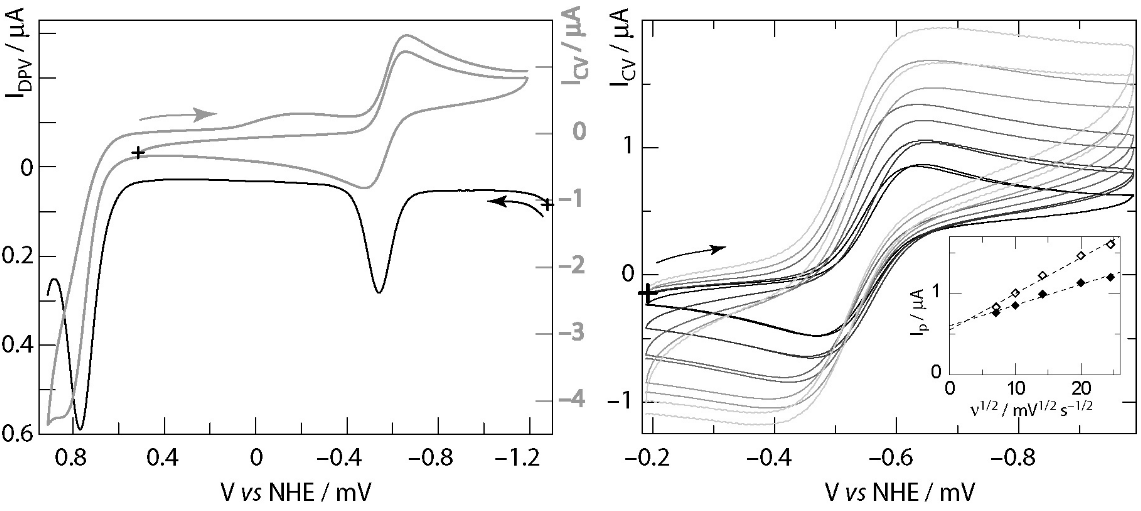

**Figure V.2.** Electrochemistry of iron porphyrinogen. Left, cyclic voltammetric (gray) and differential pulse voltammetric (black) traces of 1 mM $\mathrm{Bu_4N[LFe^{III}]}$ in 0.04 M $\mathrm{Bu_4NBPh_4}$ / $\mathrm{CH_3CN}$; CV: sweep rate 100 mV/s; DPV: sweep rate 20 mV/s, pulse amplitude 20 mV, pulse period 200 ms, pulse width 50 ms, sample width 17 ms. Right, the reversible $[\mathrm{LFe^{III}}]^{-}/[\mathrm{LFe^{II}}]^{2-}$ CV wave recorded on the same solution; scan rates: 50, 100, 200, 400, and 600 mV $\mathrm{s^{-1}}$ (from black to light gray, two full scans each). Inset: plots of the peak current $I_{\mathrm{p}}$ (open diamonds: cathodic; full diamonds: anodic) *vs* the square root of the scan rate, with linear fits.

formed is a two-equivalent hole reservoir for the porphyrinogen framework. The reduction potentials of half-reactions (1) and (2) offer the potential for the overall four-electron ligand-based reduction,

$$[\mathrm{L}^{\Delta\Delta}\mathrm{Fe}^{\mathrm{II}}]^{2+} + 4\,e^{-} \rightarrow [\mathrm{LFe}^{\mathrm{II}}]^{2-} \qquad E_{1/2} = 0.43\ \mathrm{V} \qquad (3)$$

The four-electron reduction of the porphyrinogen macrocycle was previously ascertained by inserting the redox-inactive $\mathrm{Zn}^{2+}$ ion into the porphyrinogen macrocycle (*cf*. Chapter II). For this system the consecutive two-electron processes were observed at $E_{1/2}([\mathrm{L}^{\Delta\Delta}\mathrm{Zn}^{\mathrm{II}}]^{2+}/[\mathrm{L}^{\Delta}\mathrm{Zn}^{\mathrm{II}}]) = 0.63$ V and $E_{1/2}([\mathrm{L}^{\Delta}\mathrm{Zn}^{\mathrm{II}}]/[\mathrm{LZn}^{\mathrm{II}}]^{2-}) = 0.21$ V *vs* NHE. Combining these two redox couples yields a potential for the overall four-electron ligand-centered reduction,

$$[\mathrm{L}^{\Delta\Delta}\mathrm{Zn}^{\mathrm{II}}]^{2+} + 4\,e^{-} \rightarrow [\mathrm{LZn}^{\mathrm{II}}]^{2-} \qquad E_{1/2} = 0.42\ \mathrm{V} \qquad (4)$$

The consistency between the ligand redox potentials for half-reactions (3) and (4) for macrocycles encrypting redox-active and redox-inactive metals suggests that the frontier orbitals of the ligand are not significantly perturbed by those of the metal residing at its core.

The inability to observe the partially oxidized porphyrinogen species for iron, when it is available to zinc, suggests that the disproportionation of $[\mathrm{L}^{\Delta}\mathrm{Fe}^{\mathrm{II}}]$ to the observed iron porphyrinogens is favorable,

$$3\,[\mathrm{L}^{\Delta}\mathrm{Fe}^{\mathrm{II}}] \rightarrow 2\,[\mathrm{LFe}^{\mathrm{III}}]^{-} + [\mathrm{L}^{\Delta\Delta}\mathrm{Fe}^{\mathrm{II}}]^{2+} \qquad (5)$$

The viability of this contention can be assessed if we assume that the potentials for the two-electron ligand transformations are the same for iron and zinc, *i.e.* $E_{1/2}([\mathrm{L}^{\Delta\Delta}\mathrm{M}^{\mathrm{II}}]^{2+}/[\mathrm{L}^{\Delta}\mathrm{M}^{\mathrm{II}}]) = 0.63$ V and $E_{1/2}([\mathrm{L}^{\Delta}\mathrm{M}^{\mathrm{II}}]/[\mathrm{LM}^{\mathrm{II}}]^{2-}) = 0.21$ V *vs* NHE for M = Zn and Fe. This assumption is reasonable given that the reduction potentials have already been shown to be nearly equivalent for half-reactions (3) and (4). On this basis, we calculate the following reduction potential:

$$[\mathrm{L}^{\Delta}\mathrm{Fe}^{\mathrm{II}}] + e^{-} \rightarrow [\mathrm{LFe}^{\mathrm{III}}]^{-} \qquad E_{1/2} = 0.99\ \mathrm{V} \qquad (6)$$

With this in hand, the driving force for reaction (5) is determined to be $\Delta E(5) = +0.36$ V. In contrast to the zinc porphyrinogen case, the availability of the +3 metal oxidation state and the stability of the $[LM^{III}]^{-}$ species drives disproportionation reaction (5), thus preventing the isolation of $[L^{\Delta}Fe^{II}]$.

## V.4. Structures

### V.4.a. In the solid state — by crystallography

The structures of iron porphyrinogen in its three available oxidation states are shown in Figures V.3, V.4 and V.5, and compared in Figure V.6. Crystallographic data and selected geometric measurements for the three structures are given in Tables V.3 and V.4. The structures of $[LFe^{II}]^{2-}$ and $[LFe^{III}]^{-}$ are similar to each other and to that previously reported for the dilithium salt of iron(II) octaethylporphyrinogen. As is most easily seen from the edge-on perspective, the central iron ion lies in a nearly perfect planar tetracoordinate environment defined by the four pyrrole nitrogens (4-N) and no significant intermolecular contacts are observed. Owing to the $sp^3$ hybridization of the *meso* carbon, the pyrroles cant about the N—Fe—N twofold axis. The two structures are distinguished by the Fe—N bond lengths of the macrocycle core. As expected, the Fe—N bond is significantly longer for the iron center possessing the greater valence electron count ($d_{avg}$(Fe—N) = 1.933 Å in $[LFe^{II}]^{2-}$ *vs* $d_{avg}$(Fe—N) = 1.899 Å in $[LFe^{III}]^{-}$). The only other significant differences in the structures result directly from the counter-cations. The $Na^{+}$ counter-cation of $[LFe^{III}]^{-}$ assumes a pseudo-octahedral coordination defined by the oxygens of two *fac*-diglyme solvent molecules. The $Na^{+}$ counter-cations of $[LFe^{II}]^{2-}$ are coordinated by diametrically opposite pyrroles in a $\eta^4$ fashion — $d_{avg}$(Na···N) = 3.07 Å is significantly longer than $d_{avg}$(Na—C) = 2.80 Å — and reside on opposite faces of the macrocycle. The remaining coordination sites of the $Na^{+}$ ions are occupied by three monodentate oxygen ligands, one from THF and two from symmetry-related bridging pyridine-*N*-oxides (which create a coordination polymer in the lattice). The latter coordinate the alkali cations

**Table V.3.** Summary of crystallographic data for iron porphyrinogens.

| | $[(THF)Na(Opy)]_2$ $[LFe^{II}]$ | $[Na(diglyme)_2]$ $[LFe^{III}]$ | $[L^{\Delta\Delta}Fe^{II}(NCCH_3)]$ $[(C_2B_9H_{11})_2Co]_2$ $\cdot$ 2 $CH_3CN$ $\cdot$ 2 *o*-$C_6H_4Cl_2$ |
|---|---|---|---|
| empirical formula | $C_{50}H_{58}FeN_6Na_2O_4$ | $C_{40}H_{60}FeN_4NaO_6$ | $C_{54}H_{93}B_{36}Cl_4Co_2FeN_7$ |
| formula weight | 908.85 | 771.76 | 1545.02 |
| $T$ (K) | 183(2) | 183(2) | 100(2) |
| $\lambda$ (Å) | 0.71073 | 0.71073 | 0.71073 |
| crystal system | Monoclinic | Orthorhombic | Orthorhombic |
| space group | $P2_1/c$ | *Pbca* | *Abm*2 |
| $a$ (Å) | 20.4824(13) | 15.5367(12) | 23.443(2) |
| $b$ (Å) | 11.6675(7) | 21.1012(16) | 25.146(3) |
| $c$ (Å) | 19.2151(12) | 25.2473(19) | 13.2883(13) |
| $\beta$ (deg) | 102.4720(10) | 90 | 90 |
| $V$ (Å$^3$) | 4483.6(5) | 8277.2(11) | 7833.6(14) |
| $Z$ | 4 | 8 | 4 |
| crystal size (mm$^3$) | 0.27 × 0.27 × 0.25 | 0.45 × 0.45 × 0.45 | 0.12 × 0.17 × 0.09 |
| $F(000)$ | 1920 | 3304 | 3176 |
| Abs. coeff. (mm$^{-1}$) | 0.409 | 0.423 | 0.780 |
| $\theta$ range for data coll. | 2.19 to 23.28° | 2.29 to 23.28° | 0.87 to 23.31° |
| limiting indices | $-21 \leq h \leq 22$ | $-16 \leq h \leq 17$ | $-26 \leq h \leq 25$ |
| | $-12 \leq k \leq 8$ | $-20 \leq k \leq 23$ | $-27 \leq k \leq 27$ |
| | $-21 \leq \ell \leq 21$ | $-27 \leq \ell \leq 28$ | $-9 \leq \ell \leq 14$ |
| no. of reflns collcd | 17385 | 31601 | 19041 |
| no. of ind. reflns ($R_{int}$) | 6414 (0.0501) | 5951 (0.0582) | 4642 (0.0705) |
| completeness to $\theta_{max}$ | 99.4% | 99.8% | 99.5% |
| refinement method | Full-matrix least-squares on $F^2$ | | |
| data/restraints/params | 6414 / 0 / 764 | 5951 / 0 / 482 | 4642 / 23 / 592 |
| $R_1$,[a] $wR_2$[b] ($I > 2\sigma(I)$) | 0.0345, 0.0840 | 0.0962, 0.1867 | 0.0533, 0.1385 |
| $R_1$,[a] $wR_2$[b] (all data) | 0.0419, 0.0876 | 0.0962, 0.1867 | 0.0556, 0.1411 |
| GOF[c] on $F^2$ | 1.064 | 1.479 | 1.112 |
| Largest diff. peak, hole | 0.247, –0.315 eÅ$^{-3}$ | 1.003, –0.605 eÅ$^{-3}$ | 0.927, –0.758 eÅ$^{-3}$ |

[a] $R_1 = \Sigma||F_o - |F_c||/\Sigma|F_o|$.

[b] $wR_2 = (\Sigma(w(F_o^2 - F_c^2)^2)/\Sigma(w(F_o^2)^2))^{1/2}$.

[c] GOF = $(\Sigma\, w(F_o^2 - Fc^2)^2/(n - p))^{1/2}$,
where $n$ is the number of data and $p$ is the number of parameters refined.

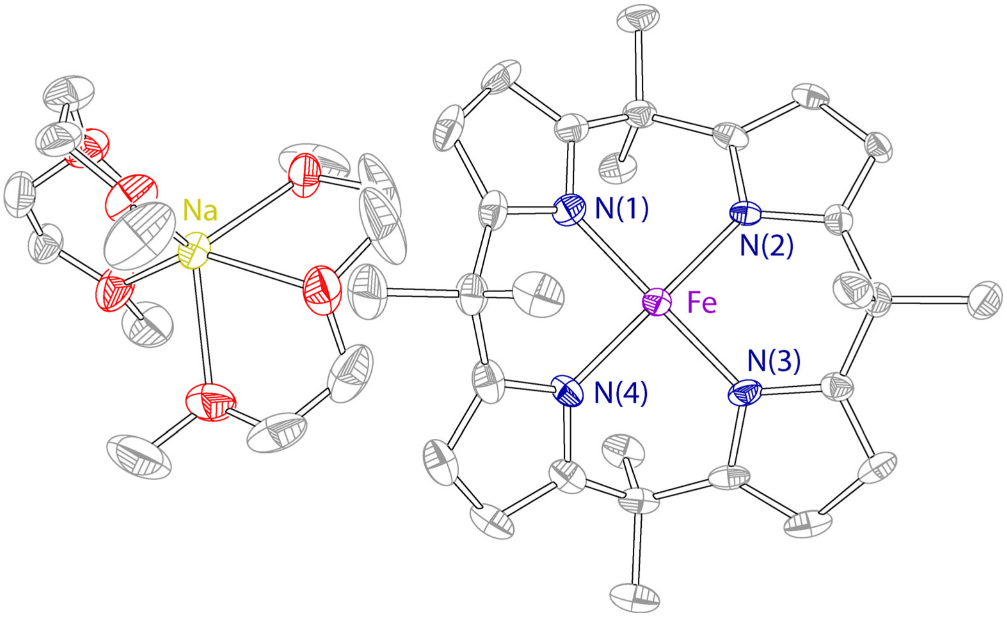

**Figure V.3.** Crystal structure of [(diglyme)$_2$Na] [LFe$^{III}$]. H atoms omitted; thermal ellipsoids at the 50% probability level. Color coding: Fe, purple; N, blue; Na, mustard yellow; O, red; C, gray.

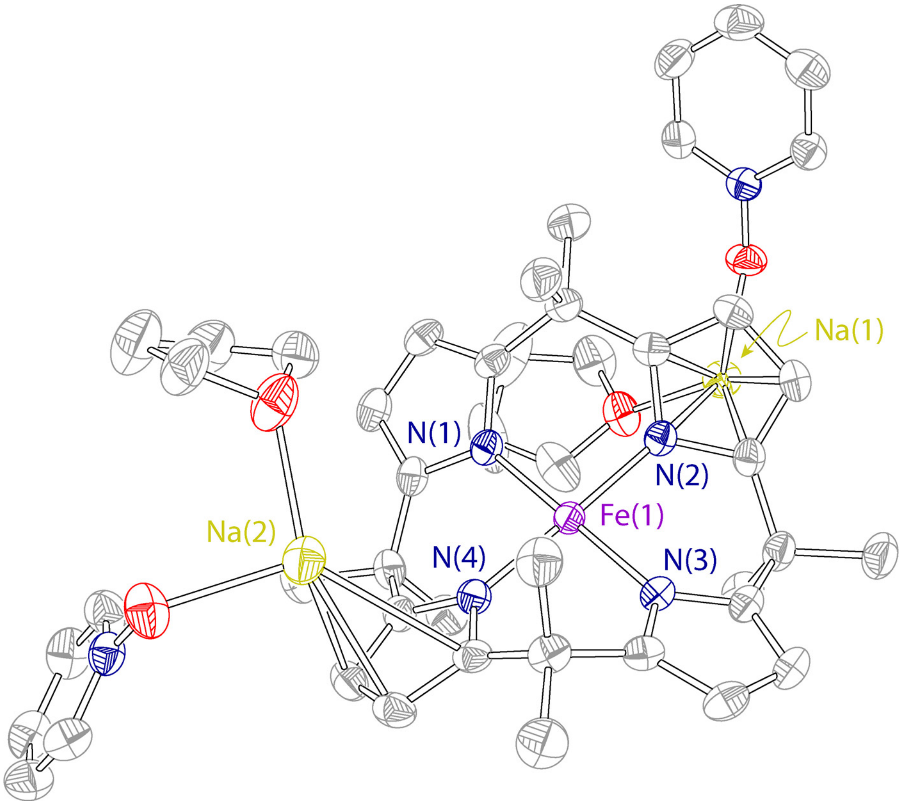

**Figure V.4.** Crystal structure of [(THF)(pyO)Na]$_2$ [LFe$^{II}$]. H atoms omitted; thermal ellipsoids at the 50% probability level. Color coding: Fe, purple; N, blue; Na, mustard yellow; O, red; C, gray.

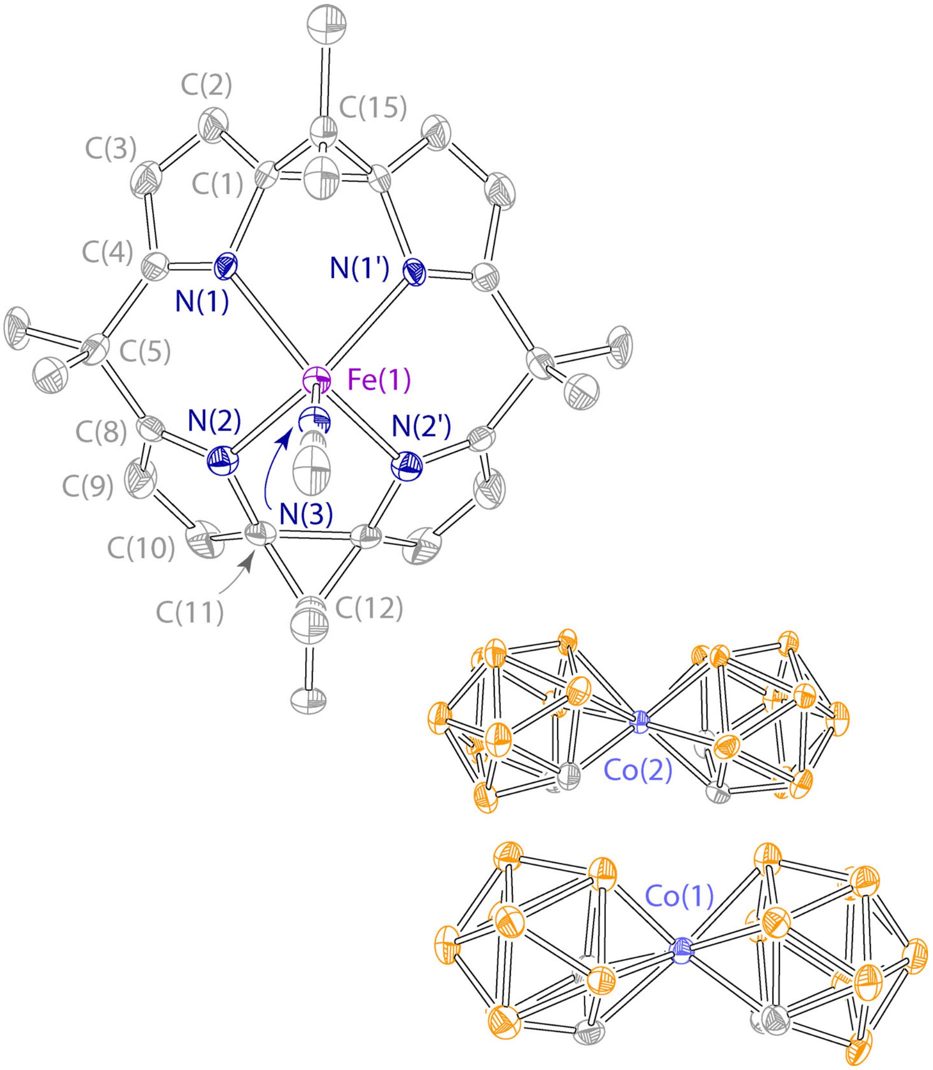

**Figure V.5.** Crystal structure of $[L^{\Delta\Delta}Fe^{II}(NCCH_3)]\ [(C_2B_9H_{11})_2Co]_2 \cdot 2\ CH_3CN \cdot 2\ o\text{-}C_6H_4Cl_2$. H atoms and solvent molecules omitted, thermal ellipsoids at the 50% probability level. Color coding: Fe, purple; N, blue; Co, powder blue; B, orange; C, gray.

and attenuate the very high oxygen sensitivity of the crystals (which in the absence of pyridine-*N*-oxide quickly turn from golden orange to deep red upon manipulation).

The X-ray crystal structures of $[LFe^{II}]^{2-}$ and $[LFe^{III}]^{-}$ indicate no direct bonding interaction between the α-carbons of adjacent pyrroles ($d_{avg}(C^{\alpha}—C^{\alpha})$ = 2.47 Å in $[LFe^{III}]^{-}$ and $d_{avg}(C^{\alpha}—C^{\alpha})$ = 2.50 Å in $[LFe^{II}]^{2-}$). This observation is consistent with no oxidation of the macrocycle. Conversely, two pairs of adjacent $C^{\alpha}$ atoms of the macrocycle in $[L^{\Delta\Delta}Fe^{II}]^{2+}$ are within single bond distance of each other ($d(C^{\alpha}—C^{\alpha})$ = 1.607(11) Å and 1.553(13) Å). The cyclopropanes are nearly equilateral triangles with

**Table V.4.** Comparison of geometric parameters for $[LFe^{II}]^{2-}$, $[LFe^{III}]^{-}$ and $[L^{\Delta\Delta}Fe^{II}]^{2+}$ in their respective crystal structures.

| $[(THF)Na(Opy)]_2$ $[LFe^{II}]$ | | $[Na(diglyme)_2]$ $[LFe^{III}]$ | | $[L^{\Delta\Delta}Fe^{II}(NCCH_3)]$ $[(C_2B_9H_{11})_2Co]_2$ • $2CH_3CN$ • $2o\text{-}C_6H_4Cl_2$ | |
|---|---|---|---|---|---|
| Distances / Å | | | | | |
| Fe(1)—N(1) | 1.9185(17) | Fe(1)—N(3) | 1.896(5) | Fe(1)—N(1) | 2.115(5) |
| Fe(1)—N(2) | 1.9353(17) | Fe(1)—N(4) | 1.897(5) | Fe(1)—N(2) | 2.117(6) |
| Fe(1)—N(4) | 1.9371(17) | Fe(1)—N(1) | 1.899(5) | Fe(1)—N(3) | 2.065(8) |
| Fe(1)—N(3) | 1.9430(16) | Fe(1)—N(2) | 1.904(5) | | |
| N(1)—C(1) | 1.376(3) | N(1)—C(1) | 1.375(7) | N(1)—C(4) | 1.278(8) |
| N(1)—C(18) | 1.381(3) | N(1)—C(4) | 1.393(7) | N(1)—C(1) | 1.446(8) |
| N(2)—C(3) | 1.381(3) | N(2)—C(8) | 1.379(7) | N(2)—C(8) | 1.334(8) |
| N(2)—C(6) | 1.385(3) | N(2)—C(11) | 1.387(7) | N(2)—C(11) | 1.447(9) |
| C(1)···C(3) | 2.53 | C(4)···C(8) | 2.47 | C(1)—C(1′) | 1.607(11) |
| C(6)···C(8) | 2.49 | C(1)···C(25) | 2.48 | C(11)—C(11′) | 1.553(13) |
| C(11)···C(13) | 2.49 | C(11)···C(15) | 2.48 | C(4)···C(8) | 2.47 |
| C(16)···C(18) | 2.51 | C(18)···C(22) | 2.46 | | |
| Angles / deg | | | | | |
| N(1)–Fe(1)–N(2) | 89.55(7) | N(1)–Fe(1)–N(2) | 89.6(2) | N(1)–Fe(1)–N(2) | 87.27(18) |
| N(2)–Fe(1)–N(3) | 90.49(7) | N(2)–Fe(1)–N(3) | 90.1(2) | N(1)–Fe(1)–N(1′) | 79.5(3) |
| N(3)–Fe(1)–N(4) | 90.15(7) | N(3)–Fe(1)–N(4) | 90.2(2) | N(2′)–Fe(1)–N(2) | 78.7(3) |
| N(4)–Fe(1)–N(1) | 89.82(7) | N(4)–Fe(1)–N(1) | 90.2(2) | N(1′)–Fe(1)–N(2) | 139.77(19) |
| | | | | N(3)–Fe(1)–N(1) | 110.3(2) |
| | | | | C(1)–C(15)–C(1′) | 63.3(6) |
| | | | | C(11)–C(12)–C(11′) | 62.3(7) |
| | | | | C(4)–C(5)–C(8) | 110.3(4) |

$C^{\alpha}$—$C^{meso}$—$C^{\alpha}$ angles of 63.3(6)° and 62.3(7)°. These metrics of the cyclopropane rings are similar to those observed in previously described dicyclopropane octaethylporphyrinogens of iron, manganese and cobalt.[70-72]

The presence of the spirocyclopropane rings distorts the macrocycle and the constituent pyrroles. The presence of alternating formal single and double bonds in the pyrroles is plainly evident: N=C double bonds ($d_{avg}$(N(1)—C(4), (N(2)—C(8)) = 1.31 Å) are significantly shorter than their neighboring N—C single bonds ($d_{avg}$(N(1)—C(1), N(2)—C(11)) = 1.45 Å). The $C^{\alpha}$—$C^{\alpha}$ straps constrain the macrocycle along one axis, causing the 4-N core to deform from a square to a rectangle (∠(N(1)–Fe–N(2)) =

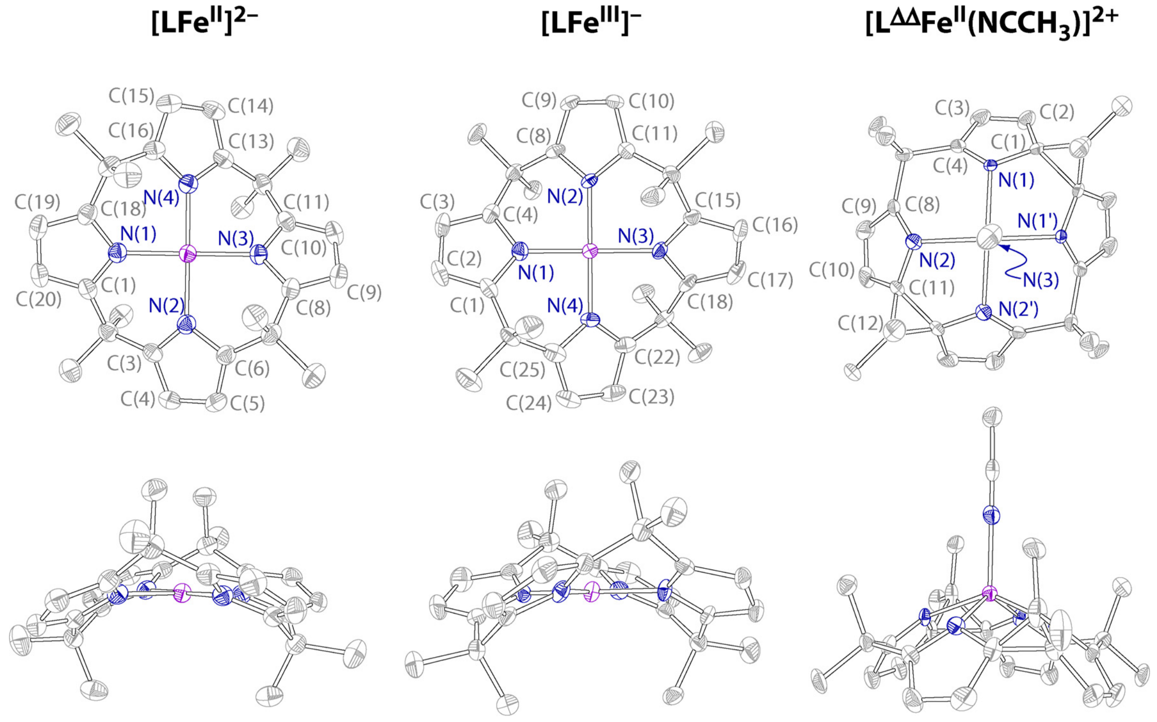

$[LFe^{II}]^{2-}$ $[LFe^{III}]^{-}$ $[L^{\Delta\Delta}Fe^{II}(NCCH_3)]^{2+}$

**Figure V.6.** Comparison of the iron porphyrinogen framework in its three available oxidation states, in the three crystal structures detailed above.

87.3° and $\angle$(N(1)–Fe–N(1A)) = 79.5°). The ruffled conformation of the $L^{4-}$ macrocycle is supplanted by a bowl conformation in $L^{\Delta\Delta}$, which is reminiscent of calixarenes[77] and "calixpyrroles",[78-82] in which all four pyrrole planes are tilted upwards relative to the 4-N plane. The conformational change from ruffle to bowl is accompanied by an upward movement of the $Fe^{II}$ center from the 4-N plane by 0.72 Å. The displaced $Fe^{II}$ center coordinates an axial $CH_3CN$ solvent molecule to engender a distorted square pyramidal coordination geometry. The four-electron oxidized macrocycle is a much weaker donor than the parent $L^{4-}$ porphyrinogen, as evidenced by long Fe—N(pyrrole) bonds; the $d_{avg}$(Fe—N(pyrrole)) = 2.12 Å is 0.18 Å longer than the average Fe—N(pyrrole) bond length of $[LFe^{II}]^{2-}$ and is longer than the Fe—N bond to the axial $CH_3CN$ ($d$(Fe—N(3)) = 2.065 Å). All five Fe—N distances in this free $[L^{\Delta\Delta}Fe^{II}(NCCH_3)]^{2+}$ entity, however, are significantly shorter than the corresponding ones in the previously reported polynuclear compound $[L^{\Delta\Delta}Fe^{II}(Cl)(Cu_4Cl_5)]$, indicating that the interacting $Cu_4Cl_5^{-}$ influences the structural properties of the iron porphyrinogen moiety.[69] Our results establish the stable existence of and intrinsic metrics for

$[L^{\Delta\Delta}Fe^{II}(solv)]^{2+}$ in the absence of an anionic axial ligand and of an interacting counter-ion.

## V.4.b. In solution — by NMR spectroscopy

The porphyrinogen framework was synthesized with deuterated *meso* methyls, allowing the solution structures of the series members to be probed by $^1H$ and $^2H$ NMR spectroscopy. As displayed in Figure V.7, NMR spectra of exceptionally high quality are obtained despite the presence of the paramagnetic iron centers. Owing to the *meso* $d_{24}$ substitution, the hydrogens on the methyl groups and pyrroles can be investigated in separate experiments and therefore are easily distinguished from each other.

The single resonance for the eight pyrrole hydrogens observed in the $^1H$ NMR spectra of $[LFe^{III}]^-$ and $[LFe^{III}]^-$ in solution (Figure V.7, top and middle trace, respectively) is consistent with the four-fold symmetry of the porphyrinogen in the solid state. The $^2H$ NMR spectra of the same compounds are also consistent with this fourfold symmetry but two signals of equal intensity are observed for the *meso* methyls. The

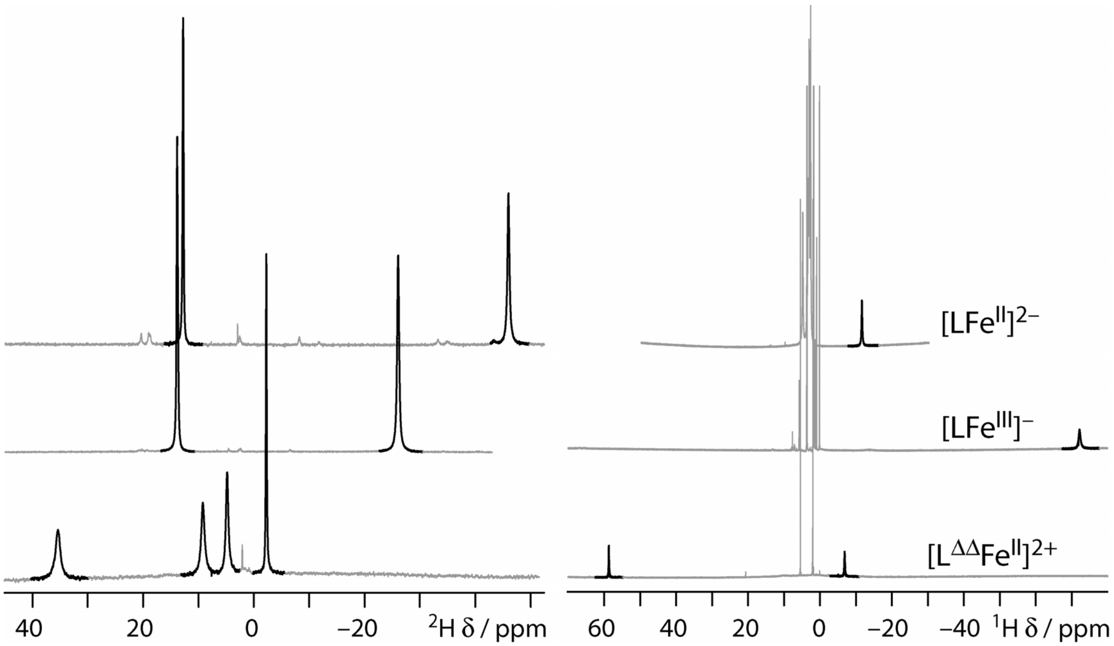

**Figure V.7.** $^2H$ (left) and $^1H$ (right) NMR spectra of the three paramagnetic iron $d_{24}$-porphyrinogen species. The $^2H$ NMR (77 MHz, $CH_3CN$) probes the *meso* methyl groups and the $^1H$ NMR (500 MHz, $CD_3CN$) probes the β pyrrole sites of the porphyrinogen macrocycle.

two distinct signals reflect a symmetry lower than $D_{4h}$, arising from either (i) coordination of the $Na^+$ ions to the one side of the macrocycle or (ii) retention of the $D_{2d}$ conformation of the solid-state structure for the molecules in solution. The invariance of the $^2H$ NMR spectrum to solvent (THF, diglyme or acetonitrile), to encryption of $Na^+$ by 18-crown-6 ether, and to replacement of $Na^+$ by $Bu_4N^+$ rules out possibility (i), thus the chair conformation of the tetrapyrrole observed in the solid state is retained in solution. The two peaks are ascribed to the axial and equatorial *meso* methyl positions (axial being defined as close to perpendicular to the 4-N plane, and equatorial rather parallel to it). This interpretation is further corroborated by the relative magnitudes of the paramagnetic shifts for the axial and equatorial methyl resonances. The paramagnetic shift, $\Delta\nu_{pc}/\nu$, of a nucleus at a position ($r$, $\theta$, $\phi$) relative to the paramagnetic iron center is given by

$$\frac{\Delta\nu_{pc}}{\nu} = \frac{\mu_0}{4\pi} \cdot \frac{\beta^2 \cdot S(S+1)}{9kT} \cdot \frac{3\cos^2\theta - 1}{r^3} \cdot \left(g_{par}^2 - g_{perp}^2\right) \tag{6}$$

as long the system has axial symmetry, the electron spin resides exclusively at iron, and the dipole coupling is purely through space ("pseudocontact").[83] In the above expression, $\mu_0$ is the magnetic permeability of vacuum, $k$ Boltzmann's constant, $T$ the absolute temperature, $S$ the electron spin quantum number, and $g_{\mathrm{par}}$ and $g_{\mathrm{per}}$ the components of the diagonalized *g*-tensor of the paramagnetic center that lie parallel and perpendicular to the molecular axis, respectively. By taking the ratio $(\Delta\nu_{pc})_{\mathrm{ax}}/(\Delta\nu_{pc})_{\mathrm{eq}}$, one only retains the geometric parameters. Equating the coordinates of the methyl hydrogens in solution to the position of the methyl carbon in the solid state, we find calculated values of $(\Delta\nu_{pc})_{\mathrm{ax}}/(\Delta\nu_{pc})_{\mathrm{eq}} = -3.0$ for $[\mathrm{LFe^{III}}]^-$ and $-4.2$ for $[\mathrm{LFe^{II}}]^{2-}$; the observed shift ratio between the axial and methyl resonances in Figure V.7 is $-2.5$ for $[\mathrm{LFe^{III}}]^-$ and $-4.6$ for $[\mathrm{LFe^{II}}]^{2-}$. Given the crudeness of the geometric approximation, the agreement is reasonable.

Relative to the two anionic iron porphyrinogens, both the $^1H$ and $^2H$ NMR spectra of $[\mathrm{L^{\Delta\Delta}Fe^{II}}]^{2+}$ show a doubling in the number of resonances (Figure V.7, bottom traces). This result is in line with the observed lowering in symmetry of the solid-state structure upon oxidation of the macrocycle. Thus the symmetry properties of the porphyrinogen system are revealed by appropriate deuteration of the tetrapyrrole.

# V.5. Conclusions

Three oxidation states of iron porphyrinogen have been unveiled in the absence of any redox or spectroscopically active counter-ions. A metal-centered Fe(II/III) redox activity, reminiscent of heme porphyrins, is observed. Owing to the highly reducing nature of the tetrapyrrole framework, the Fe(II/III) redox potential however is nearly one volt more negative than that of a typical heme cofactor. This metal-based redox activity is augmented by a multielectron chemistry of the porphyrinogen macrocycle. Two cyclopropane rings, formed by C—C coupling between the $\alpha$ carbons of adjacent pyrroles, function as two separate two-hole reservoirs within the porphyrinogen framework. The two-electron oxidized, singly $C^{\alpha}$—$C^{\alpha}$ bonded intermediate is unstable with respect to disproportionation; the ligand-based redox activity therefore proceeds in a single four-electron step. The oxidation of the tetrapyrrole is accompanied by a distortion of the 4-N core from a square to a rectangle.

The ability of the tetrapyrrole macrocycle to support redox transformations in addition to the metal establishes “artificial hemes” as more versatile redox cofactors than hemes. Redox activity based at the ligand is decoupled from the acid-base activity of the iron center. Large variations in the overall redox content can be accommodated without any changes in the metal’s primary coordination sphere. This is drastically different from the usual observation of a metal center that will have its coordination geometry and/or number change upon multielectron oxidation. For the case of hemes, oxidation is typically accompanied by an increase in metal-substrate bond order (e.g., oxo). It can be anticipated that iron porphyrinogens bearing halogen- or chalcogen-based ligand substrates will maintain more labile metal-substrate bonds in high oxidation states.

For example, Betley and Peters were able to describe an unusually wide range of oxidation states of iron within the same framework comprising a tripodal phosphine chelate and an N-based donor, from Fe(I) to Fe(IV) (Scheme V.2).[84-88] The design is based on the stepwise increase in metal-substrate bond order — from 0 (formally counting covalent bonds only) to 3 — and concomitant elimination of substituents from the substrate — from 3 (if L represents an ammine) to 0 (nitride) —

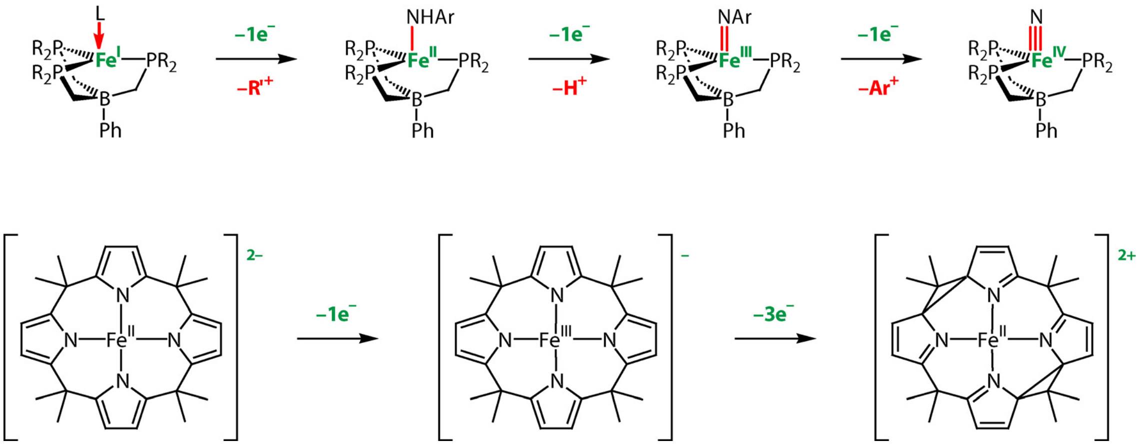

**Scheme V.2.** Two contrasting approaches to multielectron redox chemistry of mononuclear iron complexes. In the upper panel, the metal is the only redox center and a very wide range of OSs is achieved by coupling redox reactivity (green) to acid-base events (red), namely, the elimination of substituents within the substrate and the concomitant increase in metal-ligand bond order.[84-88] In the lower panel, a redox-active ligand enables the coordination complex to undergo an overall four-electron transformation without any change in the OS of the metal nor in the metal-substrate bonding (no substrate is bound). R represents an alkyl or aryl substituent, for example isopropyl or phenyl.

upon oxidation from Fe(I) to Fe(IV). In essence, a high OS is stabilized by multiple bonding and *vice versa*. In contrast to this, the participation of the redox-active ligand in the iron porphyrinogen redox series enables the overall OS to vary by up to four units without any changes in the bonding between metal and substrate (in this example, the metal-substrate bond order remains 0 throughout the series).

The next steps in the exploration of the iron porphyrinogen system will be the description of its electronic structures (Chapter VI) and its use for carrying out multielectron transformations (Chapter VII).

# V.6. Experimental section

## V.6.a. Synthesis

*Materials*

All compounds were handled, reactions were performed, and analytical samples were prepared in inert atmosphere using standard Schlenk, dry-box and vacuum-line techniques. Solvents were purchased from VWR Scientific Products and purified using a Braun solvent purification system or using standard solvent purification techniques.[89] Deuterated solvents were purchased from Cambridge Isotope Laboratories, degassed, dried and distilled by procedures similar to those used for non-isotopically enriched solvents. Ferrocenium tetrafluoroborate ($FcBF_4$) was purified as described (Chapter II). Other reagents were purchased from Aldrich and used as received. Elemental analyses were conducted at H. Kolbe Mikroanalytisches Laboratorium (Mühlheim a. d. Ruhr, Germany). Preparative methods for the $d_0$ and *meso*-perdeuteriomethyl ($d_{24}$) versions of each compound were identical; in each case, only one of both is described. Similarly, the only spectroscopic differences observed between both isotopic versions appeared in NMR and IR: reported are the NMR and IR data for the *meso*-perdeuteromethyl version.

*Synthesis of Na(THF)$_2$[LFe]*

A milky white suspension of 16.48 g (20.47 mmol) of $d_{24}$-$Na_4(THF)_4L$ in 600 mL of THF was charged with 3.89 g (30.71 mmol, 1.5 equiv) of anhydrous $FeCl_2$ beads (–10 mesh). The resulting mixture was stirred gently overnight with a large magnetic stir bar so that the $FeCl_2$ beads were maintained at the bottom of the flask. Over the course of the first hour of stirring, the mixture turned light green, then beige, brown and eventually deep red. A gray mixture of NaCl and Fe metal was filtered from the reacted solution; the filtrate was evaporated and dried to yield a solid, which was re-suspended in 400 mL pentane and subsequently stirred for 2 hr. The $d_{24}$-$Na(THF)_2[LFe]$ product was isolated by filtration and dried *in vacuo*. Yield: 13.02 g (95%) of a deep red powder. The crude product was used for further syntheses. A sample re-crystallized from a THF/pentane mixture was used to obtain the following analytical data. $^1$H NMR (500 MHz, THF-$d_8$): δ/ppm = 13.1 (ax. $CD_2H$), 3.62 (s, THF-α), 1.78 (s, THF-β), –72.2 (br, pyrrole). $^2$H NMR (76.8 MHz, THF): $\delta$= 13.1 (s, 12H, $Me_{ax}$), –27.9 (s, 12H, $Me_{eq}$). UV-vis $\lambda_{max}$/nm ($\varepsilon$/$M^{-1}cm^{-1}$) in $CH_3CN$: 332 (1200), 427 (4800), 526 (3900), ~570 (sh). IR $\nu_{max}$ / $cm^{-1}$ = 3096 m (pyrrole C–H), 2220 s (C–D), 2128 m (C–D), 2060 w (C–D), 1049 s, 917 m, 889 m, 790 w, 750 s. Anal. Calcd for $C_{36}H_{24}D_{24}FeN_4NaO_2$: C 64.36, N 8.34, Fe 8.31; Found: C 64.14, N 8.32, Fe 8.43.

*Synthesis of Na$_2$(THF)$_2$[LFe]*

The reactants $Na(THF)_2[LFe]$ (3.00 g, 4.63 mmol), Na metal (0.11 g, 4.63 mmol, 1 equiv) and naphthalene (0.30 g, 2.32 mmol, 0.5 equiv) were mixed in 200 mL of THF. The deep red mixture was refluxed until the foam was white. The cooled deep brown solution was passed through a frit in order to remove remaining solid Na and the filtrate was brought to dryness by evaporation. The solid $Na_2(THF)_2[LFe]$ residue was re-suspended in 100 mL hexane, stirred for 2 hr, and eventually filtered and dried *in vacuo*. Yield: 2.80 g (90%) of brown powder. $^1$H NMR (500 MHz, THF-$d_8$): δ/ppm = 12.1 (s, ~0.1H, $CD_2H$ impurity), 3.62 (s, 8H, THF-α), 1.78 (s, 8H, THF-β), –13.3 (br, 8H, pyrrole). $^2$H NMR (76.8 MHz, THF): δ/ppm = 12.1 (s, 12H, $Me_{ax}$), –46.9 (s, 12H, $Me_{eq}$). UV-vis $\lambda_{max}$/nm ($\varepsilon$/$M^{-1}cm^{-1}$) in $CH_3CN$: 330 (3300). IR $\nu_{max}$ / $cm^{-1}$ = 3086 m (pyrrole C–H), 2218 s (C–D), 2127 m (C–D), 2060 w (C–D), 1268 s, 1049 s, 1036 s, 919 m, 890 w, 791 w, 750 s. Anal. Calcd for $C_{36}H_{48}FeN_4Na_2O_2$: C, 64.48; H, 7.21; N, 8.35; Fe 8.33. Found: C, 64.35; H, 7.26; N, 8.28; Fe 8.32.

*Synthesis of [L$^{\Delta\Delta}$Fe](BF$_4$)$_2$.*

A sample of $d_{24}$-$Na(THF)_2[LFe]$ (1.86 g, 2.77 mmol) was dissolved in 50 mL of $CH_3CN$. Because $[L^{\Delta\Delta}Fe]^{2+}$ was found to be sensitive to ethers, the THF molecules solvating the $Na^+$ cations had to be removed. The solution was stirred at room temperature for 10 min, solvent was removed by evaporation and the remaining solid was dried, re-dissolved in 50 mL of $CH_3CN$ and added dropwise to a 50-mL blue $CH_3CN$ solution of $FcBF_4$. The green solution was stirred for 10 min, then again evaporated and dried. The resulting solid was re-suspended in 50 mL of $CH_2Cl_2$, stirred for 2 hr at room temperature, and the beige $d_{24}$-$[L^{\Delta\Delta}Fe](BF_4)_2$/$NaBF_4$ solid was separated from the green Fc/$FcBF_4$ supernatant by filtration The desired product was extracted from $NaBF_4$ by boiling the crude mixture in 500 mL of $CH_2Cl_2$. The resulting suspension was filtered and concentrated to 100 mL. The product was precipitated by dropwise addition of hexanes and it was isolated by filtration and dried *in vacuo*. A second harvest of the product, analytically identical to the first, was obtained by performing the extraction procedure an additional time on the original $d_{24}$-$[L^{\Delta\Delta}Fe](BF_4)_2/NaBF_4$ crude mixture. Combined $d_{24}$-$[LFe](BF_4)_2$ yield: 1.05 g (56%) of pale beige powder. $^1H$ NMR (500 MHz, $CD_3CN$): δ/ppm = 58.7 (br, 4H, pyrrole), –6.9 (br, 4H, pyrrole). $^2H$ NMR (76.8 MHz, $CH_3CN$): δ/ppm = 35.2 (6H, Me), 9.1 (6H, Me), 4.6 (6H, Me), –2.4 (6H, Me). UV-vis in $CH_3CN$: far UV ($\lambda_{max} < 230$ nm) band tailing into the visible. IR $\nu_{max}$ / $cm^{-1}$ = 3115 m (pyrrole C–H), 2220 w (C–D), 1575 m (C=N), 1564 m (C=N), 1117 s, 1105 s, 1071 s, 1048 s, 1035 s, 1011 s, 855 m. Anal. Calcd for $C_{28}H_8D_{24}FeN_4$: C, 49.59; N, 8.26; Fe, 8.23. Found C, 49.33; N, 8.17; Fe, 8.16.

## V.6.b. X-ray crystal structure determinations

*General technique*

X-ray quality crystals were coated with Paratone N oil and mounted on a glass fiber. X-ray diffraction data were collected on a Siemens diffractometer equipped with a CCD detector, using the Mo Kα radiation, selected by a graphite monochromator. The data were integrated to *hkℓ*-intensity and the final unit cell calculated using the SAINT v.4.050 program from Siemens. Solution and refinement were performed with the SHELXTL v.5.03 suite of programs developed by G. M. Sheldrick and Siemens Industrial Automation, 1995. Least-squares refinements were applied to $F^2$, with hydrogen atoms of organic fragments placed at calculated positions using a standard riding model and refined isotropically. No absorption correction was performed.

*$[LFe^{III}]^-$ compounds*

Red-black crystals of $[(diglyme)_2Na][LFe^{III}]$ were grown from a supersaturated diglyme solution and data were collected at –80°C. The structure was solved using direct methods; refinement proceeded and converged normally. Red-black crystals of the $\{[(THF)_3Fe^{II}(\mu\text{-}Cl)_3Fe^{II}(THF)_3][(THF)_4Fe^{II}(\mu\text{-}Cl)_2Fe^{II}(THF)_4]_{1/2}\}^{2+}$ salt of $[LFe^{III}]^-$ were grown from a supersaturated THF/toluene solution and data were collected at –80°C. The structure was solved using Patterson's method; one of the two toluene solvent molecules contained in the crystal was strongly disordered and could not be properly refined.

### *$[LFe^{II}]^{2-}$ compound*

Orange crystals containing $[LFe^{II}]^{2-}$ could be grown from pure ethereal solvents but were too oxygen-sensitive to be manipulated, turning instantaneously deep red upon breaking of the sealed ampoule in which they were grown. It was observed that crystals grown from supersaturated THF solution in the presence of pyridine-*N*-oxide were slightly more robust and a satisfactory dataset for $[(pyO)(THF)Na]_2[LFe^{II}]$ could be collected at –80 °C. The structure was solved using direct methods; refinement proceeded and converged normally.

### *$[L^{\Delta\Delta}Fe^{II}]^{2+}$ compound*

Despite repeated attempts, $[L^{\Delta\Delta}Fe^{II}]^{2+}$ would not crystallize with $BF_4^-$ as the counter-ion, but exchange of tetrafluoroborate for cobalticarborane proceeded smoothly in dichloromethane and afforded orange single crystals of $[L^{\Delta\Delta}Fe^{II}(NCCH_3)][(C_2B_9H_{11})_2Co]_2{\bullet}2CH_3CN{\bullet}2\textit{o}\text{-}C_6H_4Cl_2$ by slow vapor diffusion of toluene into an *ortho*-dichlorobenzene / acetonitrile solution. The data were collected at 100 K and the structure was solved using direct methods. Throughout the refinement, the $^2H$ atoms were treated as natural-abundance H atoms; in the initial stages of refinement, all atoms of the cobalticarborane anions (except for the metal) were treated as borons, then hydrogens were located from the difference map, and finally the carbon atoms were identified by their abnormal anisotropic thermal parameters and abnormal bond distances to hydrogens. In the end, all B—H and C—H distances were fixed to 1.10(±0.10) Å, a value measured for $C_2B_9H_{13}$ by electron diffraction.[90] The crystal of polar space group *Abm*2 was found to be a twin characterized by a value of 0.66(±0.03) for Flack's absolute structure parameter *x*.[91]

## V.6.c. Physical Measurements

*Nuclear magnetic resonance spectroscopy*

$^1$H NMR spectra were recorded at the MIT Department of Chemistry Instrumentation Facility (DCIF) on a Varian Inova-500 spectrometer, and $^2$H NMR spectra were recorded on a Varian Inova-500 equipped with an inverse probe. $^1$H NMR chemical shifts are quoted in ppm relative to tetramethylsilane and spectra have been internally calibrated to the monoprotio impurity of the deuterated solvent. $^2$H-NMR spectra were referenced to the peak of the monodeuterio impurity of the natural-abundance solvent; the chemical shift was set to be equal to that observed in $^1$H-NMR for the monoprotio impurity of the corresponding deuterated solvent. Spectra were recorded at 20 °C and a 30-s delay was used between successive pulses in order to allow for quantitative integration of the solvent peaks in $^1$H-NMR. The quality of the porphyrinogen NMR spectra was sufficiently high that even the $-CD_2H$ isotopic impurity in *meso*-$CD_3$ (99.9% D) was observable in $^1$H NMR.

*Infrared spectroscopy*

IR absorption spectra on solids dispersed in nujol mulls were recorded on a Perkin-Elmer 2000 FT-IR spectrophotometer.

## V.6.d. Electrochemistry

Electrochemistry was performed with a standard three-electrode configuration using a CV-50W potentiostat (Bioanalytical Systems). The working electrode was Pt, the auxiliary electrode was a Pt wire and the reference was an Ag/$AgNO_3$ electrode, which was externally referenced to the $Fc^+/Fc$ couple ($E^o(Fc^+/Fc) = 0.65$ V (in $CH_3CN$) and 0.69 V (in THF) vs NHE).[92] All potentials reported are *vs* NHE. The most well-behaved electrochemistry was observed for the tetrabutylammonium ($Bu_4N^+$) salts of the $[LFe^{III}]^-$ and $[LFe^{II}]^{2-}$ anions, which were prepared by adding a stoichiometric amount of $Bu_4NCl$ to a THF solution of the $Na^+$ salts of the respective complexes. The white NaCl precipitate was separated from the reaction mixture by filtration and the desired product was obtained by evaporating THF from the filtrate under vacuum. The remaining solid was triturated in hexanes and isolated by filtration. Cyclic voltammetry (CV), differential pulse voltammetry (DPV) and chronocoulometry experiments were conducted on a $CH_3CN$ solution containing 1 mM $(Bu_4N)[LFe^{III}]$ and 0.04 M $Bu_4NBPh_4$. The scan rate dependence of CV waves were recorded over the potential range of 50 - 600 mV/s. DPV was performed by polarizing the working electrode at an initial, negative potential for 2 seconds and then scanning the potential axis in the positive direction. In the chronocoulometry experiment, the working electrode was poised at +0.31 V for 2 s, after which it was jumped to either –0.90 or +0.91 V. The total charge that was passed through the electrode was measured for 250 ms. The resulting curves were analyzed and fitted in their linear regime by the CV-50W software using a least-squares procedure.

## V.7. References

1 Gray, H. B.; Winkler, J. R. In *Electron Transfer in Chemistry*; Balzani, V., Ed.; Wiley-VCH: Weinheim, Germany, 2001; Vol. 3.1.1; pp 3-23.

2 Wright, J. L.; Wang, K.; Geren, L.; Saunders, A. J.; Pielak, G. J.; Durham, B.; Millett, F. *Adv. Chem. Ser.* **1998**, *254*, 99-110.

3 Gray, H. B.; Winkler, J. R. *Annu. Rev. Biochem.* **1996**, *65*, 537-561.

4 Winkler, J. R.; Gray, H. B. *Chem. Rev.* **1992**, *92*, 369-379.

5 Tollin, G. In *Electron Transfer in Chemistry*; Balzani, V., Ed.; Wiley-VCH: Weinheim, Germany, 2001; Vol. 4.1.5; pp 202-231.

6 Wang, K.; Zhen, Y.; Sadoski, R.; Grinnell, S.; Geren, L.; Ferguson-Miller, S.; Durham, B.; Millett, F. *J. Biol. Chem.* **1999**, *274*, 38042-38050.

7 Nocek, J. M.; Zhou, J. S.; Forest, S. D.; Priyadarshy, S.; Beratan, D. N.; Onuchic, J. N.; Hoffman, B. M. *Chem. Rev.* **1996**, *96*, 2459-2489.

8 Millett, F. S. *J. Bioenerg. Biomembr.* **1995**, *27*, 261-262.

9 McLendon, G.; Hake, R. *Chem. Rev.* **1992**, *92*, 481-490.

10 Scott, R.; Mauk, A. G. *Cytochrome c: A Multidisciplinary Approach*; University Science Books: Sausalito, CA, 1996.

11 Namslauer, A.; Brzezinski, P. *FEBS Lett.* **2004**, *567*, 103-110.

12 Namslauer, A.; Braenden, M.; Brzezinski, P. *Biochemistry* **2002**, *41*, 10369-10374.

13 Qian, J; Mills, D. A.; Geren, L.; Wang, K.; Hoganson, C. W.; Schmidt, B.; Hiser, C.; Babcock, G. T.; Durham, B.; Millett, F.; Ferguson-Miller, S. *Biochemistry* **2004**, *43*, 5748-5756.

14 Antonini, E.; Brunori, M. *Hemoglobin and Myoglobin in Their Reactions with Ligands*; North-Holland: Amsterdam, 1971.

15 Kundu, S.; Trent, J. T.; Hargrove, M. S. *Trends Plant Sci*. **2003**, *8*, 387-393.

16 Momenteau, M.; Reed, C. A. *Chem. Rev.* **1994**, *94*, 659-698.

17 Riggs, A. F. *Curr. Opin. Struct. Biol.* **1991**, *1*, 915-921.

18 *Cytochrome P450*, 2nd ed; Ortiz de Montellano, P. R., Ed.; Plenum Press: New York, 1995.

19 Makris, T. M.; Davydov, R.; Denisov, I. G.; Hoffman, B. M.; Sligar, S. G. *Drug Metabol. Rev.* **2002**, *34*, 691-708.

20 Sligar, S. G. *Essays Biochem*. **1999**, *34*, 71-83.

21 Sono, M.; Roach, M. P.; Coulter, E. D.; Dawson, J. H. *Chem. Rev*. **1996**, *96*, 2841-2887.

22 Udit, A. K.; Hill, M. G.; Bittner, V. G.; Arnold, F. H.; Gray, H. B. *J. Am. Chem. Soc.* **2004**, *126*, 10218-10219.

23 Munro, A. W.; Leys, D. G.; McLean, K. J.; Marshall, K. R.; Ost, T. W. B.; Daff, S.; Miles, C. S.; Chapman, S. K.; Lysek, D. A.; Moser, C. C.; Page, C. C.; Dutton, P. L. *Trends Biochem. Sci.* **2002**, *27*, 250-257.

24 Everse, J.; Everse, K. E.; Grisham, M. B. *Peroxidases in Chemistry and Biology*; CRC Press: Boca Raton, FL, 1991; Vol. I and II.

25 Erman, J. E.; Hager, L. P.; Sligar, S. G. *Adv. Inorg. Biochem.* **1994**, *10*, 71-118.

26 Dunford, H. B. *Heme Peroxidases*; John Wiley: Chichester, 1999.

27 Ozaki, S.-I.; Matsui, T.; Roach, M. P.; Watanabe, Y. *Coord. Chem. Rev.* **2000**, *198*, 39-59.

28 *The Porphyrin Handbook*; Kadish, K. M., Smith, K. M.; Guilard, R., Ed.; Academic Press: New York, 2000; Vol. 9.

29 Rosenblatt, M. M.; Huffman, D. L.; Wang, X.; Remmer, H. A.; Suslick, K. S. *J. Am. Chem. Soc.* **2002,** *124*, 12394-12395.

30 Ghirlanda, G.; Osyczka, A.; Liu, W.; Antolovich, M.; Smith, K. M.; Dutton, P. L.; Wand, A. J.; DeGrado, W. F. *J. Am. Chem. Soc.* **2004**, *126*, 8141-8147.

31 Chen, X.; Discher, B. M.; Pilloud, D. L.; Gibney, B. R.; Moser, C. C.; Dutton, P. L. *J. Phys. Chem. B* **2002**, *106*, 617-624.

32 Fahnenschmidt, M.; Bittl, R.; Schlodder, E.; Haehnel, W.; Lubitz, W. *Phys. Chem. Chem. Phys.* **2001**, *3*, 4082-4090.

33 Willner, I.; Heleg-Shabtai, V.; Katz, E.; Rau, H. K.; Haehnel, W. *J. Am. Chem. Soc.* **1999**, *21*, 6455-6468.

34 Shifman, J. M.; Moser, C. C.; Kalsbeck, W. A.; Bocian, D. F.; Dutton, P. L. *Biochem.* **1998**, *37*, 16815-16827.

35 Reedy, C. J.; Kennedy, M. L.; Gibney, B. R. *Chem. Commun*. **2003**, *5*, 570-571.

36 Moffet, D. A.; Foley, J.; Hecht, M. H. *Biophys. Chem*. **2003**, *105*, 231-239.

37 Topoglidis, E.; Discher, B. M.; Moser, C. C.; Dutton, P. L.; Durrant, J. R *Chem. Bio. Chem.* **2003**, *4*, 1332-1339.

38 Armstrong, F. A.; Hill, H. A. O.; Walton, N. J. *Acc. Chem. Res.* **1988**, *21*, 407-413.

39 McMahon, B. H.; Fabian, M.; Tomson, F.; Causgrove, T. P.; Bailey, J. A.; Rein, F. N.; Dyer, R. B.; Palmer, G.; Gennis, R. B.; Woodruff, W. H. *Biochim. Biophys. Acta* **2004**, *1655*, 321-331.

40 Telford, J. R.; Wittung-Stafshede, P.; Gray, H. B.; Winkler, J. R. *Acc. Chem. Res.* **1998**, *31*, 755-763.

41 Schultz, B. E.; Chan, S. I. *Proc. Natl. Acad. Sci.* **1998**, *95*, 11643-11648.

42 Nocek, J. M.; Zhou, J. S.; Forest, S. D.; Priyadarshy, S.; Beratan, D. N.; Onuchic, J. N.; Hoffman, B. M. *Chem. Rev.* **1996**, *96*, 2459-2489.

43 Winkler, J. R.; Malmstroem, B. G.; Gray, H. B. *Biophys. Chem.* **1995**, *54*, 199-209.

44 Dunn, A. R.; Dmochowski, I. J.; Winkler, J. R.; Gray, H. B. *J. Am. Chem. Soc.* **2003**, *125*, 12450-12456.

45 Millett, F.; Durham, B. *Photosynth. Res.* **2004**, *82*, 1-16.

46 Springs, S. L.; Bass, S. E.; Bowman, G.; Nodelman, I.; Schutt, C. E.; McLendon, G. L. *Biochemistry*, **2002**, *41*, 4321-4328.

47 McLendon, G.; Komar-Panicucci, S.; Hatch, S *Adv. Chem. Phys.* **1999**, *107*, 591-600.

48 Zhou, J. S.; Tran, S. T.; McLendon, G.; Hoffman, B. M. *J. Am. Chem. Soc.* **1997**, *119*, 269-277.

49 Scott, J. R.; McLean, M.; Sligar, S. G.; Durham, B.; Millett, F. *J. Am. Chem. Soc.* **1994**, *116*, 7356-7362.

50 Durham, B.; Pan, L. P.; Long, J. E.; Millett, F. *Biochemistry* **1989**, *28*, 8659-8665.

51 Windsor, M. W.; Holten, D. *Phi. Trans. R. Soc. Lond. A* **1980**, *298*, 335-349.

52 Yeh, C.-Y.; Chang, C. J.; Nocera, D. G. *J. Am. Chem. Soc.* **2001**, *123*, 1513-1414.

53 Pistorio, B. J.; Chang, C. J.; Nocera, D. G. *J. Am. Chem. Soc.* **2002**, *124,* 7884-7885.

54 Loh, Z.-H.; Miller, S. E.; Chang, C. J.; Carpenter, S. D.; Nocera, D. G. *J. Phys. Chem. A.* **2002,** *106,* 11700-11708.

55 Thompson, D. W.; Kretzer, R. M.; Lebeau, E. L.; Scaltrito, D. V.; Ghiladi, R. A.; Lam, K.-C.; Rheingold, A. L.; Karlin, K. D.; Meyer G. J. *Inorg. Chem.* **2003**, *42*, 5211-5218.

56 Chng, L. L.; Chang, C. J.; Nocera, D. G. *Org. Lett.* **2003,** *5*, 2421-2424.

57 Chang, C. J.; Chng, L. L.; Nocera, D. G. *J. Am. Chem. Soc.* **2003,** *125,* 1866-1876.

58 Chang, C. J.; Yeh, C.-Y.; Nocera, D. G. *J. Org. Chem.* **2002**, *67*, 1403-1406.

59 Collman, J. P.; Wang, Z.; Straumanis, A.; Quelquejeu, M.; Rose, E. *J. Am. Chem. Soc.* **1999**, *121*, 460-461.

60 Nam, W.; Oh, S.-Y.; Sun, Y. J.; Kim, J.; Kim, W.-K.; Woo, S. K.; Shin, W. *J. Org. Chem.* **2003**, *68*, 7903-7906.

61 Mansuy, D. *Coord. Chem. Rev.* **1993**, *125*, 129-141.

62 Collman, J. P.; Boulatov, R.; Sunderland, C. J.; Fu, L. *Chem. Rev.* **2004**, *104*, 561-588.

63 Watanabe, Y. in *The Porphyrin Handbook*; Kadish, K. M., Smith, K. M.; Guilard, R., Ed.; Academic Press: New York, 2000; Vol. 4, pp 97-118.

64 Schulz, C. E.; Devaney, P. W.; Winkler, H.; Debrunner, P. G.; Doan, N.; Chiang, R.; Rutter, R.; Hager, L. P. *FEBS Lett.* **1979**, *103*, 102-105.

65 Groves, J. T.; Haushalter, R. C.; Nakamura, M.; Nemo, T. E.; Evans, B. J. *J. Am. Chem. Soc.* **1981**, *103*, 2884-2886.

66 Penner-Hahn, J. E.; Smith Eble, K.; McMurry, T. J.; Renner, M.; Balch, A. L.; Groves, John T.; Dawson, J. H.; Hodgson, K. O. *J. Am. Chem. Soc.* **1986**, *108*, 7819-7825.

67 Nam, W.; Ryu, Y. O.; Song, W. J. *J. Biol. Inorg. Chem.* **2004**, *9*, 654-660.

68 Floriani, C.; Floriani-Moro, R. in *The Porphyrin Handbook*; Kadish, K. M., Smith, K. M.; Guilard, R., Ed.; Academic Press:New York, 2000; Vol. 3, pp 405-420.

69 Jubb, J.; Floriani, C.; Chiesi-Villa, A.; Rizzoli, C. *J. Am. Chem. Soc.* **1992**, *114*, 6571-6573.

70 De Angelis, S.; Solari, E.; Floriani, C.; Chiesi-Villa, A.; Rizzoli, C. *J. Am. Chem. Soc.* **1994**, *116*, 5691-5701.

71 De Angelis, S.; Solari, E.; Floriani, C.; Chies-Villa, A.; Rizzoli, C. *J. Am. Chem. Soc.* **1994**, *116*, 5702-5713.

72 Piarulli, U.; Solari, E.; Floriani, C.; Chiesi-Villa, A.; Rizzoli, C. *J. Am. Chem. Soc.* **1996**, *118*, 3634-3642.

73 Crescenzi, R.; Solari, E.; Floriani, C.; Chiesi-Villa, A.; Rizzoli, C. *J. Am. Chem. Soc.* **1999**, *121*, 1695-1706.

74 Janas, Z.; Sobota, P.; Lis, T. J. *Chem. Soc. Dalton Trans.* **1991**, 2429-1434.

75 Lee, W. K.; Lio, B.; Park, C. W.; Shine, H. J.; Guzman-Jimenez, I. Y.; Whitmire, K. H. *J. Org. Chem.* **1999**, *64*, 9206-9210.

76 Battistuzzi, G.; D'Onofrio, M.; Borsari, M.; Sola, M.; Macedo, A. L.; Moura, J. J. G.; Rodrigues, P. *J. Biol. Inorg. Chem.* **2000**, *5*, 748-760.

77 Gutsche, C. D.; Muthukrishnan, R. *J. Org. Chem.* **1978**, *43*, 4905-4906.

78 Gale, P. A.; Sessler, J. L.; Lynch, V.; Sansom, P. I. *Tet. Lett.* **1996**, *37*, 7881-7884.

79 Anzenbacher, P., Jr.; Jursíková, K.; Lynch, V. M.; Gale, P. A.; Sessler, J. L. *J. Am. Chem. Soc.* **1999**, *121*, 11020-11021.

80 Sessler, J. L.; Anzenbacher, P., Jr.; Miyaji, H.; Jursiková, K.; Bleasdale, E. R.; Gale, P. A. *Ind. Eng. Chem. Res.* **2000**, *39*, 3471-3478.

81 Nielsen, K. A.; Jeppesen, J. O.; Levillain, E.; Becher, J. *Angew. Chem. Int. Ed.* **2003**, *42*, 187-191.

82 Yoon, D.-W.; Hwang, H.; Lee, C.-H. *Angew. Chem. Int. Ed.* **2002**, *41*, 1757-1759.

83 Bertini, I.; Luchinat, C. *Physical Methods for Chemists*; Drago, R. S., Ed.; Saunders College: Ft. Worth, 1977; Vol. 3, pp 500-556.

84 Brown, S. D.; Peters, J. C. *J. Am. Chem. Soc.* **2005**, *127*, 1913-1923

85 Betley, T. A.; Peters, J. C. *J. Am. Chem. Soc.* **2004**, *126*, 6252-6254

86 Brown, S. D. Peters, J. C. *J. Am. Chem. Soc.* **2004**, *126*, 4538-4539

87 Betley, T. A.; Peters, J. C. *J. Am. Chem. Soc.* **2003**,*125*, 10782-10783

88 Brown, S. D.; Betley, T. A.; Peters, J. C. *J. Am. Chem. Soc.* **2003**, *125*, 322-323

89 Armarego, W. L. F.; Perrin, D. D. *Purification of Laboratory Chemicals*, 4th ed.; Butterworth-Heinmann: Oxford, 1996.

90 Mackie, I. D.; Robertson, H. E.; Rankin, D. W. H.; Fox, M. A.; Malget, J. M. *Inorg. Chem.* **2004**, *43*, 5387-5392.

91 Flack, H. D. *Acta Cryst.* **1983**, *A39*, 876-881.

92 Connelly, N. G.; Geiger, W. E. *Chem. Rev.* **1996**, *96*, 877-910.

# Chapter VI

# Electron transfer series of iron porphyrinogen — electronic structures

Parts of this Chapter have been published:

Bachmann, J.; Nocera, D. G. *J. Am. Chem. Soc.* **2005**, *127*, 4730-4743

## VI.1. Introduction

In a coordination complex between a redox-active metal ion and a redox-active ligand, the assignment of individual oxidation states for each of the two entities is inherently delicate. One can argue that OSs are not a physical observable, therefore their determination does not provide any tangible information on the system — it definitely does not supplant the full description of the ground-state electronic structure. However, the intuition of inorganic chemists tends to be guided by simple concepts and formalisms, and consequently, oxidation states in metal dithiolenes,[1-28] in hemes,[29-45] and in related systems[46-51] all have given rise to controversy, and have justified thorough experimental and theoretical investigations.

The electronic structures of oxidized metal porphyrinogens have not to date been explored because the compounds have been isolated as salts of iron-halo and polynuclear copper-halo counter-anions and with axial halide ligands,[52-57] which have obscured the spectroscopy of the porphyrinogen moieties. The development of synthetic procedures that allow the isolation and characterization of porphyrinogen complexes of redox-inert and redox-active metals (Chapters II and V, respectively) has now rendered their experimental and theoretical description accessible. Chapter III unveiled the mixed-valent nature of the intermediary oxidation state $L^{\Delta 2-}$. This Chapter considers the three oxidation states of iron porphyrinogen — dianion, monoanion and dication. Experimental techniques selectively probing the metal, on the one hand, and the ligand, on the other hand, and theoretical computations converge to build a consistent picture of their electronic structures. They establish that individual OSs for metal and ligand are well defined and integer.

## VI.2. Experimental characterization of the ground state

### VI.2.a. Results from NMR and X-ray crystallography

The techniques most sensitive to the oxidation state of the macrocycle are structural in nature, given that oxidation of $L^{4-}$ to $L^{\Delta\Delta}$ translates into the formation of two new C—C bonds. In this respect, the data presented in Chapter V are unambiguous. Paramagnetic $^1$H and $^2$H NMR spectroscopies both clearly indicate a lowering of the symmetry from fourfold in the anionic OSs to twofold in the dication. The crystal structures of the anions show no $C^\alpha$—$C^\alpha$ contact (2.46 Å ≤ $C^\alpha \cdots C^\alpha$ ≤ 2.53 Å), whereas in the dication two $C^\alpha$—$C^\alpha$ bonds are observed, of lengths 1.55 and 1.61 Å, respectively — slightly elongated relative to the 1.55-Å $C^\alpha$—$C^\alpha$ bond of $[L^\Delta Zn(NCMe)]$.

### VI.2.b. UV-vis absorption spectroscopy

Solutions of $[LFe^{III}]^-$ are blood red whereas those of $[LFe^{II}]^{2-}$ are pale yellow and those of $[L^{\Delta\Delta}Fe^{II}]^{2+}$ even paler in color. Figure VI.1 reproduces the absorption spectra of $[LFe^{II}]^{2-}$, $[LFe^{III}]^-$ and $[L^{\Delta\Delta}Fe^{II}]^{2+}$ in $CH_3CN$. The intense color of $[LFe^{III}]^-$ arises from two bands at

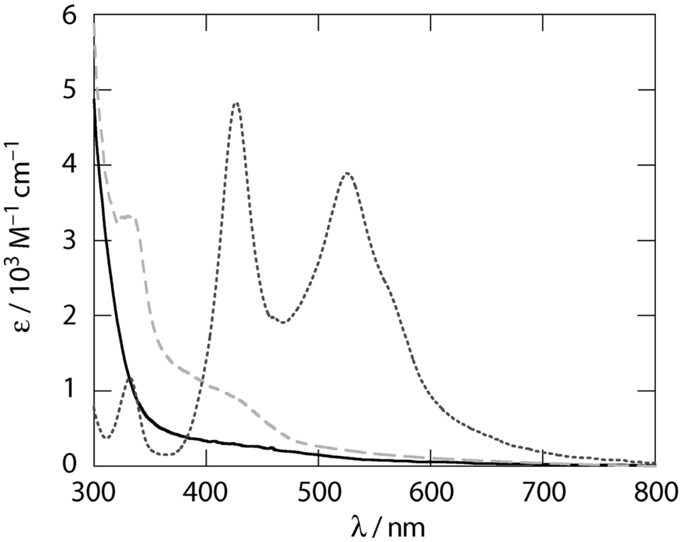

**Figure VI.1.** UV-visible absorption spectra of $Na_2(THF)_2[LFe^{II}]$ (– – –), $Na(THF)_2[LFe^{III}]$ (----), and $[L^{\Delta\Delta}Fe^{II}](BF_4)_2$ (——) in MeCN.

427 and 526 nm that dominate the absorption profile; a ~570 nm shoulder is observed on the trailing edge of the lowest energy absorption band. The molar absorption coefficients of both bands suggest a charge-transfer nature for the transitions. A ligand-to-metal character for this charge transfer concurs with the very reducing nature of the $L^{4-}$ ligand and the presence of an oxidizing $Fe^{III}$ center. The featureless profiles of both $[LFe^{II}]^{2-}$ and $[L^{\Delta\Delta}Fe^{II}]^{2+}$ support this LMCT assignment: reduction of the metal and oxidation of the ligand would cause a LMCT to blue shift into the ultraviolet spectral region. Accordingly, a charge-transfer absorption is not observed for either compound.

## VI.2.c. EPR spectroscopy

The EPR spectrum of $(Bu_4N)[LFe^{III}]$, shown in Figure VI.2, immediately establishes the half-integer spin of $[LFe^{III}]^{-}$. It is similar to those of $Fe^{III}$ ($S = 3/2$) ions residing in the square ligand fields of corroles and porphyrins in the absence of axial ligands.[58,59] The observed $g$ values of 4.2 (at $\delta A/\delta H = 0$) and 1.95 (at $\delta^2 A/\delta H^2 = 0$) are typical of an intermediate-spin $Fe^{III}$ ($g_x = g_y = 4$, $g_z = 2$) with large axial zero-field splitting (zfs) ($D >> h\nu$) but no rhombic asymmetry ($E/D = 0$).[60] These zfs features are in agreement with the fourfold $D_{2d}$ symmetry of the tetrapyrrole complexes. Per the results of Sakai *et al.*,[58] the small high-field deviation from $g_z = 2$ indicates a single electron occupancy for $d_{xz}$, $d_{yz}$ and $d_{z^2}$; this result is to be confirmed theoretically. Spectra of more dilute samples exhibit a complicated fine structure which we did not attempt to interpret. Although intermediate spin states are relatively rare for Fe(II) and Fe(III), they are by far the most prevalent in the few reported square planar complexes of those ions.[61-65]

$(Bu_4N)_2[LFe^{II}]$ was found to be EPR silent, consistent with an integer-spin Fe(II) subjected to a large zfs ($D >> h\nu$, $E/D = 0$). The observation of an EPR spectrum (Figure VI.2) for $[L^{\Delta\Delta}Fe^{II}](BF_4)_2$ indicates rhombic distortion from a square coordination environment, $E/D \neq 0$. The formation of both cyclopropane rings, observed by crystallography and by NMR, presumably results in $m_s$ state mixing, giving rise to otherwise forbidden transitions.

## VI.2.d. Mössbauer spectroscopy

Definitive experimental oxidation state and spin state assignments for the inorganic centers of $[LFe^{II}]^{2-}$ and $[L^{\Delta\Delta}Fe^{II}]^{2+}$ were afforded by their Mössbauer spectra, displayed in

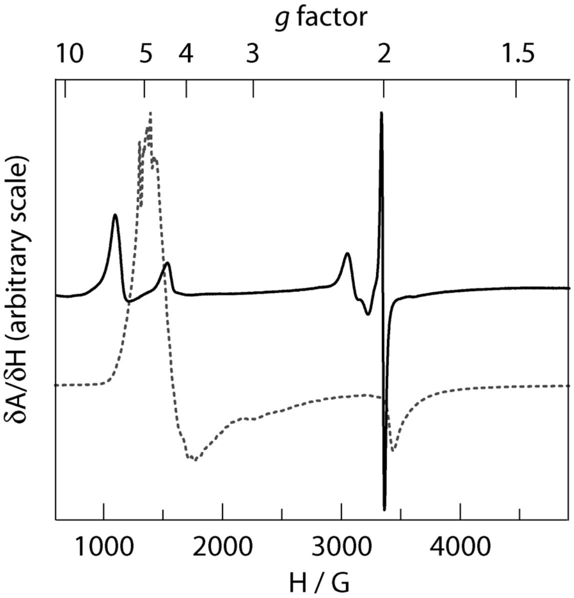

**Figure VI.2.** Frozen-solution X-band (9.385 GHz) EPR spectra of $(Bu_4N)[LFe^{III}]$ (----) in frozen THF and $[L^{\Delta\Delta}Fe^{II}](BF_4)_2$ (——) in frozen $CH_3CN$ at 4.5 K. $[LFe^{II}]^{2-}$ is EPR silent.

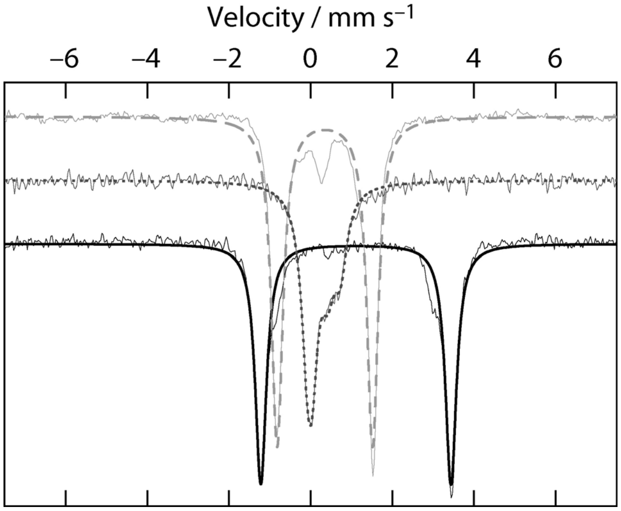

**Figure VI.3.** Fitted $^{57}Fe$ Mössbauer spectra of powdered $Na_2(THF)_2[LFe^{II}]$ (– – –), $(Cp^*{}_2Fe)[LFe^{III}]$ (----), and $[L^{\Delta\Delta}Fe^{II}](BF_4)_2$ (——) at 4.2 K. Thin lines link the corresponding experimental datapoints. The vertical axis is an arbitrary transmission scale.

Figure VI.3. The single quadrupole doublet exhibited by $[LFe^{II}]^{2-}$ ($\delta$ = 0.35 mm/s, $\Delta E_q$ = 2.34 mm/s) is characteristic of an intermediate spin, $S = 1$.[64,65] Given the similarity of the Fe coordination environments in $[LFe^{III}]^{-}$ and $[LFe^{II}]^{2-}$, it is not surprising that both exhibit the intermediate spin corresponding to a purely planar geometry.

Because our samples of $Na[LFe^{III}]$ always displayed a weak signal corresponding to a $[LFe^{II}]^{2-}$ impurity, the redox purity of $[LFe^{III}]^{-}$ was ensured by reaction of $Na[LFe^{III}]$ with excess decamethylferrocenium hexafluorophosphate ($Cp^*_2FePF_6$). The redox potential of decamethylferrocenium (–0.1 V *vs* NHE in $CH_2Cl_2$ and in MeCN)[66] is sufficient to convert any remaining $[LFe^{II}]^{2-}$ to $[LFe^{III}]^{-}$ without further oxidizing $[LFe^{III}]^{-}$ to $[L^{\Delta\Delta}Fe^{II}]^{2+}$. The Mössbauer spectrum of the resulting $(Cp^*_2Fe)[LFe^{III}]$ displays, in addition to the known signal of $Cp^*_2Fe^+$ (found at $\delta$ = 0.57 mm/s, $\Delta E_q$ = 0.31 mm/s, within the range of values reported for various salts of $Cp_2Fe^+$ and $Cp^*_2Fe^+$),[67-69] a very narrow doublet at very low isomer shift ($\delta$ = –0.02 mm/s, $\Delta E_q$ = 0.11 mm/s). The signal observed in solids of $Na[LFe^{III}]$ and $(Bu_4N)[LFe^{III}]$ is similar; it is virtually independent of temperature between 4.2 K and 250 K, which confirms that the identity of the compound studied under the experimental conditions of Mössbauer spectroscopy is the same as that observed by different techniques at different temperatures. The small values of both $\delta$ and $\Delta E_q$ for $[LFe^{III}]^{-}$ are somewhat unexpected for an intermediate-spin Fe(III) ion; however, the literature is very scarce in Mössbauer data of planar Fe(III) compounds, and therefore, no benchmark is available for planar, $S = 3/2$ Fe(III). In fact, the most relevant data are provided by Seppelt for $Fe(OTeF_5)_3$, which is likely high spin and the adduct-free form of which is not characterized structurally, with $\delta \sim 0.2$ mm/s, $\Delta E_q$ = 2.26 mm/s.[70]

The Mössbauer spectrum of the $[L^{\Delta\Delta}Fe^{II}]^{2+}$ cation ($\delta$ = 1.11 mm/s, $\Delta E_q$ = 4.66 mm/s) is very intriguing as well. The large quadrupole splitting clearly indicates a high spin state, $S = 2$;[71] but also, this $\Delta E_q$ is to the best of our knowledge the largest reported to date, surpassing the value of 4.55 mm/s that is observed for the distorted tetrahedral $Fe^{II}$ ($S = 2$) center in $[Fe_3(SC_6H_2{}^{i}Pr_3\text{-}2,4,6)_4\{N(SiMe_3)_2\}_2]$.[72]

### VI.2.e. Magnetism

The magnetism of $[\mathrm{LFe^{III}}]^-$ complies with the Curie-Weiss law including temperature-independent paramagnetism (TIP), yielding an effective moment of $\mu_{\mathrm{eff}} = 3.7\ \beta$,[a] which is near the spin-only value for $S = 3/2$ ($\mu_{\mathrm{eff}} = 3.9$, $g = 2$). A Curie-Weiss fit of the magnetism of $[\mathrm{L^{\Delta\Delta}Fe^{II}}](\mathrm{BF_4})_2$ yields an overall $\mu_{\mathrm{eff}} = 5.0\ \beta$ ($\mu_{\mathrm{eff}} = 4.9\ \beta$ calculated for spin-only $S = 2$, $g = 2$).

### VI.2.f. In summary

All the information gathered from several structural, spectroscopic and magnetic techniques is consistent in the assignment of formal oxidation and spin states for Fe, on the one hand, and the macrocycle, on the other hand, in the redox series of iron porphyrinogen spanning the dianion, the monoanion and the dication. Structural data show that the ligand is $\mathrm{L}^{4-}$ in the former two OSs, and $\mathrm{L}^{\Delta\Delta}$ in the latter; UV-vis absorption suggests Fe(II) in the dianion and the dication, and Fe(III) in the monoanion. The Fe(III) OS of the monoanion is confirmed and its spin state $S = 3/2$ established by SQUID magnetometry and a clear EPR signal. The integer OS and spin state of the dianion is indicated by its EPR silence, and its Fe(II, $S = 1$) state identified by Mössbauer. Finally, the dication clearly contains a high-spin ($S = 2$) Fe(II) because of its Mössbauer and SQUID characteristics.

## VI.3. Theory

### VI.3.a. On the assignment of individual oxidation states

More quantitative insight into the frontier molecular orbitals of the iron porphyrinogens is provided by DFT calculations. Full geometry optimizations on

---

[a] β represents the Bohr magneton, $\beta = 9.2740154 \times 10^{-24}\ \mathrm{J\,T^{-1}}$, such that the spin Hamiltonian in cubic symmetry is $\mathscr{H}_S = g\,\beta\,\mathbf{B}\cdot\mathbf{S}$ (**B**: magnetic induction; **S**: nuclear spin).

$[Na(THF)_2]_2[LFe^{II}]$ and $[Na(THF)_2][LFe^{III}]$ were performed and the $Na^+$ ions and their attendant coordination spheres were removed to afford the isolated porphyrinogen frameworks. The optimized geometry and the details of the MO diagram for these calculations were found to reproduce those obtained for single-point calculations of $[LFe^{II}]^{2-}$ and $[LFe^{III}]^-$ at the geometries imposed by the crystal structures of $[(THF)Na(Opy)]_2[LFe^{II}]$ and $[Na(digly)_2][LFe^{III}]$. On the basis of these results, the electronic structure of $[L^{\Delta\Delta}Fe^{II}(NCCH_3)]^{2+}$ was determined from a single-point calculation at the geometry defined by the crystal structure of $[L^{\Delta\Delta}Fe^{II}(NCCH_3)][(C_2B_9H_{11})_2Co]_2$.

Figure VI.4 displays the energy level diagrams and the Kohn-Sham representations of the frontier molecular orbitals[b,73-83] of $[LFe^{II}]^{2-}$ and $[LFe^{III}]^-$. Because spin restriction is lifted, there is no common spatial wavefunction for each $\alpha/\beta$ spin pair and accordingly two manifolds of "orbitals" are represented. Pairs of spinors with antiparallel spin and similar spatial extension for the metal-based functions are correlated by dashed lines. The relative energies and characters of the molecular orbitals for the iron porphyrinogen in both Fe(III) and Fe(II) oxidations states are similar. As expected, the d orbitals of the more electropositive Fe(III) center are slightly stabilized with respect to those of its Fe(II) congener. Both $[LFe^{II}]^{2-}$ and $[LFe^{III}]^-$ are predicted to assume an intermediate spin state arising from the electronic configurations $(d_{xy})^2(d_{z^2})^2(d_{xz}, d_{yz})^2(d_{x^2-y^2})^0$ and $(d_{xy})^2(d_{z^2})^1(d_{xz},d_{yz})^2(d_{x^2-y^2})^0$, respectively, in complete agreement with the experimental data (EPR of $[LFe^{III}]^-$ indicated single occupancy for $d_{xz}$, $d_{yz}$ and $d_{z^2}$). The $d_{xy}$, $d_{xz}$ and $d_{yz}$ orbitals are effectively nonbonding, as is the $d_{z^2}$ in the absence of an axial ligand. Conversely, the $d_{x^2-y^2}$ is strongly destabilized by its σ-antibonding interaction with the pyrrole lone pairs, thus

---

[b] We note that Kohn-Sham orbitals differ from those derived from a Hartree-Fock (HF) formalism by the inclusion of the exchange correlation energy;[73] but comparative analysis establishes that the shapes and symmetries of the Kohn-Sham orbitals accord well with those calculated by more traditional HF and extended Hückel approximations[74,75] and indeed these orbitals have found widespread use in electronic structure descriptions.[76-83]

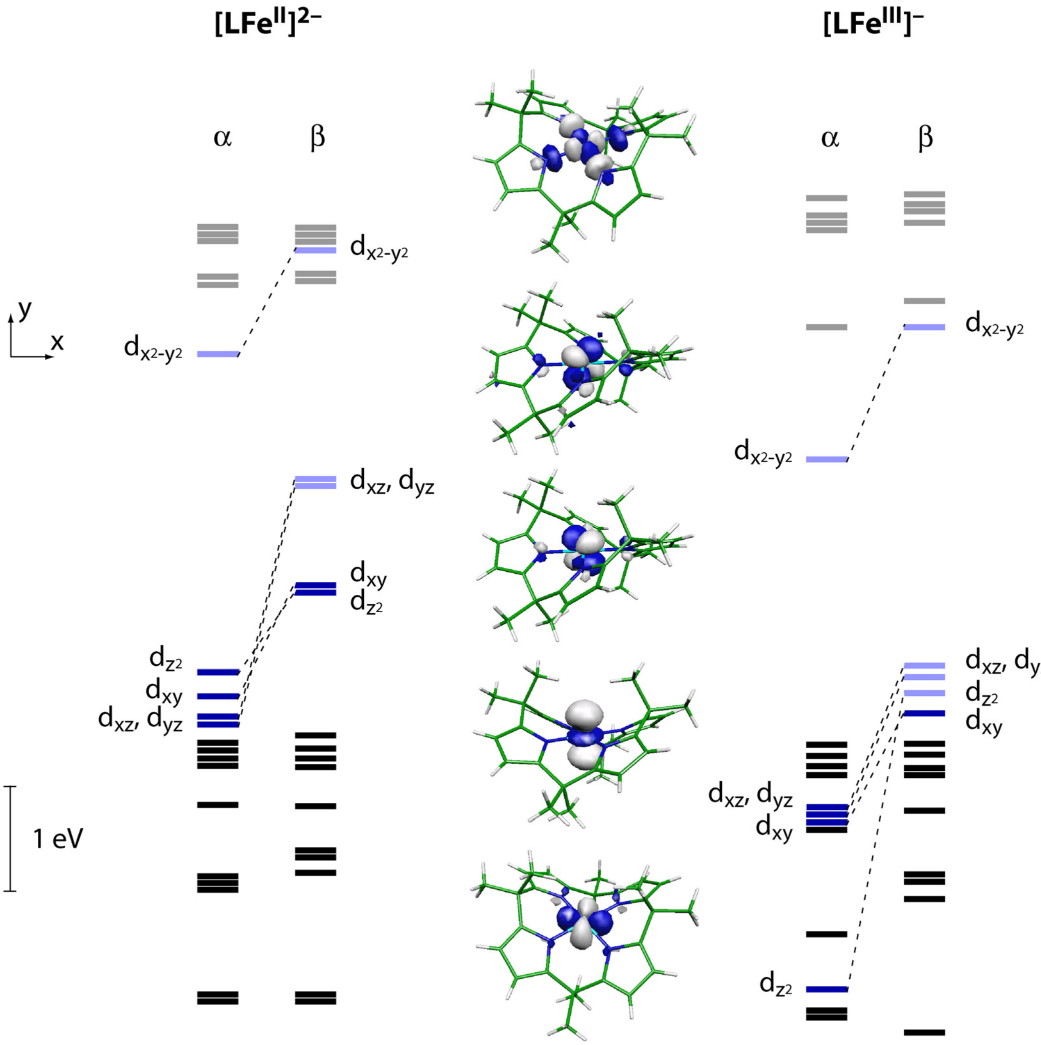
[LFe$^{II}$]$^{2-}$
[LFe$^{III}$]$^{-}$
α
β
α
β
y
x
$d_{x^2-y^2}$
$d_{x^2-y^2}$
$d_{xz}$, $d_{yz}$
$d_{xy}$
$d_{z^2}$
$d_{z^2}$
$d_{xy}$
$d_{xz}$, $d_{yz}$
1 eV
$d_{x^2-y^2}$
$d_{x^2-y^2}$
$d_{xz}$, $d_{yz}$
$d_{z^2}$
$d_{xy}$
$d_{xz}$, $d_{yz}$
$d_{xy}$
$d_{z^2}$

**Figure VI.4.** DFT computed Kohn-Sham MO diagrams for [LFe$^{II}$]$^{2-}$ (left) and [LFe$^{III}$]$^{-}$ (right) in the gas phase, with metal-centered functions highlighted in blue. Occupied orbitals are in dark color, virtual ones in lighter hue. Because spin restriction is lifted, there is not a common spatial wave function for each α/β spin pair, and two manifolds of "orbitals" are drawn separately. The metal-centered spatial wavefunctions are visually similar for [LFe$^{II}$]$^{2-}$ and [LFe$^{III}$]$^{-}$ and for α and β spinors. The orbitals shown in the middle of the diagram are depicted at the 95% probability level for the β spinors of [LFe$^{III}$]$^{-}$.

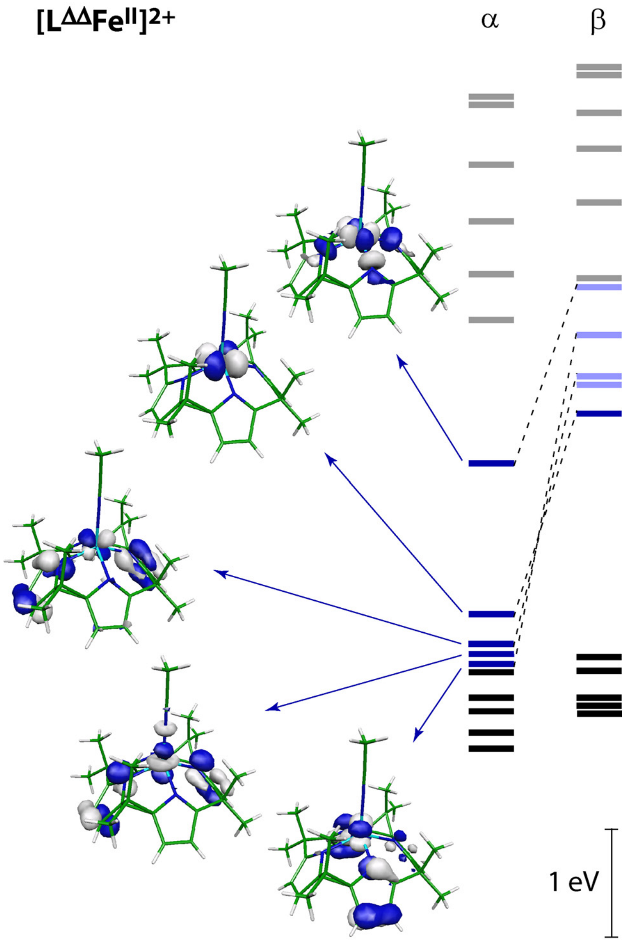

**Figure VI.5.** DFT computed Kohn-Sham MO diagram for $[L^{\Delta\Delta}Fe^{II}(NCMe)]^{2+}$ in the gas phase. The conventions used for Figure VI.6. are valid for this Figure as well.

accounting for the inaccessibility of the high spin state. We find that >99% of the overall unpaired spin is carried within the d orbital manifold, with little spin observed about the porphyrinogen periphery. This result is highlighted by the representations of the frontier molecular orbitals, which are similar for α and β spinors of both $[LFe^{II}]^{2-}$ and $[LFe^{III}]^{-}$. For brevity, the spatial extent of the β spinors of $[LFe^{III}]^{-}$ is depicted in the center of Figure VI.4. These frontier orbitals exhibit nearly exclusive metal d orbital character with no contribution from the porphyrinogen framework. This result is consistent with the electrochemical measurements, which reveal that the ligand-based oxidation is not affected by the nature of the metal ion, as evidenced by the similarity of the redox potentials for the couples $[L^{\Delta\Delta}M^{II}]^{2+}$ / $[LM^{II}]^{2-}$, M = Zn, Fe (Chapter V).

The ligand field of the oxidized porphyrinogen, $L^{\Delta\Delta}$, is significantly weakened relative to that of $L^{4-}$, to the extent that Fe(II) in $[L^{\Delta\Delta}Fe^{II}(NCCH_3)]^{2+}$ assumes a high-spin electron configuration (predicted by DFT in agreement with experiment). Figure VI.5 displays the Kohn-Sham orbitals of $[L^{\Delta\Delta}Fe^{II}(NCCH_3)]^{2+}$. The ~4-eV span for the d-orbital splitting in $[LFe]^{n-}$ complexes is reduced to ~1.5 to 2 eV in $[L^{\Delta\Delta}Fe^{II}(NCCH_3)]^{2+}$. The diminished ligand field arises from the confluence of a smaller metal-ligand σ interaction and a decreased basicity of the oxidized ligand. The former effect results from the distortion of the $L^{\Delta\Delta}$ porphyrinogen macrocycle from the perfect square coordination geometry that characterizes the $L^{4-}$ ligand environment. The most significant perturbation of this distortion is the stabilization of the $d_{x^2-y^2}$ orbital, thus allowing for its occupation by an unpaired electron, and this yields a high spin state ($S = 2$). The decreased basicity is a direct consequence of the oxidation of the macrocycle by four electrons. As for the complexes of the fully reduced ligand, more than 99% of the total unpaired spin is localized on the iron center.

## VI.3.b. On the nature of the $C^{\alpha}$—$C^{\alpha}$ bonding

The nature of the symmetry lowering of the macrocycle upon four-electron oxidation transpires from the comparison of the frontier molecular orbitals of $L^{4-}$ and $L^{\Delta\Delta}$ shown in Figure VI.6. The $L^{4-}$ macrocycle in $[LFe^{II}]^{2-}$ and $[LFe^{III}]^{-}$ features four essentially degenerate HOMOs that arise from the four possible combinations of the $a_2$ π orbitals of the constituent pyrroles to yield one completely in-phase combination (with respect to the interpyrrole $C^{\alpha}\cdots C^{\alpha}$ interactions), a completely out-of-phase one, and each of the last two featuring two in-phase and two out-of-phase nearest-neighbor $C^{\alpha}\cdots C^{\alpha}$ interactions. In the ruffled conformation of $L^{4-}$, the four pyrroles are electronically isolated from each other and the four linear combinations are isoenergetic and completely occupied (eight electrons) to give a net bond order of zero. As schematically represented in Figure VI.7, four-electron oxidation of this set of frontier molecular orbitals lifts the fourfold degeneracy (top panel). The four remaining electrons pair up in the two orbitals that are bonding with respect to the newly established $C^{\alpha}$—$C^{\alpha}$ bonds, yielding a net bond order of two. If only the nodal structure between pyrroles is represented (middle panel), then the overall

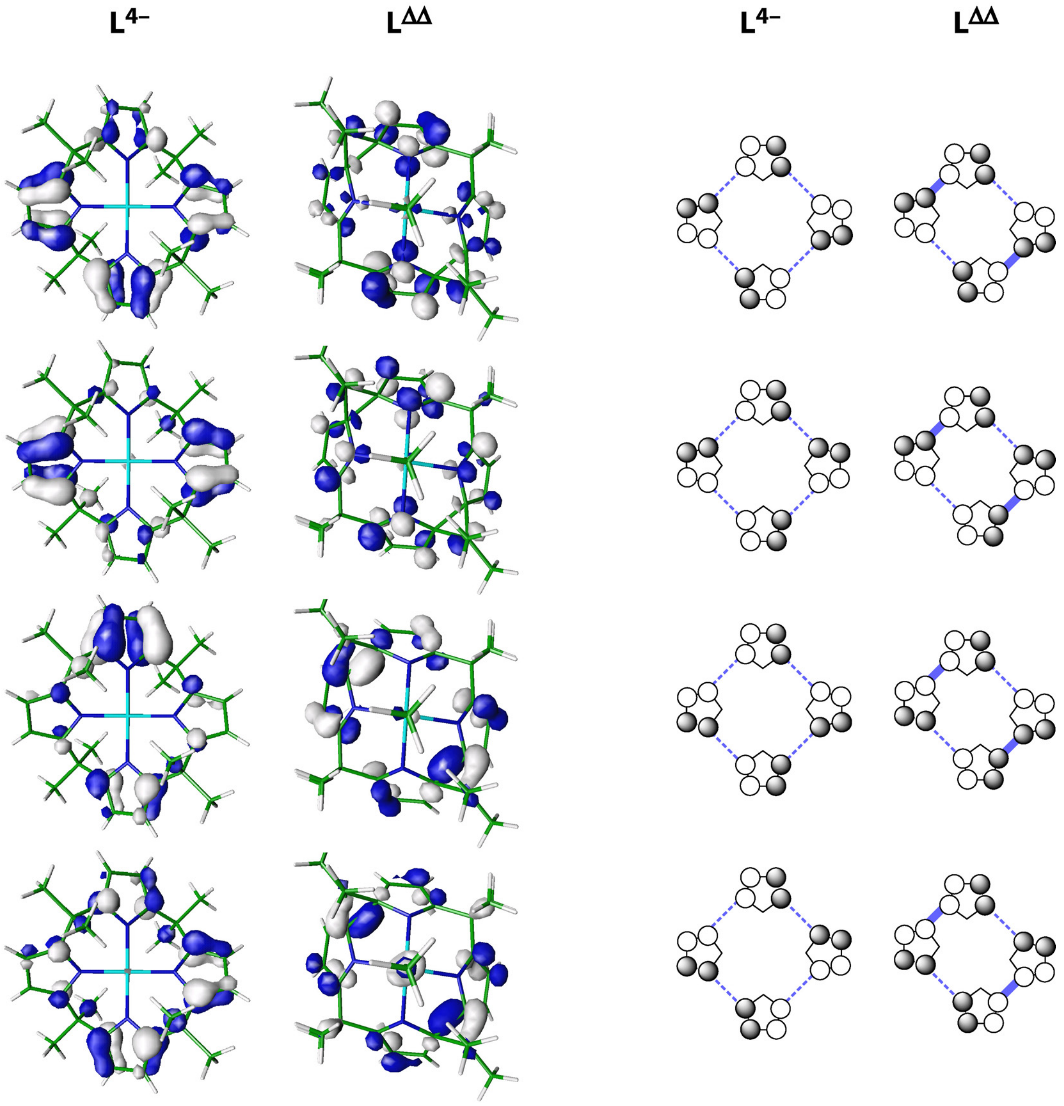

**Figure VI.6.** Comparison of relevant ligand-based π-type Kohn-Sham orbitals of $L^{4-}$ and $L^{\Delta\Delta}$. The computed orbitals are shown on the left, and their schematic simplification on the right.

stereoelectronic transformation between $L^{4-}$ and $L^{\Delta\Delta}$ becomes reminiscent of a classic problem in physical organic chemistry — the distortion of the square cyclobutadiene dianion (with four electrons in two, filled, degenerate π orbitals) to the rectangular neutral cyclobutadiene upon removal of half of its highest-lying π electrons (bottom panel). The tetrapyrrole oxidation is a four-electron equivalent of that of the cyclobutadiene dianion; in both cases, the oxidized species has to distort (in Jahn-Teller fashion) from the fourfold symmetric geometry in order to lift the frontier orbital degeneracy, yielding two diametrically situated bonds.

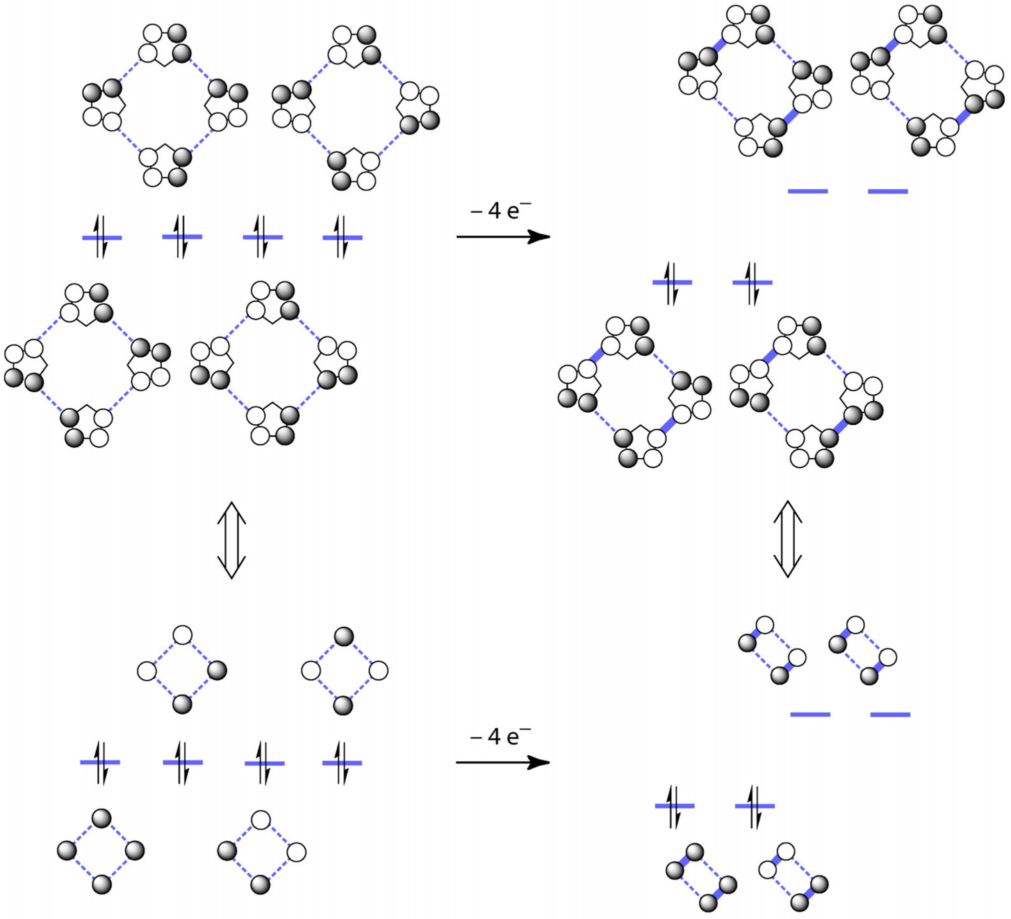

Porphyrinogen

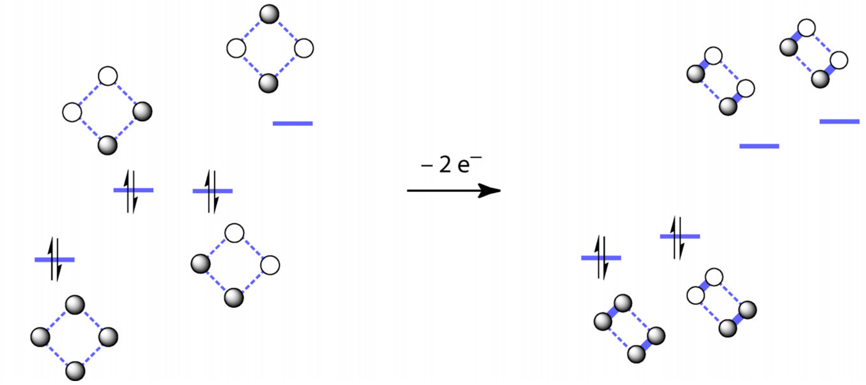

Cyclobutadiene

**Figure VI.7.** Schematic view of the symmetry lowering caused by oxidation of the porphyrinogen tetraanion, compared with a similar phenomenon encountered for the cyclobutadiene dianion.

## VI.4. Excited-state dynamics

The transient absorption signal of Na[LFe$^{III}$], which features a simple one-electron ligand-to-metal charge transfer (LMCT) from the pyrroles to empty d(Fe) orbitals, is displayed in Figure VI.8.

The spectral resolution of the observed transient spectrum (black trace) most obviously features the bleach of the ground-state absorption (shown in dotted black). Visual inspection of the signal does not allow one to clearly distinguish whether the bleach is superimposed on an excited-state absorption, and thereby to determine what the nature of the transient species is. To assess this, two complementary experiments were performed. The first consists of measuring the decay rate as a function of probe wavelength: the decay rate of an electronic excited state to the ground state is independent of wavelength, whereas a vibrationally hot electronic ground state cascading down to thermal vibrational equilibrium is signified by a characteristic wavelength dependence of the observed decay rate.[84] The second

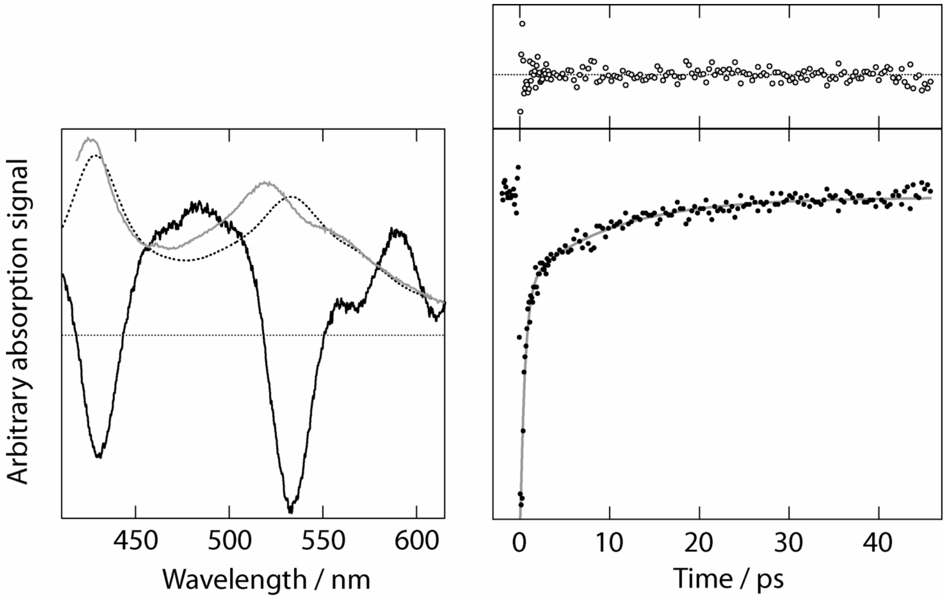

**Figure VI.8.** Transient absorption of Na[LFe$^{III}$]. Left: observed transient spectrum at t = 5 ps (black) compared with the ground-state absorption (dotted black), and reconstructed spectrum for the transient state (gray); the horizontal line represents the zero. Right: transient absorption decay signal probed at $\lambda = 530$ nm (black dots) upon excitation at 403 nm, along with exponential fit (gray line, $\tau = 10$ ps) and corresponding residuals (open circles).

experiment is the deconvolution of the ground-state bleach and true transient-state absorption, the sum of which composes the observed transient spectral signal: an electronic excited state has a distinct spectrum, whereas a vibrationally hot electronic ground state features a broadened and possibly shifted version of the “cold” ground-state spectrum. Time resolution of the transient decay of $[LFe^{III}]^{-}$ indicates a monoexponential behavior (beyond the initial spike attributed to pump-probe cross-correlation) with a $\tau = 13(\pm 3)$ ps lifetime at all wavelengths probed (500, 530, 535, 540, 550, 600, 620, 640, and 660 nm); the experimental signal-to-noise ratio does not allow the observed small variations of $\tau$ with $\lambda$ to be interpreted conclusively. Measurement of the concentration of transient state initially created by the pump pulse by comparison with a standard with known spectral properties ((TMP)Zn) permitted the calculation of the absorption spectrum of the transient species. The resulting spectrum (gray trace) suggests that after 5 ps, no measurable amount of true electronic excited state is leftover, and that the dynamics recorded on the timescale of ~13 ps correspond to the vibrational relaxation from a very short-lived electronic excited state that is not observed within the time window of the experimental technique.

## VI.5. Conclusions

Experimental techniques that selectively probe each of the two partners within an iron porphyrinogen, namely metal and ligand, as well as theoretical computations concur to draw a detailed picture of electronic structures in this system of a “non-innocent’ ligand. The orbitals involved in the ligand’s redox activity feature practically no electron density at the coordinating nitrogens, therefore they are well separated from the metal d orbitals. Consequently, formal individual oxidation states, as indicated in the shorthand notations $[LFe^{II}]^{2-}$, $[LFe^{III}]^{-}$, $[L^{\Delta\Delta}Fe^{II}]^{2+}$, are a good approximation of the physical reality. In stark contrast to the situation of nickel bis(dithiolenes), which feature frontier orbitals of very mixed metal-ligand character,[1-28] the description of iron porphyrinogen involves a clear-cut demarcation.

The ligand-to-metal charge transfer state of the iron(III) porphyrinogen anion is very short-lived, similar to the intervalence charge transfer state of [$L^{\Delta}$Mg]. Most likely, large reorganization upon partial oxidation of the macrocycle in the excited state contributes to efficiently coupling the excited state to high-lying vibrational levels of the electronic ground state.

# VI.6. Experimental section

## VI.6.a. Steady-state measurements

*UV-vis absorption spectroscopy*

UV-visible absorption spectra were recorded on a Spectral Instruments 440 spectrophotometer. Molar absorptivity coefficients were determined on solutions of sub-mM concentrations of iron porphyrinogens.

*EPR spectroscopy*

X-band EPR measurements were carried out on frozen solutions on a Bruker EMX spectrometer; the cavity was maintained at 4.5 K by an Oxford liquid helium cryostat. The spectra were not fitted and the *g* values presented in the text correspond to zeros of the first or second derivative of the signal with respect to the field.

*Mössbauer spectroscopy*

Mössbauer absorption data were recorded at 4.2 K on an MS1 spectrometer (WEB Research Co.) equipped with a $^{57}$Co source and a Janus cryostat, and referenced to elemental iron.

For the preparation of ($Cp^*_2$Fe)[$LFe^{III}$], Na$(THF)_2$[$LFe^{III}$] and $Cp^*_2FePF_6$ were mixed in approximate equal mass amounts in MeCN; after a minute, some yellow $Cp^*_2Fe$ was filtered off and diethylether (three times the volume of MeCN) was added to the filtrate. Green $Cp^*_2FePF_6$ in excess was filtered off and the new filtrate was evaporated and dried *in vacuo*; the resulting solid was triturated in $CH_2Cl_2$ and filtered one more time to remove some white $NaPF_6$. After evaporation of the filtrate, trituration in pentane yielded a suspended solid that was isolated by filtration and dried *in vacuo*. $^1H$ NMR (600 MHz, $CD_3CN$): δ/ppm = –37 (30 H, $Cp*_2Fe^+$ methyls), –72 (8 H, $[LFe^{III}]^-$ pyrroles).

$Cp*_2FePF_6$ was prepared from $Cp*_2Fe$ by a literature method,[85] then recrystallized under anhydrous conditions from MeCN / $Et_2O$ to yield an emerald green crystalline solid.

*SQUID magnetometry*

Magnetic susceptibilities were determined at 50 Oe on powders contained in gelatin capsules using a Quantum Design MPMSR2 SQUID Susceptometer, at the MIT Center for Materials Sciences and Engineering; the data were corrected for diamagnetism of the sample holder and the diamagnetic component of the samples was evaluated from Pascal's constants.[86] The inverse molar paramagnetic susceptibility data, $1/\chi$, were fitted over the entire temperature range according to the following,

$$\frac{1}{\chi} = \frac{T-\theta}{C+\chi_{TIP}\cdot(T-\theta)}$$

where $\chi_{\mathrm{TIP}}$, $C$ and $\theta$ are the temperature-independent paramagnetism, the Curie constant, and the Weiss constant, respectively.

## VI.6.b. Transient absorption spectroscopy

Samples for transient absorption spectroscopy were contained in a 2-mm pathlength high-vacuum cell and prepared to yield an optical density of ~0.5 at the excitation wavelength. The setup used for ultrafast transient absorption experiments was described previously.[87] In brief, the pulsed 806-nm output (~150 fs-wide pulse) of a regeneratively amplified Ti-Sapphire laser system was separated into two beams. The weaker component was focused into either a sapphire or a calcium fluoride substrate to generate the broadband probe pulse. The major component was either frequency-doubled to 403 nm, or tuned throughout the visible range with an optical parametric amplifier, then propagated along a computer-controlled optical delay-line to furnish time resolution. The excitation energy was set to ~5 μJ/pulse, and both beams were spatially overlapped on the sample; the pump beam was then blocked, and the probe was spectrally resolved in a monochromator. Transient spectra were recorded with a CCD camera and derived using a ‘negative time’ reference spectrum; single-wavelength kinetics were obtained with a lock-in amplified photodiode detector.

### VI.6.c. Computational methods

Density functional theory calculations (DFT) were performed using the Amsterdam Density Functional (ADF2002.02) program[88,89] on a home-built Linux cluster comprising sixty Intel processors organized in groups of twelve running in parallel. The generalized gradient approximation was used as implemented in ADF by the Becke-88 functional for exchange,[90] and the Perdew-Wang-91 functional for correlation.[91] A basis set of triple-$\zeta$ Slater-type functions augmented by a polarization set (TZP) was used for Fe and N atoms and double-$\zeta$ with polarization (DZP) for other atoms, with frozen core approximation; spin restriction was lifted for all $S \neq 0$ cases. Energies reported are gas-phase internal energies at 0 K, without zero-point vibrational energy, of the entity in the experimental solid-state structure. Orbitals were visualized using the software Molekel.[92,93]

## VI.7. References

1 Schrauzer, G. N.; Mayweg, V. P. *J . Am. Chem. Soc.* **1962**, *84*, 3221.

2 Schrauzer, G. N.; Mayweg, V. P. *J. Am. Chem. Soc.* **1965**, *87*, 3585-3592.

3 Davison, A.; Edelstein, N.; Holm, R. H.; Maki, A. H. *J. Am. Chem. Soc.* **1963**, *85*, 2029-2030.

4 Davison, A.; Edelstein, N.; Holm, R. H.; Maki, A. H. *J. Am. Chem. Soc.* **1963**, *85*, 3049-3050.

5 Davison, A.; Edelstein, N.; Holm, R. H.; Maki, A. H. *Inorg. Chem.* **1964**, *3*, 814-823.

6 Davison, A.; Edelstein, N.; Holm, R. H.; Maki, A. H. *J. Am. Chem. Soc.* **1964**, *86*, 2799-2805.

7 Maki, A. H.; Edelstein, N.; Davison, A.; Holm, R. H. *J. Am. Chem. Soc.* **1964**, *86*, 4580-4587.

8 Davison, A.; Edelstein, N.; Holm, R. H.; Maki, A. H. *Inorg. Chem.* **1963**, *2*, 1227-1232.

9 Davison, A.; Edelstein, N.; Holm, R. H.; Maki, A. H. *Inorg. Chem.* **1965**, *4*, 55-59.

10 Maki, A. H.; Berry, T. E.; Davison, A.; Holm, R. H.; Balch, A. L. *J. Am. Chem. Soc.* **1966**, *88*, 1080-1082.

11 Holm, R. H.; Balch, A. L.; Davison, A.; Maki, A. H.; Berry, T. E. *J. Am. Chem. Soc.* **1967**, *89*, 2866-2874.

12 Davison, A.; Holm, R. H. *Inorg. Synth.* **1967**, *10*, 8-26.

13 Latham, A. R.; Hascall, V. C.; Gray, H. B. *Inorg. Chem.* **1965**, *4*, 788-792.

14 Billig, E.; Williams, R.; Bernal, I.; Waters, J. H.; Gray, H. B. *Inorg. Chem.* **1964**,*3*, 663-666.

15 Shupack, S. I.; Billig, E.; Clark, R. J. H.; Williams, R.; Gray, H. B. *J. Am. Chem. Soc.* **1964**, *86*, 4594-4602.

16 Gray, H. B.; Billig, E. *J. Am. Chem. Soc.* **1963**, *85*, 2019-2020.

17 Stiefel, E. I.; Waters, J. H.; Billig, E.; Gray, H. B. *J. Am. Chem. Soc.* **1965**, *87*, 3016-3017.

18 Herebian, D.; Ghosh, P.; Chun, H.; Bothe, E.; Weyhermuller, T.; Wieghardt, K. *Eur. J. Inorg. Chem.* **2002**, 1957-1967.

19 Arion, V.; Wieghardt, K.; Weyhermueller, T.; Bill, E.; Leovac, V.; Rufinska, A. *Inorg. Chem.* **1997**, *36*, 661-669.

20 De Bruin, B.; Bill, E.; Bothe, E.; Weyhermueller, T.; Wieghardt, K. *Inorg. Chem.* **2000**, *39*, 2936-2947.

21 Ray, K.; Weyhermueller, T.; Goossens, A.; Craje, M. W. J.; Wieghardt, K. *Inorg. Chem.* **2003**, *42*, 4082-4087.

22 Ghosh, P.; Bill, E.; Weyhermueller, T.; Wieghardt, K. *J. Am. Chem. Soc.* **2003**, *125*, 3967-3979.

23 Min, K. S.; Weyhermueller, T.; Bothe, E.; Wieghardt, K. *Inorg. Chem.* **2004**, *43*, 2922-2931.

24 Bill, E.; Bothe, E.; Chaudhuri, P.; Chlopek, K.; Herebian, D.; Kokatam, S.; Ray, K.; Weyhermueller, T.; Neese, F.; Wieghardt, K. *Chem. Eur. J.* **2005**, *11*, 204-224.

25 Ray, K.; Bill, E.; Weyhermueller, T.; Wieghardt, K. *J. Am. Chem. Soc.* **2005**, *127*, 5641-5654.

26 Blanchard, S.; Neese, F.; Bothe, E.; Bill, E.; Weyhermueller, T.; Wieghardt, K. *Inorg. Chem.* **2005**, *44*, 3636-3656.

27 Ray, K.; Weyhermueller, T.; Neese, F.; Wieghardt, K. *Inorg. Chem.* **2005**, *44*, 5345-5360.

28 Chlopek, K.; Bill, E.; Ueller, T. W.; Wieghardt, K. *Inorg. Chem.* **2005**, *44*, 7087-7098.

29 Dolphin, D.; Forman, A; Borg, D. C.; Fajer, J.; Felton, R. H. *Proc. Nat. Acad. Sci.* **1971**, *68*, 614-618.

30 Groves, J. T.; Haushalter, R. C.; Nakamura, M.; Nemo, T. E.; Evans, B. J. *J. Am. Chem. Soc.* **1981**, *103*, 2884-2886.

31 Dunford, H. B.; Stillman, J. S. *Coord. Chem. Rev.* **1976**, 19, 187-251.

32 Theorell, H.; Ehrenberg, A. *Arch. Biochem. Biophys.* **1952**, *41*, 442-461.

33 Maeda, Y.; Morita, Y. *Biochem. Biophys. Res. Commun.* **1967**, *29*, 680-685.

34 Moss, T. H.; Ehrenberg, A.; Bearden, A. *Biochemistry* **1969**, *8*, 4159-4162.

35 Schulz, C. E.; Devaney, P. W.; Winkler, H.; Debrunner, P. G.; Doan, N.; Chiang, R.; Rutter, R.; Hager, L. P. *FEBS Lett.* **1979**, *103*, 102-105.

36 Harami, T.; Maeda, Y.; Morita, Y.; Trautwein, A.; Gonser, U. *J. Chem. Phys.* **1977**, *67*, 1164-1169.

37 Morishima, I.; Ogawa, S. *J. Am. Chem. Soc.* **1978**, *100*, 7125-7127.

38 Morishima, I.; Ogawa, S. *Biochem. Biophys. Res. Commun.* **1978**, *83*, 946-953.

39 Morishima, I.; Ogawa, S. *Biochemistry* **1978**, *17*, 4384-4388.

40 La Mar, G. H.; de Ropp, J. S. *J. Am. Chem. Soc.* **1980**, *102*, 395-397.

41 Maltempo, M. M.; Ohlsson, P. I.; Paul, K. G.; Peterson, L.; Ehrenberg, A. *Biochem.* **1979**, *18*, 2935-2941.

42 Loew, G. H.; Herman, Z. S. *J. Am. Chem. Soc.* **1980**, *102*, 6173-6174.

43 Green, M. T. *J. Am. Chem. Soc.* **1999**, *121*, 7939-7940.

44 de Visser, S. P.; Ogliaro, F.; Sharma, P. K.; Shaik, S. *Angew. Chem. Int. Ed.* **2002**, *41*, 1947-1951.

45 Schoeneboom, J. C.; Neese, F.; Thiel, W. *J. Am. Chem. Soc.* **2005**, *127*, 5840-5853.

46 Ozawa, S.; Watanabe, Y.; Morishima, I. *J. Am. Chem. Soc.* **1994**, *116*, 5832-5838.

47 Renner, M. W.; Buchler, J. W. *J. Phys. Chem.* **1995**, *99*, 8045-8049.

48 Van Caemelbecke, E.; Will, S.; Autret, M.; Adamian, V. A.; Lex, J.; Gisselbrecht, J.-P.; Gross, M.; Vogel, V.; Kadish, K. M. *Inorg. Chem.* **1996**, *35*, 184-192.

49 Cai, S.; Walker, F. A.; Licoccia, S. *Inorg. Chem.* **2000**, *39*, 3466-3478.

50 Simkhovich, L.; Goldberg, I.; Gross, Z. *Inorg. Chem.* **2002**, *41*, 5433-5439.

51 Steene, E.; Wondimagegn, T.; Ghosh, A. *J. Inorg. Biochem.* **2002**, *88*, 113-118.

52 Floriani, C.; Floriani-Moro, R. in *The Porphyrin Handbook*; Kadish, K. M., Smith, K. M.; Guilard, R., Ed.; Academic Press:New York, 2000; Vol. 3, pp 405-20.

53 Jubb, J.; Floriani, C.; Chiesi-Villa, A.; Rizzoli, C. *J. Am. Chem. Soc.* **1992**, *114*, 6571-6573.

54 De Angelis, S.; Solari, E.; Floriani, C.; Chiesi-Villa, A.; Rizzoli, C. *J. Am. Chem. Soc.* **1994**, *116*, 5691-5701.

55 De Angelis, S.; Solari, E.; Floriani, C.; Chies-Villa, A.; Rizzoli, C. *J. Am. Chem. Soc.* **1994**, *116*, 5702-5713.

56 Piarulli, U.; Solari, E.; Floriani, C.; Chiesi-Villa, A.; Rizzoli, C. *J. Am. Chem. Soc.* **1996**, *118*, 3634-3642.

57 Crescenzi, R.; Solari, E.; Floriani, C.; Chiesi-Villa, A.; Rizzoli, C. *J. Am. Chem. Soc.* **1999**, *121*, 1695-1706.

58 Sakai, T.; Ohgo, Y.; Ikeue, T.; Takahashi, M.; Takeda, M.; Nakamura, M. *J. Am. Chem. Soc.* **2003**, *125*, 13028-13029.

59 Simkhovich, L.; Goldberg, I.; Gross, Z. *Inorg. Chem.* **2002**, *41*, 5433-5439.

60 Palmer, G. in *Physical Methods in Bioinorganic Chemistry*; Que, L., Jr., Ed.; University Science Books: Sausalito, CA, 2000; p 153.

61 Oh, Y.; Shin, B.-C.; Swenson, D.; Goff, H. M.; Kang, S. K. *Acta Cryst.* **2004**, *C60*, m57-m59.

62 Strauss, S. H.; Silver, M. E.; Long, K. M.; Thompson, R. G; Hudgens, R. A.; Spartalian, K.; Ibers, J. A. *J. Am. Chem. Soc.* **1985**, *107*, 4207-4215.

63 Riley, D. P.; Stone, J. A.; Busch, D. H. *J. Am. Chem. Soc.* **1977**, *99*, 767-777.

64 Sellers, S. P.; Korte, B. J.; Fitzgerald, J. P.; Reiff, W. M.; Yee, G. T. *J. Am. Chem. Soc.* **1998**, *120*, 4662-4670.

65 Weber, B.; Käpplinger, I.; Görls, H.; Jäger, E.-G. *Eur. J. Inorg. Chem.* **2005**, 2794–2811.

66 Connelly, N. G.; Geiger, W. E. *Chem. Rev.* **1996**, *96*, 877-910.

67 Herber, R. H. *Inorg. Chem.* **1969**, *8*, 174-176.

68 Birchall, T.; Drummond, I. *Inorg. Chem.* **1971**, *10*, 399-401.

69 Miller, J. S.; Calabrese, J. C.; Harlow, R. L.; Dixon, D. A.; Zhang, J. H.; Reiff, W. M.; Chittipeddi, S.; Selover, M. A.; Epstein, A. J. *J. Am. Chem. Soc.* **1990**, *112*, 5496-5506.

70 Drews, T.; Seppelt, K. *Z. Anorg. Allg. Chem.* **1991**, *606*, 201-207.

71 Münck, E. in *Physical Methods in Bioinorganic Chemistry*; Que, L., Jr., Ed.; University Science Books: Sausalito, CA, 2000; p. 291.

72 Evans, D. J. *Chem. Phys. Lett.* **1996**, *255*, 134-136.

73 Kohn, W.; Becke, A. D.; Parr, R. G. *J. Phys. Chem.* **1996**, *100*, 12974-12080.

74 Stowasser, R.; Hoffmann, R. *J. Am. Chem. Soc.* **1999**, *121*, 3414-3420.

75 Hamel, S.; Duffy, P.; Casida, M. E.; Salahub, D. R. *J. Electron Spectrosc. Rel. Phenom.* **2002**, *123*, 345-363.

76 Lehnert, N.; Neese, F.; Ho, R. Y. N.; Que, L., Jr.; Solomon, E. I. *J. Am. Chem. Soc.* **2002**, *124*, 10810-10822.

77 Chen, P.; Root, D. E.; Campochiaro, C.; Fujisawa, K.; Solomon, E. I. *J. Am. Chem. Soc.* **2003**, *125*, 466-474.

78 Chisholm, M. H.; Gallucci, J.; Hadad, C. M.; Huffman, J. C.; Wilson, P. J. *J. Am. Chem. Soc.* **2003**, *125*, 16040-16049.

79 Gray, T. G.; Rudzinski, C. M.; Meyer, E.; Holm, R. H.; Nocera, D. G. *J. Am. Chem. Soc.* **2003**, *125*, 4755-4770.

80 Gray, T. G.; Rudzinski, C. M.; Meyer, E. E.; Nocera, D. G. *J. Phys. Chem. A* **2004**, *108*, 3238-3243.

81 Chang, C. J.; Loh, Z.-H.; Shi, C.; Anson, F. C.; Nocera, D. G. *J. Am. Chem. Soc.* **2004**, *126,* 10013-10020.

82 Manke, D. R.; Loh, Z.-H.; Nocera, D. G. *Inorg. Chem.* **2004**, *43*, 3618-3624.

83 Gray, T. G.; Veige, A. S.; Nocera, D. G. *J. Am. Chem. Soc.* **2004**, *12,* 9760-9768.

84 Bilsel, O.; Milam, S. N.; Girolami, G. S.; Suslick, K. S.; Holten, D. *J. Phys. Chem.* **1993**, *97*, 7216-7221.

85 Duggan, M. D.; Hendrickson, D. N. *Inorg. Chem.* **1975**, *14*, 955-970.

86 Girerd, J.-J; Journaux, Y. in *Physical Methods in Bioinorganic Chemistry*; Que, L., Jr., Ed.; University Science Books: Sausalito, CA, 2000; p. 324.

87 Hodgkiss, J. M.; Chang, C. C.; Pistorio, B. J.; Nocera, D.G. *Inorg. Chem.* **2003**, *42*, 8270-8277.

88 te Velde, G.; Bickelhaupt, F. M.; van Gisbergen, S. J. A.; Fonseca Guerra, C.; Baerends, E. J.; Snijders, J. G.; Ziegler, T. *J. Comput. Chem.* **2001**, *22*, 931-967.

89 Fonseca Guerra, C.; Snijders, J. G.; te Velde, G.; Baerends, E. J. *Theor. Chem. Acc.* **1998**, *99*, 391-403.

90 Becke, A. D. *Phys. Rev. A* **1988**, *38*, 3098-3100.

91 Perdew, J. P.; Chevary, J. A.; Vosko, S. H.; Jackson, K. A.; Pederson, M. R.; Singh, D. J.; Fiolhais, C. *Phys. Rev. B* **1992**, *46*, 6671-6687.

92 Molekel v.4.2/3, Flükiger, P.; Lüthi, H. P.; Portmann, S.; Weber, J., Swiss Center for Scientific Computing, Manno (Switzerland), 2000-2002.

93 Portmann, S.; Lüthi, H. P. *Chimia* **2000**, *54*, 766-769.

# Chapter VII

# Multielectron reactivity of the iron porphyrinogen dication, $[L^{\Delta\Delta}Fe^{II}]^{2+}$

## VII.1. Introduction

When adequately controlled, ligand-based redox activity (ligand “non-innocence”) could potentially expand the redox possibilities of metal-organic compounds. Since its recognition in the 1960’s,[1-10] the phenomenon has mostly been documented in transition metal complexes of dithiolenes, catecholates, and related chelates (Chapter I).[1-13] The commonalities of compounds of this type include (a) *one-electron* ligand-based redox couples, and (b) frontier orbitals of *mixed metal-ligand* character. The macrocyclic ligand porphyrinogen goes beyond those limitations in that (a) it reacts in discrete *two-electron* steps, and (b) the orbitals that support the redox chemistry are cleanly *localized* on the organic part, in the formation or breaking of one or two cyclopropane C—C bond (Chapters III and VI).

Although transition metal complexes of oxidized porphyrinogens have been characterized structurally for several metal-halo inorganic centers,[14-18] the coordination and redox chemistry of such compounds has remained largely unexplored. However, the electron transfer series described for iron porphyrinogen (Chapter V) suggests that the metal-ligand redox cooperativity engenders possibly unique multielectron steps, such as the three-electron redox couple $[\mathrm{LFe^{III}}]^{-}$ / $[\mathrm{L^{\Delta\Delta}Fe^{II}}]^{2+}$. This Chapter investigates basic types of reactivity (coordination capabilities, potential for multielectron oxidations) originating from the oxidized iron porphyrinogen dication, $[\mathrm{L^{\Delta\Delta}Fe^{II}}]^{2+}$ — an oxidant based on a low-valent metal cation. The $d_{24}$-octamethylporphyrinogen ligand is used solely, for simplicity of the $^{1}$H NMR spectroscopic characterization.

## VII.2. Results

Both $[\mathrm{LFe^{II}}]^{2-}$ and $[\mathrm{LFe^{III}}]^{-}$ are surprisingly inert with respect to axial coordination. No reaction is observed upon contact of the sodium salts with a variety of Lewis bases and O atom donors, in particular MeCN, CO, pyridine and pyridine-*N*-oxide. Although no single simplistic rationale is likely to justify the observed lack of coordinative reactivity, it seems reasonable that both the negative charge of the overall complexes and the intermediate-spin square planar $d^6$ / $d^5$ configuration (with occupied $d_{z^2}$ orbital) contribute to putting a kinetic barrier to nucleophilic attack.

Unlike the anionic oxidation states, $[L^{\Delta\Delta}Fe^{II}]^{2+}$ reacts with anionic ligands. Exposure of $[L^{\Delta\Delta}Fe^{II}](BF_4)_2$ to stoichiometric or excess amount of $Bu_4NCl$ in acetonitrile causes the $^1$H β-pyrrole signals of $[L^{\Delta\Delta}Fe^{II}]^{2+}$ at +59 and −7 ppm to be cleanly converted to a new set of peaks at +55 and −9 ppm. Therefore, the symmetry of the entity is maintained in the reaction and its oxidation state is not affected,[a] consistent with axial coordination of $Cl^-$to Fe. Indeed, the same NMR signals are obtained upon three-electron oxidation of $Na[LFe^{III}]$ with $AuCl_3$, $KAuCl_4$, or 1.5 $PhICl_2$. Crystallographic analysis of the isolated material proves its identity to be $[L^{\Delta\Delta}Fe^{II}—Cl](FeCl_4)$ (Figure VII.1, Tables VII.1 and VII.2); the geometry of the porphyrinogen moiety is comparable to that of $[L^{\Delta\Delta}Fe^{II}(NCMe)]^{2+}$ (Chapter V) and of Floriani's closely related chloroiron(II) octaethylporphyrinogen cation with the $Cu_4Cl_5^-$ counter-ion.[17] The UV-visible spectrum of the material is independent of the synthetic path and confirms the identity of the $FeCl_4^-$ counter-anion, the conspicuous bands of which appear at 313 and 363 nm.[19] Thus, the presence of excess chloride causes extrusion of the Fe ion from a fraction of the metalloporphyrinogens units, rationalizing the low yields obtained by Floriani in the preparation of a similar compound.[16] The Mössbauer spectrum of $[L^{\Delta\Delta}Fe^{II}—Cl](FeCl_4)$ displays (in addition to the $FeCl_4^-$ doublet)[b] large quadrupole splitting and isomer shift, $\delta = 1.0$ mm/s, $\Delta E_q = 3.8$ mm/s, similar to those observed for $[L^{\Delta\Delta}Fe^{II}](BF_4)_2$ (Chapter VI), arising from high-spin Fe(II).

With alcoholates such as $KOCMe_3$ or NaOMe, the reactivity of $[L^{\Delta\Delta}Fe^{II}]^{2+}$ switches to redox in nature: $^1$H NMR shows reduced $[LFe^{III}]^-$ (β-pyrrole peak at −72 ppm) as the only observable product. Reduction can be prevented with the silanolate $NaOSiMe_3$:

---

[a] $L^{4-}$ displays fourfold rotational symmetry in solution and in the solid state, $L^{\Delta\Delta}$ twofold, and $L^{\Delta 2-}$ none (although it keeps a *plane* of symmetry).

[b] Crystal packing forces seem to slightly distort the anion from its ideal tetrahedral symmetry: $\delta = 0.3$ mm/s, $\Delta E_q = 0.3$ mm/s.

**Table VII.1.** Summary of X-ray crystallographic data for $[L^{\Delta\Delta}Fe^{II}Cl]$ $(FeCl_4)$.

| | |
|---|---|
| empirical formula (formula weight) | $C_{28}H_{32}Cl_5Fe_2N_4$ (713.53) |
| $T$ (K) | 100(2) |
| $\lambda$ (Å) | 0.71073 |
| crystal system, space group | Orthorhombic, *Pbca* |
| $a$ ; $b$ ; $c$ (Å) | 18.552(3) ; 18.820(3) ; 35.926(5) |
| $Z$ ; $V$ (Å$^3$) | 16 ; 12543(3) |
| crystal size (mm$^3$) | $0.33 \times 0.07 \times 0.02$ |
| Abs. coeff. (mm$^{-1}$) | 1.376 |
| $F$(000) | 5840 |
| $\theta$ range for data collection | 1.13 to 23.31° |
| limiting indices | $-20 \le h \le 14$, $-20 \le k \le 20$, $-39 \le \ell \le 39$ |
| no. of reflns collcd ; no. of ind. reflns ($R_{int}$) | 58729 ; 9053 (0.1033) |
| completeness to $\theta = 23.31°$ | 99.8 % |
| refinement method | Full-matrix least-squares on $F^2$ |
| data / restraints / parameters | 9053 / 0 / 756 |
| $R_1$,[a] $wR_2$[b] ($I > 2\sigma(I)$) | 0.0465, 0.1077 |
| $R_1$,[a] $wR_2$[b] (all data) | 0.0645, 0.1215 |
| GOF[c] on $F^2$ | 1.059 |
| largest diff. peak and hole | 0.871 and –0.453 eÅ$^{-3}$ |

[a] $R_1 = \Sigma||F_o - |F_c||/\Sigma|F_o|$.

[b] $wR_2 = (\Sigma(w(F_o^2 - F_c^2)^2)/\Sigma(w(F_o^2)^2))^{1/2}$.

[c] $GOF = (\Sigma\, w(F_o^2 - F_c^2)^2/(n - p))^{1/2}$,
where $n$ is the number of data and $p$ is the number of parameters refined.

**Table VII.2.** Selected geometric parameters for $[L^{\Delta\Delta}Fe^{II}Cl]$ $(FeCl_4)$.

| | | | |
|---|---|---|---|
| Distances / Å | | | |
| Fe(2)—N(5) | 2.141(3) | N(5)—C(32) | 1.309(5) |
| Fe(2)—N(5) | 2.148(3) | N(5)—C(29) | 1.447(5) |
| Fe(2)—N(5) | 2.157(4) | N(6)—C(36) | 1.307(6) |
| Fe(2)—N(5) | 2.159(3) | N(6)—C(39) | 1.445(5) |
| Fe(2)—Cl(2) | 2.2740(12) | N(7)—C(46) | 1.313(5) |
| | | N(7)—C(43) | 1.433(6) |
| C(39)—C(43) | 1.585(6) | N(8)—C(50) | 1.304(5) |
| C(29)—C(53) | 1.583(6) | N(8)—C(53) | 1.438(5) |
| Angles / deg | | | |
| C(39)–C(40)–C(43) | 62.6(3) | C(29)–C(54)–C(53) | 62.6(3) |

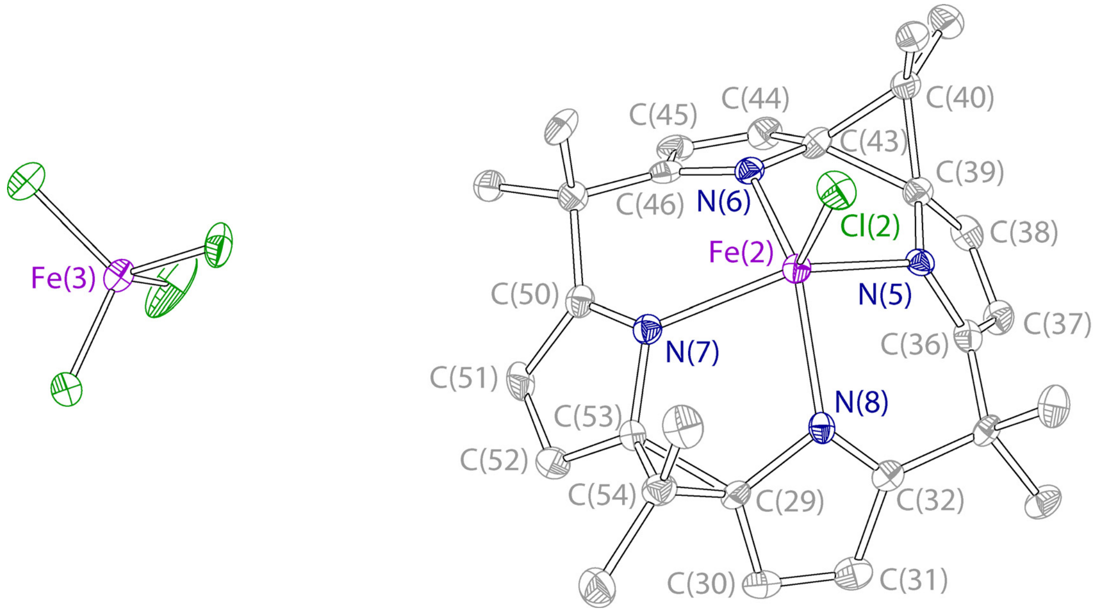

**Figure VII.1.** Crystal structure of [$L^{\Delta\Delta}Fe^{II}Cl$] ($FeCl_4$). Only one of two chemically identical ion pairs constituting the asymmetric unit is displayed. H atoms are omitted. Thermal ellipsoids are drawn at the 50% probability level. Color coding: Fe, purple; N, blue; Cl, green; C, gray.

according to elemental analysis, the material obtained can be formulated as [$L^{\Delta\Delta}Fe^{II}$—$OSiMe_3$] ($OSiMe_3$). In solution, rotation around the Fe—O bond is hindered by steric constraints, according to $^1H$ NMR (β-pyrrole: +107, +89, +84 and +27 ppm,

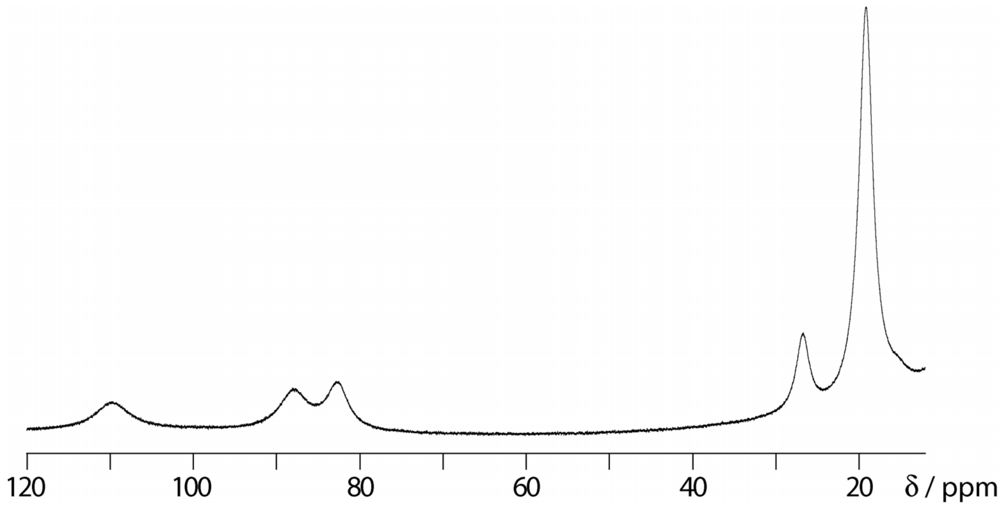

**Figure VII.2.** Paramagnetic region in the $^1H$ NMR spectrum (500 MHz, $CD_2Cl_2$) of [$L^{\Delta\Delta}Fe^{II}$—$OSiMe_3$] ($OSiMe_3$). The FID has been submitted to a 5-Hz Gaussian line broadening, then Fourier transformed, and a polynomial baseline has been subtracted from the resulting spectrum.

Figure VII.2). In the powder, its Mössbauer spectrum is consistent with the Fe(II) oxidation state, with $\delta = 0.4$ mm/s and $\Delta E_q = 1.0$ mm/s.

As an entry into the potential oxidative reactivity of $[L^{\Delta\Delta}Fe^{II}]^{2+}$, its interaction with iodide was considered. Thermodynamics are favorable to the formation of diiodine (or its iodide adduct, triiodide),[20]

$$I_3^- + 2\,e^- \rightarrow 3\,I^- \qquad E^\circ = +0.53\text{ V} \tag{1}$$

$$[L^{\Delta\Delta}Fe^{II}]^{2+} + 3\,e^- \rightarrow [LFe^{III}]^- \qquad E_p = +0.77\text{ V} \tag{2}$$

$$2\,[L^{\Delta\Delta}Fe^{II}]^{2+} + 9\,I^- \rightarrow 2\,[LFe^{III}]^- + 3\,I_3^- \qquad \Delta E \approx +0.24\text{ V} \tag{3}$$

however, depending on the strength of the Fe—I bond, the reaction risks being frozen at the $[L^{\Delta\Delta}Fe^{II}{-}I]^+$ adduct instead of proceeding to redox reactivity. This is not the case, and upon mixing $[L^{\Delta\Delta}Fe^{II}](BF_4)_2$ with $Bu_4NI$, the characteristic UV-visible signature of triiodide appears immediately at 291 and 362 nm. Experimental conditions do not affect the oxidation of $I^-$ to $I_3^-$, but the fate of the iron porphyrinogen byproduct was found to strongly depend on them. Under slow addition of a cold (–40°C) solution of $[L^{\Delta\Delta}Fe^{II}](BF_4)_2$ to an excess (≥ 6 equivalents) of a cold $Bu_4NI$ solution, more than 80% of $[L^{\Delta\Delta}Fe^{II}]^{2+}$ is converted to $[LFe^{III}]^-$, according to (3), the rest reacting further to $LH_4$, presumably by $H^\bullet$ atom abstraction from the solvent. However, when a stoichiometric amount of $I^-$ (4.5 equivalents) is added to $[L^{\Delta\Delta}Fe^{II}]^{2+}$ at room temperature, all of the

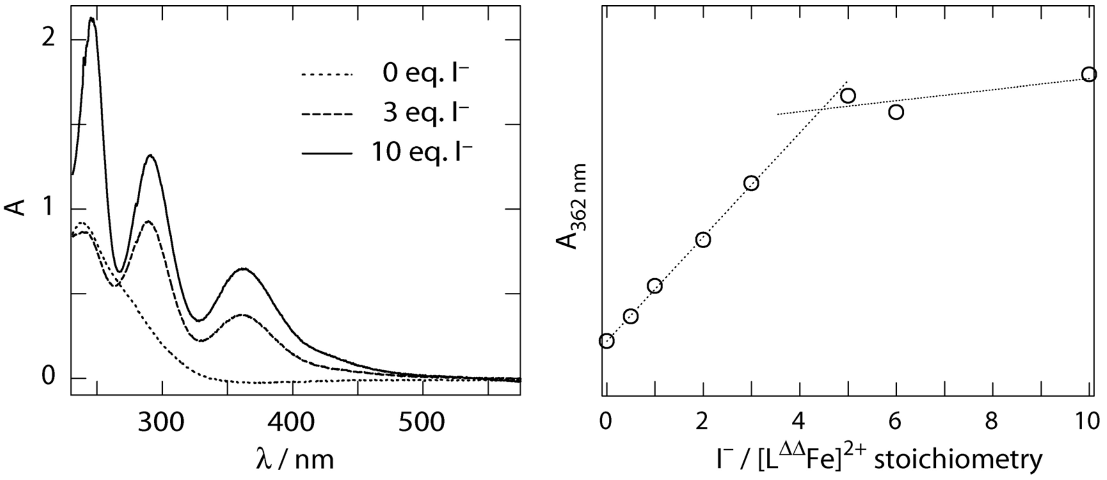

**Figure VII.3.** Stoichiometry of $[L^{\Delta\Delta}Fe^{II}]^{2+} + I^-$. Left, UV-visible spectra of $[L^{\Delta\Delta}Fe^{II}](BF_4)_2 + n\,Bu_4NI$ reaction mixtures of varying stoichiometries *n*. The bands at 291 and 362 nm are due to $I_3^-$, and that at 245 nm to $I^-$. Right, 362-nm signal as a function of the stoichiometry, with linear fits intersecting at $n = 4.5$.

porphyrinogen is found as $LH_4$. The stoichiometry of the reaction was identified spectroscopically at room temperature (Figure VII.3), yielding a 9:2 ratio, as expected on the basis of equation (3). This reduction of $[L^{\Delta\Delta}Fe^{II}]^{2+}$ to $[LFe^{III}]^{-}$ by iodide is to be contrasted to the recently reported[15] oxidation of iron(III) *meso*-tetrakis(penta-1,5-diyl)porphyrinogen, $[{}^{*}LFe^{III}]^{-}$ by excess molecular iodine to $[{}^{*}L^{\Delta\Delta}Fe^{II}—I](I_3)$:[c] solvent and substituents can likely mitigate electrostatic energies, and thereby affect thermodynamics.

The mechanism of $I_2$ formation from $I^-$ and $[L^{\Delta\Delta}Fe^{II}]^{2+}$ is unknown, and could possibly involve either *(a)* formation of a cationic $[L^{\Delta\Delta}Fe^{II}I]^{+}$ intermediate followed by nucleophilic attack by $I^-$, or *(b)* electron transfer to form an $I^{\bullet}$ radical which then further reacts. Mechanism *(a)* is appealing firstly because $[L^{\Delta\Delta}Fe^{II}Cl]^{+}$ and even $[{}^{*}L^{\Delta\Delta}Fe^{III}I]^{+}$ are known as stable species, and secondly because it involves a direct two-electron process as the crucial redox step, which would be a manifestation of the two-electron nature of the “delta” C—C bond of the porphyrinogen. More generally, we would like to determine whether iron porphyrinogen behaves as a selective even-electron redox agent (effecting group transfer transformations, as in *(a)*) or reacts in single-electron steps (*via* radical pathways, as in *(b)*). In this respect, the silanolate $[L^{\Delta\Delta}Fe^{II}—OSiMe_3]^{+}$ furnishes an entry towards a potential O atom transfer agent. Its reaction with excess fluoride, if it were to cleave the Si—O bond, would generate a terminal iron(II) oxo which would likely be unstable and further react intra- or intermolecularly.[21] When the reaction is carried out in dichloromethane, a solid precipitates which redissolves in acetonitrile. Its NMR shows the presence of a single paramagnetic product, with two-fold symmetry ($^1H$, β-pyrrole: +20 and +15 ppm; $^2H$, methyl: +7, +4, –4 and –21 ppm) and its Mössbauer a large quadrupole splitting but small isomer shift ($\delta = 0.3$ mm/s, $\Delta E_q = 3.2$ mm/s). The compound does not react with the electron-rich substrates *cis*-cyclooctene, $PPh_3$ and $P(n\text{-}Bu)_3$. On the other hand, its reactions with $P(C_6F_5)_3$,

---

[c] The CIF file provided as Supporting Information by Bhattacharya *et al.*[15] shows that their implausible claim of a $[{}^{*}L^{\Delta\Delta}Fe^{II}—I]^{+}(I_3)^{-} \bullet (I_2)^{+}(I_3)^{-}$ cocrystal is erroneous. Correction of a mistaken count of the $I_3^-$ ions placed at special positions in the lattice yields $[{}^{*}L^{\Delta\Delta}Fe^{II}—I]^{+}(I_3)^{-} \bullet (I_2)$.

**Table VII.3.** Summary of X-ray crystallographic data for {(Ph$_4$P) [LFe$^{III}$]}$_2$ • MeCN • *o*-C$_6$H$_4$Cl$_2$.

| | |
|---|---|
| empirical formula (formula weight) | $C_{112}H_{111}Cl_2Fe_2N_9P_2$ (1827.64) |
| $T$ (K) | 150(2) |
| $\lambda$ (Å) | 0.71073 |
| crystal system, space group | Monoclinic, $P2_1/c$ |
| $a$ ; $b$ ; $c$ (Å) | 25.59(2) ; 16.64(2) ; 23.384(16) |
| $\beta$ (deg) | 107.15(7) |
| $Z$ ; $V$ (Å$^3$) | 4 ; 9516(15) |
| crystal size (mm$^3$) | 0.40 × 0.11 × 0.02 |
| Abs. coeff. (mm$^{-1}$) | 0.449 |
| $F$(000) | 3848 |
| $\theta$ range for data collection | 0.83 to 23.27° |
| limiting indices | $-28 \le h \le 16$, $-17 \le k \le 18$, $-25 \le \ell \le 23$ |
| no. of reflns collcd ; no. of ind. reflns ($R_{int}$) | 21102 ; 13140 (0.0402) |
| completeness to $\theta$ = 23.27° | 96.0 % |
| refinement method | Full-matrix least-squares on $F^2$ |
| data / restraints / parameters | 13140 / 0 / 1162 |
| $R_1$,[a] $wR_2$[b] ($I > 2\sigma(I)$) | 0.0592, 0.1397 |
| $R_1$,[a] $wR_2$[b] (all data) | 0.0976, 0.1611 |
| GOF[c] on $F^2$ | 1.028 |
| largest diff. peak and hole | 0.511 and −0.681 eÅ$^{-3}$ |

[a] $R_1 = \Sigma||F_o - |F_c||/\Sigma|F_o|$.

[b] $wR_2 = (\Sigma(w(F_o^2 - F_c^2)^2)/\Sigma(w(F_o^2)^2))^{1/2}$.

[c] $GOF = (\Sigma\, w(F_o^2 - F_c^2)^2/(n - p))^{1/2}$,
where $n$ is the number of data and $p$ is the number of parameters refined.

**Table VII.4.** Selected bond lengths (Å) in {(Ph$_4$P) [LFe$^{III}$]}$_2$ • MeCN • *o*-C$_6$H$_4$Cl$_2$.

| | | | |
|---|---|---|---|
| Fe(1)—N(1) | 1.905(4) | Fe(1)—N(3) | 1.898(4) |
| Fe(1)—N(2) | 1.902(4) | Fe(1)—N(4) | 1.898(4) |

tetracyanoethane, water, pyridinium chloride, and Ph$_4$PBr yield [LFe$^{III}$]$^-$ as the single paramagnetic product (see the crystal structure of (Ph$_4$P)[LFe$^{III}$], Figure VII.4 and Tables VII.3 and VII.4 — its metrics are similar to those of the sodium salt presented in Chapter V), however, in no case was a byproduct of O atom transfer (such as the epoxide, phosphine oxide, hypobromite) detected. We interpret these data as indicative of single-electron redox reactions of the iron porphyrinogen species with substrate and solvent: C—H activation and H$^\bullet$ atom abstraction most likely produce water and/or hydroxide along with reduced iron porphyrinogen.

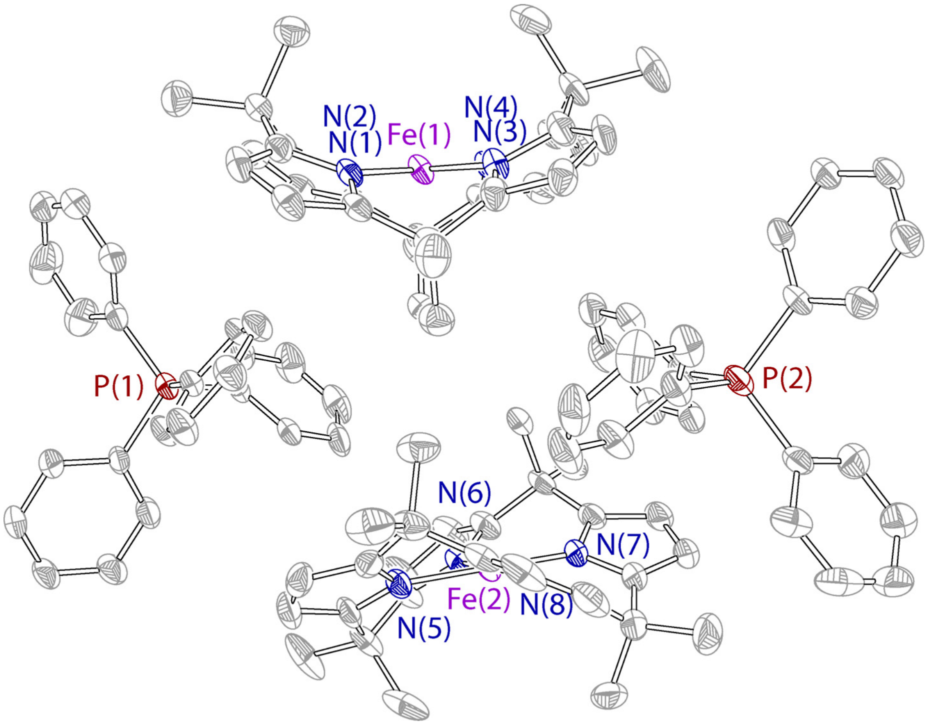

**Figure VII.4.** Crystal structure of $\{(Ph_4P)[LFe^{III}]\}_2 \cdot MeCN \cdot o\text{-}C_6H_4Cl_2$. H atoms and lattice solvent molecules are omitted. Thermal ellipsoids are drawn at the 50% probability level. Color coding: Fe, purple; N, blue; P, brown; C, gray.

The acyloin condensation is a rare example of a *four*-electron transformation that can be performed in aprotic conditions and only requires a redox agent, that is, does not involve group transfers to and from the metal center (Scheme VII.1). However, treatment of diethyladipate with the tetrabutylammonium salt of $[LFe^{II}]^{2-}$ in the presence of excess chlorotrimethylsilane ($Na_2[LFe^{II}]$ reacts with $Me_3SiCl$ but $(Bu_4N)_2[LFe^{II}]$ does not) at temperatures between 20 and 130°C and in toluene, THF, DME or MeCN does not yield any observable amount of the reduced product (by GC-MS). This result may be a consequence of insufficient reducing power of iron porphyrinogen: unlike that of sodium metal, the thermodynamic reducing ability of iron porphyrinogen is diminished upon each electron transfer.

As a final step, we turned our attention to the potential photochemistry of oxidized iron porphyrinogens. While electronic excitations caused by absorption of a photon correspond (in a first approximation) to the motion of a *single* electron from one orbital to another, formation or breaking of the "delta" C—C bond can be expected to stabilize processes in which a *pair* of electrons moves in either a

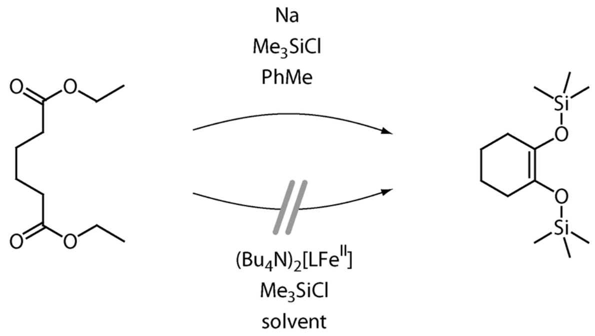

**Scheme VII.1.** Acyloin condensation of diethyl adipate to 1,2-bis(trimethylsilyloxy)-cyclohexene.

concerted or a consecutive fashion. Therefore, the question arises as to whether two-electron photochemistry can be derived from the two-electron essence of the C—C bond. Following an initial one-electron photoexcitation process, will the thermodynamic preference of porphyrinogen for two-electron chemistry be sufficient to drive the transfer of a second electron? This essentially translates the topic of the above paragraphs from the ground state into the excited state.[d,22] Experimentally, $[L^{\Delta\Delta}Fe^{II}Cl]^+$ is attractive because it is a likely intermediate along pathway (4),

$$[L^{\Delta\Delta}Fe^{II}]^{2+} + 2\,X^- \quad\rightarrow\quad [L^{\Delta\Delta}Fe^{II}X]^+ + X^- \quad\rightarrow\quad [L^{\Delta}Fe^{II}] + X_2 \qquad (4)$$

where $[L^{\Delta}Fe^{II}]$ is known to further disproportionate to $[LFe^{III}]^-$ and $[L^{\Delta\Delta}Fe^{II}]^{2+}$ (Chapter V). For X = I, the reaction does proceed to completion (see (3)), whereas the thermodynamics of X = Cl do not allow it without light absorption. Furthermore, given that the LUMOs of oxidized porphyrinogens are ligand-based (Chapter VI), the excited state can be expected to be of "chloride-to-porphyrinogen" nature and presenting a reactive chloride moiety. When $[L^{\Delta\Delta}Fe^{II}Cl](FeCl_4)$ is irradiated in the presence of the diene α-terpinene, no olefin dichlorination is observed. Irradiation at wavelengths $\lambda > 515$ nm, *i. e.* outside the high-ε region of $FeCl_4^-$ but within the absorption envelope of $[L^{\Delta\Delta}Fe^{II}Cl]^+$, causes no reaction. Irradiation of the $FeCl_4^-$ component ($\lambda > 350$ nm) yields $H^\bullet$ atom abstraction from terpinene and a clean, quantitative aromatization to cymene, in other words, single-electron chemistry originating from Fe(III).

---

[d] The relevance of this question to photoredox applications has already been noted.[22]

The reasons for the photochemical inertness of the $[L^{\Delta\Delta}Fe^{II}Cl]^+$ entity were investigated by ultrafast transient absorption (UV-visible pump-probe) spectroscopy. 500-nm excitation of $[L^{\Delta\Delta}Fe^{II}Cl]^+$ is followed by monoexponential decay of the transient signal with a lifetime $\tau = 30(\pm 10)$ ps. This short-lived excited states, in line with those observed for $[L^{\Delta}Mg]$ and $[LFe^{III}]^-$ (Chapters III and VI, respectively) precludes any photochemistry from occurring: non-productive vibrational relaxation occurs before the transient state has a chance to be funneled into the geometric reorganization and bonding changes that would accompany two-electron transformations of the ligand.

This phenomenon is in stark contrast to the photochemistry originating from higher-valent iron centers. In particular, chloroiron(III) porphyrins, $PFe^{III}$—Cl ($P^{2-}$ = a porphyrin dianion), have been shown to undergo a variety of thermal reactions originating from the $PFe^{II} + Cl^{\bullet}$ state obtained upon LMCT excitation.[23-25] In this case, the chloride-to-iron(III) LMCT excited state is extremely short-lived, even shorter than that of $[L^{\Delta\Delta}Fe^{II}Cl]^+$, but the excitation entails transfer of a Cl—Fe π-bonding electron into an orbital of antibonding character with respect to the same bond. Therefore, the structural rearrangement caused by the excited state directly activates the chemically relevant vibrational mode. Consistent with this interpretation, $\pi \rightarrow \pi^*$ excitation of the porphyrin ring of $PFe^{III}$—Cl does not cause any chemistry. Essentially, moving from an oxidant based on a high-valent iron center ($PFe^{III}Cl$) to one relying on an oxidized ligand coordinating a low-valent iron ion ($[L^{\Delta\Delta}Fe^{II}Cl]^+$) does weaken the Fe—Cl bond in thermodynamic terms, but it also causes the frontier orbitals to partly withdraw from the bond to be broken, thereby preventing productive photochemistry.

## VII.3. Conclusions

A general picture of the reactivity of ligand-oxidized iron porphyrinogen is obtained (Scheme VII.2). The neutral charge of the oxidized macrocycle $L^{\Delta\Delta}$ bears consequences on its coordination chemistry. Firstly, it makes the iron center more prone to axial coordination than within the reduced, tetraanionic version, and secondly, it significantly weakens the metal-macrocycle bonding. From a redox perspective,

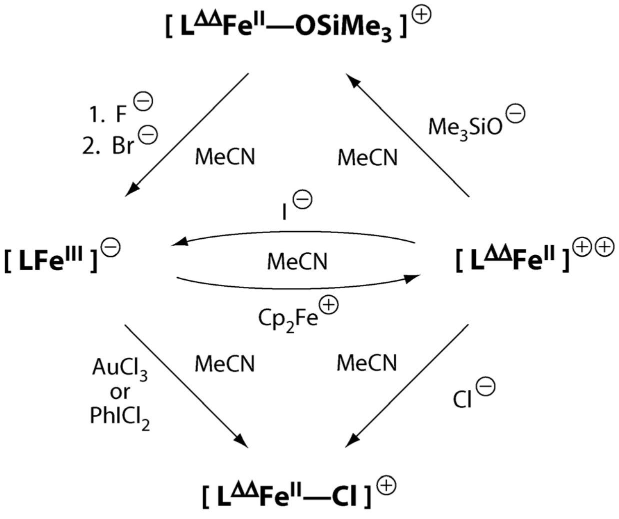

**Scheme VII.2.** Reactivity of oxidized iron porphyrinogen.

$[L^{\Delta\Delta}Fe^{II}]^{2+}$ is very labile, being reduced to $[LFe^{III}]^{-}$ by iodide and alcoholates; however, its preferred mode of redox reactivity seems to be single-electron transfer, which often translates into attack of somewhat weak solvent C—H bonds and $H^{\bullet}$ atom abstraction instead of group transfer chemistry. The same trend is evident in the photophysics of iron porphyrinogens. Photon-induced charge transfer is followed by fast back-transfer — the stabilization of even-electron events in "delta" C—C bond formation and breaking does not translate into the transfer of a second electron followed by further reactions. Instead, since the charge-transfer excited state within a flexible ligand framework causes a large structural reorganization, it strongly couples to vibrational modes of the electronic ground state. This coupling efficiently drags the electron back to its starting point before the thermodynamically favorable two-electron chemistry can occur.

In terms of the general design of redox agents based on a redox-active ligand in addition to (or instead of) the central metal ion, the results delineated in this Chapter suggest two broad conclusions. Firstly, a redox-active ligand enables its complexes to behave as oxidizers while maintaining a high metal d electron count, thereby maintaining a low Lewis acidity — in this case, reaction with $I^-$ yields $I^-$ *oxidation*, instead of the $I^-$ *coordination* more often observed when the oxidizer has an open coordination site. This property pleasantly conforms to the design concept delineated earlier. Secondly, the presence of a C—C bond as the redox-active element *enables* reactions that are overall multielectron in nature (such as $I^-$ to $I_2$), but does not *drive* the system to prefer even-electron pathways over odd-electron ones. This falls somewhat short of the initial hopes, and could potentially be due to the presence of a central metal with a one-electron redox couple (which could allow one-electron events that porphyrinogen itself would not enable), to an insufficient stability of the redox-active C—C bond, or to a combination of both.

The emerging picture of the reactivity of the $[L^{\Delta\Delta}Fe^{II}]^{2+}$ fragment, an oxidant in which the ligand (neutral $L^{\Delta\Delta}$) is the sole source of holes, is distinct from that observed for the "Compound I" of heme monooxygenases and their model complexes, $[XPFeO]^{(1-x)+}$ ($P^{2-}$ = a porphyrin dianion, $X^{x-}$ = an axial ligand, x = 0 or 1), which stores one hole at the metal (Fe(IV) oxidation state) and one at the ancillary ligand ($P^{\bullet-}$ radical anion).[26-32] In the case of hemes, oxidation of the ligand only occurs at high potential *after* the iron center has reached its extreme OS, and it is stabilized by extensive delocalization of the hole, whereas in the porphyrinogen complexes the ligand is easier to oxidize than the Fe(III) ion, in part thanks to the localization of paired holes in redox-active C—C bonds. The high-valent iron center of Compound I imposes an electrophilic character on its coordinated oxo, which is not observed for the the bound chloro of $[L^{\Delta\Delta}Fe^{II}Cl]^+$. It also strengthens the Fe=O bond, a thermodynamic effect in part compensated for by the instability of the very high oxidation state of the "$[PFe]^{3+}$" fragment. Finally, Compound I selectively performs O atom transfers (hydroxylation of C—H bonds, epoxidation of C=C bonds) whereas no such reactivity has been evidenced on the $[L^{\Delta\Delta}Fe^{II}]^{2+}$ platform, a fact most likely indicative of odd-electron chemistry. However, the propensity of iron porphyrinogen to undergo reactions *via* radical pathways is partly mirrored by the chemistry of hemes. Oxygenations by Compound I occur through the intermediacy of radicals as well, the first step being H atom abstraction (from the alkane substrate) or electron transfer (from the olefin substrate) to yield a heme species reduced by one electron and an organic radical. Both then quickly "rebound" together to generate the product.

# VII.4. Experimental section

## VII.4.a. Synthesis and reactivity

*General technique*

All compounds were handled, reactions were performed, and analytical samples were prepared in inert atmosphere using standard Schlenk, dry-box and vacuum-line techniques. Solvents were purchased from VWR Scientific Products or Sigma Aldrich and purified using a Braun solvent purification system or using standard solvent purification techniques.[33] Deuterated solvents were purchased from Cambridge Isotope Laboratories, degassed, dried and distilled by procedures similar to those used for non-isotopically enriched solvents. Other reagents were purchased from Aldrich, Acros or Strem Chemicals and used as received.

*Synthesis of* $[L^{\Delta\Delta}Fe^{II}Cl](FeCl_4)$

*Method A.* A sample of $[L^{\Delta\Delta}Fe^{II}](BF_4)_2$ (56 mg, 83 µmol) was dissolved in 5 mL of 1:1 MeCN / $CH_2Cl_2$ mixture then cooled to −75°C on a $CO_2$ / acetone slurry. $Bu_4NCl$ (23 mg, 83 µmol) was separately dissolved in 5 mL of $CH_2Cl_2$, then added dropwise to the first solution. The mixture was left to slowly warm up to room temperature, then hexanes (70 mL) were added to the brown solution, yielding $[L^{\Delta\Delta}Fe^{II}Cl](FeCl_4)$ (33 mg, 55%) as a brown solid after filtering and drying.

*Method B.* A sample of $[Na(THF)_{2.5}][LFe^{III}]$ (84 mg, 120 µmol) was dissolved in 2 mL of MeCN, then the solvent was removed; the solid residue was redissolved in 2 mL of $CH_2Cl_2$ and $AuCl_3$ (36 mg, 120 µmol) was added at room temperature. After 5 minutes of stirring, the dark slurry was filtered on Celite to remove NaCl and Au metal. The filtrate was layered with pentane to cause precipitation of $[L^{\Delta\Delta}Fe^{II}Cl](FeCl_4)$ (32 mg, 36%) as a brown solid after drying.

*Method C.* A sample of $[Na(THF)_{2.5}][LFe^{III}]$ (171 mg, 240 µmol) was dissolved in 5 mL of MeCN, then the solvent was removed; the solid residue was redissolved in 5 mL of MeCN, then an excess of $PhICl_2$ (180 mg, 650 µmol) was added. After 5 minutes of stirring at room temperature, the mixture was evaporated and the solid residue was triturated in 2 mL of toluene. The brown solid obtained by filtration was recrystallized from $CH_2Cl_2$ / pentane, yielding $[L^{\Delta\Delta}Fe^{II}Cl](FeCl_4)$ (50 mg, 56%) as a brown powder.

*Analyses.* (+)-ESI-TOF-MS: *m/z* = 539.3 ($[L^{\Delta\Delta}Fe^{II}Cl]^+$, $[C_{28}H_8D_{24}ClFeN_4]^+$: 539.3). $^1$H NMR ($CDCl_3$, 500 MHz): *δ*/ppm = 55 (4 H, pyrr.), –9 (4 H, pyrr.). Mössbauer: δ = 1.0 mm/s, $\Delta E_q$ = 3.8 mm/s.

*Synthesis of $[L^{\Delta\Delta}Fe^{II}OSiMe_3](OSiMe_3)$*

A $CH_2Cl_2$ solution of $NaOSiMe_3$ (2.76 mL, 1.0 M, 2.76 mmol) was diluted to 50 mL and added to solid $[L^{\Delta\Delta}Fe^{II}](BF_4)_2$ (0.935 g, 1.38 mmol); the brown solution was refluxed for 50 minutes, then cooled to room temperature and filtered. The filtrate was evaporated and dried. The brown solid residue was triturated in 50 mL of hexanes, filtered and dried, yielding $[L^{\Delta\Delta}Fe^{II}OSiMe_3](OSiMe_3)$ (0.51 g, 54%) as a dark brown powder. Found: C, 59.5; N, 8.0; Fe, 8.0; Si, 8.3; calc. for $C_{34}H_{26}D_{24}FeN_4O_2Si_2$: C, 59.8; N, 8.2; Fe, 8.2; Si, 8.2. $^1$H NMR ($CD_2Cl_2$, 500 MHz): *δ*/ppm = 107 (2 H, pyrr.), 89 (2 H, pyrr.), 84 (2H, pyrr.), 27 (2H, pyrr.), 19 (>10 H, -$OSiMe_3$). Mössbauer: δ = 0.4 mm/s, $\Delta E_q$ = 1.0 mm/s.

*Iodide oxidation by $[L^{\Delta\Delta}Fe^{II}](BF_4)_2$*

*Low-temperature reaction.* Two 1-mL $CD_3CN$ solutions were prepared independently and cooled to freezing: $[L^{\Delta\Delta}Fe^{II}](BF_4)_2$ (10 mg, 15 µmol) and an excess of $Bu_4NI$ (33 mg, 89 µmol). As soon as they started thawing, cold $[L^{\Delta\Delta}Fe^{II}](BF_4)_2$ was added dropwise to $Bu_4NI$: the mixture darkened and was left to warm up to room temperature under stirring. A crude sample was analyzed by $^1$H NMR (400 MHz): *δ*/ppm = –73 (0.85 × 8 H, $[LFe^{III}]^-$), 5.62 (0.15 × 8 H, $LH_4$ pyrr.), 7.25 (0.15 × 4 H, $LH_4$ NH), 3.12 (quartet, *J* 10, ~6 × 8 H, $Bu_4N^+$ α), 1.64 (quintet, *J* 8, ~6 × 8 H, $Bu_4N^+$ β), 1.38 (sextet, *J* 7, ~6 × 8 H, $Bu_4N^+$ γ), 1.00 (quartet, *J* 9, ~6 × 12 H, $Bu_4N^+$ δ).

*Stoichiometry.* Two stock solutions were prepared in MeCN: **sfe**, 10.7 mg of $[L^{\Delta\Delta}Fe^{II}](BF_4)_2$ in 0.11 mL (0.14 M); **si**, 167 mg of $Bu_4NI$ in 0.33 mL (1.4 M). Solutions **A** through **I**, representing $I^-$ / $[L^{\Delta\Delta}Fe^{II}]^{2+}$ stoichiometries $0 \leq n \leq 10$, were then prepared by mixing the following amounts of stock solutions,

| | µL **sfe** | µL **si** | *n* |
|---|---|---|---|
| **A** | 5 | 0 | 0 |
| **B** | 15 | 0.75 | 0.5 |
| **C** | 15 | 1.5 | 1 |
| **D** | 10 | 2 | 2 |
| **E** | 10 | 3 | 3 |
| **F** | 10 | 4 | 4 |
| **G** | 10 | 5 | 5 |
| **H** | 10 | 6 | 6 |
| **I** | 10 | 10 | 10 |

then opening the solutions to air, diluting **A** to 100 µL, **B** and **C** to 300 µL, and all others to 200 µL, and finally diluting a 50-µL sample of each to 1 mL for UV-visible absorption analysis in an optical cell of 1-mm pathlength.

*Reactivity of* $[L^{\Delta\Delta}Fe^{II}OSiMe_3](OSiMe_3)$

A sample of $Me_4NF$ (33 mg, 350 µmol) was dissolved in 10 mL of $CH_2Cl_2$, then added to solid $[L^{\Delta\Delta}Fe^{II}OSiMe_3](OSiMe_3)$ (119 mg, 170 µmol). The mixture was heated to reflux shortly, and after cooling it was filtered and dried to yield 61 mg of a brown solid. $^1H$ NMR ($CD_3CN$, 500 MHz): $\delta$/ppm = +20 (4 H, pyrr.), +15 (4 H, pyrr.), +2.2 (br, $Me_4N^+$, overlapping with acetonitrile). $^2H$ NMR ($CH_3CN$, 67 MHz): $\delta$/ppm = +7 (6 H, –$CD_3$), +4 (6 H, –$CD_3$), –4 (6 H, –$CD_3$), –21 (6 H, –$CD_3$). Mössbauer: $\delta = 0.3$ mm/s, $\Delta E_q = 3.2$ mm/s.

*Photochemistry of* $[L^{\Delta\Delta}Fe^{II}Cl](FeCl_4)$

A sample of $\alpha$-terpinene was degassed by three cycles of freeze-pump-thaw and kept under high vacuum. A small sample of $[L^{\Delta\Delta}Fe^{II}Cl]$ ($FeCl_4$) was loaded into a J. Young NMR tube, which was then evacuated to $<10^{-4}$ Torr on a high-vacuum line and maintained in the dark. $CD_3CN$, then some $\alpha$-terpinene were condensed into the tube. $^1H$ NMR (600 MHz) was used to assess the terpinene / $[L^{\Delta\Delta}Fe^{II}Cl]^+$ ratio to be 7:1. Not all couplings within the organic compound were resolved due to paramagnetic broadening. $\delta$/ppm = 54 (4 H, $[L^{\Delta\Delta}Fe^{II}Cl]^+$), –10 (4 H, $[L^{\Delta\Delta}Fe^{II}Cl]^+$), 5.62 (d, 15 Hz, 14 H, terpinene =C*H*–C*H*=), 2.32 (s, 7 H, terpinene –C*H*$Me_2$), 2.13 (s, 28 H, –C$H_2$–C$H_2$–), 1.78 (s, 21 H, –C$H_3$), 1.05 (s, 42 H, –CH(C$H_3$)$_2$). The mixture was irradiated between 350 and 490 nm for 2 hr. $^1$H NMR (600 MHz) of the crude mixture showed that all $[L^{\Delta\Delta}Fe^{II}Cl]^+$ had been converted to $LH_4$, while roughly 6 equivalents of α-terpinene remained and 1 equivalent of α-cymene had been formed. δ/ppm = 7.61 (4 H, $LH_4$ N*H*), 5.79 (8 H, $LH_4$ pyrr.), 5.60 (d, 12 Hz, 12 H, terpinene =C*H*–C*H*=), 2.09 (q, 7 Hz, 24 H, terpinene –C$H_2$–C$H_2$–), 1.76 (s, 18 H, terpinene –C$H_3$), 1.02 (s, 36 H, terpinene –CH(C$H_3$)$_2$), 7.13 (d, 12 Hz, 4 H, cymene arom.), 2.87 (quintet, 8 Hz, 1 H, cymene –C*H*Me$_2$), 1.21 (d, 6 Hz, 6 H, cymene –CH(C$H_3$)$_2$), 2.30 (s, 9 H, terpinene –C*H*Me$_2$ overlapping with cymene –C$H_3$). A sample was taken, exposed to air and analyzed by GC-MS(EI): M$^+$ ions were found at *m/z* = 136 (α-terpinene), 134 (α-cymene), 453 ($LH_4$), and 488 (minor, $LH_3Cl$). The rest of the reaction mixture was again degassed, then the volatiles were vacuum-transferred into a new J. Young NMR tube, for an additional, cleaner $^1$H NMR (600 MHz) analysis which allowed observation of all *J*-couplings. δ/ppm = 5.62 (dd, 17 and 4 Hz, 12 H, terpinene =C*H*–C*H*=), 2.10 (dd, 20 and 8 Hz, 24 H, terpinene –C$H_2$–C$H_2$–), 1.78 (s, 18 H, terpinene –C$H_3$), 1.04 (d, 7 Hz, 36 H, terpinene –CH(C$H_3$)$_2$), 7.13 (q, 8 Hz, 4 H, cymene arom.), 2.89 (septuplet, 7 Hz, 1 H, cymene –C*H*Me$_2$), 1.23 (d, 7 Hz, 6 H, cymene –CH(C$H_3$)$_2$), 2.31 (s, 9 H, terpinene –C*H*Me$_2$ overlapping with cymene –C$H_3$).

*Control experiments*. The experiment was repeated with a 20:1 α-terpinene / $[L^{\Delta\Delta}Fe^{II}Cl]^+$ ratio, irradiating at $\lambda > 515$ nm for 8 hrs: $^1$H NMR showed no conversion of terpinene to cymene. It was also repeated replacing $[L^{\Delta\Delta}Fe^{II}Cl](FeCl_4)$ with $(18C6)K(FeCl_4)$ (18C6 is 1,4,7,10,13,16-hexaoxacyclooctadecane): irradiation of a 1:1 ratio of α-terpinene $(18C6)K(FeCl_4)$ between 350 and 490 nm for 2 hrs showed a 50% conversion of terpinene to cymene.

## VII.4.b. X-ray crystal structure determinations

*General parameters*

X-ray quality crystals were coated with Paratone N oil and mounted on a glass fiber. X-ray diffraction data were collected on a Siemens diffractometer equipped with a CCD detector, using the Mo Kα radiation, selected by a graphite monochromator. The data were integrated to *hkℓ*-intensity and the final unit cell calculated using the SAINT v.4.050 program from Siemens. Solution and refinement were performed with the

SHELXTL v.5.03 suite of programs developed by G. M. Sheldrick and Siemens Industrial Automation, 1995. Least-squares refinements were applied to $F^2$, with hydrogen atoms of organic fragments placed at calculated positions using a standard riding model and refined isotropically. No absorption correction was performed.

*X-ray crystal structure of* $[L^{\Delta\Delta}Fe^{II}Cl]\ (FeCl_4)$

An orange plate was grown by diffusion of a cyclohexane layer into a concentrated solution of $[L^{\Delta\Delta}Fe^{II}Cl](FeCl_4)$ (from method B) in MeCN / *ortho*-dichlorobenzene. Data were collected at 100 K. The structure was solved by direct methods. The asymmetric unit was found to contain two chemically equivalent $[L^{\Delta\Delta}Fe^{II}Cl](FeCl_4)$ units; one of the $FeCl_4^-$ anion was disordered between two orientations sharing the same Fe center, and the relative populations of the two orientations were refined.

*X-ray crystal structure of* $(Ph_4P)[LFe^{III}]$

A black plate was grown by diffusion of an *n*-heptane layer into a concentrated solution of $(Ph_4P)[LFe^{III}]$ (from $[L^{\Delta\Delta}Fe^{II}(OSiMe_3)](OSiMe_3)$ + $Me_4NF$ + $Ph_4PBr$) in MeCN / *ortho*-dichlorobenzene. Data were collected at 150 K. Because a cooling problem occurred after the 600th frame, only the first 600 frames were used for further data processing. The structure was solved by direct methods. The asymmetric unit was found to contain two chemically equivalent $(Ph_4P)[LFe^{III}]$ units and two solvent molecules (one MeCN and one $o$-$C_6H_4Cl_2$).

## VII.4.c. Physical methods

*Steady-state methods*

$^1$H-NMR spectra were recorded at the MIT Department of Chemistry Instrumentation Facility (DCIF) on a Varian Inova-500 spectrometer, a Bruker Avance-600 or a Bruker Avance-400. Chemical shifts are quoted in ppm relative to tetramethylsilane and spectra have been internally calibrated to the monoprotio impurity of the deuterated solvent. $^2$H-NMR spectra were recorded on a Varian Inova-500 equipped with a direct-probe. Mössbauer absorption data were obtained at 4.2 K on an MS1 spectrometer

(WEB Research Co.) equipped with a $^{57}$Co source and a Janus cryostat, and referenced to elemental iron. UV-visible absorption spectra were measured on a Spectral Instruments 440 spectrophotometer. Elemental analyses were conducted at H. Kolbe Mikroanalytisches Laboratorium (Mühlheim a. d. Ruhr, Germany). ESI-MS analyses were performed at the Mass Spectroscopy Laboratory at the University of Illinois at Urbana-Champaign.

*Transient absorption spectroscopy*

Samples for transient absorption spectroscopy were contained in a 2-mm pathlength high-vacuum cell and prepared to yield an optical density of ~0.5 at the excitation wavelength. The setup used for ultrafast transient absorption experiments was described previously.[34] In brief, the pulsed 806-nm output of a regeneratively amplified Ti-Sapphire laser system was separated into two beams. The weaker component was focused into either a sapphire or a calcium fluoride substrate to generate the broadband probe pulse. The major component was either frequency-doubled to 403 nm, or tuned throughout the visible range with an optical parametric amplifier, then propagated along a computer-controlled optical delay-line to furnish time resolution. The excitation energy was set to ~5 μJ/pulse, and both beams were spatially overlapped on the sample; the pump beam was then blocked, and the probe was spectrally resolved in a monochromator. Transient spectra were recorded with a CCD camera and derived using a ‘negative time’ reference spectrum; single-wavelength kinetics were obtained with a lock-in amplified photodiode detector.

## VII.5. References

1 Schrauzer, G. N.; Mayweg, V. P. *J . Am. Chem. Soc.* **1962**, *84*, 3221.

2 Schrauzer, G. N.; Mayweg, V. P. *J. Am. Chem. Soc.* **1965**, *87*, 3585-3592.

3 Davison, Edelstein, N.; Holm R. H.; Maki, A. H. *J. Am. Chem. Soc.* **1963**, *85*, 2029-2030.

4 Maki, A. H.; Edelstein, N.; Davison, A.; Holm, R. H. *J. Am. Chem. Soc.* **1964**, *86*, 4580-4587.

5 Holm, R. H.; Balch, A. L.; Davison, A.; Maki, A. H.; Berry, T. E. *J. Am. Chem. Soc.* **1967**, *89*, 2866-2874.

6 Latham, A. R.; Hascall, V. C.; Gray, H. B. *Inorg. Chem.* **1965**, *4*, 788-792.

7 Billig, E.; Williams, R.; Bernal, I.; Waters, J. H.; Gray, H. B. *Inorg. Chem.* **1964**,*3*, 663-666.

8 Shupack, S. I.; Billig, E.; Clark, R. J. H.; Williams, R.; Gray, H. B. *J. Am. Chem. Soc.* **1964**, *86*, 4594-4602.

9 Gray, H. B.; Billig, E. *J. Am. Chem. Soc.* **1963**, *85*, 2019-2020.

10 Stiefel, E. I.; Waters, J. H.; Billig, E.; Gray, H. B. *J. Am. Chem. Soc.* **1965**, *87*, 3016-3017.

11 Ray, K.; Bill, E.; Weyhermüller T.; Wieghardt, K. *J. Am. Chem. Soc.* **2005**, *127*, 5641-5654.

12 Ray, K.; Weyhermüller, T.; Goossens, A.; Craje, M. W. J.; Wieghardt, K. *Inorg. Chem.* **2003**, *42*, 4082-4087.

13 Blackmore, K. J.; Ziller, J. W.; Heyduk, A. F. *Inorg. Chem.* **2005**, *44*, 5559-5561.

14 Jubb, J.; Floriani, C.; Chiesi-Villa, A.; Rizzoli, C. *J. Am. Chem. Soc.* **1992**, *114*, 6571-6573.

15 De Angelis, S.; Solari, E.; Floriani, C.; Chiesi-Villa, A. Rizzoli, C. *J. Am. Chem. Soc.* **1994**, *116*, 5691-5701.

16 De Angelis, S.; Solari, E.; Floriani, C.; Chiesi-Villa, A.; Rizzoli, C. *J. Am. Chem. Soc.* **1994**, *116*, 5712-5713.

17 Crescenzi, R.; Solari, E.; Floriani, C.; Chiesi-Villa, A.; Rizzoli, C. *J. Am. Chem. Soc.* **1999**, *121*, 1695-1706.

18 Bhattacharya, D.; Dey, S.; Maji, S.; Pal, K.; Sarkar, S. *Inorg. Chem.* **2005**, *44*, 7699-7701.

19 Shapley, P. A.; Bigham, W. T.; Hay, M. T. *Inorg. Chim. Acta* **2003**, *345*, 255-260.

20 P. W. Atkins, P. W. in *Physical Chemistry*, Oxford University Press, Oxford, 6th edn., 1988, p. 937.

21 MacBeth, C. E.; Gupta, R.; Mitchell-Koch, K. R.; Young, V. G., Jr.; Lushington, G. H.; Thompson, W. H.; Hendrich, M. P.; Borovik, A. S. *J. Am. Chem. Soc.* **2004**, *126*, 2556-2567.

22 K. J. Takeuchi, M. S. Thompson, D. W. Pipes and T. J. Meyer, *Inorg. Chem.* **1984**, *23*, 1845-1851.

23 Hendrickson, D. N.; Kinnaird, M. G.; Suslick, K. S. *J. Am. Chem. Soc.* **1987**, *109*, 1243-1244.

24 Suslick, K. S.; Watson, R. A. *Inorg. Chem.* **1991**, *30*, 912-919.

25 Suslick, K. S.; Watson, R. A. *New J. Chem.* **1992**, *16*, 633-642.

26 Watanabe, Y. *J. Biol. Inorg. Chem.* **2001**, *6*, 846-856.

27 Ortiz de Montellano, P. R. *Ann. Rev. Pharmacol. Toxicol.* **1992**, *32*, 89-107.

28 Newcomb, M.; Chandrasena, R. E. P. *Biochem. Biophys. Res. Commun.* **2005**, *338*, 394-403.

29 Gross, Z. *J. Biol. Inorg. Chem.* **1996**, *1*, 368-371.

30 Groves, J. T.; Haushalter, R. C.; Nakamura, M.; Nemo, T. E.; Evans, B. J. *J. Am. Chem. Soc.* **1981**, *103*, 2884-2886.

31 de Visser, S. P.; Ogliaro, F.; Shaik, S. *Chem. Commun.* **2001**, 2322-2323.

32 Kim, S. H.; Perera, R.; Hager, L. P.; Dawson, J. H.; Hoffman, B. M. *J. Am. Chem. Soc.* **2006**, *128*, 5598-5599.

33 Armarego, W. L. F.; Perrin, D. D. in Purification of Laboratory Chemicals; Butterworth-Heinmann: Oxford, 4th ed. 1996.

34 Hodgkiss, J. M.; Chang, C. C.; Pistorio, B. J.; Nocera, D. G. *Inorg. Chem.* **2003**, *42*, 8270-8277.

# Chapter VIII

# Photochemical reduction of a proton by cobalt porphyrinogen

## VIII.1. Introduction

Hydrogenases catalyze the redox interconversion of $H^+$ and $H_2$ in biological systems. They contain polynuclear inorganic active sites, with ancillary redox clusters providing the holes or electrons, and acid-base groups routing the protons, to the reaction centers (Scheme VIII.1.A).[1,2] To date, research on hydrogenase models has mostly focused on mimicking the *structure* of the crystallographically characterized enzymes, in some cases with quite elaborate constructs.[3-5] However, approaches to *functional* models based on quite different structures are conceivable. In particular, the ability of some cobalt(II) complexes to reduce $H^+$ to $H_2$ photocatalytically,[6,7] as well as $CO_2$ to CO,[8] is well established. In such systems, an excited ligand-to-metal charge transfer state featuring a strongly reducing formal Co(I) center intermolecularly reacts with a proton source and generates a hydrogen radical, $H^\bullet$, which then further decays.[9] Even though $H_2$ is one of the main products of $H^\bullet$ decay, the radical intermediate lacks selectivity and photocatalyst decomposition results.[6-9] Thus, in essence, the Co(II) salt is the source of the most crucial ingredient in the photoproduction of $H_2$, that is, a high-energy electron, but it lacks the other three components (which hydrogenase enzymes manage), namely, two protons and a second electron. Therefore, improvement of the catalyst would logically require to supplement the Co(II) reaction center with *(a)* an additional redox reservoir able to quickly provide a second electron, and *(b)* two Brønsted acid-base sites that would deliver the protons. In the proteins and model systems, those requirements are met by the design of intricate multicomponent molecular or supramolecular systems featuring several functional sites able to work in concert.[3-5] The porphyrinogen ligand, however, could be the ideal "2-in-1" packaging for Co(II):[10,11] *(a)* its redox activity enables it to provide two electrons with the formation of the spirocyclopropane C—C bond, and *(b)* metalloporphyrinogens have the capacity to take up one or two protons in the proximity of the metal center.[12] These considerations imply the intriguing possibility of the following set of transformations,

$$2\,H^+ \;+\; [\,L^{(4-)}Co^{II}\,]^{2-} \;\rightarrow\; [\,(H_2L)^{(2-)}Co^{II}\,] \;\rightarrow\; [\,(H_2L)^{(\bullet\,-)}Co^{I}\,]^* \;\rightarrow\; H_2 \;+\; [\,L^{(\Delta,2-)}Co^{II}\,]$$

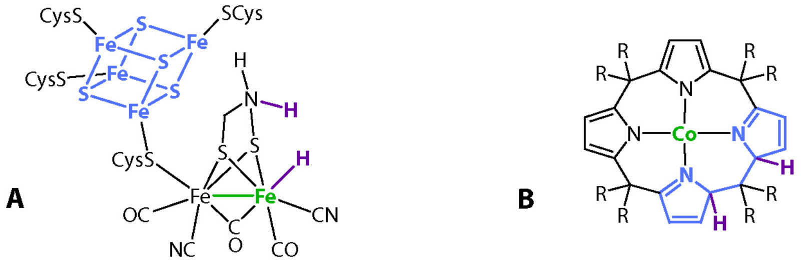

**Scheme VIII.1.** The active site of the Fe-only hydrogenase according to Rauchfuss' interpretation of the crystal structure (left, **A**),[2,5] and a hypothetical cobalt porphyrinogen in equivalent protonation and redox states (right, **B**). Color coding highlights the presence of corresponding functional units, namely a metal ion which could potentially present a hydride for protonation (green), a reservoir of electrons (blue), and two protons (purple).

where the asterisk denotes a charge transfer excited state obtained by absorption of a UV or visible photon.

Conceptually, metalloporphyrinogens are multifunctional entities (Scheme VIII.1.**B**) that pack *(i)* redox activity (at the metal and at the pyrroles), *(ii)* Lewis acidity (at the metal), *(iii)* Lewis and Brønsted basicity (at the pyrroles), and even *(iv)* a chromophore (in the LMCT) in a conveniently small molecule, which contrasts with the rather heavy reactive core found in the enzymes (Scheme VIII.1.**A**). This Chapter describes investigations probing the possibility of using cobalt porphyrinogens as a stoichiometric photoinduced hydrogenase mimic. Two versions of the ligand are used, the octakis(perdeuteromethyl)- and the octabenzylporphryinogen, abbreviated $L^{4-}$ and $^{Ph}L^{4-}$, respectively, in their lowest oxidation state.

## VIII.2. Cobalt porphyrinogens, synthesis and structure

### VIII.2.a. Metallation and oxidation

Reaction of the tetrasodium salt of either octa(perdeuteriomethyl)- or octabenzyl-porphyrinogen with cobalt(II) chloride yields the disodium salt of the corresponding yellow Co(II)-porphyrinogen complex. The corresponding red Co(III) oxidation state can also be obtained by oxidation with ferrocenium. The electrochemistry of $[LCo^{II}]^{2-}$,

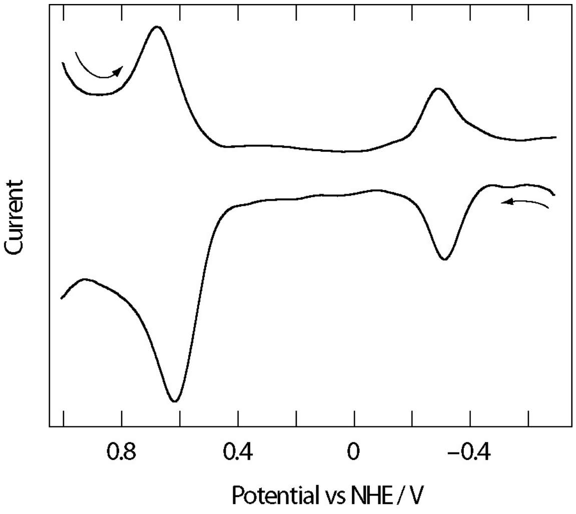

**Figure VIII.1.** Electrochemistry of cobalt octamethylporphyrinogen: DPV traces for 1 mM $Na_2[LCo^{II}]$ in 0.9 M $Bu_4NBF_4$ / MeCN. Experimental parameters: sweep rate 20 mV/s, pulse amplitude 50 mV, period 200 mV, pulse width 50 ms, sample width 17 ms.

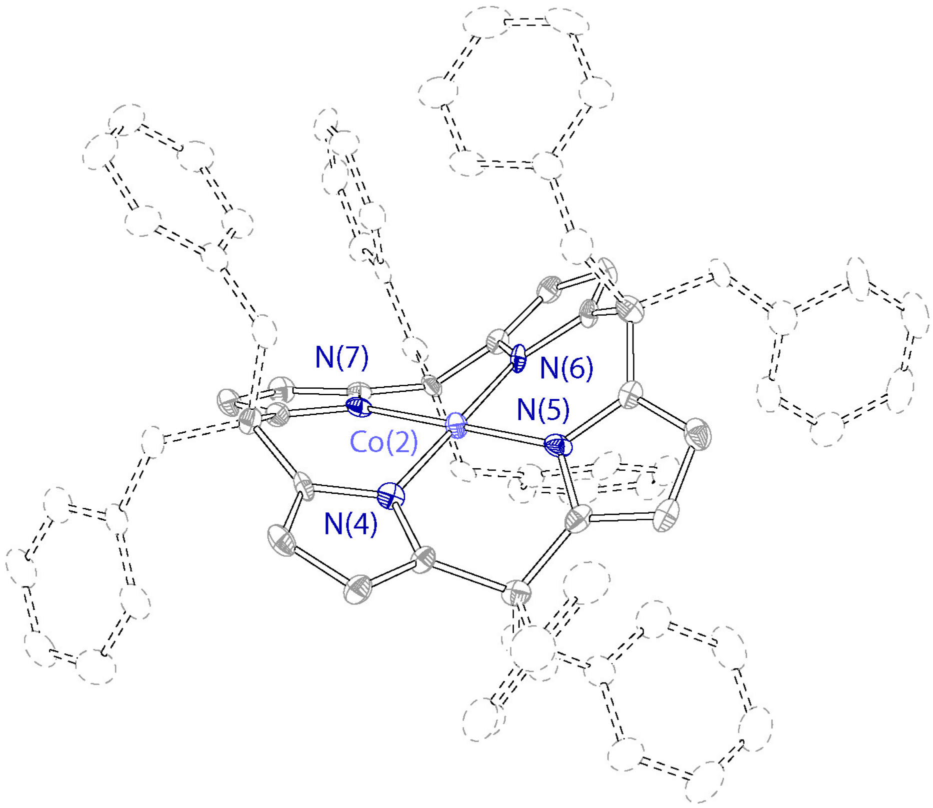

**Figure VIII.2.** Crystal structure of the Co(II) octabenzylporphyrinogen dianion. The asymmetric unit contains 1.5 chemically identical $[^{Ph}LCo]^{2-}$ moieties and 3 well-separated $\{Na(DME)_3\}^+$ counter-ions; only one $[^{Ph}LCo]^{2-}$ ion is displayed, and H atoms are omitted. Thermal ellipsoids are drawn at the 50% probability level. Color coding: Co, powder blue; N, blue; C, gray.

displayed in Figure VIII.1, is qualitatively similar to that observed for iron porphyri-nogen (Chapter V), with a first wave at negative potential and a second, more intense one at positive potential, assigned to the $[LCo^{III}]^{-}$ / $[LCo^{II}]^{2-}$ and $[L^{\Delta\Delta}Co^{II}]^{2+}$ / $[LCo^{III}]^{-}$ couples, respectively. Quantitative differences observed between the iron and cobalt systems are consistent with the better stability of the +III oxidation state usually observed for Fe relative to Co: the $[LCo^{III}]^{-}$ / $[LCo^{II}]^{2-}$ couple appears at –0.30 V *vs* NHE for M = Co (instead of –0.57 V for Fe), and the $[L^{\Delta\Delta}Co^{II}]^{2+}$ / $[LCo^{III}]^{-}$ wave at +0.65 V (+0.77 V for M = Fe). In other words, the window in which the $[LM^{III}]^{-}$ OS is stable shrinks on both its high- and low-potential sides for M = Co with respect to M = Fe, but a sufficient driving force for the disproportionation of neutral and monocationaic species remains nevertheless, resulting in a maintained three-electron couple between $[L^{\Delta\Delta}M^{II}]^{2+}$ and $[LM^{III}]^{-}$.

## VIII.2.b. Structures

*Crystal structure of* $Na(DME)_3$ $[^{Ph}LCo^{II}]$

The crystal structure of the disodium salt of cobalt(II) octabenzylporphyrinogen, $[^{Ph}LCo^{II}]^{2-}$, is presented in Tables VIII.1 and VIII.2 and in Figure VIII.2. The sodium cations are separated from the dianion by triple chelation by DME in pseudo-octahedral fashion. The cobalt ion lies at the center of a nearly perfect square defined by the four pyrrole nitrogens; no intermolecular close contacts are observed, and the distances between cobalt and the $\alpha$-H atoms of the *meso* benzyl substituents comprise between 2.7 and 3.0 Å.[a] The average Co—N distances of 1.931 and 1.918 Å, respectively, for the two crystallographically independent $[^{Ph}LCo^{II}]^{2-}$ units, appear to be somewhat short when compared to the average Fe—N distance of 1.933 Å found in $Na_2(THF)_2(pyO)_2$ $[LFe^{II}]$, given the presence of an additional metal d electron. They are, however, slightly longer than the average Co—N distance in dilithium cobalt(II) octaethylporphyrinogen, which features $\pi$-bonded $Li^+$ ions.[13]

---

[a] Note that in the refinement of the crystal structure the positions of the H atoms are *modeled* and that therefore metrics involving them are not direct physical measurements.

**Table VIII.1.** Summary of X-ray crystallographic data for $\{Na(DME)_3\}_2$ [$^{Ph}LCo^{II}$].

| | |
|---|---|
| empirical formula (formula weight) | $C_{100}H_{124}CoN_2O_{12}$ (1678.94) |
| $T$ (K) | 100(2) |
| $\lambda$ (Å) | 0.71073 |
| crystal system, space group | Monoclinic, $C2/c$ |
| $a$ ; $b$ ; $c$ (Å) | 35.6211(19) ; 23.2660(13) ; 33.2209(19) |
| $\beta$ (deg) | 90.337(2) |
| $Z$ ; $V$ (Å$^3$) | 12 ; 27532(3) |
| crystal size (mm$^3$) | $0.12 \times 0.08 \times 0.04$ |
| Abs. coeff. (mm$^{-1}$) | 0.259 |
| $F$(000) | 10764 |
| $\theta$ range for data collection | 1.05 to 23.24° |
| limiting indices | $-31 \le h \le 39$, $-25 \le k \le 25$, $-31 \le \ell \le 36$ |
| no. of reflns collcd ; no. of ind. reflns ($R_{int}$) | 65983 ; 19709 (0.1647) |
| completeness to $\theta = 23.24°$ | 99.8 % |
| refinement method | Full-matrix least-squares on $F^2$ |
| data / restraints / parameters | 19709 / 0 / 1627 |
| $R_1$,[a] $wR_2$[b] ($I > 2\sigma(I)$) | 0.0723, 0.1451 |
| $R_1$,[a] $wR_2$[b] (all data) | 0.1667, 0.1859 |
| GOF[c] on $F^2$ | 1.009 |
| largest diff. peak and hole | 0.620 and −0.526 eÅ$^{-3}$ |

[a] $R_1 = \Sigma||F_o| - |F_c||/\Sigma|F_o|$.

[b] $wR_2 = (\Sigma(w(F_o^2 - F_c^2)^2)/\Sigma(w(F_o^2)^2))^{1/2}$.

[c] $GOF = (\Sigma\, w(F_o^2 - F_c^2)^2/(n - p))^{1/2}$,
where $n$ is the number of data and $p$ is the number of parameters refined.

**Table VIII.2.** Selected bond lengths (Å) in $\{Na(DME)_3\}_2$ [$^{Ph}LCo^{II}$].

| | | | |
|---|---|---|---|
| Co(2)—N(4) | 1.933(5) | Co(2)—N(6) | 1.928(4) |
| Co(2)—N(5) | 1.935(5) | Co(2)—N(7) | 1.927(5) |

### *Solution structures observed by NMR*

As noted in Chapter V, the interpretation of the NMR characteristics of paramagnetic octamethylporphyrinogen compounds is facilitated by deuteration. It then provides the basis for the assignment of the corresponding octabenzylporphyrinogen NMR lines, with the assumption that the solution geometry of a given compound will be similar in its octamethyl and octabenzyl versions.

$Na_2[LCo^{II}]$ gives rise to a single, broad $^1H$ NMR signal at +0.2 ppm, and two $^2H$ NMR peaks at +8.4 and −31.2 ppm. This result is consistent with the $D_{2d}$ symmetry of the ruffled tetrapyrrole observed in the solid state and in solution for all $L^{4-}$ compounds: all eight pyrrolic β protons are equivalent, whereas the methyl deuterons appear in distinct axial and equatorial sites. The origin of the near-zero paramagnetic shift for the β-pyrrole protons is unclear. The nuclei are close to the 90° angle relative to the Co center and the main axis of the magnetic tensor (which, according to the symmetry of the molecule, should coincide with the $S_4$ axis). Therefore, a downfield shift is expected for the β-pyrrole protons given that the axial *meso* methyls, found inside the double cone defined by the magic angle relative to $S_4$, are shifted upfield — and this is indeed observed experimentally for $[LFe^{II}]^{2-}$ and $[LFe^{III}]^{-}$. Most likely, "through-bond coupling" (that is, the effect of spin density delocalized on the organic periphery of Co) is non-zero and of sign opposite that of the "through-space" (dipole-dipole) coupling between the nuclear spin of β-H and the electronic spin of $Co^{II}$. However, the effect of the nearby paramagnetic ion is clearly visible in the breadth of the β-H peak, therefore the assignment is unambiguous.

In the $^1H$ NMR spectrum of $[^{Ph}LCo^{II}]^{2-}$ (Figure VIII.3), the THF peaks can be identified immediately by the lack of paramagnetic shift and by the presence of isotopically shifted signals corresponding to $d_7$- and $d_0$-THF. The signals at +8.2 and −33.3 ppm are assigned unambiguously to the *meso*-methylenes by comparison with the $^2H$ NMR signals of $[LCo^{II}]^{2-}$. Similarly, the β-pyrrole protons must give rise to the −0.76 ppm peak given its correspondence to the single paramagnetic $^1H$ NMR peak of $[LCo^{II}]^{2-}$. The remaining peaks arise from the three inequivalent positions on the phenyl groups. The *para* protons can be clearly identified by their integration (7.67 and 5.05 ppm). There remains a slight ambiguity as to the assignment of the *ortho* and *meta* hydrogens, which are represented in the same number in the molecule. However, the *meta* H's are expected to be less paramagnetically shifted and broadened than their *ortho* neighbors, given that they are farther from the metal ion, thus the 7.76 and 4.98 ppm peaks can be considered with reasonable certainty as being due to the *meta* H's, and the +10.2 and −3.2 ppm peaks to their *ortho* counterparts.

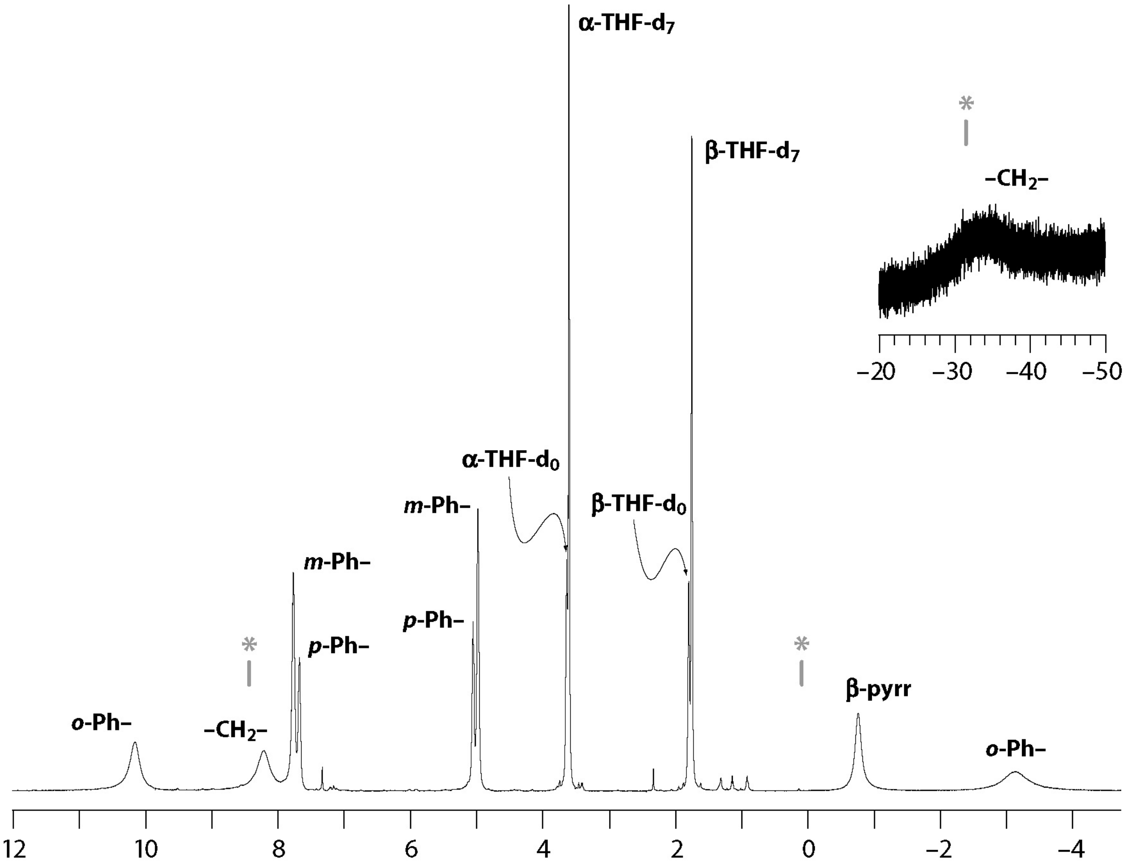

**Figure VIII.3.** $^1$H NMR spectrum (500 MHz, THF-$d_8$) of disodium cobalt(II) octabenzylporphyrinogen, $Na_2(THF)[^{Ph}LCo^{II}]$. The inset showing the high-field peak is on a different scale. Peak assignments (bold) are in part based on the positions of the $^1$H- and $^2$H-NMR signals of $Na_2(THF)_x[LCo^{II}]$ at +0.2 ppm (β-pyrrole) and at +8.4 and −31.2 ppm ($-CD_3$), respectively: those positions are indicated by a gray mark with an asterisk.

As observed for the equivalent Fe compounds, oxidation of $[LCo^{II}]^{2-}$ to $[LCo^{III}]^{-}$ results in an increase in all paramagnetic shifts, with the methyls moving from +8.4 and −31.2 ppm to +14.5 and −50.3 ppm in $^2$H NMR, and the β-pyrrole position from +0.2 to −85.6 ppm.

# VIII.3. Protonation and photoreaction

## VIII.3.a. Protonation

Reaction of $Na_2[LCo^{II}]$ with two equivalents of pyHCl (pyridinium chloride) in acetonitrile results in the immediate formation of a green solution, which becomes a brown powder upon removal of the solvent.[b] The isolated brown material displays a complete loss of symmetry in $^1H$ and $^2H$ NMR, with ten proton peaks of equal intensity for the pyrrolic protons (see the bottom spectrum of Figure VIII.4) and eight deuterium peaks for the methyls, which is consistent with double protonation of the macrocycle at the $\alpha$ or $\beta$ positions (as observed in the case of zirconium[c] and nickel[12] porphyrinogens, respectively), to yield $H_2LCo^{II}$. The paramagnetically shifted peaks in both spectroscopies (range of chemical shifts ~80 ppm) indicate that the metal ion has been retained. The $^2H$ NMR signals are clustered in two groups of four peaks each, respectively shifted upfield and downfield relative to the diamagnetic range, corresponding to the pseudo-axial and pseudo-equatorial positions, and they prove that the structural integrity of the tetrapyrrole is retained upon protonation. Finally, the protonation reaction is also apparent in vibrational spectroscopy. The IR spectrum of $H_2LCo^{II}$ displays bands at 3438 and at 1624, 1607 and 1582 $cm^{-1}$ which $Na_2[LCo^{II}]$ does not have. They are attributed to the stretching motions of the acidic protons and of the localized C=N and C=C bonds in the protonated pyrroles, respectively.

$Na_2[^{Ph}LCo^{II}]$ reacts in a manner that parallels $Na_2[LCo^{II}]$. A solution of $Na_2[^{Ph}LCo^{II}]$ turns green upon exposure to 2 equivalents of pyHCl, and the isolated beige powder displays $^1H$ NMR peaks consistent with its formulation as $H_2{}^{Ph}LCo^{II}$: in particular, the four high-field pyrrole peaks are clearly resolved at −41.5, −43.0, −44.3 and −45.2 ppm.

---

[b] The brown powder obtained after isolation yields a brown, not green, solution in MeCN; the IR and NMR spectral characteristics of the green reaction mixture and the brown solution of the isolated material are similar. Therefore, the origin of the green color is unclear; it can possibly originate from a small amount of $CoCl_2$, removed upon isolation.

[c] See Chapter IV.

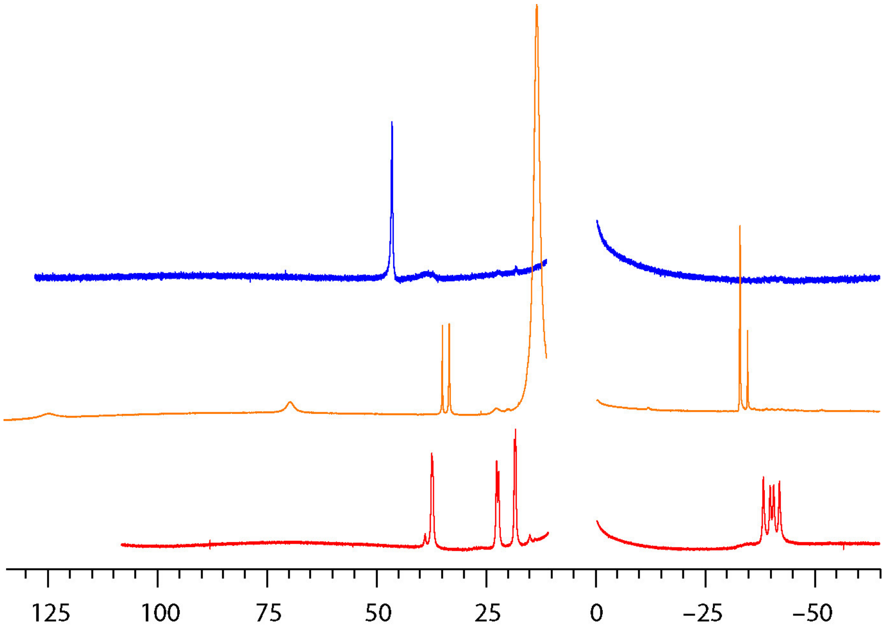

**Figure VIII.4.** $^1$H NMR spectra of (from bottom to top) $H_2LCo^{II}$ in $CD_2Cl_2$ (red), $H_2LCo^{II}$ in pyridine / $CD_3CN$ (orange), and its photoproduct in $CD_2Cl_2$ (blue). The photoproduct also has a weak peak at ~+166 ppm (not shown). $L^{4-}$ = *meso*-octakis(perdeuteromethyl)porphyrinogen.

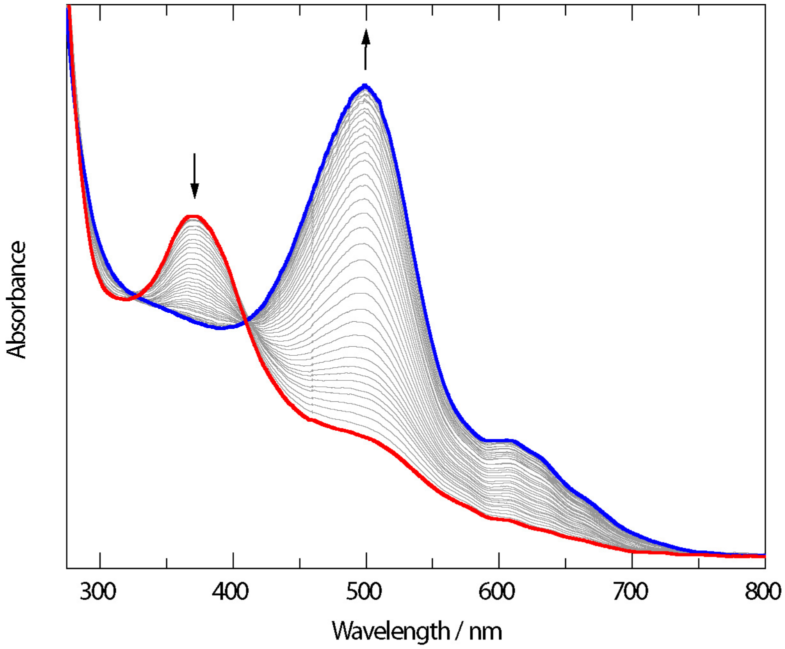

**Figure VIII.5.** Time evolution (UV-vis absorption spectra) of the photoreaction ($\lambda > 309$ nm) of $H_2LCo^{II}$ in $CH_2Cl_2$. The first spectrum (mostly $H_2LCo^{II}$) is in red, the last one (mostly photoproduct) in blue. The arrows indicate the growth or decay of particular peaks. $L^{4-}$ = *meso*-octakis(perdeuteromethyl)porphyrinogen.

Unlike $[LCo^{II}]^{2-}$, $H_2LCo^{II}$ is sensitive to axial coordination by neutral Lewis bases. It decomposes when dissolved alone in MeCN, but is stable in that solvent in the presence of excess pyridine; in the latter conditions, $^1H$ NMR shows evidence forassociation of py both from the paramagnetically shifted py peaks and from the dramatic shifts experienced by the $H_2L^{2-}$ protons[d] relative to the dichloromethane solution (center spectrum of Figure VIII.4).

## VIII.3.b. Photoreaction

The UV-vis absorption spectrum of $H_2LCo^{II}$ shows a peak in the near-UV (371 nm) on top of a strong far-UV band that monotonically tails into the visible region. Irradiation of a $CH_2Cl_2$ solution of $H_2LCo^{II}$ at $\lambda > 309$ nm results in its conversion to a new photoproduct of darker brown color. When the photoreaction is monitored by UV-vis spectroscopy in a quartz cell, the growth of a new band is observed at 499 nm concomitantly with the decay of the 309-nm band of $H_2LCo^{II}$ (Figure VIII.5). Isosbestic points are maintained at 325 and 410 nm, showing that the reaction is quantitative and that no intermediate accumulates in measurable amount during its course. When performed in $CD_2Cl_2$ in an NMR tube, the same photoreaction can also be monitored by $^1H$ NMR spectroscopy: the disappearance of the 10 signals of $H_2LCo^{II}$ is accompanied by the growth of two new paramagnetic peaks in the low-field region of the spectrum (top spectrum of Figure VIII.4), an intense one (set to 8H) found at +46.5 ppm at the end of the reaction[e] and a weaker one (~1 or 2H) at ~+166 ppm,[f,14,15] along with some decomposed diamagnetic material (attributed to $LH_4$). Free, dissolved $H_2$ is not detected in $CD_2Cl_2$ at 4.6 ppm[16] by $^1H$ NMR, nor as a gas in volumetric measurement by Toepler pumping.

---

[d] Between +125 and −35 ppm for eight observable H's.

[e] At the beginning of the reaction, this peak is observed at slightly higher field, and it consistently moves to lower field as the reaction approaches completion.

[f] Because it is so broad and weak, this peak can easily be overlooked; moreover, if the experimental spectral range is too narrow, it can appear as a spurious "foldover" at high field.[14,15]

According to monitoring by $^1$H NMR spectroscopy, the same product is obtained when the photoreaction is carried out in similar conditions in $CDCl_3$ or *ortho*-dichlorobenzene, although in both cases precipitation of some other material occurs, along with the observation of other colors (red in $CDCl_3$, green in *o*-$C_6H_4Cl_2$).[g] The photoreaction does not occur in $CH_3CN$, because $H_2LCo^{II}$ is not stable to it, however, after completion of the reaction, dissolution of the photoproduct in $CD_3CN$ only causes a shift of the $^1$H NMR signal from 46.5 to 39.0 ppm. Moreover, $H_2LCo^{II}$ dissolved in $CD_3CN$ in the presence of an excess of pyridine (which protects it against decomposition) does not give rise to an observable photoreaction. Finally, $H_2{}^{Ph}LCo^{II}$ photoreacts in $CD_2Cl_2$ in a manner that parallels $H_2LCo^{II}$, with a characteristic β-pyrrole peak at 40.3 ppm and a weaker peak (~1 or 2H) at ~+145 ppm.

In infrared, a set of three new bands of similar intensity appear during the photoreaction at 1951, 1880 and 1811 $cm^{-1}$, in an otherwise blank spectral region (Figure VIII.6). Given that all known cobalt hydrides and polyhydrides are characterized

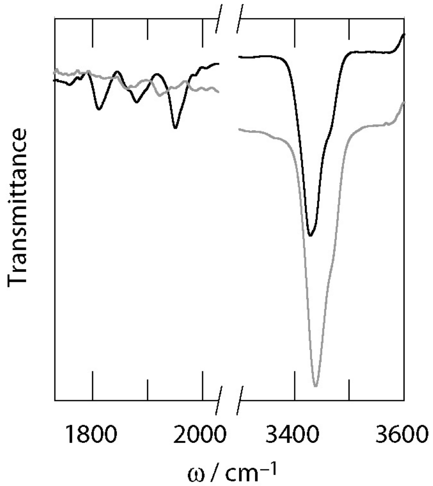

**Figure VIII.6.** Two regions of the infrared spectra of dichloromethane solutions of (gray) unirradiated $H_2LCo^{II}$ and of (black) $H_2{}^{Ph}LCo^{II}$ after partial photoreaction. The low-energy region is that in which the Co—H stretches appear for known cobalt hydrides,[17-20] and the high-energy region corresponds to acidic organic protons. The spectrum of the pure solvent has been subtracted.

---

[g] The red color can be tentatively attributed to a small amount of $[LCo^{III}]^-$, and the green color to a small amount of $CoCl_2$.

by a vibrational absorption between 1870 and 1980 $cm^{-1}$ (sometimes accompanied by others at lower energies)[17-20] the three bands observed for the photoproduct can be assigned to Co—H stretches with reasonable confidence.

Thus, the presence of a weak, strongly paramagnetically shifted $^1H$ NMR signal (indicative of a very short distance to the metal center) is consistent with the ~1900-$cm^{-1}$ vibrational bands. Both are adequately rationalized by the presence of a direct metal-hydride bond in the photoproduct. At this point, the exact structural identity of the compound is not uniquely defined — monohydrides and polyhydrides, terminal and bridging, alone and in an equilibrium mixture, are all conceivable. Unfortunately, the compound has resisted all attempts to grow X-ray quality crystals to date.

## VIII.4. Conclusions

The first forays into the possibility of exploiting ligand-based redox activity for the design of reactivity related to that of hydrogenases have proven encouraging. Cobalt(II) porphyrinogen is a relatively mild reducing agent, with redox potential of approximately –0.30 V *vs* NHE. It supports the same oxidation states as the iron system, namely $[LCo^{II}]^{2-}$, $[LCo^{III}]^{-}$, and $[L^{\Delta\Delta}Co^{II}]^{2+}$, with slight differences in the redox potentials as expected on the basis of the aqueous M(II/III) couples. A first crucial property of the system is its ability to take up two protons while maintaining its structural integrity — a manifestation of the multifunctional nature of porphyrinogen already mentioned. More precisely, the large negative charge of the reduced ligand, $L^{4-}$, allows it to maintain a sufficient Lewis basic nature towards the metal after losing two charge units upon double protonation, and the spread of the charge over an aromatic cycle (as opposed to its concentration at the coordinating N atom) creates protonation sites that are more than one bond away from the metal. The second important finding is the presence of an electronic transition in the reduced, protonated state of cobalt porphyrinogen, that is coupled to *productive* bond rearrangements. This results in a clean photoconversion, evidenced by isosbestic behavior in electronic absorption spectroscopy. Finally, from a methodology viewpoint, it is clear that in a field where paramagnetic complexes are the rule, the assignment of NMR spectra can be based on structural simplicity, and if possible symmetry, as well as deuteration.

The most desirable reaction conceivable in the cobalt porphyrinogen system, that is, the direct photochemical conversion of $[H_2LCo^{II}]$ to $[L^{\Delta}Co^{II}]$ with elimination of $H_2$ (reduction of *two* protons by *two* electrons) is not observed. However, incorporation of a Co(II) center into the redox-active ligand porphyrinogen seems to alter the reactivity of the Co(I) charge transfer excited state fundamentally. Instead of generating $H^{\bullet}$ (reduction of *one* proton by *one* electron) as observed traditionally,[6-9] cobalt porphyrinogen photochemically produces $H^{-}$ — the *two*-electron reduction product of *one* proton. Further development of the concept to include the second $H^{+}$ will be contingent on *(1)* full structural characterization of the cobalt-hydride photoproduct, with consequent elucidation of the reaction stoichiometry, and *(2)* control of the regiochemistry of the protonation. In the system studied, the two protons are likely to reside on pyrroles situated *trans* to each other, whereas the ideal case for $H_2$ elimination would be the protonation of adjacent pyrroles. This could presumably be achieved by unsymmetrical substitution of the macrocycle.

In the inorganic literature, the chemical properties of the element cobalt coordinated by oxidized ligands, in particular porphyrins, have not been investigated as extensively as those of iron in similar environments. In biological systems, cobalt is found coordinated to the tetrapyrrole macrocycle corrin in the cofactor cobalamin: the corrin lacks the extensive delocalization of porphyrin, as well as one of its *meso* methylenes. The reactions performed by cobalamin-dependent enzymes are radical rearrangements initiated by homolysis of the weak $Co^{III}$—C bond to a methyl or deoxyadenosyl group.[21-23] This is in fact very reminiscent of the photoreactivity of chloroiron(III) porphyrins mentioned in the previous Chapter (VII.3). One of the approaches towards multielectron reactivity mentioned in Chapter I of this thesis (I.1.c), however, has been explored with quite some success, in particular for the activation of $O_2$ and its use for oxygenation reactions, namely the use of dinuclear coordination compounds. Although the structural variety of known dinuclear complexes of Co is extensive, the reaction of the Co(II,II) state with $O_2$ is quite general.[24-54] A bridging peroxide is usually the product formed initially, and depending on the availability of external reducing agents, the reaction can proceed to a bis-μ-oxo, water, or an oxygenated substrate. In contrast to this, exposure of dissolved cobalt(II) porphyrinogen, $[LCo^{II}]^{2-}$, to air produces a solution the UV-vis spectrum of which is identical to that of $[LCo^{III}]^-$. An interesting analogy between metal porphyrinogen and a dinuclear cobalt system is found with Bosnich's examples of "one-site addition two-metal oxidation" reactions.[37-39] In these cases, the endproduct of the reaction of the Co(II,II) compound with an oxidant features two new ligands coordinated at a single Co center, the second metal ion functioning exclusively as an ancillary redox reservoir — just as the porphyrinogen ligand in the present thesis.

## VIII.5. Experimental section

### VIII.5.a. Synthesis

*General technique*

All compounds were handled, reactions were performed, and analytical samples were prepared in inert atmosphere using standard Schlenk, dry-box and vacuum-line techniques. Solvents were purchased from VWR Scientific Products or Sigma Aldrich and purified using a Braun solvent purification system or using standard solvent purification techniques.[55] Deuterated solvents were purchased from Cambridge Isotope Laboratories, degassed, dried and distilled by procedures similar to those used for non-isotopically enriched solvents. Other reagents were purchased from Aldrich, Acros or Strem Chemicals and used as received. $LH_4$ was prepared as its *meso*-$d_{24}$ version from acetone-$d_6$ and pyrrole. Photochemical experiments were carried out using the light from a 1000-W high-pressure Hg—Xe lamp by Oriel, which was passed through a water bath to remove its infrared component and a cutoff filter to remove short wavelengths as desired, then collimated through a lens.

*Synthesis of $Na_2(THF)_2\,[LCo^{II}]$*

The reactants $LNa_4(THF)_4$ (6.00 g, 7.24 mmol) and anhydrous $CoCl_2$ powder (0.94 g, 7.24 mmol) were suspended in 200 mL of THF and stirred at r.t. overnight. The white NaCl precipitate was filtered off and the filtrate was evaporated and dried *in vacuo*. The solid residue was triturated in hexanes for two hr, then filtered and dried to yield 4.38 g (87%) of beige powder. $^1H$ NMR (500 MHz, $CD_3CN$): δ/ppm = 3.67 (m, 8H, THF-β), 1.84 (m, 8H, THF-α), 0.19 (br, 8H, β-pyrr.). $^2$H NMR (77 MHz, $CH_3CN$): δ/ppm = 8.4 (s, 12H, $-CD_3$), −31.2 (s, 12H, $-CD_3$).

*Synthesis of Na(MeCN)$_x$ [LCo$^{II}$]*

A sample of $Na_2(THF)_2$ [LCo$^{II}$] (1.00 g, 1.43 mmol) was dissolved in 20 mL of THF and $FcBF_4$ (0.40 g, 1.43 mmol) was added. After 10 min., 150 mL of $CH_2Cl_2$ were added and the precipitate was removed by filtration; the filtrate was evaporated and dried *in vacuo*. The solid residue was triturated in hexanes for 2 hr, then filtered and dried to yield 0.70 g of dark powder. $^1$H NMR (500 MHz, $CD_3CN$): δ/ppm = −85.7 (s, β-pyrr.).

*Preparation of anhydrous pyHCl*

A sample of pyridine (20 mL, 250 mmol) was dissolved in 100 mL of toluene, then $CaH_2$ was added; the mixture was degassed, then stirred under $N_2$ for 15 min. After filtration, the flask containing the clear filtrate solution was evacuated; gaseous HCl was then slowly allowed to enter the flask and react with the stirred solution. Precipitation of white pyHCl was accompanied by a strong exothermy. Once the mixture returned to r.t. under 1 atm HCl gas, the system was again degassed and the atmosphere reverted to $N_2$; the product was filtered and dried *in vacuo*. The solid residue was triturated in pentane for 2 hr, then filtered and dried to yield 12 g (43%) of white powder. $^1$H NMR (500 MHz, $CD_3CN$): δ/ppm = 18.10 (br, 1H, NH), 8.73 (d, 6 Hz, 2H, *o*-H), 8.52 (tt, 8 Hz and 2 Hz, 1H, *p*-H), 8.00 (t, 7 Hz, 2H, *m*-H).

*Synthesis of H$_2$LCo$^{II}$*

A beige solution of $Na_2(THF)_2$ [LCo$^{II}$] (1.00 g, 1.43 mmol) was prepared in 50 mL of MeCN, then pyHCl (0.33 g, 2.9 mmol, 2 equiv.) was added and the solution immediately turned green. After 5 min. it was evaporated and dried; the beige solid residue was triturated in $CH_2Cl_2$ and NaCl was filtered off. The filtrate was again evaporated, then the solid was triturated in hexanes for 2 hr, filtered and dried *in vacuo* to yield 0.62 g (85%) of brown powder. $^1$H NMR (500 MHz, $CD_2Cl_2$): δ/ppm = 37.2, 37.0, 22.4, 22.0, 18.3, 18.1, −38.5, −40.0, −40.8, −42.2. $^2$H NMR (77 MHz, $CH_2Cl_2$): δ/ppm = 10.2, 9.9, 9.4, 9.2, −37.5, −38.0, −38.3, −39.1 (the integration of $\delta > 0$ peaks and of the $\delta < 0$ peaks are equal). UV-VIS ($CH_2Cl_2$): $\lambda_{max}$ = 368 nm.

*Photoreaction of $H_2LCo^{II}$*

A dilute yellow solution of $H_2LCo^{II}$ was prepared in $CH_2Cl_2$ in a UV-vis cell; the absorption spectrum featured an absorption maximum at 371 nm. It was then irradiated at $\lambda > 309$ nm until the absorption spectrum remained constant, with a maximum at 499 nm. Isosbestic points were maintained throughout the course of the irradiation at 325 and 410 nm. The solvent was removed, $CD_2Cl_2$ was added, and the mixture was filtered into an NMR tube. $^1H$ NMR (500 MHz): $\delta$/ppm = +46.5 (8H, $\beta$-pyrr.), +166 (~2H, Co—H).

*Controls. (1)* The reaction was run on a more concentrated sample in $CD_2Cl_2$ in an NMR tube, and the NMR spectral changes monitored periodically. The peaks of the starting material disappeared concomitantly with the appearance of the product signal; no intermediate built up in the course of the reaction. *(2)* The reaction was run in $CDCl_3$, in *ortho*-dichlorobenzene-$d_4$ and in $CD_3CN$: in the first two cases, it yielded the same NMR signal, and in the third no reaction was observed.

## VIII.5.b. Physical techniques

*Nuclear magnetic resonance spectroscopy*

$^1H$ NMR spectra were recorded at the MIT Department of Chemistry Instrumentation Facility (DCIF) on a Varian Inova-500, a Bruker Avance-600 or a Bruker Avance-400 spectrometer, and $^2H$ NMR spectra were recorded on a Varian Inova-500 equipped with a direct probe. Chemical shifts are quoted in ppm relative to tetramethylsilane and spectra have been internally calibrated to the monoprotio impurity of the deuterated solvent, or the monodeutero impurity of the natural-abundance solvent (the chemical shift was set to be equal to that observed in $^1H$-NMR for the monoprotio impurity of the corresponding deuterated solvent). Spectra were recorded at 20 °C and a 30-s delay was used between successive pulses in order to allow for quantitative integration of the solvent peaks in $^1H$-NMR.

*Crystal structure of* $Na_2(DME)_6\,[^{Ph}LCo^{II}]$

Yellow trigonal prismatic single crystals of $Na_2(DME)_6\,[^{Ph}LCo^{II}]$ were grown by layering a concentrated DME solution of $Na_2(THF)\,[^{Ph}LCo^{II}]$ with cyclohexane. A crystal was coated with paratone N oil and mounted on a glass fiber. X-ray diffraction data were collected on a Siemens diffractometer euipped with a CCD detector, using the Mo Kα radiation, selected by a graphite monochromator. The data were integrated to *hkℓ*-intensity and the final unit cell calculated using the SAINT v.4.050 program from Siemens. Solution and refinement were performed with the SHELXTL v.5.03 suite of programs developed by G. M. Sheldrick and Siemens Industrial Automation, 1995 — the SHELXTL softwares XM and XH had to be used for solution and for refinement instead of XS and XL, respectively, which are used more routinely for small-molecule structures. An empirical absorption correction was performed as implemented by the program SADABS in the SHELX package. The asymmetric unit in *C*2/*c* was found to contain one and a half $Na_2(DME)_6\,[^{Ph}LCo^{II}]$ moieties, one Co center and two of the N atoms coordinated to it lying at special positions. Least-squares refinements were applied to $F^2$, with hydrogen atoms placed at calculated positions using a standard riding model and refined isotropically.

## VIII.6. References

1 Volbeda, A.; Charon, M.-H.; Piras, C.; Hatchikian, E. C.; Frey, M.; Fontecilla-Camps, J. C. *Nature* **1995**, *373*, 580-587.

2 Peters, J. W.; Lanzilotta, W. N.; Lemon, B. J.; Seefeldt, L. C. *Science* **1998**, *282*, 1853-1858.

3 Tard, C.; Liu, X.; Ibrahim, S. K.; Bruschi, M.; De Gioia, L.; Davies, S. C.; Yang, X.; Wang, L.-S.; Sawers, G.; Pickett, C. J. *Nature* **2005**, *433*, 610-613.

4 Liu, X.; Ibrahim, S. K.; Tard, C.; Pickett, C. J. *Coord. Chem. Rev.* **2005**, *249*, 1641-1652.

5 Rauchfuss, T. B. *Inorg. Chem.* **2004**, *43*, 14-26.

6 Krishnan, C. V.; Sutin, N. *J. Am. Chem. Soc.* **1981**, *103*, 2141-2142.

7 Creutz, C.; Sutin, N. *Coord. Chem. Rev.* **1985**, *64*, 321-341.

8 Dhanasekaran, T.; Grodkowski, J.; Neta, P.; Hambright, P.; Fujita, E. *J. Phys. Chem. A* **1999**, *103*, 7742-7748.

9 Eaton, D. R.; Suart, S. R. J. Phys. Chem. **1968**, *72*, 400-405.

10 Jubb, J.; Floriani, C.; Chiesi-Villa, A.; Rizzoli, C. *J. Am. Chem. Soc.* **1992**, *114*, 6571-6573.

11 De Angelis, S.; Solari, E.; Floriani, C.; Chiesi-Villa, A.; Rizzoli, C. *J. Am. Chem. Soc.* **1994**,*116*, 5702-5713.

12 Bonomo, L.; Solari, E.; Floriani, C.; Chiesi-Villa, A.; Rizzoli, C. *J. Am. Chem. Soc.* **1998**, *120*, 12972-12973.

13 Jubb, J.; Jacoby, D.; Floriani, C.; Chiesi-Villa, A.; Rizzoli, C. *Inorg. Chem.* **1992**, *31*, 1306-1308.

14 Eggenberger, U.; Pfandler, P.; Bodenhausen, G. *J. Magn. Res.* **1988**, *77*, 192-196.

15 Jeannerat, D. *Magn. Reson. Chem.* **2003**, *41*, 3-17.

16 Sellmann, D.; Lauderbach, F.; Geipel, F.; Heinemann, F. W.; Moll, M. *Angew. Chem. Int. Ed.* **2004**, *43*, 3141–3143.

17 Kaesz, H. D.; Saillant, R. B. *Chem. Rev.* **1972**, *72*, 231-281.

18 Whitfield, J. M.; Watkins, S. F.; Tupper, G. B.; Baddley, W. H. *J. Chem. Soc. Dalton* **1977**, 407-413.

19 Ciancanelli, R.; Noll, B. C.; DuBois, D. L.; Rakowski DuBois, M. *J. Am. Chem. Soc.* **2002**, *124*, 2984-2992.

20 Fryzuk, M. D.; Ng, J. B.; Rettig, S. J.; Huffman, J. C.; Jonas, K. *Inorg. Chem.* **1991**, *30*, 2437-2441.

21 Babior, B. M. *Acc. Chem. Res.* **1975**, *8*, 376-384.

22 Banerjee, R. *Biochem.* **2001**, *40*, 6191-6198.

23 Matthews, R. G. *Acc. Chem. Res.* **2001**, *34*, 681-689.

24 Larsen, P. L.; Parolin, T. J.; Powell, D. R.; Hendrich, M. P.; Borovik, A. S. *Angew. Chem. Int. Ed.* **2003**, *42*, 85-89.

25 Steinfeld, G.; Lozan, V.; Kersting, B. *Angew. Chem. Int. Ed.* **2003**, *42*, 2261-2263.

26 Ghiladi, M.; Gomez, J. T.; Hazell, A.; Kofod, P.; Lumtscher, J.; McKenzie, C. J. *Dalton Trans.* **2003**, 1320-1325.

27 Kadish, K. M.; Ou, Z.; Shao, J.; Gros, C. P.; Barbe, J.-M.; Jerome, F.; Bolze, F.; Burdet, F.; Guilard, R. *Inorg. Chem.* **2002**, *41*, 3990-4005.

28 Chang, C. J.; Deng, Y.; Nocera, D. G.; Shi, C.; Anson, F. C.; Chang, C. K. *Chem. Commun.* **2000**, 1355-1356.

29 Sasaki, Y.; Kobayashi, T.; Masuda, H.; Einaga, H.; Ohba, S.; Nishida, Y. I*norg. Chem. Commun.* **1999**, *2*, 244-246.

30 Hikichi, S.; Komatsuzaki, H.; Kitajima, N.; Akita, M.; Mukai, M.; Kitagawa, T.; Moro-oka, Y. *Inorg. Chem.* **1997**, *36*, 266-267.

31 Heinze, K.; Huttner, G.; Zsolnai, L.; Jacobi, A.; Schober, P. *Chem. Eur. J.* **1997**, *3*, 732-743.

32 Reinaud, O. M.; Yap, G. P. A.; Rheingold, A. L.; Theopold, K. H. *Angew. Chem. Int. Ed. Engl.* **1995**, *34*, 2051-2052.

33 Mandal, S. K.; Clase, H. J.; Bridson, J. N.; Ray, S. *Inorg. Chim. Acta* **1993**, *209*, 1-4.

34 Collman, J. P.; Hutchison, J. E.; Lopez, M. A.; Tabard, A.; Guilard, R.; Seok, W. K.; Ibers, J. A.; L'Her, M. *J. Am. Chem. Soc.* **1992**, *114*, 9869-9877.

35 Fryzuk, M. D.; Ng, J. B.; Rettig, S. J.;, J. C.; Jonas, K. *Inorg. Chem.* **1991**, *30*, 2437-2441.

36 Bouwman, E.; Driessen, W. L. *J. Am. Chem. Soc.* **1988**, *110*, 4440-4441.

37 Gavrilova, A. L.; Bosnich, B. *Inorg. Chim. Acta* **2003**, *352*, 24-30.

38 Gavrilova, A. L.; Qin, C. Jin; Sommer, R. D.; Rheingold, A. L.; Bosnich, B. *J. Am. Chem. Soc.* **2002**, *124*, 1714-1722.

39 Incarvito, C.; Rheingold, A. L.; Gavrilova, A. L.; Qin, C. J.; Bosnich, B. *Inorg. Chem.* **2001**, *40*, 4101-4108.

40 Harris, W. R.; McLendon, G. L.; Martell, A. E.; Bess, R. C.; Mason, M. *Inorg. Chem.* **1980**, *19*, 21-26.

41 Basak, A. K.; Martell, A. E. *Inorg. Chem.* **1986**, *25*, 1182-1190.

42 Raleigh, C. J.; Martell, A. E. *Inorg. Chem.* **1986**, *25*, 1190-1195.

43 Chen, D.; Martell, A. E. *Inorg. Chem.* **1987**, *26*, 1026-1030.

44 Basak, A., K.; Martell, A. E. *Inorg. Chem.* **1988**, *27*, 1948-1955.

45 Motekaitis, R. J.; Martell, A. E. *J. Chem. Soc. Chem. Commun.* **1988**, 1020-1022.

46 Martell, A. E.; Motekaitis, R. J. *J. Chem. Soc. Chem. Commun.* **1988**, 915-916.

47 Motekaitis, R. J.; Martell, A. E. *J. Am. Chem. Soc.* **1988**, *110*, 7715-7719.

48 Chen, D.; Motekaitis, R. J.; Martell, A. E. *Inorg. Chem.* **1991**, *30*, 1396-1402.

49 Motekaitis, R. J.; Martell, A. E. *Inorg. Chem.* **1991**, *30*, 694-700.

50 Rockcliffe, D. A.; Martell, A.r E. *Inorg. Chem.* **1993**, *32*, 3143-3152.

51 Rosso, N. D.; Szpoganicz, B.; Martell, A. E. *Inorg. Chim. Acta* **1999**, *287*, 193-198.

52 Kong, D.; Mao, J.; Martell, A. E.; Clearfield, A. *Inorg. Chim. Acta* **2002**, *335*, 7-14.

53 Wang, J.; Martell, A. E.; Reibenspies, J. H. *Inorg. Chim. Acta* **2002**, *328*, 53-60.

54 Kong, D.; Ouyang, X.; Martell, A. E.; Clearfield, A. *Inorg. Chem. Commun.* **2003**, *6*, 317-321.

55 Armarego, W. L. F.; Perrin, D. D. in Purification of Laboratory Chemicals; Butterworth-Heinmann: Oxford, 4th ed. 1996.

# Chapter IX

# Conclusions and outlook

Several years of work with metal porphyrinogens have yielded experimental results detailed in the previous seven chapters of this dissertation. They have also given rise to some thoughts concerning the significance of the results and their rationalization, in part based on heuristics and intuition. Thus, this last chapter attempts to put the material of this thesis in perspective and uncover some underlying principles. Naturally, it contains less scientific facts and more personal opinions. With this limitation, it is meant to be helpful to somebody about to get started on a project involving the redox chemistry of porphyrinogens.

# IX.1. Electron transfer series of metal-porphyrinogens

## IX.1.a. Preparation with "simple" counter-ions

Prior to the work reported in this dissertation, the published examples of transition metal complexes of ligand-oxidized porphyrinogens were limited to $[{}^{*}L^{\Delta}V{\equiv}NAr]$, $[{}^{*}L^{\Delta}Mn^{II}]$, $[{}^{*}L^{\Delta\Delta}Mn^{II}{-}Cl]\,(Cu_9Cl_{11})_{1/2}$, $[{}^{*}LFe^{II}{-}Cl]\,(Cu_4Cl_5)$, $[{}^{cy}L^{\Delta\Delta}Fe^{II}{-}Cl]\,(Cu_2Cl_4)_{1/2}$, $[{}^{cy}L^{\Delta\Delta}Fe^{II}{-}I]\,(I_3)\bullet I_2$, $[{}^{*}L^{\Delta\Delta}Fe^{III}{-}Cl]\,(FeCl_4)$, $[{}^{*}L^{\Delta}Co^{II}]$, $[{}^{*}L^{\Delta\Delta}Co^{II}{-}Cl]\,(Cu_4Cl_5)$, $[{}^{*}L^{\Delta}Ni]$, and $[{}^{*}L^{\Delta}Cu^{II}]$ (where ${}^{*}L^{4-}$, ${}^{*}L^{\Delta 2-}$ and ${}^{*}L^{\Delta\Delta}$ represent the three available oxidation states of the *meso*-octaethylporphyrinogen macrocycle, and ${}^{cy}L^{4-}$, ${}^{cy}L^{\Delta 2-}$ and ${}^{cy}L^{\Delta\Delta}$ represent the related *meso*-tetrakis(penta-1,5-diyl)porphyrinogens).[1-7] For the present work, the goal of characterizing electron transfer series of this type of high-valent metal-porphyrinogens by spectroscopic and electrochemical methods dictated that, in contrast to the above examples, the compounds be prepared in their simplest form, that is, *(a)* with counter-ions that are strictly redox-inactive, spectroscopically silent, and not Lewis basic, and *(b)* with *meso* substituents that are inert to redox decomposition.[8-10] It was shown that the first condition can be met for the counter-anions by $BF_4^-$. The anions tetraphenylborate and hexafluorophosphate, in particular, were found to cause rapid decomposition of $[L^{\Delta\Delta}Fe^{II}]^{2+}$ and $[L^{\Delta\Delta}Zn]^{2+}$. Cobalticarborane, $Co(C_2B_9H_{11})_2^-$, also can yield stable ion pairs with cationic metalloporphyrinogens, which was put to use for crystallographic purposes. Condition *(b)* was fulfilled with the use of the smallest possible *meso* substituent, methyl. This choice, however, presents a drawback, namely a limited solubility in organic solvents of low to medium polarity.

The traditional metallation route *via* reaction of an alkali ($M'^{+}$) salt of the porphyrinogen tetraanion ($L^{4-}$) with a halide ($X^{-}$) of the metal ion (typically, $M^{II}$) to be inserted is plagued by several limitations. Firstly, it is a two-step procedure, and the the deprotonation is cumbersome in the case of sodium (a week-long reflux). Secondly, it causes separation difficulties: the desired product ($M'_2\,[LM^{II}]$) is a salt, and so are the starting materials ($M'_4L$ and $MX_2$) and the byproduct ($M'X$), with the consequence that the four compounds have quite similar solubilities. And thirdly, it may result in the formation of solvated polynuclear μ-halo cations of the type $[(solv)_nM^{II}_xX_y]^{(2x-y)+}$, a problem which becomes more acute when $M'_4L$ is less soluble than $M^{II}X_2$. It was found that homoleptic (or solvated) alkyl, amido, or arene complexes of $M^{II}$, when available, are convenient reagents for the direct installation of the metal ion into the free ligand $LH_4$, albeit with less generality. The byproduct, alkane, amine, or arene + $H_2$, is most easily separated from the desired product. Dialkylzinc, dialkylmagnesium, zirconium tetrakis(dialkylamide), and arene-calcium fall in that category.

## IX.1.b. Electrochemistry

The quadruple negative charge of the reduced porphyrinogen ligand makes it a strong σ base, and the d orbitals of the central metal ion are thereby very significantly destabilized compared to their energies in aquo, porphyrin, and bipyridine complexes, for example. The M(II/III) electrochemical couples are correspondingly shifted cathodically. On the other extreme, the oxidized, neutral $L^{\Delta\Delta}$ ligand is such a poor donor that within it the Fe(II/III) couple is not observed, and attempts to oxidize $[L^{\Delta\Delta}Fe^{II}]^{2+}$ to $[L^{\Delta\Delta}Fe^{III}]^{3+}$ failed even with very strong oxidants. Both consecutive two-electron oxidation steps of the ligand when coordinating a metal(II) ion are consistently found to be at relatively mild potentials of roughly +0.2 and +0.6 V. Even though the CV waves involving oxidized versions of the ligand are rarely observed to be reversible in the electrochemical sense ($[L^{\Delta\Delta}Zn]^{2+}$ / $[L^{\Delta}Zn]$ is fully reversible, however), both cathodic and anodic signals are observed for each of the redox couples involved, which corresponds, at the macroscopic level, to the reversibility of the same transformations carried out on the preparative scale. The most dramatic electrochemical feature of metal porphyrinogen complexes is the appearance of a three-electron redox couple between $[LM^{III}]^-$ and $[L^{\Delta\Delta}M^{II}]^{2+}$ if the M(III) oxidation state is sufficiently stable to drive the disproportionation of $[L^{\Delta}M^{II}]$ to $[L^{\Delta\Delta}M^{II}]^{2+}$ and $[LM^{III}]^-$. A fundamental difference needs to be pointed out between this situation and that of systems that display an *n*-electron electrochemical wave due to the presence of *n* identical redox units that are electronically and electrostatically isolated from each other: such systems have no selectivity for the multielectron process, instead, the *n* isolated units separately undergo *n* one-electron processes at the same redox potential. In principle, a selective three-electron couple is a crucial design element towards the goal of evolving $O_2$ from $H_2O$: it forces the system to oxidize two oxos directly to the superoxo oxidation state instead of the peroxide. Bypassing the possibility that $H_2O_2$ be an intermediate eliminates the problems inherent to it in electrocatalysis, namely, overpotentials and catalyst decomposition.

In practical terms, the electrochemistry of metal-porphyrinogens is not trivial. In the course of the experiments reported in this thesis, it was oftentimes observed that the electrochemical signal of a given sample would change irreversibly upon repeated voltage sweeps. The quality of the I–V curves usually would decrease drastically, and new waves would grow in. Such behavior results from radical reactions of odd-electron intermediates, from the limited stability of oxidized porphyrinogen complexes, and from solubility problems. Such difficulties can to some extent be circumvented by fast sweeps and by judicious choices of electrolyte and solvent, however the solubility constraints and the reactivity of certain solvents with strong reductants do not always allow a set of conditions to be found in which all redox transformations are reversible. Moreover, aggregation of metal porphyrinogens *via* C—C coupling or coordinative bonding is documented even in the absence of interference from external reagents.[11]

An interesting fundamental question concerning the electrochemistry of compounds in which a two-electron redox process translates into the formation or breaking of a C—C bond was brought up in a discussion with Prof. François Gabbaï.

Gabbaï's 1,8-bis(diarylmethylium)naphthalene dications are powerful oxidants, and their reaction with some hydrides and halides results in their reduction to the neutral state, in which a direct C—C bond is formed between the former methylium centers. The electrochemistry of those compounds is strongly irreversible: the neutral state displays a cathodic wave at ~1.1 V *vs* Fc/Fc$^+$, whereas the corresponding reduction occurs at a much less positive potential (~+0.3 to –0.2 V).[12,13] This behavior is rationalized as a special case of so-called ECE mechanism, whereby oxidation of the C—C bonded neutral molecule yields a C—C bonded dication, which then reacts in a subsequent chemical step to the ground-state open dication, the re-reduction of which (to the open neutral state) is shifted cathodically by an amount corresponding the stability of the C—C bond. In essence, this bistability mechanism is the intramolecular version of a well-known phenomenon, the irreversibility of the Fe(II/III) couple in some porphyrinic systems due to the axial coordination of chloride in the Fe(III) OS (bottom of Scheme IX.1). From this perspective, the fact that metal complexes of porphyrinogen exhibit cathodic and anodic DPV signals at practically the same potential becomes difficult to reconcile with the C—C bond breaking/making that also has to occur upon redox changes. On the other hand, if such changes in bonding are considered simply as an extreme case of the bond lengthening/shortening that accompanies any electron transfer reaction (see the example of hexaaquoiron, top of Scheme IX.1), then no bistability is expected.

Those two apparently conflicting views can be reconciled. If the bond making/breaking step has an activation barrier such that it is slow on the timescale of the electrochemical experiment, then bistability will be observed. Conversely, the electrochemical experiment will be blind to a "chemical" (that is, bond rearrangement) event if it is much faster than the CV sweep, and reversible electrochemistry will result. Such will be the case when structural reorganization between the geometries of the two redox states is barrierless, only corresponding to a motion along a harmonic vibrational coordinate (as is the case for the hexaaquoiron ion), but also when the two geometries (corresponding to the ground state of the oxidized and reduced versions, respectively) are, in a given oxidation state, distinct minima separated by a barrier of sufficiently low energy, such that their interconversion is faster than the CV sweep. In fact, we know from theory (Chapter III) that the equilibrium between $^1[L^{(2-,\Delta)}Zn^{(2+)}]$

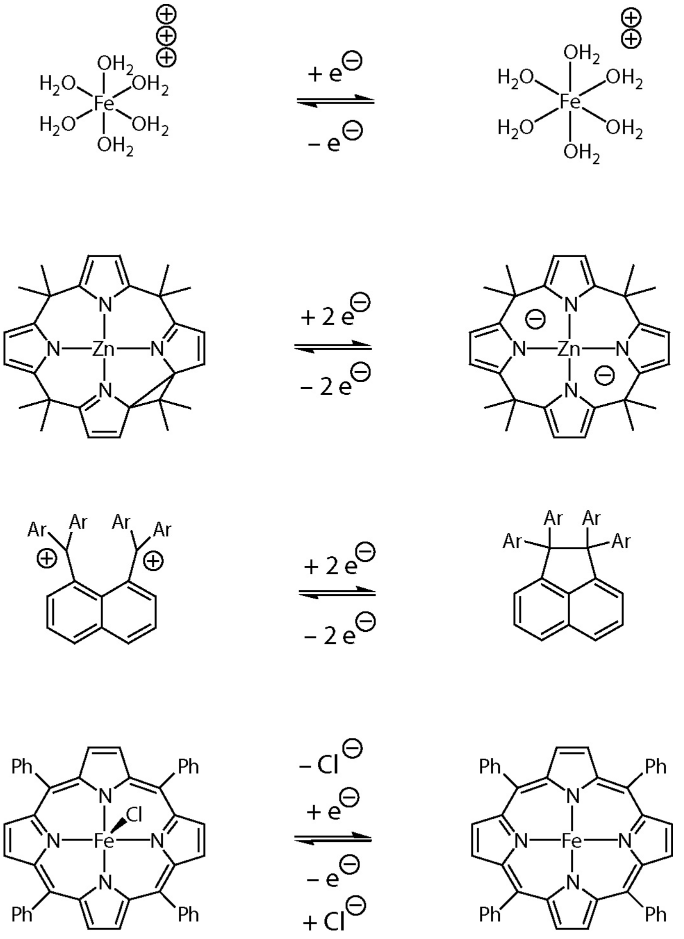

**Scheme IX.1.** Four examples of electrochemical processes involving increasing amounts of structural reorganization, or changes in bonding. Ar = Ph or substituted phenyl.[12,13]

(C—C bonded) and $^{3}[L^{(2-)}Zn^{(2+)}]$ (no C—C bond, roughly identical in its geometry to the reduced state $[L^{(4-)}Zn^{(2+)}]^{2-}$) has a small energy difference. A correspondingly low energy barrier between the two states is sufficient to explain the reversible electrochemical behavior of metalloporphyrinogens, as opposed to the di(methylium) ions mentioned above.

## IX.2. Electronic structures

The four pyrrole anions behave as very strong $\sigma$ bases within the reduced ligand $L^{4-}$. However, because the $\pi$ pair of electrons on N is involved in the aromatic system of pyrrole, porphyrinogen is not π-basic towards the central metal (in its all-$\eta^1$ coordination mode), as observed experimentally with the absence of M—N bond lengthening when M is changed from Fe to Co in $[LM^{II}]^{2-}$ (Chapters V and VIII).

The reduced $L^{4-}$ remains nucleophilic even when coordinated to a metal di- or tetracation, with the pyrrole α-C's contributing the largest coefficients to the four degenerate HOMOs. Accordingly, metal complexes of porphyrinogen are able to coordinate alkali counter-cations in $\eta^5$ fashion, and protons at the α-C. Thus, porphyrinogen is the antithesis of the so-called "ancillary ligands", the purpose of which is to not participate in any chemistry, remain inert to chemical changes at the metal, and only provide a physical barrier shielding the metal center. Porphyrinogen assists the metal in redox transformations, it also offers basic sites in the vicinity of the inorganic acidic center. This active participation of the ligand is an advantageous feature in that it allows for several reactants to be assembled prior to a bond-making reactive step — this thesis explored a path in which two $H^+$ ions were positioned in the vicinity of the two-electron reservoir before photolysis, and one could in principle conceive more involved coupling schemes. Of course, this very advantage carries an inherent drawback, namely, the difficulty of predicting and controlling reactive outcomes in a system comprising several reactive sites.

In its redox chemistry, porphyrinogen does in favorable conditions undergo well-defined two-electron transformations — even a four-electron one in a single step when coordinating Fe(III) (Fe(III) is simultaneously reduced to Fe(II) in the process). The formation and breaking of a C—C bond drives what is essentially a controlled, intramolecular version of the electropolymerization of pyrrole to become a selective two-electron event, as evidenced electrochemically and structurally. However, the short C—C "delta" bonds observed in the solid state are somewhat deceptive in that they do not reflect the bond strength. Theoretical methods show that, even though the singlet state is characterized by a well-defined bond, its homolysis yields a triplet in which the unpaired, nonbonding spins are unusually stabilized by extensive delocalization over all four pyrroles. And in fact, several experimental observations concur to offer indirect evidence in support of the DFT result: the ill-defined NMR spectrum of $[L^{\Delta}M]$, M = Mg, Zn, Ca, the fully reversible $[L^{\Delta\Delta}Zn]^{2+}$ / $[L^{\Delta}Zn]$

electrochemical couple, and the propensity of oxidized porphyrinogens to decompose, presumably *via* the formation of radicals.

The oxidation state [$L^{\Delta}M$] exhibits the hallmark of mixed valency, an IVCT optical transition. Moreover, it offers a possibility which prior to this work did not exist, the controlled modification of a single structural parameter of importance to the IVCT. In the extensive literature describing the measurement of IVCT properties in series of structurally related mixed-valent compounds and aiming to extract data on electronic coupling and electron transfer rates through different types of bridges,[14-18] comparison of series of mixed-valent dinuclear complexes differing by the size and nature of the bridge is tenuous inasmuch as replacement of a bridge with another simultaneously affects several of the crucial parameters of mixed valency, namely the electronic coupling between both metal ions, the distance separating them, and the energies of the orbitals at the metals. In contrast to this, the Mg / Zn / Ca porphyrinogen system maintains a structurally constant mixed-valent framework with set coupling and distance, while only orbital energies are tuned by the electric field imposed by the position of the electronically independent central metal ion. Moreover, the very short lifetimes observed for the excited state of [$L^{\Delta}Mg$] serve as a reminder of a fundamental difference between one- and two-electron mixed valency. In one-electron mixed valency, the spin of the valence-symmetrical state is the same as that of the localized state, whereas in two-electron mixed-valent systems the valence-symmetrical state is a diradical triplet as opposed to the singlet obtained when localization of both electrons at the same site allows for their pairing in a bonding interaction.

## IX.3. Potential for multielectron reactivity

### IX.3.a. The facts

Several published instances established the multielectron *reducing* potential of low-valent metal porphyrinogens, in particular for the binding and (in some cases) cleavage of $N_2$, although in no case was the redox ability of the ligand put to use for that purpose.[19,20] This thesis explored the reaction chemistry of some porphyrinogen complexes in transformations actively involving the macrocycle in redox fashion. The ability of the oxidized iron porphyrinogen $[L^{\Delta\Delta}Fe^{II}]^{2+}$ to carry out the oxidation of iodide to diiodine, while concomitantly being reduced to $[LFe^{III}]^{-}$, was proven, while reactions of $[LZn]^{2-}$ with $CO_2$ and of $[LZr^{IV}]$ with $O_2$ and $XeF_2$ do take place but could not be fully characterized.

One difficulty mentioned above is the possibility for the ligand to react, and potentially decompose, as already documented in the literature.[21-23] This can potentially happen *via* electrophilic / nucleophilic pathways (as postulated by the articles reporting the decomposition products), but the recurrent observation of H atom abstraction from the solvent in the systems studied here, as well as the possibility of triplet oxidized porphyrinogens, favor the hypothesis that radicals may be involved as well.

## IX.3.b. Novel avenues

One approach that could potentially shut down odd-electron reaction pathways is the use of porphyrinogen in concert with a metal ion featuring a selective two-electron redox couple. Palladium, platinum, tin, lead, phosphorus, arsenic and antimony are suitable candidates.

Preliminary forays into the octamethylporphyrinogen chemistry of antimony show that metallation is possible and that Sb-porphyrinogens can be obtained in at least two distinct oxidation states. Room temperature reaction of a THF suspension of solvated tetrasodium porphyrinogen with an equimolar amount of $SbCl_3$ results in a lightly orange mixture which, after removal of undissolved NaCl and the solvent, yields $Na(THF)_{1.5}$ $[LSb^{III}]$ in 76% yield, characterized in $^1H$ NMR by signals at 5.79 (s, 8H, β-pyrrole), 3.62 (m, 6H, THF-α), 1.78 (m, 6H, THF-β), 1.66 (s, 12H, $-CH_3$), and 1.52 ppm (s, 12H, $-CH_3$), and of adequate elemental analysis (calc. for $C_{34}H_{44}N_4NaO_{1.5}Sb$, C 60.28, H 6.55, and N 8.27%, meas. C 60.37, H 6.68, and N 8.33%). Additionally, dropwise addition of a $CH_2Cl_2$ solution of $SbCl_5$ over two hours to a cold (–78°C) $CH_2Cl_2$ suspension of solvated tetrasodium porphyrinogen in equimolar amount, followed by warming up

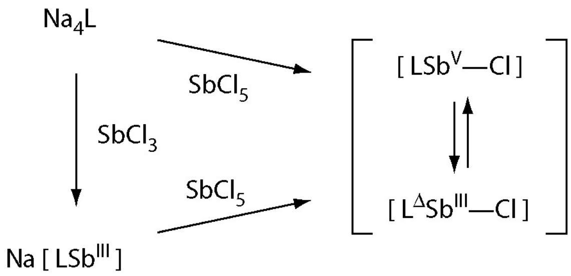

**Scheme IX.2.** Preparation of antimony porphyrinogen in two oxidation states.

to 0°C over 12 hr, then removal of NaCl and the solvent, yields $L^{\Delta}Sb^{III}Cl$ (or $LSb^{V}Cl$) as a deep purple powder in 63% yield, of elemental analysis C 57.95, H 5.63, N 9.55, and Cl 6.14% (calc. for $C_{28}H_{32}ClN_4Sb$ C 57.81, H 5.54, N 9.63, and Cl 6.09%). Finally, $L^{\Delta}Sb^{III}Cl$ (or $LSb^{V}Cl$) can also be obtained from $Na(THF)_{1.5}$ $[LSb^{III}]$ by oxidation by a stoichiometric amount of $SbCl_5$. The three transformations are summarized graphically in Scheme IX.2.

At this stage, the electronic structure of "LSbCl" is unknown, and both the $L^{\Delta}Sb^{III}Cl$ and $LSb^{V}Cl$ valence isomers can be proposed. The purple material has very limited thermal stability, turning to red, then orange, in a matter of minutes to hours at room temperature in solution, depending on the solvent. Given the relatively large size of Sb(III) and the unfavorable strain imposed by large ions on the constrained oxidized porphyrinogens, it is probable that replacement of Sb by the smaller congener P would improve the stability of the system in high-valent states, although the lesser metallic character of P might have the opposite effect in low-valent states.

## IX.3.c. Hydrogen atom abstraction in chemistry and biology

Reaction of $[L^{\Delta\Delta}Fe^{II}—OSiMe_3]^+$ with fluoride yields a single paramagnetic product that is soluble in acetonitrile, and with characteristic NMR signature. If "$LFe^{2+}$" were a traditional oxidizing agent, such as an Fe(IV) center coordinated by a dianionic ligand, then the product would naturally be formulated as "LFe=O" and expected to perform OAT chemistry, at least on thermodynamically favorable substrates. However, the peculiar nature of $[L^{\Delta\Delta}Fe^{II}]^{2+}$, an oxidant based on the *low-valent* metal ion Fe(II), means that the transient terminal oxo species formed initially cannot be the stable product isolated. Its nature as a valence-isomerized [$L^{\Delta}Fe^{IV}$=O] is excluded by the symmetry apparent in NMR and by the Mössbauer parameters. In all likelihood, the low oxidation state of the metal is maintained in a product arising from bimolecular stabilization of the initially formed oxo.

This species reacts accordingly. Instead of performing OAT to phosphines, it reverts back to its reduced [$LFe^{III}$]$^-$ state by decomposing the phosphines to a mixture of low-symmetry products, most likely indicative of radical chemistry. Although less satisfying to an inorganic chemist trained to cherish reductive eliminations and group transfers, this behavior corresponds to the lack of electrophilic character that is to be expected when the nonbonding pairs of electrons on the O atom of the oxidant do not take part in bonding because the metal center is electron-rich. The system takes the path of outer-sphere electron transfer to the oxidizing reservoir (the macrocycle in this case) with concomitant or consecutive protonation of the oxo, resulting in net H atom abstraction. In high-valent metal oxos, the level of control achieved is correlated with the stability of the M=O bond; but the strength of this bond is also a kinetic bottleneck and puts an upper limit on the range of substrates amenable to oxygenation. Enzymes that hydroxylate unactivated alkanes do not perform the well-defined and well-controllable concerted OAT into the C—H bond (as mentioned in Chapter I). Instead, they abstract the H atom in the first place, then "rebound" a hydroxyl radical onto the carbon-based radical. This is exactly the behavior that the iron porphyrinogen cation displays (and in principle, any oxidant based on an electron-rich transition metal center). The problem to solve — and a very severe one — is the control of the reactivity of such intermediate radicals. Biological catalysts achieve outstanding control by recognizing and allowing a single substrate into the vicinity of the reactive agent, and positioning reactants in a geometry so ideal that the desired reactive pathway is faster than its unproductive competitors. Inorganic chemists need to develop strategies to organize the second coordination sphere of a metal ion in a simple and versatile manner that will confer to the active center the required substrate selectivity.

## IX.3.d. A last word

The study of metalloporphyrinogen chemistry was undertaken on the premise that oxidation of the ligand instead of the metal center would weaken metal-substrate (typically metal-oxo) bond by maintaining a high d electron count, thereby enabling facile oxidative coupling of (loosely) coordinated substrates with external agents. This idea has proven to be valid, and in fact, oxidized iron porphyrinogens seem to react mostly without directly binding the substrate at all, preferring fast outer-sphere electron transfers — often resulting in decomposition *via* radical pathways unless the products of odd-electron oxidation are particularly stable (such as $I^\bullet$ in the oxidation of $I^-$). It was also realized that this type of reactivity is in fact quite akin to that of oxygenase enzymes, the difference being in the level of control over the fate of reactive radical intermediates.

Porphyrinogens may not provide a platform suitable to being developed to the level of molecular elaboration that will be needed to eventually achieve adequate substrate organization and control. Nevertheless, they have proven a very satisfying model system, one in which structures bear characteristic spectral signatures because of changes in symmetry, electronic structures can be easily rationalized theoretically in simple terms (integer oxidation states, localized spins), and spectroscopic methods can be used to cleanly interrogate specific parts of the system. And the recent burgeoning of research activity in the field of “non-innoncent” ligands[24-32] indicates that the conceptual degrees of freedom gained by unlocking the redox activity of a ligand will be put to use by inorganic chemists in the near future to carry out novel transformations.

## IX.4. References

1 Floriani, C.; Floriani-Moro, R. in *The Porphyrin Handbook*; Kadish, K. M., Smith, K. M.; Guilard, R., Ed.; Academic Press: New York, 2000; Vol. 3, pp 405-420.

2 Jubb, J.; Floriani, C.; Chiesi-Villa, A.; Rizzoli, C. *J. Am. Chem. Soc.* **1992**, *114*, 6571-6573.

3 De Angelis, S.; Solari, E.; Floriani, C.; Chiesi-Villa, A.; Rizzoli, C. *J. Am. Chem. Soc.* **1994**, *116*, 5691-5701.

4 De Angelis, S.; Solari, E.; Floriani, C.; Chiesi-Villa, A.; Rizzoli, C. *J. Am. Chem. Soc.* **1994**, *116*, 5702-5713.

5 Piarulli, U.; Solari, E.; Floriani, C.; Chiesi-Villa, A.; Rizzoli, C. *J. Am. Chem. Soc.* **1996**, *118*, 3634-3642.

6 Crescenzi, R.; Solari, E.; Floriani, C.; Chiesi-Villa, A.; Rizzoli, C. *J. Am. Chem. Soc.* **1999**, *121*, 1695-1706.

7 Bhattacharya, D.; Dey, S.; Maji, S.; Pal, K.; Sarkar, S. *Inorg. Chem.* **2005**, *44*, 7699-7701.

8 Benech, J.-M.; Bonomo, L.; Solari, E.; Scopelliti, R.; Floriani, C. *Angew. Chem. Int. Ed.* **1999**, *38*, 1957-1959.

9 Bonomo, L.; Solari, E.; Scopelliti, R.; Floriani, C.; Re, N. *J. Am. Chem. Soc.* **2000**, *122*, 5312-5326.

10 Bonomo, L.; Solari, E.; Martin, G.; Scopelliti, R.; Floriani, C. *Chem. Commun.* **1999**, 2319-2320.

11 Bonomo, L.; Solari, E.; Latronico, M.; Scopelliti, R.; Floriani, C. *Chem. Eur. J.* **1999**, *5*, 2040-2047.

12 Wang, H.; Gabbaï, F. P. *Angew. Chem. Int. Ed.* **2004**, *43*, 184-187.

13 Wang, H.; Gabbaï, F. P. *Org. Lett.* **2005**, *7*, 283-285.

14 Tom, G. M.; Creutz, C.; Taube, H. *J. Am. Chem. Soc.* **1974**, *96*, 7827-7828.

15 Kaim, W.; Klein, A.; Glockle, M. *Acc. Chem. Res.* **2000**, *33*, 755-763.

16 Londergan, C. H.; Kubiak, C. P. *Chem. Eur. J.* **2003**, *9*, 5962-5969.

17 Demadis, K. D.; Hartshorn, C. M.; Meyer, T. J. *Chem. Rev.* **2001**, *101*, 2655-2685.

18 Creutz, C. *Prog. Inorg. Chem.* **1983**, *30*, 1-73.

19 Jubb, J.; Gambarotta, S. *J. Am. Chem. Soc.* **1994**, *116*, 4477-4478.

20 Campazzi, E.; Solari, E.; Floriani, C. ; Scopelliti, R. *Chem. Comm.* **1998**, 2603-2604.

21 Solari, G.; Solari, E.; Lemercier, G.; Floriani, C.; Chiesi-Villa, A.; Rizzoli, C. *Inorg. Chem.* **1997**, *36*, 2691-2695.

22 Korobkov, I.; Gambarotta, S.; Yap, G. P. A. *Organometallics* **2001**, *20*, 2552-2559.

23 Korobkov, I.; Aharonian, G.; Gambarotta, S.; Yap, G. P. A. *Organometallics* **2002**, 21, 4899-4901.

24 Rotthaus, O.; Jarjayes, O.; Thomas, F.; Philouze, C.; Del Valle, C. P.; Saint-Aman, E.; Pierre, J.-L. *Chem. Eur. J.* **2006**, *12*, 2293-2302.

25 Butin, K. P.; Beloglazkina, E. K.; Zyk, N. V. *Russian Chem. Rev.* **2005**, *74*, 531-553.

26 Bill, E.; Bothe, E.; Chaudhuri, P.; Chlopek, K.; Herebian, D.; Kokatam, S.; Ray, K.; Weyhermueller, T.; Neese, F.; Wieghardt, K. *Chem. Eur. J.* **2005**, *11*, 204-224.

27 Massue, J.; Bellec, N.; Chopin, S.; Levillain, E.; Roisnel, T.; Clerac, R.; Lorcy, D. *Inorg. Chem.* **2005**, *44*, 8740-8748.

28 Evangelio, E.; Ruiz-Molina, D. Eur. J. *Inorg. Chem.* **2005**, *15*, 2957-2971.

29 Remenyi, C.; Kaupp, M. *J. Am. Chem. Soc.* **2005**, *127*, 11399-11413.

30 Blackmore, K. J.; Ziller, J. W.; Heyduk, A. F. *Inorg. Chem.* **2005**, *44*, 5559-5561.

31 Guerro, M.; Roisnel, T.; Pellon, P.; Lorcy, D. *Inorg. Chem.* **2005**, *44*, 3347-3355.

32 Siemeling, U.; Scheppelmann, I.; Heinze, J.; Neumann, B.; Stammler, A.; Stammler, H.-G. *Chem. Eur. J.* **2004**, *10*, 5661-5670.

# Acknowledgements

*Men who for truth and honor's sake*
*Stand fast and suffer long*
*Brave men who work while others sleep*
*Who dare while others fly*[a]

— those men and women, for the most part, can only turn to their colorful test tubes and reaction flasks or to their labmates for help, support, and comfort. A chemistry laboratory at a major research institution represents much more than the physical space in which to conduct experiments… A place to work, eat, sometimes sleep, usually not leave until well after dark. A collection of individuals from a variety of backgrounds, all of them peculiar characters to say the least, none willing to adjust to the mold. An almost self-sufficient community in which each member plows and sows (the harvesting is done by the faculty), repairs the tools, sometimes builds them, is the confessor and psychiatrist of others, propagates his or her knowledge and wisdom, and does a share of the housework and cleaning. A continuously reenacted farcical tragedy of teamwork, trust and friendship and of power, selfishness and betrayal, watched by no audience and only played by the actors for their own entertainment… I may be overly dramatic, but in short, during the five years of a Ph.D. work, one delves sufficiently deeply into research that fellow students and postdocs become the main criterion determining whether that life period is one of intense learning and personal growth or one of misery. And in the research group that I joined as an incoming student at MIT, I have been so fortunate as to meet some of the most extraordinary people I know. I would like to say a very sincere thank you to all of them.

The other students who started in the lab at the same time I did (the J-Crew) are Jenny Yang, Justin Hodgkiss, and Joel Rosenthal. Jenny's friendship has been precious from the very beginning, when we were taking classes and cumes and worried about them… Knowing that I can always rely on her and on Dave Lahr when I need a hand is invaluable, and the way this couple easily offer their efficient help, with a smile and no fanfare, allows one to accept it easily. Jenny also contributed more than her share in the tedious task of cooling the cryostats of Mössbauer and EPR instruments down to 4 K and maintaining them at that temperature as long as the experiments needed it. Justin roams in the darkness of his windowless laser lab, along with the other spectroscopists Niels Damrauer, Elizabeth Young and Steven Reece (Streece). Justin, Niels, Liz and Steve have other characteristics in common, namely an understanding of the mysterious world of wavefunctions, electrons and photons so keen, and simultaneously an intellect so generous, that they always find time, energy, and the proper words to explain physicochemical phenomena to someone like me in a simple and intelligible fashion. I have observed repeatedly that scientists who do not master the matter they are dealing with will attempt to drown it in a slew of hollow but smart-sounding (or so they think) jargon in order to cover up for their weaknesses — to me, Justin, Niels, Liz and Steve embody the exact opposite. They also agreed to spend days to carry out ultrafast measurements of my compounds, something which I would have been helplessly unable to do myself but which I think provided a very valuable perspective on my chemistry. In this respect, their contribution to this thesis has been very significant and crucial. Finally, Joel wears the organic chemist's hat in the Nocera lab, and mostly the NY Mets hat too, none of which is ideal for attracting the gratitude of us inorganic people. Nevertheless, his suggestions concerning synthesis are always insightful and often useful. And when a few of us are stranded in a shifty downtown on my birthday, he invites us all out for a good dinner !

---

[a] From "A Nation's Strength," attributed to Ralph Waldo Emerson

Among the more senior students who made up the group when I joined it, Chris Chang took me under his wing and accompanied my first few months with his knowledgeable advice and perspicacious ideas. David Manke was the crystallographer, and without his patience with my puny crystals and help with my X-ray structures, a lot of this thesis would be missing — the rest being due to his successors Matthew Shores and Arthur Esswein. The time that those three people spent looking for decent crystals of mine is truly outrageous… Without Dave, I would not have deuterated porphyrinogen either, and would probably still be looking for a way to properly characterize my paramagnetic compounds ! Additionally, his interpretation of the word "whatever" (worth a whole phrase, if not a speech, in his mouth) gave the lab material for amusement for good five years, and is probably the reason why his lunatic political opinions still cannot obliterate my high esteem for him. Bart Bartlett used to be the living summary of the Nocera lab, with its manic-depressive mood swings, its predictable and mostly inappropriate humor, its binge drinking, and that is why we all love Bart. He also furnished a helping hand for the handling of EPR and Mössbauer, and he carried out the magnetic SQUID measurements presented for iron porphyrinogens. Aetna Wun always impressed me with her combination of calm and energy, her determination, and her scientific courage. I enjoyed talking to her about all subjects, lab-related and otherwise. Lastly, Brad Pistorio gave me the perf' introduction to photochemistry, and he totally wore the coolest shoes, too.

I am much indebted to the students who joined the group in the years after me, as well. In many instances, the encouragements and kind words of Steve and Arthur, already mentioned above in other contexts, were enjoyable to hear. Liz embodies, in my eyes, the MIT grad student as he or she should be (and usually is not): dedicated to her chemistry *and* interested in other aspects of the arts and sciences; spending long hours in lab *and* maintaining a social life outside of it; serious about defending her opinions *and* able to take criticism; always smiling and energetic, interested in others, willing to help. I have learnt a lot from Becky Somers in our discussions, both from her knowledge of nanocrystals and from her natural ability to listen to others and find the proper words. Finally, Emily Nytko, Glen Alliger, Montana Childress, Emily McLaurin and Tim Cook all contributed to the good times I have had in this lab.

During those five years, I have had the chance to meet a good number of postdocs, each of whom brought in an original approach to our science, either an new experimental technique or another way of thinking about chemical problems. My immediate desk neighbors have been Leng Leng Chng (Leng$^2$) and then Shih-Yuan Liu. Both, as well as Deqiang An and Matthew Kanan, excel in an art where I have a lot to learn, that of organic synthesis, and have been willing to take the time to answer my questions in detail. Jeff Hirsch was the one who put some life, a wide, happy smile, and some decibels in lab early in the morning. This function of Jeff's was taken over (after a lengthy gap) by Ted Betley, who also impresses me every day with his acute and seemingly intuitive understanding of d orbitals and his creativity in inorganic chemistry. Alex Krivokapic and Daniel Grohol brought a pleasant touch of old Europe into our lab — maybe a different approach to the law, definitely a higher tolerance to risk (or an addiction to it). Matt Shores and Niels Damrauer, already presented above, have become the outgrowth of the Nocera lab in Colorado. Both are recognizable as outstanding personalities and outstanding scientists by the extraordinary attention, the esteem and the kind words they give to others. Adam Veige introduced me to the Canadian "eh!" and to the beauty and cleanliness of high-vacuum line technique. Jake Soper will remain in the annals of the group for the discipline he established in the use and maintenance of some of the lab's utilities. The expertise of Thomas Gray in theoretical methods allowed me to deepen my understanding of them and to correct my sometimes frivolous use of them in details. Preston Snee and Andrew Greytak have a lot to share on the chemistry and physics of quantum dots. And even though Dino Villagran really has just arrived among us (and even dislodged me from my hood), he already has shared with me a lot of his very thorough understanding of magnetism, theoretical methods, and of course Schlenk technique, and he has become a close friend.

A few superb undergraduate students were part of our lab for extended periods of time, quickly became completely autonomous in their work and in their thinking, and contributed crucially to the results, the discussions, and the atmosphere of the group. Zhi-Heng Loh (Z-Lo) was able to set up both the group's computational cluster and an IR OPA (the LoPA), on his own and of his own design. He also provided me with all the help I needed in my initial familiarization with the group's cluster. After him, his little sister Huanquian (H-Lo) did not disappoint us. Jill Dempsey and I often worked in the dry box next to one another, and during those long hours spent sweating in the butyl gloves, having somebody to chat with was more than welcome — Jill's smile, enthusiasm and humor have been missed since her departure. And the time spent working with Heiko Dückert during his summer internship was for me an especially lively and fun one.

Despite the mostly antisocial behavior of our lab towards outsiders, I have had the opportunity to meet and work with students in other groups. In the Lippard lab, Jane Kuzelka, Sungho Yoon, Emily Carson and Simone Friedle taught me the use of their Mössbauer spectrometer and helped me with the lengthy refills of liquid helium. In the Cummins group, Josh Figueroa was always ready to discuss synthesis, DFT, or any other subject. Finally, the first-year classes and teaching allowed me to befriend Ph.D. students of other chemical interests, and later on, each encounter with them in the hallways of the department on the way to an instrument was the occasion of an enjoyable, albeit often short, chat: Chudi Ndubaku, Liz Nolan, Gigi Bailey, Amrit Sinha, David Laitar, Charles Hamilton, Yin-Thai Chan, John Zimmer, Jonny Steckel.

Now of course research groups do not consist exclusively of students and postdocs, and the principal investigator, directly or indirectly, exerts a profound influence on the atmosphere of the group and on the learning experience of its members. Daniel Nocera, my advisor, is a brilliant scientist as well as an extraordinarily generous man. Over five years, he has taught me, in his own very personal way, the proper rigor in scientific experimentation, a concise yet in an odd manner flowery style of writing (which, to his defense, this prose does not even approximate), the efficient way of searching literature, the details of conducting and reporting electrochemical experiments, the state of mind necessary to distinguish a charlatan from a great scientist, and the ideal length of a minus sign — among other things. Dan's style probably does not please everyone, but it worked well with me. I was left the freedom to experiment with my own ideas, explore a chemistry of mine, and learn from my mistakes. Even though this type of management and teaching is less smooth than a more directive one, I believe that lessons learnt from it are remembered once and for all.

The other faculty in the inorganic division, Richard Schrock (chair of my thesis committee), Stephen Lippard (member of my thesis committee), Christopher Cummins, Joseph Sadighi, Alan Davison, and Dietmar Seyferth, also all had a profound influence on me. From their truly awesome example, their classes, their stimulating questions, comments and criticism, I have been able to grow in many aspects of how I conduct and think about chemical research — an invaluable intellectual evolution. Our lab hosted several visiting faculty during my time in it, and the interaction with them was a considerable enrichment to my grad student experience: Michael Sailor, Silvio Decurtins, Jeffrey Zaleski, Dai Ooyama, Xiaotai Wang (Prof X), and Darren Hamilton. I am particularly indebted to Mike for motivating me to think about aspects of materials science, an area which I am going to explore in the coming years, and to Silvio for all the time he spent discussing a variety of subjects with me, from topics of research to academia, career, skiing and hiking. Silvio's *Kirsch* has allowed Sandrine and me to prepare quite a few *fondues* since his stay in Boston, all of which have been duly savored !

The instrumentation of the department is maintained by first-class staff, to whose advice and support I owe a lot of analytical successes. In the DCIF, Mark Wall, Dave Bray and Bob Kennedy in particular have often been ready to help with less-routine techniques, jump up from their office chair to solve a problem, and accommodate special needs, and I will miss their help and their cheerfulness. Peter Müller is in charge of the X-ray facility, which he animates with his amazing energy. He also corrected mistaken assignments in my crystal structure of $Zn(O_2PF_2)_2$.

I would not have been able to graduate now had it not been for two women of extraordinary valor, Gretchen Kappelmann and Susan Brighton. Without their reminders, their efficiency, their superhuman multitasking ability, and their very human way of lending a favorable ear to all last-minute (or post-last-minute) requests of students, there is no question that deadlines would have been missed, signatures would have been lacking, and otherwise catastrophic events would not have been prevented throughout my thesis. As the persons to be addressed by both faculty and students (two categories of people who can be hard to deal with), they deserve a medal of merit.

Although I came to the United States and to Boston in order to study, I was fortunate enough to get to know people outside of MIT. They have allowed Sandrine and me to feel close to and better understand "real Americans." In particular, Johnna, Mark, Nicholas and Alexander Coggin, our host family in Central Massachusetts, immediately adopted us and made us feel at ease when we first arrived. Without their friendship, we would have missed essentials such as trips to the White Mountains and the delicious traditional Thanksgiving dinner. Betty and Arthur Roderick, our landlords and neighbors in Somerville, have been helpful for all of our everyday needs, ranging from baby-sitting to light bulbs. Friends and family from Switzerland who visited us here have also provided valued encouragement — among them, my brother Sven especially !

Several people deserve special gratitude, whose guidance and friendship in the years preceding the beginning of my Ph.D. work allowed me to learn, develop a taste of science and eventually come to Boston to earn a doctoral degree: my parents, who taught me all one needs to know about life, work, and people; my high school chemistry teacher Martine Rebstein, who awoke my passion for chemistry; and my mentor in Lausanne, Prof. Carlo Floriani. Prof. Floriani and the members of his lab, particularly Lucia Bonomo, Geoffroy Guillemot, Euro Solari, and Prof. Floriani's wife, warmly welcomed me in their group in spite of the events that unfolded at the time, helped me in all possible ways (experiments, discussions, explanations), conveyed to me their enthusiasm about inorganic synthesis, and really enabled me to apply to MIT. Their generosity and their talent remain unrivaled, and their friendship and wisdom mean a lot to me.

To all the people I named in the above paragraphs I would like to say my gratitude: your companionship and guidance have made this Ph.D. work possible. For the coming years, each of you has projects of which I am aware, both professional and personal, and to each I wish all the success that you deserve in the accomplishment of your plans. I also encourage you to keep in touch, and in the future, visits by old friends from the MIT years will always be welcome !

This last paragraph is for the two most important people of my life, my wife Sandrine and our son Igor. I cannot possibly even give an idea of Sandrine's pivotal role in what I did during these past five years — but I will try nevertheless. Sandrine abandoned her friends, her family, and her career in 2001 in order to follow me to Boston and support me in my undertaking. For the better part of our time here she spent her energy fighting an iniquitous administration that condemns a well-educated and energetic young foreigner to remain unemployed. Every day of my Ph.D. work, her loving smile, her kind words, and simply her charming presence at home every morning and every night when I would come back late from lab gave me the stamina that I needed. Sandrine is the one who confers a meaning and a goal on my life, who challenges me to think big, and who allows me to relax and breathe freely no matter what. Our hiking, backpacking, canoeing, camping excursions together, long and short, have been my rejuvenation, and the fondest memories I will keep of these five years. There is much more I want to say to Sandrine, but the rest is better said in person than written on paper. Sandrine's love, calm, determination and dedication have been necessary all the more since our little one appeared in our life. With Igor's presence, our common existence completely changed — and only for the better. Watching Igor starting to explore his surroundings, discover how to control his own body, and smile in contentment or amusement is a joy comparable to no other. Igor also made a significant contribution to this dissertation by sitting on my lap while I was working at my computer and intervening to type (or rather tap) on the keyboard when my wording did not fully satisfy him — the minor drawback of his help is the amount of baby drool that landed on the keyboard !

In March 1978, the news headlines were concerned with the invasion of South Lebanon by Israel, the kidnapping of Italian prime minister Aldo Moro by the Red Brigades, and the catastrophic wreckage of the oil tanker *Amoco Cadiz* off the shore of Brittany. The same year, the Eagles' *Hotel California* was recognized as the "record of the year". Thus, when Julien was born on March 30th in Bienne, Switzerland, 'This could be Heaven or this could be Hell,' and it was unclear in which of the two directions the world was going to evolve. To date, the balance has kept swaying on the razor's edge, and the purgatory state of our Earth has allowed Julien to grow and learn for twenty-eight years.

His father hoped to see him and his little brother Sven become downhill skiing champions or biologists. Indeed, at two and a half years of age Julien was able to ski down his first snowy slope; at four, he would crouch in front of the monstrous ant-hills common on Mont-Sujet above Bienne and observe the workers carry their loads and the soldiers defend the precious larvae. During the grade school years in his home village of Evilard and later in Bienne, a mother extraordinarily supportive in all school-related matters strongly encouraged Julien to invest all his energy into his classes and homework. In his free time, he would still mostly enjoy skiing in the Alps, mountain-biking up and down the Jura hills around Evilard, and walking in the woods with Sven to observe birds and pick mushrooms. In the late 1980s, the alpine ski racing community was dominated by Swiss legend Pirmin Zurbriggen, whose elegance on the slopes, fair play and determination impressed and inspired young Julien.

During high school at the *Gymnase Français de Bienne* on the shore of Lake Bienne, Julien was exposed to new influences that fostered other long-lasting interests. He learnt to appreciate jazz, starting from Oscar Peterson and moving on to Thelonius Monk and Michel Petrucciani. He discovered that mathematics were an invention of ancient Babylone, classical India and the Middle East, not the European Renaissance. The Bachmann family vacations in the United States left to Julien a taste of the vastness of America and the (apparent) optimism of its inhabitants. Finally, the energy and wit of his young and talented chemistry teacher — possibly her smile too — lured him into the science of matter and its transformations.

Thus, in 1997 Julien moved to Lausanne to study chemistry on the shore of Lake Léman (Lake Geneva) at the *Université de Lausanne*. He fell under the spell of his future wife Sandrine while working on lab reports, over coffees shared during monotonous classes, and sledding down the snowy slopes around Grindelwald in the Bernese Alps on a starry night. Thus, he was able to discover chemistry with the keen eagerness of those in love. He found a mentor whose style corresponded to his in the late Prof. Carlo Floriani. Julien's interaction with Prof. Floriani and members of the Floriani group taught him the magic of inorganic synthesis, the creative delight of engaged chemistry conversations, and the art of making Italian espresso.

During his Ph.D. work at the Massachusetts Institute of Technology, Julien became aware of the delicacies of *dim sum* in Chinatown, of the fears of many Americans materialized in oversized military and oversized cars, and of the breathtaking beauty of the vast, lonesome Canadian landscapes. On their honeymoon in Algonquin country, Sandrine and Julien carried their canoe from lake to lake, camped on tiny islands, confronted bears. Later, they learnt cross-country skiing in thigh-deep powdery snow in the forests of Québec. Since the birth of their son Igor in December 2005, they have discovered the delight of a toothless smile, a few syllables of baby chatter, and the tight grip of a little hand on one finger.

In the summer of 2006, the Bachmanns are headed for Halle in Germany, where Julien will join the *Max-Planck Institut für Mikrostrukturphysik* as an Alexander von Humboldt fellow.

**Julien Bachmann**

Chemistry Department, Room 2-301
Massachusetts Institute of Technology
Cambridge, MA 02139 (USA)

(617) 258 7268 — bachmann@mit.edu — http://web.mit.edu/bachmann/www

## EDUCATION

| | |
|---|---|
| 2006 | Ph. D., inorganic chemistry, Massachusetts Institute of Technology |
| 2001 | *Diplôme de chimiste*, University of Lausanne (Switzerland) |

## RESEARCH EXPERIENCE

| | |
|---|---|
| from 2006 | Nielsch research group, Experimental Department II (Gösele), Max-Planck-Institute of Microstructure Physics (Halle, Germany):<br>ordered porous membranes, atomic layer deposition, inorganic nanotubes, surface functionalization, chemical sensing, electron microscopy |
| 2001-2006 | Nocera research group, MIT:<br>molecular inorganic synthesis, physical methods, electrochemistry, crystallography, photochemistry, theoretical methods |
| 2000-2001 | Floriani research group, University of Lausanne:<br>molecular inorganic synthesis |
| 2000 | R&D Department of Cosmital SA (Marly, Switzerland):<br>organic synthesis, cosmetics (summer internship) |
| 1999 | Laboratory of Polymers and Biomaterials, Swiss Institute of Technology Lausanne (*EPFL*):<br>polymer chemistry, water treatment (summer internship) |
| 1998 | R&D Department of Orgamol SA (Evionnaz, Switzerland):<br>organic synthesis, pharmaceuticals (summer internship) |

## TEACHING EXPERIENCE

| | |
|---|---|
| 2001-2002 | Teaching assistantship, MIT:<br>Principles of Chemical Sciences (lecture course)<br>Introduction to Chemical Experimentation (laboratory course) |
| 1999-2000 | Teaching assistantship, Swiss Institute of Technology Lausanne (*EPFL*):<br>Applied Chemistry (lecture course) |

## DISTINCTIONS

| | |
|---|---|
| 2006 | Alexander von Humboldt postdoctoral fellowship |
| 2005 | Morse travel grant, MIT |
| 2005 | Bruker/MIT poster prize |
| 2002 | Award for Excellence in Teaching by a Graduate Student, MIT Chemistry |
| 2002 | *Prix Syngenta Monthey*, University of Lausanne |
| 2001 | Presidential Fellowship, MIT |
| 2000 | *Prix Louis Pelet*, University of Lausanne |
| 1999 | *Prix de Faculté*, University of Lausanne |

# List of publications

## Journal articles

**Bachmann, J.**; Nocera, D. G. *Inorg. Chem.* **2005**, *44*, 6930-6932
"Structural Tuning of Ligand-Based Two-Electron Intervalence Charge Transfer"

Rosenthal, J.; **Bachman, J.**; Dempsey, J. L.; Esswein, A. J.; Gray, T. G.; Hodgkiss, J. M.; Manke, D. R.; Luckett, T. D.; Pistorio, B. J.; Veige, A. S.; Nocera, D. G. *Coord. Chem. Rev.* **2005**, *249*, 1316-1326
"Oxygen and hydrogen photocatalysis by
two-electron mixed-valence coordination compounds"

**Bachmann, J.**; Nocera, D. G. *J. Am. Chem. Soc.* **2005**, *127*, 4730-4743
"Multielectron Redox Chemistry of Iron Porphyrinogens"

**Bachmann, J.**; Nocera, D. G. *J. Am. Chem. Soc.* **2004**, *126*, 2829-2837
"Multielectron Chemistry of Zinc Porphyrinogen:
A Ligand-Based Platform for Two-Electron Mixed Valency"

## Conference presentations

**Bachmann, J.**; Nocera, D. G.: ACS Spring National Meeting 2006
"Multielectron chemistry of metal-porphyrinogens:
How a ligand can store and release up to four redox equivalents"

**Bachmann, J.**; Nocera, D. G.: Bruker/MIT Symposium 2005
"Structural and Spectroscopic Basis of Ligand-Based Two-Electron Redox Chemistry"

**Bachmann, J.**; Nocera, D. G.: Gordon Research Conference on Inorganic Chemistry 2005
"Two- and four-electron redox activity on the ligand:
Multielectron chemistry of metal-porphyrinogens"